Technical University of Munich
Department of Physics
Dense and Strange Hadronic Matter

First observation of the p–Ξ^- interaction via two-particle correlations

Bernhard Hohlweger

Technical University of Munich
Department of Physics
Dense and Strange Hadronic Matter

First observation of the p–Ξ^- interaction via two-particle correlations

Bernhard Hohlweger

Vollständiger Abdruck der von der Fakultät für Physik der Technischen Universität München zur Erlangung des akademischen Grades eines

Doktors der Naturwissenschaften (Dr. rer. nat.)

genehmigten Dissertation.

Vorsitzender:		apl. Prof. Dr. Norbert Kaiser
Prüfer der Dissertation:	1.	Prof. Dr. Laura Fabbietti
	2.	Prof. Dr. Lothar Oberauer

Die Dissertation wurde am 23.10.2020 bei der Technischen Universität München eingereicht und durch die Fakultät für Physik am 25.11.2020 angenommen.

Abstract

The strong interaction among the different hadrons at relatively small momentum transfers is difficult to describe via direct solutions of Quantum Chromodynamics, due to the running of the coupling constant. Only very recently, attempts of first principle calculations based on lattice simulations have been made and these have yet to be tested. Typically, the description of the interaction among hadrons relies on phenomenological models and effective theories, where several free parameters have to be constrained from experimental observations. Since numerous measurements are available in the nucleonic sector, a sound understanding of N–N interactions is well established. In the strangeness sector however, the experimental knowledge is rather limited and the constraints to pin down precisely the interaction involving hyperons are missing. The lack of experimental data also hinders the validation of novel approaches to describe the baryon interaction based on lattice QCD, which currently provide applicable results for baryon pairs, including at least two or more strange quarks. Furthermore, the poor constraints available for descriptions of interactions involving hyperons, limit the understanding of their appearance and behavior in cold nuclear matter at extreme densities, which thereby hampers a solid modeling of the inner parts of neutron stars.

Femtoscopy is based on a study of the two-particle correlation function, where final-state effects among specific particle pairs induce a signal that is characterized by the space-time extend of the particle emission source. Recent studies demonstrate that the strong interaction can be studied from this observable if the characteristics of the emission region are sufficiently constrained. This work extends this approach to investigate the strong interaction of p–Ξ^- pairs. In the first part of this analysis, the p–p, $\overline{\mathrm{p}}$–$\overline{\mathrm{p}}$, p–Λ and $\overline{\mathrm{p}}$–$\overline{\Lambda}$ correlation functions are measured in elementary p–Pb and pp collisions at the LHC with the ALICE detector. In a detailed study the source radius is measured as a function of the pair transverse mass m_{T} considering, for the first time in a quantitative way, the effect of strong resonance decays. After correcting for this effect, the radii extracted for pairs of different particle species agree. This indicates that protons, antiprotons, Λs and $\overline{\Lambda}$s, as well as Ξ^- and $\overline{\Xi}^+$ originate from the same source. In the second part, these results are applied to constrain the source size of p–Ξ^- pairs. The two-particle correlation function of p–Ξ^- and $\overline{\mathrm{p}}$–$\overline{\Xi}^+$ pairs is measured with ALICE in both collision systems. The comparison of the measurement with the prediction, assuming only an attractive Coulomb interaction, is not compatible with the data. The enhancement above the Coulomb prediction indicates the presence of an additional component due to the attractive strong interaction among a proton and a Ξ^- baryon, which is observed in this way for the first time. Furthermore, the comparison of the data to predictions of this strong interaction from lattice QCD calculations by the HAL QCD collaboration exhibits a qualitative agreement. This serves as a first direct test of these first principle calculations, which supports the description of the N–Ξ^- interaction in this approach. The lattice potentials are therefore useful to investigate the role of the Ξ^- in the context of neutron stars. Consequently, its interaction within a neutron rich environment is expected to be more repulsive than typically assumed, which suggests a stiffening of the Equation of State of neutron star matter at large densities.

Kurzfassung

Die starke Wechselwirkung zwischen verschiedenen Hadronen bei niedrigen Impulsüberträgen direkt mittels der Quantenchromodynamik zu beschreiben ist schwierig, da die Kopplungskonstante relativ große Werte annimmt. Erst seit kurzem gibt es Versuche von Grundlagenberechnungen basierend auf Gitter-Simulationen, welche allerdings noch verifiziert werden müssen. Typischerweise wird die Wechselwirkung zwischen Hadronen durch phänomenologische Modelle und effektive Theorien beschrieben, wobei mehrere freie Parameter durch experimentelle Beobachtungen eingegrenzt werden müssen. Da zahlreiche Messungen im nukleonischen Sektor zur Verfügung stehen, besteht ein fundiertes Verständnis der N–N Wechselwirkung. Im Sektor seltsamer Teilchen ist das experimentelle Wissen jedoch eher begrenzt, und es fehlen die Randbedingungen, um die Wechselwirkungen, an denen sich Hyperonen beteiligen, präzise zu beschreiben. Das Fehlen von experimentellen Daten verhindert außerdem einen Test neuer Ansätze die Wechselwirkung von Baryonen basierend auf Gitter-Berechnungen direkt zu beschreiben, die gegenwärtig anwendbare Ergebnisse für Baryonen-Paare mit mindestens zwei seltsamen Quarks liefern. Die spärliche Beschreibung der Wechselwirkung, an der Hyperonen beteiligt sind, macht es nur eingeschränkt möglich ihr Erscheinen und Verhalten in kalter Kernmaterie bei extremen Dichten zu verstehen und verhindert dadurch eine solide Beschreibung der inneren Region von Neutronensternen.

Femtoskopie basiert auf der Untersuchung der Zwei-Teilchen-Korrelationsfunktion, wo aufgrund der Wechselwirkung von Teilchen im Endzustand ein Signal erzeugt wird, welches durch die raum-zeitliche Ausdehnung der Emissionsquelle zum Zeitpunkt der Teilchenproduktion gekennzeichnet ist. Neuere Studien zeigen, dass es möglich ist die starke Wechselwirkung mittels dieses Signals zu untersuchen, falls die Ausdehnung der Emissionsregion ausreichend bekannt ist. In dieser Arbeit wird dies angewendet, um die starke Wechselwirkung von p–Ξ^--Paaren zu untersuchen. Im ersten Teil dieser Analyse werden die p–p-, $\overline{\mathrm{p}}$–$\overline{\mathrm{p}}$-, p–Λ- und $\overline{\mathrm{p}}$–$\overline{\Lambda}$-Korrelationsfunktionen in elementaren pp- und p–Pb-Kollisionen am LHC mit dem ALICE-Detektor gemessen. In einer detaillierten Studie wird der Radius der Quelle als Funktion der transversalen Masse des Paares gemessen, wobei zum ersten Mal auf quantitative Weise der Effekt starker Resonanzzerfälle berücksichtigt wird. Nach Korrektur dieser Modifikationen stimmen die extrahierten Radien für Paare unterschiedlicher Teilchensorten überein. Dies deutet darauf hin, dass Protonen, Antiprotonen, Λ, und $\overline{\Lambda}$, aber auch Ξ^- und $\overline{\Xi}^+$ aus der gleichen Quelle stammen. Im zweiten Teil werden diese Ergebnisse angewandt, um die Quellengröße von p–Ξ^--Paaren abzuschätzen. Die Zwei-Teilchen-Korrelationsfunktion von p–Ξ^-- und $\overline{\mathrm{p}}$–$\overline{\Xi}^+$-Paaren wird mittels des ALICE-Detektors in beiden Kollisionssystemen gemessen. Der Vergleich der Messung mit der Vorhersage, für die ausschließlich eine attraktive Coulomb-Wechselwirkung angenommen wird, zeigt das Vorhandensein einer zusätzlichen Komponente auf. Daher kann zum ersten Mal die attraktive starke Wechselwirkung zwischen einem Proton und einem Ξ^--Baryon beobachtet werden. Darüber hinaus werden die Daten durch Vorhersagen der starken Wechselwirkung mittels Gitter-Berechnungen der HAL QCD-Kollaboration qualitativ beschrieben. Dies dient als erster direkter Test dieser Grundlagenberechnungen und unterstützt die Gültigkeit der Beschreibung der N–Ξ^--Wechselwirkung auf diese Weise. Die Gitterpotentiale sind daher nützlich, um die Rolle des Ξ^- im Zusammenhang mit Neutronensternen zu untersuchen. Folglich wird erwartet, dass in einem neutronenreichen Umfeld die Wechselwirkung des Ξ^- abstoßender ist als typischerweise angenommen, was letztendlich auf eine Versteifung der Zustandsgleichung der Materie von Neutronensternen bei höheren Dichten hindeutet.

For Lukas

Contents

1. Introduction

The fundamental Lagrangian that describes the physics of the Standard Model at high energies is gauge invariant under $SU(3) \times SU(2)_L \times U(1)_Y$ transformations and is derived within the context of Quantum Field Theory. Coupling terms, which connect fields of matter particles (fermions) with those of exchange particles (bosons), represent interactions in the standard model [1]. The $SU(3)$ component leads to Quantum Chromodynamics (QCD), where the exchange of massless gluons mediates the strong interaction. The $SU(2)_L \times U(1)_Y$ component constitutes the electroweak interaction, which at lower energies separates into the electromagnetic and weak interactions. The former constitutes the $U(1)$ component of the symmetry group and is mediated by the exchange of massless photons, as it is described by Quantum Electrodynamics (QED). For the weak force, however, the gauge symmetry is lost since it requires the exchange of massive $W^{\pm}$ and Z^0 bosons.

1.1. Quantum Chromodynamics (QCD)

The Lagrangian of QCD can be written as [2]

$$\mathcal{L} = \sum_q \overline{\psi}_{q\,a} \left(\gamma^{\mu} D_{ab\,\mu} + m_q \right) \psi_{q\,b} - \frac{1}{4} F^{A\,\mu\nu} F^{A}_{\mu\nu}, \tag{1.1}$$

where γ^{μ} are the Dirac matrices and $\psi_{q,a}$ are the spinors of the quark fields in each flavor q, up (u), down (d), charm (c), strange (s), top (t) and bottom (b), as well as their mass m_q and color $a = 1, 2, 3(r, g, b)$. Furthermore,

$$D_{ab\,\mu} = i\partial_{\mu}\delta_{ab} - \frac{g_S}{2} \lambda^{C}_{ab} A^{C}_{\mu} \tag{1.2}$$

is the Gauge invariant derivative. The first term represents the propagation of free quarks and the second term the coupling to the gluon fields A^{C}_{μ}, where the index C runs over $1, 2, \ldots, 8$ and the λ^{C} denote the eight generators of $SU(3)$. Correspondingly, there also exist eight configurations of the gluon fields carrying different combinations of color and anti-color. This term is governed by the strong coupling constant $g_S = \sqrt{4\pi\alpha_S}$ and rotates the color of the quark field spinor upon interaction with the gluon field. Additionally, the A^{C}_{μ} themselves are propagated by the last term in Eq. 1.1, which is defined as

$$F^{A}_{\mu\nu} = \partial_{\mu} A^{A}_{\nu} - \partial_{\nu} A^{A}_{\mu} - g_S f^{ABC} A^{B}_{\mu} A^{C}_{\nu}. \tag{1.3}$$

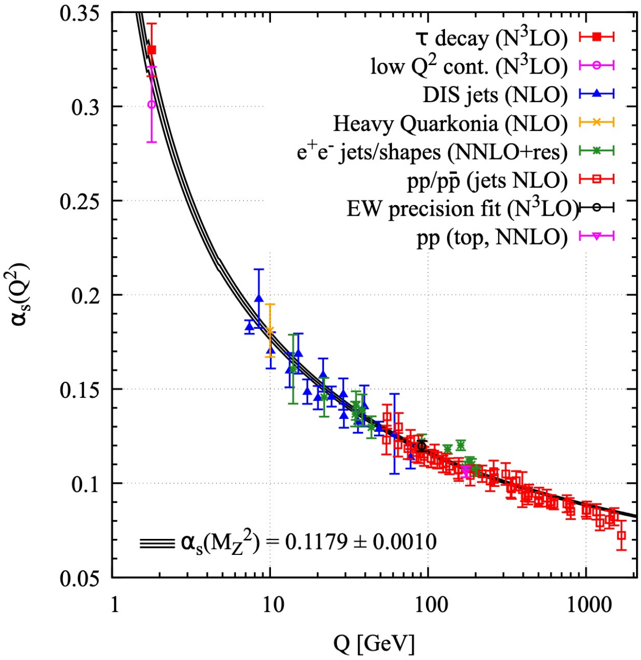

Figure 1.1.: Running of the coupling constant α_S as a function of the energy transfer Q compared to different measurements, from [2].

Here, f^{ABC} is the structure constant of $SU(3)$, and the indices A, B and C run over all eight color configurations of the gluon field. The last term of this equation corresponds to a coupling of the gluon field with itself. As a result, for the strong force there exist not only interaction vertices among quarks and gluons but also among gluons themselves. The only free parameters in QCD are the quark masses as well as the coupling constant that defines the strength of the interaction.

Contrary to the coupling constant of QED, the one of QCD is said to be running, since it exhibits a strong dependence on the momentum transfer upon interaction Q, as it is depicted from several measurements in Fig. 1.1. The equations of QCD can be solved based on perturbation theory if $\alpha_S \ll 1$ and upon renormalization of QCD Lagrangian it is evident that with increasing Q the interaction strength α_S decreases. Since Q is inversely proportional to the distance, the behavior of α_S at large Q suggests an anti-screening of color charges at small interaction distances and a weakening of the strong force to a point where quarks are quasi-free particles. This gives rise to a phenomenon known as asymptotic freedom [1]. At the same time the behavior of the coupling constant, prohibits to employ perturbative approaches as Q decreases. The strength of the strong interaction grows as the separation among the quarks and gluons increases. This suggests that isolating a single quark requires an infinite amount of energy and that it is instead energetically favorable to create a new quark anti-quark pair [3]. This means that quarks and gluons are supposed to be bound to color neutral objects. This and the fact that quarks and gluons were experimentally never individually observed gives ground to the confinement hypothesis that color-charged particles cannot be isolated and clump together in color-neutral bound states, so-called hadrons [3].

The current masses of the lightest quarks, as they are generated by the Higgs mechanism [4–6], are $(2.16^{+0.49}_{-0.26})$ MeV for the u quark, $(4.67^{+0.48}_{-0.17})$ MeV for the d quark and (93^{+11}_{-5}) MeV for the s quark [2]. As the building blocks of hadrons they themselves contribute only very little to the total mass, for example that of a proton with 938 MeV. In general, the Lagrangian of Eq. 1.1 can be written by Weyl spinors [1] in terms of left- and right-handed chirality. In the chiral limit with massless quarks of three flavors the Lagrangian is symmetric under rotations of $SU_L(3) \otimes SU_R(3)$. This implies that hadrons should exist in degenerate parity doublets, which is not observed in nature. Therefore the symmetry has to be spontaneously broken [7], which means that it is realized by the Lagrangian, but not the QCD ground state or vacuum. The latter is characterized as a quark anti-quark condensate with a non-vanishing expectation value $\langle q\bar{q}\rangle = \langle \bar{q}_L q_R + \bar{q}_R q_L\rangle \approx -(250\,\mathrm{MeV})^3$ [8], which connects left- and right-handed quarks [9]. The quarks propagate through this condensate and are therefore dressed by their interactions, which leads to the generation of a larger mass. For quarks with finite mass, the term enclosing m_q in Eq. 1.1 also breaks this symmetry explicitly. But due to the small masses of quarks, this effect can be treated systematically in terms of perturbation theory [9]. Consequently, there exists an approximate $SU(3)$ flavor symmetry between u, d and s quarks, which motivates i.a. the arrangement of spin 1/2 (3/2) baryons in octet (decuplet) states according to their Isospin I_3 and Strangeness S, as depicted for the baryon octet in Fig. 1.2. A baryon with at least one s quark has the quantum number $|S| > 0$ and is considered a hyperon, denoted as Y. The mass splitting of the isospin states can be interpreted for the most part by the fact that flavor symmetry is only approximate. The large mass difference of the s quark to the u or d quark then leads to a larger degeneracy between states with different S than between those with different I_3.

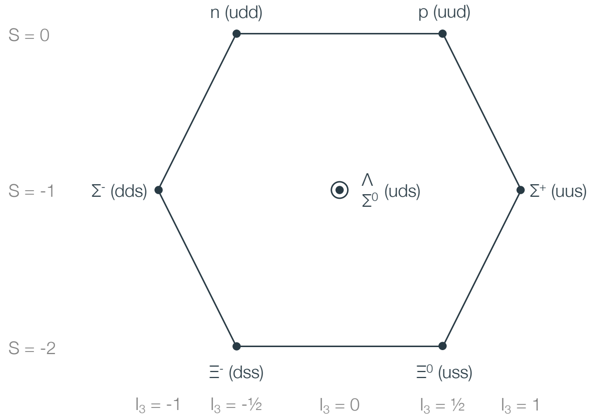

Figure 1.2.: Baryon octet for $J^P = 1/2^+$ from [10].

1.2. Interactions among Hyperons and Nucleons

The strong force mediates not only the interaction among quarks, but also among hadrons. In nature it is responsible for the formation of nuclei composed of protons and neutrons, where the lightest being the deuteron, a bound state of one proton and one neutron. For pairs of octet baryon, 36 flavor states exist, but if $SU(3)$ flavor symmetry is fully realized, only six irreducible representations remain [11, 12][1]:

$$8 \otimes 8 = 27 \oplus 8_s \oplus 1 \oplus 10 \oplus \overline{10} \oplus 8_a. \tag{1.4}$$

The first three terms correspond to the $L + S$ symmetric configurations, the last three terms to the $L + S$ anti-symmetric configurations. Different elements contribute depending on the pair of octet baryons and their state to define their interaction. For example, the deuteron is described solely by the $\overline{10}$ element [11], while the N–N interaction receives contribution from 27 and $\overline{10}$ [14].

1.2.1. Theoretical Frameworks

The Lagrangian of QCD is the starting point to derive any description of the interactions among hadrons. Nuclear physics takes place in the regime of low Q, where α_S is too large to apply perturbative approaches. Instead the description of the interaction among hadrons relies on effective approaches via phenomenological models and effective field theories or on numerical approaches via lattice QCD.

In a picture, where the substructure of baryons is ignored, the interaction at larger distances can not be mediated by a single gluon due to confinement. In 1935 Yukawa proposed to describe interaction among elementary particles, meaning protons and neutrons, by the exchange of a boson with a mass approximately 200 times that of the electron mass. Later, the particle was discovered to be the pion, the lightest known color neutral object. Phenomenological models typically split the interaction into three regions [15]: the long range region ($r \gtrsim 2\,\text{fm}$) mediated by a one pion exchange, the intermediate region ($1\,\text{fm} \lesssim r \lesssim 2\,\text{fm}$) mediated by exchanges of multiple pions or mesons with larger masses as the σ or ω, and the short range region ($r \lesssim 1\,\text{fm}$) with a repulsive core.

A power counting scheme to describe the interaction in a more systematic, perturbative manner is developed in chiral effective field theory (χ EFT) [7, 9]. The Lagrangian of this theory is defined such that it is consistent with the symmetries of low-energy QCD [7]. The short-range dynamics, which are impossible to observe at low energies, are replaced by effective degrees of freedom described by Goldstone bosons and nucleons or Hyperons [7]. Pions, but also kaons and η mesons, are Goldstone bosons, which appear due to spontaneous breaking of chiral symmetry. They become massive, since

---

[1] A comprehensible overview over the individual states can be found in the appendix of [13]

the symmetry is also explicitly broken, but are noticeably lighter than any of the other hadrons with similar quark content, e.g. the ρ meson. In the limit $m_q \to 0$, these Goldstone bosons are massless and non-interacting. Correspondingly, a chiral Lagrangian is ordered in a power counting scheme of pion masses and corresponding derivatives via the order parameter Q/Λ_χ, where $Q \sim m_\pi$ and $\Lambda_\chi \sim m_\rho$, the chiral symmetry breaking scale, and is then expanded in terms of a small pion masses or momentum transfers [7]. In turn, the interaction between hadrons can be described up to a certain precision also called order and visualized by Feynman diagrams. The unknown details of the interaction at each vertex are encapsulated in low-energy constants, which have to be constrained with experimental input.

Lattice QCD is an alternative approach to calculations within QCD and is based on the evaluation of path integrals by using Monte Carlo sampling methods. Observables, e.g. hadron masses, are calculated by solving the equations of motion obtained from the QCD Lagrangian by propagating quarks and gluons on a discretized space-time lattice with a spacing a and size L. Divergences within QCD and the renormalization of the Lagrangian are easy to handle due to the cut offs defined by the finite size and width of the lattice. The interpolation to $a \to 0$ produces predictions at the so-called physical point. If L is large enough to accommodate two hadrons, also their interaction can be observed. At the same time, however, a has to be small enough to provide the means for a stable interpolation towards the physical point. An observable could be estimated with infinite precision if all possible path integrals were computed in a simulation. Since this is impossible, the observable has an uncertainty that decreases the more path integrals are sampled or the smaller the total number of path integrals is. The latter is influenced by the distance a particle can propagate, which is inversely proportional to its mass [16]. While these calculations are only feasible on large scale computers, it is often still necessary to work with increased quark masses in order to obtain observables with reasonable uncertainties. Even though this circumstance leads to an inaccurate estimate, e.g. pion masses of $m_\pi > 400\,\mathrm{MeV}$ at the physical point [13, 15], it is possible to demonstrate key features of nuclear potentials, such as the existence of a repulsive core [15]. At the same time, however, these results fail to reproduce the properties of the deuteron [17]. Only very recently, the HAL QCD collaboration [18] succeeded to produce results close to the physical pion masses ($m_\pi = 146\,\mathrm{MeV}$). As sketched in Fig. 1.3, predictions with reasonable uncertainties are available, however, only for pairs with $|S| > 2$, since they contain an increasing number of s quarks, which are heavier than u and d quarks.

1.2.2. Experimental Measurements

Both, effective theories and lattice calculations, need experimental constraints, either to fit the low-energy constants or to validate predictions. The availability of experimental data for different baryon pairs as a function of strangeness is schematically indicated as the height of light blue bar in Fig. 1.3. The nucleonic sector is well constrained by

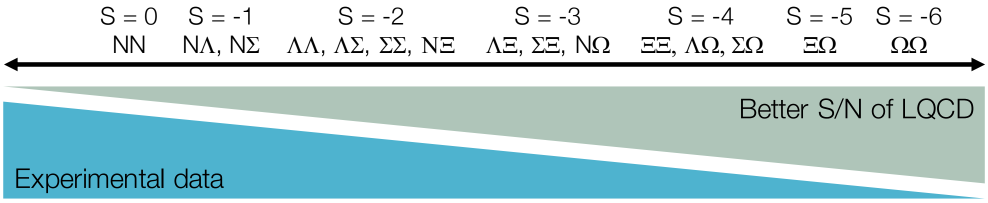

Figure 1.3.: Comparison of the prediction strength of lattice QCD for different baryon-baryon pairs versus the available data. Reproduced from [19].

numerous experimental observations. An example is the fact that more than 4000 data points [20] are available solely for low momentum N–N scattering experiments.

Already in the strangeness $|S| = 1$ sector experimental measurements are complicated by the fact that hyperons are unstable and as a result low momentum N–Y and Y–Y reactions are difficult or even impossible to perform. Some attempts were made to produce low momentum Λ and Σ baryons and to observe them in hydrogen bubble chambers [21, 22]. Due to the difficulty to produce and to detect such events, the measured N–Σ and N–Λ elastic and inelastic cross sections are associated with large uncertainties and cover only a very limited kinematic range (lab momenta $p_{\mathrm{Lab}} > 100\,\mathrm{MeV}/c$). Recent studies based on measurements of the p–Λ [23, 24] and p–Σ^0 [25] correlation function promise to improve on the uncertainties and to examine the interaction at lower momenta in the future.

Studies of hypernuclei, which are bound states of hyperons that are absorbed within different nuclei, are experimentally easier to realize. In these measurements the kinematic analysis of the decay products yields the binding energy of a hyperon inside a specific nucleus. The interaction of the hyperon inside the hypernucleus usually involves multiple neighboring nucleons and several quantum numbers. In practice, however, the details of the many-body problem are absorbed by models within an effective average interaction of the hyperon with the whole nucleus, which is characterized by a so-called single-particle potential. Due to the substantial amount of measurements of Λ hypernuclei and their binding energies [26], a smaller version of the nuclear chart can be drawn and a depth of the single-particle potential at the nuclear saturation density $\rho_0 \approx 0.17\,\mathrm{fm}^{-3}$ of $U_\Lambda \approx -30\,\mathrm{MeV}$ is well established [27]. Experimental observations of the in-medium behavior of the Σ are however limited to a single finding of a hypernucleus [28, 29], and a few measurements of the excitation spectrum from (π^-,K^+) reactions on different targets [30, 31]. Even though analysis of these measurements point towards a repulsive single-particle potential of the Σ at ρ_0, there is significant uncertainty due to the model dependence of these results.

For increasing strangeness the experimental data becomes rather scarce. Since several decades, particular experimental interest in the $|S| = 2$ sector is triggered by the search for a stable bound state of six quarks, the H-dibaryon. Its signature is expected to appear in the coupled system $\Lambda\Lambda$-$\mathrm{N}\Xi$-$\Sigma\Sigma$ [32], but so far attempts to locate any structure in the invariant mass spectrum of Λ–Λ pairs failed [33–35]. The $|S| = 2$ sector is explored experimentally with (K^-,K^+) reactions induced by a K^- beam with energies between $1\,\mathrm{GeV}/c$ to $2\,\mathrm{GeV}/c$ on a nuclear target. Typically, a quasi-free Ξ^- is produced if the momentum of the outgoing K^+ is larger than $1\,\mathrm{GeV}/c$ [36]. A direct investigation of the Λ–Λ interaction, however, is not possible in this way and no scattering data of this pair exist. Instead, their interaction is directly studied via correlation measurements. In Au–Au collisions at a center-of-mass energy of $\sqrt{s_{\mathrm{NN}}} = 200\,\mathrm{GeV}$ the STAR collaboration reported a repulsive interaction [37]. A repeated analysis of the same data [38] with a more careful treatment of background contributions, as well as a measurement by the ALICE collaboration in elementary proton-proton (pp) and proton-lead (p–Pb) collisions [39] point towards a weakly attractive interaction. The latter measurement, also delivered the most stringent experimental limit on the maximum binding energy of a hypothetical $\Lambda\Lambda$ bound state of $3.2^{+1.6}_{-2.4}(\mathrm{stat.})^{+1.8}_{-1.0}(\mathrm{syst.})\mathrm{MeV}$.

The (K^-,K^+) reaction is useful nevertheless to produce double Λ hypernuclei via the absorption of the Ξ^- and in order to study the Λ–Λ interaction at ρ_0. The so-called Nagara Event [40] is an unambiguously identified nucleus containing two Λ baryons. Its analysis results in an interaction energy of $\Delta B_{\Lambda\Lambda} = 0.67 \pm 0.17\mathrm{MeV}$ and also points towards a weakly attractive Λ–Λ interaction [41].

A few scattering events of Ξ^- hyperons are detected by observing their trajectories either directly in bubble chamber experiments [42–45], by emulsion experiments [46], in scintillating fiber (SCIFI) active targets [47, 48] or indirectly by reconstructing them in other setups [49]. Two examples for Ξ^- scattering events, one in a bubble chamber and one in the SCIFI target, are shown in Fig. 1.4. The lifetime of the Ξ^- is $c\tau = 4.9\,\mathrm{cm}$ and is long enough to directly observe its trajectory, but since it decays into a Λ and a π^-, the neutral Λ itself is invisible in these experiments. In p–Ξ^- reactions, also the proton itself can be observed. (In-)elastic scattering cross sections are calculated from these events and an overview is presented in Table 1.1. It is clear, that the low cross section of the initial (K^-,K^+) reaction and the complicated detection of Ξ scattering events, severely limits the available data, in particular, in the low momentum region ($p \lesssim 1\,\mathrm{GeV}/c$).

Additional information of the $\mathrm{N}\Xi$ interaction is inferred from measurements of the invariant and missing mass distributions in hypernuclear production experiments that are induced by (K^-,K^+) reactions on d, C and Cu targets [50–52]. The smooth behavior of these distributions around the $\mathrm{N}\Xi^-$ threshold is interpreted as an indication for small scattering lengths of the p–Ξ^- and n–Ξ^- interaction [53]. As shown in in Fig. 1.5, bound states of the Ξ^- are investigated by measuring the excitation energy spectrum in $^{12}\mathrm{C}(\mathrm{K}^-,\mathrm{K}^+)$ reactions via the outgoing K^+ [54]. The missing mass resolution of the measurement is insufficient to resolve individual hypernuclear states. Instead, the production cross section of $^{12}_{\Xi^-}\mathrm{Be}$ is calculated with the distorted wave impulse approximation, where scattering off a single nucleon within C produces a quasi-free Ξ^-, which then interacts with the spectator nucleons. The latter is described by a mean

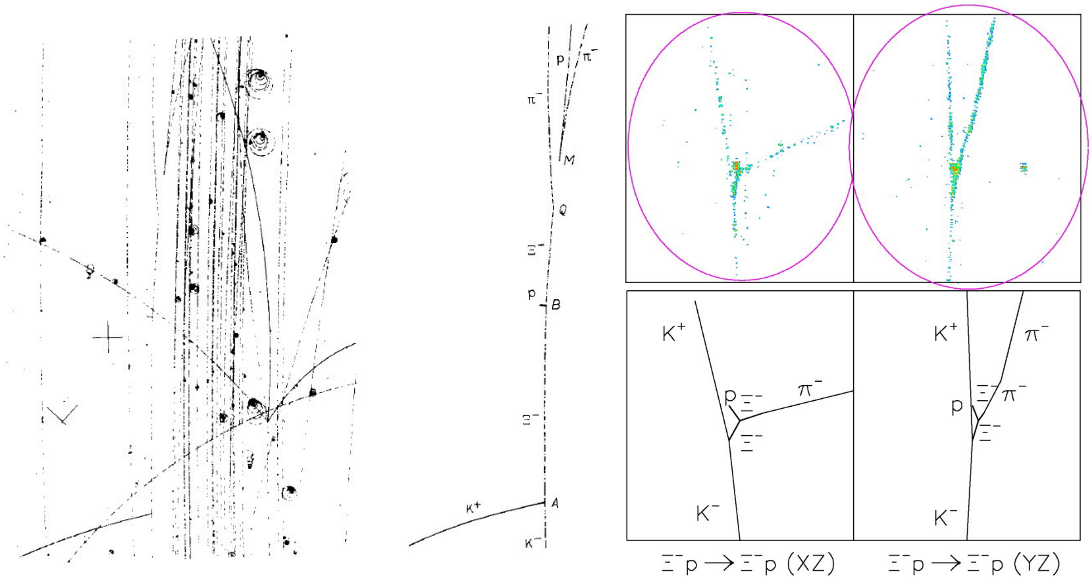

Figure 1.4.: Examples for the (K^-,K^+) reaction and subsequent elastic scattering of the Ξ^- as observed by a bubble chamber [42](left) and in a SCIFI target [48](right).

Ref.	p (GeV/c)	Channel	σ (mb)	Comment
[48]	0.2-0.8	Ξ^-p_{elastic}	< 24	scattering on free p
		$\Xi^-p \to \Lambda\Lambda$	< 12	scattering on free p
		$\Xi^-p \to \Lambda\Lambda$	$4.3^{+6.3}_{-2.7}$	quasi-free in ^{12}C
[46]	0.4-0.6	$\Xi^-p_{\text{inel.}}$	$12.7^{+3.5}_{-3.6}$	emission prob. in nuclear emulsion
[47]	$\simeq 0.6$	$\Xi^-p_{\text{inel.}}$	15	abs. prob. in ^{12}C
			13	abs. prob. in nuclear emulsion
[49]	0.55	Ξ^-N_{elastic}	$30.7 \pm 6.7^{+6.3}_{-2.7}$	$\sigma(\Xi^-p)/\sigma(\Xi^-n) = 1.1^{+1.4}_{-0.7}{}^{+0.7}_{-0.4}$
[43]	1-4	Ξ^-p_{elastic}	13 ± 6	On ^{2}H in bubble chambers
		Ξ^0p_{elastic}	19 ± 10	
[44]	2	Ξ^0p_{elastic}	8	
		$\Xi^0p_{\text{el. + inel.}}$	61 ± 20	
[42]	2.9	Ξ^-p_{elastic}	23	
		Ξ^-p_{total}	> 25	
[45]	1.5-12	Ξ^0p_{inel}	21 ± 4	
		$\Xi^0p_{\text{tot., inel}}$	≈ 25	

Table 1.1.: Overview of measurements of $N\Xi^-$ elastic and inelastic cross sections. [42–45] are observations in bubble chambers, [46] in emulsion experiments, [47, 48] in scintillating fiber (SCIFI) active targets and [49] from direct reconstruction and analysis of the Ξ^- after scattering on ^{9}Be.

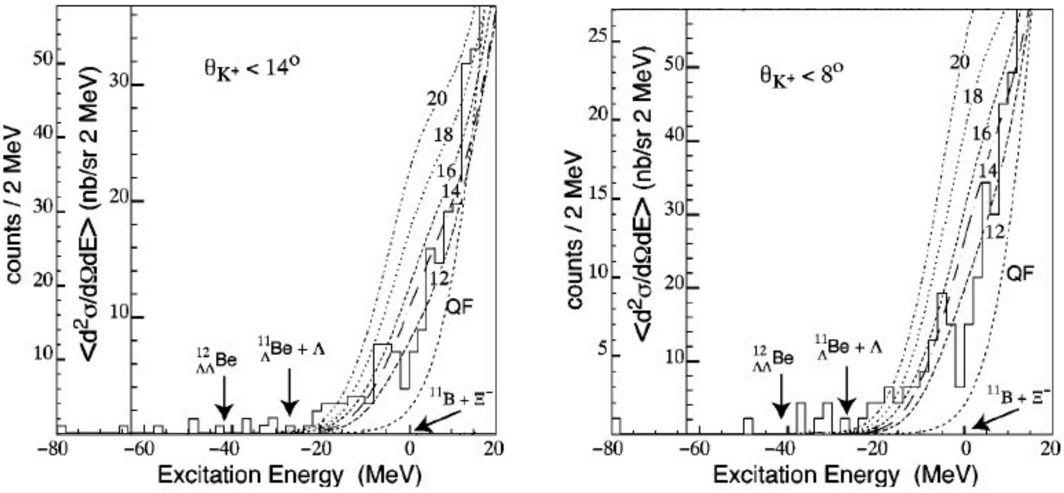

Figure 1.5.: Excitation energy spectrum from [54] measured in ^{12}C(K$^-$,K$^+$) for different ranges of the acceptance of the spectrometer: (left) full acceptance $\theta_{K^+} < 14°$, (right) limited acceptance $\theta_{K^+} < 8°$. The curves represent model calculations for the quasi-free production of Ξ^-, and for the production of $^{12}_{\Xi^-}$Be for different potential depths of the Wood-Saxon Ξ^- potential.

field, which is computed by describing the N–Ξ^- interaction by Wood-Saxon potentials with different depth parameters. The data discard the result for the solely quasi-free production of Ξ^- and seem to favor an interaction described by a Wood-Saxon potential with a depth of $U_{\Xi^-} = -14\,\text{MeV}$. This result, however, is rather model dependent, as calculations of the same cross section within the context of the semi-classical distorted wave method [55] seem to favor a potential $U_{\Xi^-} \approx 0\,\text{MeV}$.

The so-called Kiso event [56], is the first Ξ^- hypernucleus that is directly observed and unambiguously identified in an emulsion experiment, as shown in Fig.1.6. The reaction is induced by a Ξ^- which is produced in a (K$^-$,K$^+$) reaction. It is absorbed by the

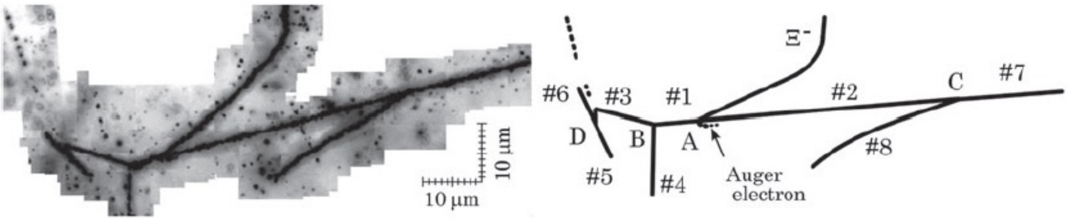

Figure 1.6.: (left) Decay of a Ξ^- hypernucleus, the Kiso Event [56], observed in emulsion. (right) Schematic drawing of the event.

nucleus of a N atom, which decays as $\Xi^- + ^{14}\mathrm{N} \rightarrow ^{10}_{\Lambda}\mathrm{Be} + ^{5}_{\Lambda}\mathrm{He}$. The binding energy of the Ξ^- within the nucleus is then estimated to be $B_{\Xi^-} = 4.38 \pm 0.25\mathrm{MeV}$, in case the $^{10}_{\Lambda}\mathrm{Be}$ is produced in its ground state or $B_{\Xi^-} = 1.11 \pm 0.25\mathrm{MeV}$ in case it is produced in an excited state. In a second Ξ^- hypernucleus event, the so-called Ibuki event [57, 58], the binding energy is estimated in a preliminary analysis as $B_{\Xi^-} = 1.27 \pm 0.21\mathrm{MeV}$.

1.2.3. Theoretical descriptions of the Interaction among Hyperons and Nucleons

Due to the large amount of experimental data in the nucleonic sector, the interaction among nucleons can be precisely described by phenomenological approaches as the Argonne v_{18} [59] potential or by χ EFT in up to fourth order (N^3LO), which incorporates effects of two- and three-body nuclear forces. The latter thereby successfully describes the structure of few nucleon systems [7] and can be used as a basis for a realistic description of the EoS of nuclear matter [60–63].

In the $|S| = 1$ sector χ EFT is available at NLO and uses mainly 36 scattering data points to fit 13 low-energy constants[2] [66]. The resulting scattering parameters and/or two-particle wave functions can be used to independently reproduce the behavior of the measured p–Λ and p–Σ^0 correlation function [23, 25] and the depth of the computed single-particle potential at ρ_0 [67] is in agreement with hypernuclear measurements. In this context, first attempts to approximate the effect of three body forces at NLO [68] highlight the importance of the latter for an accurate description of the behavior of the Λ at larger densities. A comparison between the single particle potentials computed with and without three-body forces is shown in Fig. 1.7 for symmetric nuclear matter and neutron matter in the left and right panel, respectively. It can be seen, that at finite densities the repulsive three-body force among ΛNN causes a much shallower single-particle potential in both environments and further, lowers the density, where the Λ interaction becomes overall repulsive. Unfortunately, the limited amount of experimental measurements, prohibits a meaningful calculations of χ EFT at NNLO, where three-body forces are estimated more precisely.

The measurements in the $|S| = 2$ sector are not suited to determine the low-energy constants of χ EFT at NLO directly. Instead, in an exploratory study [53], the parameters obtained from the experimental data in the $|S| = 1$ sector for χ EFT at NLO, are carefully adjusted. The authors recently published an update [69] to investigate the in-medium properties of the Ξ^- and thereby further adjust a few parameters. As indicated by Fig. 1.3, for increasing strangeness the uncertainties of lattice calculations shrink and for $|S| = 2$ they reach a level, where it becomes feasible to compare them to experimental measurements. In the following, the discussion focuses on the most recent

---

[2] In fact there are 20 low-energy constants at NLO, which are reduced to 13 by assuming $SU(3)$ flavor symmetry and only S-wave contributions [64]. Further, an updated version is available, which uses additional constraints from the N–N sector [65]

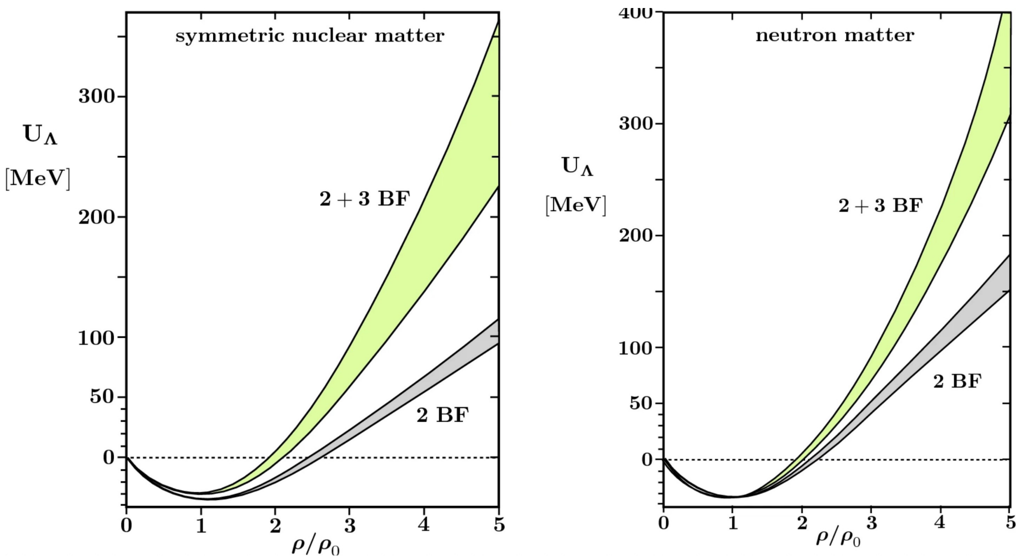

Figure 1.7.: Single particle momentum U_Λ of a hyperon at rest in symmetric nuclear matter (left) and neutron matter (right) based on χ EFT at NLO [64]

results of (2+1)-flavor lattice simulation by the HAL QCD collaboration at physical pion and kaon masses ($m_\pi \simeq 146\,\text{MeV}$ and $m_\text{K} \simeq 525\,\text{MeV}$) [19, 70, 71]. The Λ–Λ scattering length[3] and effective range agrees between χ EFT [53] ($a_0 = (0.62 - 0.70)$ fm and $r_0 = (4.65 - 6.95)$ fm) and lattice QCD [71] ($a_0 = (0.81 \pm 0.23^{+0.00}_{-0.13})$ fm and $r_0 = (5.47 \pm 0.78^{+0.09}_{-0.55})$ fm) within uncertainties. Even though these values correspond to an attractive interaction, it is too weak to allow a H-dibaryon to form as a bound state of two Λ. The values are also well in agreement with the correlation measurement by the ALICE collaboration [39], and are similar to those predicted by models tuned to describe hypernuclear measurements like the Nagara event [72, 73].

For both calculations the coupling between ΛΛ and NΞ states is expected to be weak at low energies. The potentials of the N–Ξ interaction obtained from lattice simulations in the different isospin and spin states are depicted in the left panel of Fig. 1.8. The width of the individual curves is estimated by observing the potentials at different sink-times of the lattice simulation. All isospin and spin channels reproduce the typical features of the short-ranged strong interaction. A repulsive core is visible at $r \to 0$, an attractive pocket appears at intermediate particle distances and it converges to zero for distances $r > 2\,\text{fm}$, which hints to an overall attractive interaction. This can be more clearly seen from the corresponding phase shifts, which is shown as an example for pairs in the $I = 0$ and $S = 0$ state in the right panel of Fig. 1.8. In this specific case a sudden increase by almost 60° is observed indicating a significant attraction. Also the phase shifts of all other isospin and spin combinations are positive, except for $I = 1$ and $S = 0$ state. A

---

[3] Here and in the following the convention of femtoscopy is used, where a positive scattering length corresponds to a attractive interaction

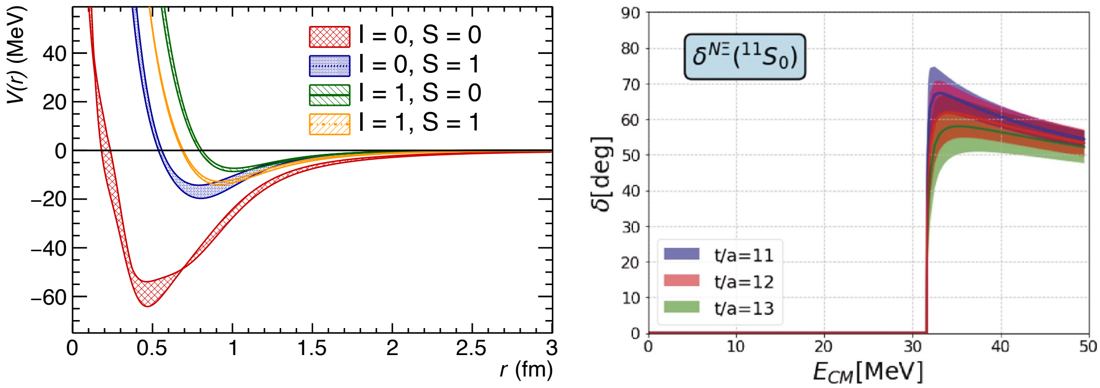

Figure 1.8.: (left) N–Ξ potentials for individual isospin and spin states computed from lattice simulations by the HAL QCD collaboration. The width of the bands are estimated by combining the potentials extracted at different sink-times t/a [71]. (right) Corresponding scattering phase shift for N–Ξ pairs in the $I = 0$ and $S = 0$ state from lattice calculations [71].

similar behavior is seen from the phase shifts calculated with χ EFT at NLO [69]. All four states of isospin and spin combinations are occupied by p–Ξ^- pairs and therefore an attractive interaction among these particles is expected.

The in-medium properties of the Ξ^- have to be calculated in order to compare them to measurements of the excitation energy and of the binding energy B_{Ξ^-} in hypernuclei. At ρ_0 the Ξ^- single-particle potential based on χ EFT at NLO is estimated to have a depth of $U(\mathrm{p}_{\Xi^-} = 0) = -(4.1 - 5.5)$MeV [69]. More refined calculations [74], which are based on an updated version of χ EFT at NLO [69], are able to obtain the binding energy for individual energy levels of the Ξ^- bound state in ^{12}C and ^{14}N, which reproduce those reported for the Kiso event. Furthermore, the single-particle potential based on lattice simulations of the Ξ^- interaction are obtained by utilizing a BHF approach [75], where the interaction potentials of all $|S| = 2$ pairs as well as the single-particle potentials of the Λ, Σ and N have to be taken into account. While U_{N} is computed in a straight forward way from phenomenological models of the N–N interaction, the U_Λ and U_Σ are computed in the same way as U_{Ξ^-}, where the relevant potentials are obtained from those in the $|S| = 2$ sector by assuming $SU(3)$ flavor symmetry. The resulting single-particle potentials at ρ_0 for the different particle species are depicted in Fig. 1.9 by the curves of different color. They are reported for pure neutron matter (PNM) and for symmetric nuclear matter (SNM). The uncertainties associated with the lattice simulations of the potentials for the $|S| = 1$ sector are large [76], but as a qualitative cross check their central values are used to investigate the effect of flavor symmetry breaking. The results for the Ξ^- potential is depicted by the light blue curve and agrees reasonably well with the result assuming flavor symmetry. For a Ξ^- in SNM a potential value of $U(\mathrm{k}_{\Xi^-} = 0) = -(4.0 \pm 2.0)$ MeV is calculated, which indicates a shallow attractive

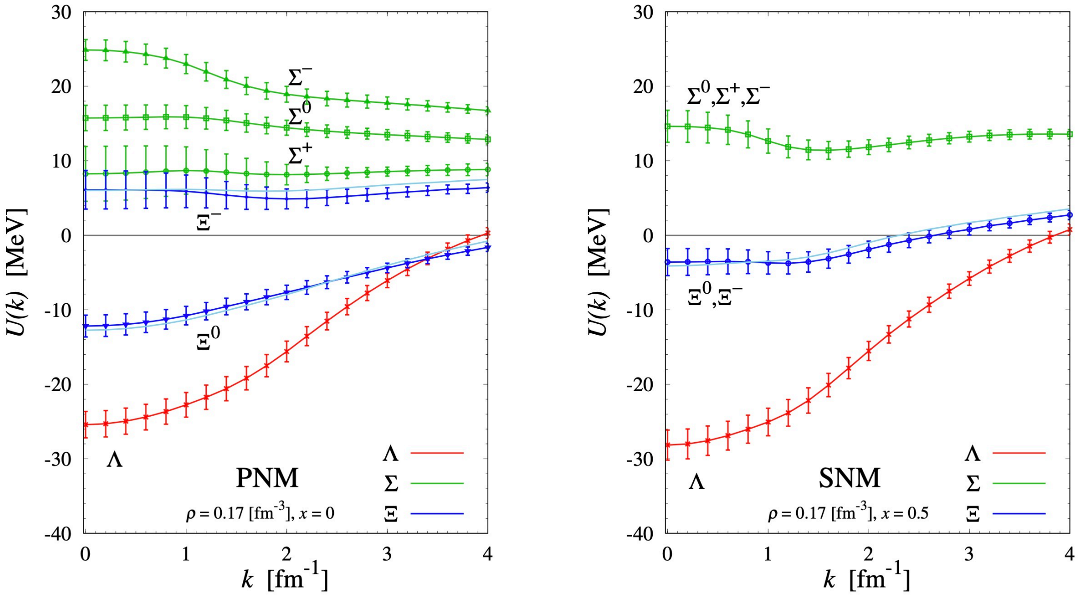

Figure 1.9.: Single-particle potentials of hyperons in pure neutron matter (PNM) and symmetric nuclear matter (SNM) utilizing the predictions of the potentials from lattice calculations by the HAL QCD collaboration in Brueckner-Hartree-Fock calculations. Figure taken from [75].

interaction and is in a experimental observations. It is worth noting the agreement of the single-particle potential of the Λ, $U(\mathrm{k}_\Lambda = 0) = -(28.0 \pm 2.0)$ MeV with the value extracted from measurements.

Experimental data of the interaction among $|S| = 3$ pairs is absent so far, but a measurements and an analysis of the p–Ω^- correlation function has been performed [77]. Studies of pairs with $|S| \geq 3$ are particularly intriguing, since lattice calculations predict bound states in the p–Ω^- [78] and Ω–Ω system [79]. Unfortunately, at this point firm statements based on these lattice calculations are hampered due to the presence of strangeness rearrangement processes, e.g. $\mathrm{p}\Omega^- \rightarrow \Lambda\Xi^-$, and further measurements to pin down the contribution to the p–Ω^- interaction from inelastic channels are necessary.

Correlation studies in general are emerging as the only alternative to scattering experiments to deliver direct experimental measurements related to the two- and maybe even multi-particle interaction in the strangeness sector. These constraints are needed to validate lattice predictions in a direct way and to improve the estimation of low energy constants of χ EFT [69]. In this context, a unified description of the N–N and N–Y sector provides the means to evaluate quantitatively the effect of $SU(3)$ flavor symmetry breaking, as it is assumed by theories and models. Additionally, advancing χ EFT with strangeness to higher orders will incorporate more precisely many-body forces [68]. The latter is particularly important, in order to obtain precise estimates of the single-particle potentials that characterize the behavior of hyperons in dense nuclear matter. This is particularly relevant in astrophysics, since it appears to provide a solution to the so-called hyperon puzzle of neutron stars, which is discussed in the next section.

1.3. Neutron Stars and Strangeness

In laboratories collisions of various projectiles at different energies create systems, which range from those with very high temperatures and negligible densities [80] to those at moderate temperatures and densities of a few ρ_0 [81]. However, terrestrial experiments are unable to create an environment similar to that in the core of a neutron stars, where at zero temperature densities of $5 - 10\rho_0$ are expected to be reached [82]. Hence, these stellar objects are a unique laboratory to test QCD at extreme conditions and their description has become an active field of research.

From astrophysical observations neutron stars are found to have masses between $1 - 2M_\odot$, with $M_\odot$ being the mass of the sun, and radii of around 10 km [83]. Consequently, gravitational forces subject the system to an enormous pressure, which is directed towards its center and threatens to collapse the neutron star into a black hole. Unlike in our sun, where the photon pressure due to the burning of nuclear fuel in fusion processes counteracts the gravitational collapse, in neutron stars this process comes to a stop and instead, the constituents themselves have to provide this pressure by their interactions [82]. The many-body effects on a microscopic scale translates to the Equation of State (EoS) on the macroscopic scale. The EoS relates the pressure or the energy per nucleon to the matter or energy density and is said to be either stiff or soft depending on the compressibility of the system. Due to the gravitational forces acting on a neutron star, the EoS cannot be too soft and needs a certain stiffness in order to withstand the pressure. The requirement to balance the pressure from gravity and the pressure from the interaction among particles can be converted via the Tolman-Oppenheimer-Volkoff (TOV) equations into a relation between mass and radius of a neutron star [84, 85]. These equations are derived within general relativity for a non-rotating spherical neutron star.

In this context, observations of neutron stars with masses of about $2M_\odot$ [86–88] are particularly interesting, since these provide a benchmark for the stiffness of the EoS to support such masses. A similarly precise knowledge of the radii would deliver another valuable constraint, but unfortunately their measurements are associated with large uncertainties up to now [83]. Observations of neutron star mergers via gravitational waves are sensitive to a parameter called the tidal deformability Λ of neutron star matter, which can be linked to the EoS. The initial analysis by the Ligo/Virgo collaboration estimated a value of $\Lambda < 800$ [89] and a later analysis using stricter assumptions estimated a value $\Lambda = 190^{+390}_{-120}$ [90].

The actual EoS of dense nuclear matter is currently reasonably well determined at two opposing limits. At extremely large densities calculations within QCD applying

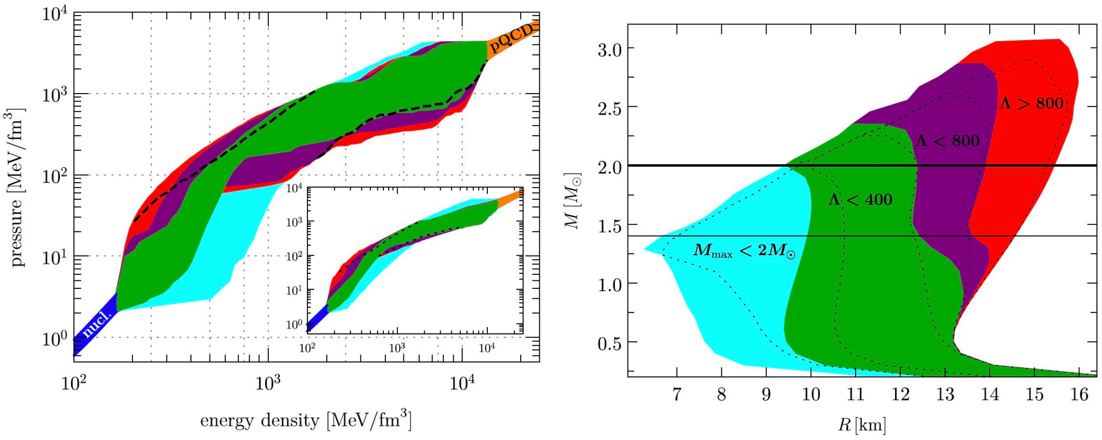

Figure 1.10.: EoS (left) and resulting mass radius relation (right) estimated by interpolation between the nuclear EoS (blue) and the pQCD EoS (orange) taking into account astrophysical constraints. The region excluded by the $2M_\odot$ limit is indicated in cyan, the regions excluded by a constraining the tidal deformability of a $1.4M_\odot$ neutron star to values of i) $\Lambda < 800$, ii) $400 < \Lambda < 800$ and iii) $\Lambda < 400$ are indicated in i) red, ii) violet and iii) green. Figures taken from [91].

perturbation theory (pQCD) deliver an EoS with uncertainties of around 20% at $\rho \gtrsim 40\rho_0$ [91]. On the other end, earth-bound experiments are able to test and to constrain the EoS of matter up few ρ_0. A reliable theoretical description of the neutron-rich phase dominated by nucleon interactions obtained by e.g. χ EFT. [63] with similar uncertainties as pQCD is obtained up to ρ_0.

In the region between low and high densities the combined constraints from observations can be used to estimate limits of the EoS via interpolation methods [91, 92], as it is depicted in the left panel of Fig. 1.10. The area excluded by the requirement to support a star with $2M_\odot$ are indicated in cyan, and those areas corresponding to additionally limiting i) $\Lambda < 800$, ii) $400 < \Lambda < 800$ and iii) $\Lambda < 400$ are indicated in i) red, ii) violet and iii) green. The resulting constraints in terms of mass and radius are calculated via the TOV equations and are displayed in the same color code in the right panel of the same figure. As expected, the EoS needs to be sufficiently stiff to support a star with a mass of $2M_\odot$. Thereby, neutron stars with small radii $r \lesssim 10\,\mathrm{km}$ in the intermediate mass range are excluded. As it can also be seen, limiting the upper range of Λ, excludes those EoS that are too stiff and in this way limits the upper range of radii in the intermediate mass range to $r \lesssim 14\,\mathrm{km}$. This already indicates that a precise and simultaneous measurement of mass and radius of a neutron star, as well as further observations of neutron star mergers via gravitational waves will add valuable constraints to the EoS. Nevertheless, these limits already help to understand the inner structure of neutron star on a microscopic scale. There are strong hints that the inner structure of neutron stars with intermediate masses of up to $1.5M_\odot$ remains compatible with hadronic degrees of freedom [93]. In the core of the heaviest neutron stars with masses close to $2M_{\odot}$, however, densities are reached, where the behavior of the EoS might be linked to the appearance of quark matter [93].

These limits can be used to test detailed descriptions of the EoS on a microscopic scale. The neutron-rich matter is thought to be in an equilibrium against weak decays [94]. Neutrons are fermions and are therefore affected by Pauli blocking. Consequently, with increasing densities their Fermi momentum and thereby also their chemical potential increases. If the chemical potential of nucleons reaches the same level as that of other particles, it becomes energetically favorable to produce these particles instead and the appearance of hyperons via leptonic channels, e.g. $\mathrm{p} + \mathrm{e}^- \rightarrow \Lambda + \nu_e$, becomes possible [95]. In this context the interaction of these particles at finite densities becomes relevant. In a simplified picture, an attractive (repulsive) interaction decreases (increases) the chemical potential of a particle and thereby shifts the threshold for its appearance to lower (higher) densities [96].

Starting from measurements in vacuum or at ρ_0, calculations of the interaction at finite densities rely on relativistic mean field models (RMF), which are based on phenomenological descriptions of particle interactions via the exchange of different mesons [97], or other methods like Dirac–Brueckner–Hartree–Fock approaches [98] or Quantum Monte Carlo approaches [99]. Several measurements constraining the interaction of nuclear matter at finite densities exist, e.g. see Sec. 5.3.1 of [94] for a recent review. Therefore, two- and three-body forces are included in state-of-the-art descriptions of the EoS, which can be extrapolated to higher densities in a controlled way [63, 97]. In contrast, the experimental knowledge of hyperonic matter, as discussed in the previous section, is limited to vacuum densities and ρ_0, where the single-particle potential of $U_\Lambda = -28\,\mathrm{MeV}$ is well established, but canonical values of $U_\Sigma \approx 30\,\mathrm{MeV}$ and $U_\Xi \approx -18\,\mathrm{MeV}$ have to be assumed. The composition of matter in a neutron star as a function of the density calculated via a RMF approach is shown in Fig. 1.11. As the density increases, the Λ appears at a density of approximately 2 ρ_0, followed by the Σ^- and Ξ^- at approximately 2.5 ρ_0. At even larger densities, it is expected that hyperons constitute a significant fraction of the matter present in a neutron star.

The new degree of freedom and the fact that these particles interact with their surroundings, influence the behavior of the EoS. Figure 1.11 shows the mass radius relation for different calculations of the EoS within a Quantum Monte Carlo approach [99]. In case of pure nuclear matter the interaction among nucleons leads to a stiff EoS and the resulting mass radius relation (green curve) reaches the limit of $2M_{\odot}$. Moreover, the presence of the Λ and an additional and an attractive N–Λ interaction yields a much softer EoS and as a consequence, the mass radius relation (red curve) is unable to reach the $2M_{\odot}$ limit at all. This is referred to as the hyperon puzzle, which states that the appearance of hyperons as an additional degree of freedom is expected at large enough densities, which consequently softens the EoS to a point, where it is unable to support the masses of the heaviest neutron stars. The solution appears to be the

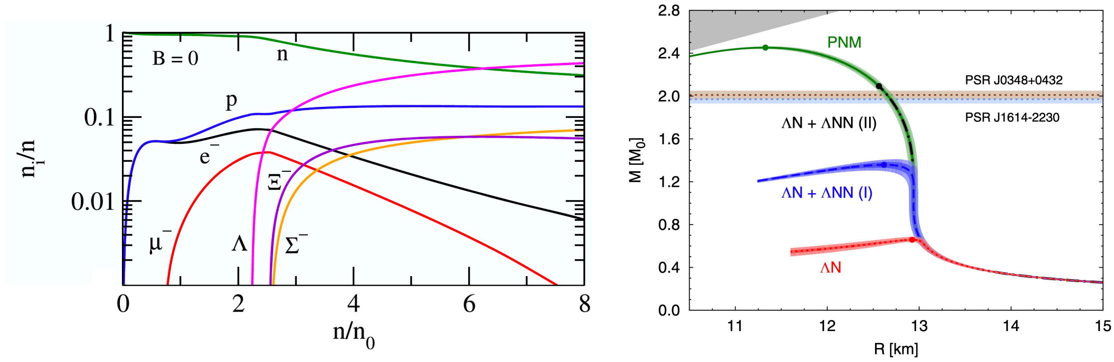

Figure 1.11.: (left) Particle fractions as a function of the density, using the FSU2H model to describe the nucleonic interaction and for different hyperons single-particle potentials of $U_\Lambda = -28\,\text{MeV}$, $U_\Sigma = 30\,\text{MeV}$ and $U_\Xi = -18\,\text{MeV}$ [97]. (right) Resulting mass radius relation from the EoS computed via Quantum Monte Carlo simulations under different assumptions of the composition and Λ interaction inside a neutron star: i) purely nucleonic matter (green curve), ii) (attractive) two-body NΛ interaction (red curve). iii) (attractive) two-body NΛ interaction combined with a (repulsive) three-body NNΛ interaction obtained in two different parametrizations (blue and black curve) [99]

.

inclusions of a repulsive interaction either among hyperons themselves [96] or due to a three-body N–N–Λ interaction. As discussed in Sec. 1.2.3, there are indications for the presence of the latter from χ EFT calculations [68, 100], which turn the Λ single-particle potential repulsive around $2\rho_0$. Such a possibility is explored in the same Quantum Monte Carlo calculations [99]. Two different parametrizations of a repulsive three-body N–N–Λ interaction are obtained from measurements of the separation energy of different hypernuclei. The resulting EoS becomes stiffer and can support larger neutron star masses, as it can be seen from the corresponding mass radius relations (blue and green curve) presented in the right panel of Fig. 1.11. The repulsion of the three-body force in one parameterization is even strong enough, to prohibit the production of the Λ at all and hence the curve follows that of pure neutron matter. It needs to be stressed, however, that both parametrizations reproduce experimental observations. Furthermore, These calculations only investigates the Λ, but also other hyperons as the Σ and the Ξ has to be taken into account in the computation of a realistic EoS. So far, however, the lack of precise experimental data on their interactions prohibits any firm conclusions on the presence and effect of their interaction, in particular concerning three-body interactions. This highlights the uncertainty of current calculations and the need for a better experimental understanding of the two- and three-body interaction of hyperons.

In case of the Ξ^-, current calculations, as they are presented in Fig. 1.11, assume a single-particle potential of $U_{\Xi^-} \approx -18\,\text{MeV}$. It should be obvious from the discussion of experimental constraints in the previous section that this value can only be considered a good guess. Therefore, it is interesting to see the effect of its variation on the EoS and

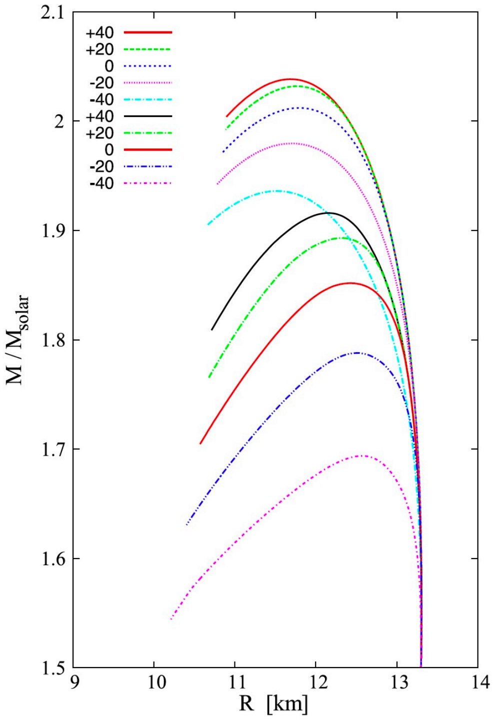

Figure 1.12.: Mass radius relations for variations of U_{Ξ^-}. The curves in the upper (lower) branch represent the calculations with (without) a repulsive Y–Y interaction [96].

the corresponding mass radius relation. Within the context of RMF calculations [96] U_{Ξ^-} is varied to values of $(-40, -20, 0, +20, +40)$MeV. The resulting mass radius relations are depicted in Fig. 1.12. Furthermore, these calculations explore the effect of an additional repulsive Y–Y interaction, where the upper branch corresponds to calculations that incorporate a repulsive Y–Y interaction, the lower branch to those with no Y–Y interaction. There is a strong dependence on the value of U_{Ξ^-} as well as on the presence of a repulsive Y–Y interaction. At this point, it is clear that precise experimental data of the hyperon interaction, as it is presented in this work for the Ξ^-, plays a crucial role to constrain and validate theoretical calculations within χ EFT or lattice QCD, in order to establish a sound EoS for neutron stars.

2. Femtoscopy

Part of the motivation for this work is to help in the understanding of astronomical objects, neutron stars. It is a delightful coincidence that the method, femtoscopy, originates at least partially in astrophysics. At the end of the 50s, Hanburry Brown and Twiss used the principle of intensity interferometry to measure the correlation strength between photons emitted from Sirius and deduced successfully the angular extend of the star [101]. At the beginning of the 60s, particle physicists started to investigate differences of angular distributions of like and unlike-sign combinations of pion pairs that were produced in proton-antiproton reactions [102]. It was quickly realized that the discrepancy could be explained by correlations between like-sign pion pairs caused by the interference and symmetric nature of their two-particle wave function [103]. Correlations between particles arise not only due to the (anti-)symmetrization of the two-particle wave function, but also due to modifications of the latter by Coulomb and strong interactions. In the following years, the developments in theory, phenomenology and experiments further refined the formalism. Correlation measurements became the tool to study the space time properties of the particle emitting region created in heavy-ion collisions [104]. The term Femtoscopy was coined by the typical extent of the source in heavy-ion collisions of a few fm. Crucial for this work, however, is the fact that final-state interactions (FSIs) and final-state effects produce these correlations, which means that measurements are sensitive to the strong interaction of different particle pairs.

2.1. Two Particle Correlation Function

The observable is the two-particle correlation function and it is defined as the ratio of the Lorentz-invariant pair spectra and the product of the single particle spectra [105],

$$C(\vec{p}_1, \vec{p}_2) = \frac{E_1 E_2 \mathrm{d}N^{12} / (\mathrm{d}^3 p_1 \mathrm{d}^3 p_2)}{(E_1 \mathrm{d}N^1 / \mathrm{d}^3 p_1)(E_2 \mathrm{d}N^2 / \mathrm{d}^3 p_2)} = \frac{N(\vec{p}_1, \vec{p}_2)}{N(\vec{p}_1)\, N(\vec{p}_2)}. \tag{2.1}$$

Here, $\vec{p}_i$, $i = 1, 2$ is the momentum[1] of each particle, and the above can also be understood as the ratio between $N(\vec{p}_1, \vec{p}_2)$, the probability to find a pair of particles with

---

[1] Absolute (scalar) values will be italic (a), three vectors will be marked by the arrow ($\vec{a}$), four vectors are bold ($\mathbf{a}$).

momenta $\vec{p}_1$ and $\vec{p}_2$, and $N(\vec{p}_i)$, the probability to find each particle with a momentum $\vec{p}_i$.

The link of Eq. 2.1 to quantities that can be obtained experimentally is rather straightforward. A convenient choice of reference system is the pair rest frame (PRF)[2]. The particles are boosted such that $\vec{p}_1^{\,*} = -\vec{p}_2^{\,*}$ and

$$C(\vec{p}_1^{\,*}, \vec{p}_2^{\,*}) = C(k^*) = \xi(k^*) \otimes \cdot \frac{N_{\text{same}}(k^*)}{N_{\text{mixed}}(k^*)}, \tag{2.2}$$

with the relative momentum of the pair $k^* = 1/2 \mid \vec{p}_1^{\,*} - \vec{p}_2^{\,*} \mid$. The spectrum in the numerator $N_{\text{same}}(k^*)$ is obtained from particle pairs in the same event where correlations due to the two-particle final-state effects and their interaction are present. These have to be absent in the spectrum in the denominator $N_{\text{mixed}}(k^*)$, which has to be obtained from uncorrelated pairs. Typically, this is achieved by building pairs from particles in separate events, such that this distribution exhibits a much smaller statistical uncertainty than $N_{\text{same}}(k^*)$. For this reason, in the simplest case a normalization constant $\xi(k^*) = \mathcal{N}$ has to be introduced, chosen such that $C(k^*) = 1$ in the region $k^* \gtrsim 200\,\text{MeV}/c$, where the femtoscopic signal is expected to be absent. In most cases the correction has a more complex, k^* dependent behavior in order to account for experimental effects, as they will be discussed in detail in the later chapters.

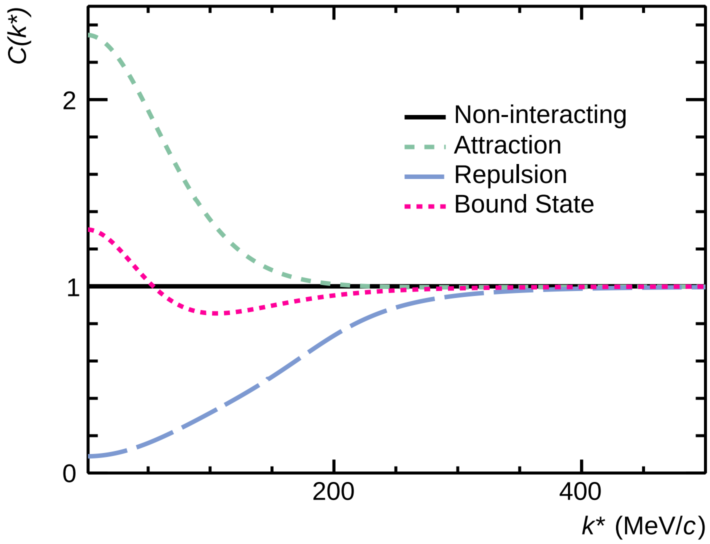

Figure 2.1.: Examples of the behavior of the correlation function for a pair of non-interacting particles (black solid line), a pair attractively interacting particles (green dashed line), a pair of repulsively interacting particles (blue long dashed line) and a pair of particles that form a bound state (magenta short dashed line).

---

[2] In the following all quantities in the PRF are denoted by an asterisk ($\vec{a}^{\,*}$)

Already at this point the sensitivity of the observable to any kind of interaction can be seen by assuming a simplified interaction, limited to three cases: 1) no interaction, 2) attraction and 3) repulsion. The behavior of the correlation functions for those cases is depicted by the exemplary curves in Fig. 2.1. In the first case, it does not matter if the two-particles are observed alone or as a pair, $N\left(\vec{p}_1, \vec{p}_2\right)$ factorizes to $N\left(\vec{p}_1\right) \cdot N\left(\vec{p}_2\right)$ and $C(k^*)$, as it is depicted by the black line, remains at unity. In the second (third) case, particle pairs are pulled together (apart) and correspondingly, the probability to find them at small k^* is enhanced (reduced) compared to the product of the single particle probabilities. Consequently, the $C(k^*)$, as it is depicted by the green (blue) curve, is enhanced above (diminished below) unity. But also more complex details of the interaction are reflected in the behavior of the correlation function. For example, the appearance of a bound state, e.g. that of a deuteron formed by a proton and a neutron, causes pairs to disappear in the measurement of their correlated yield. Therefore, the probability to find particles as pairs is reduced compared to the product of the single particle probabilities. As expected, the also corresponding $C(k^*)$, depicted by the magenta line, shows a depletion, albeit at intermediate k^*. It should be noted, however, that the overall behavior of $C(k^*)$ in this case is more involved, see e.g. [106]. This sensitivity of the correlation function to the details of the interaction means that femtoscopy is a unique tool to investigate the presence and the effects of the strong force among particles.

In order to model Eq. 2.1, it has to be linked to quantities that can be easily calculated. In the following, this is sketched in coarse steps, a more detailed description and also discussion of this can be found in [104, 107]. Starting from a quantum mechanical description [104, 108] it can be shown that

$$C(\mathbf{P}, \mathbf{q}) = \frac{\int \mathrm{d}^4x_1\, \mathrm{d}^4x_2\, s_1(\mathbf{p}_1, \mathbf{x}_1) \cdot s_2(\mathbf{p}_2, \mathbf{x}_2) \mid \psi(\mathbf{q}, \mathbf{r}^*) \mid^2}{\int \mathrm{d}^4x_1\, s_1(\mathbf{p}_1, \mathbf{x}_1) \int \mathrm{d}^4x_2\, s_2(\mathbf{p}_2, \mathbf{x}_2)}. \tag{2.3}$$

Here, $\mathbf{P} = \mathbf{p}_1 + \mathbf{p}_2$ denotes the total momentum of the pair. According to the formalism worked out in [104], the relative momentum of the pair $\mathbf{q}$, is defined as

$$q^\mu = \frac{1}{2}\left[(p_1 - p_2)^\mu - \frac{1}{\mathbf{P}^2}(p_1 - p_2)_\nu \cdot P^\nu \cdot P^\mu\right]. \tag{2.4}$$

The function $s(\mathbf{p}_i, \mathbf{x}_i)$ are the emission functions, representing the probability to emit a particle with momentum $\mathbf{p}_i = (E_i, \vec{p}_i)$ at the space-point $\mathbf{x}_i = (t_i, \vec{x}_i)$. The Lorenz-invariant particle spectra are then given as

$$E\frac{\mathrm{d}N}{\mathrm{d}^3p} = \int \mathrm{d}^4x\; s(\mathbf{p}, \mathbf{x}). \tag{2.5}$$

At last, in Eq. 2.3, the weight is given by square of the Bethe-Salpeter amplitude [109] $|\psi(\mathbf{q}, \mathbf{r}^*)|^2$ and gives the probability to also observe the particles in this state after emission. Under the equal time approximation [104, 110] that in the PRF $t_1^* - t_2^* = 0$, the time dependence drops out, and $\psi(\mathbf{q}, \mathbf{r}^*) \rightarrow \psi(\vec{q}, \vec{r}^*)$ reduces to the stationary two-particle wave function. The only time dependence in Eq. 2.3 left is hence only contained in the source. Here the smoothness assumption is used that in the emission function $\mathbf{p}_i \rightarrow \bar{\mathbf{p}}_i = m_i/(m_1 + m_2)\mathbf{P}$ can be expressed in terms of the total momentum $\mathbf{P}$. With $\mathbf{r}^* = \mathbf{x}_1 - \mathbf{x}_2$, the pair emission function in Eq. 2.3 is normalized by the single particle emission functions and can be replaced by

$$S_{\mathbf{P}}(\vec{r}^*) = \int \mathrm{d}t^* \mathcal{S}_{\mathbf{P}}(\mathbf{r}^*). \tag{2.6}$$

In the PRF $\mathbf{P} = \vec{p}_1 + \vec{p}_2 = 0$, and $\vec{q} \rightarrow k^*$ becomes a scalar quantity, where $k^* = \frac{1}{2} \mid \vec{p_1}^* - \vec{p_2}^* \mid$. Equation 2.3 can then be written as [111]

$$C(k^*) = \int \mathrm{d}^3 r^* \mid \psi(k^*, \vec{r}^*) \mid^2 S(\vec{r}^*). \tag{2.7}$$

At this point the correlation function $C(k^*)$ depends only on two separate factors: the space-time configuration of the emitted particles described by $S(r^*)$ and the propagation of particles accounted for by $\psi(k^*, \vec{r}^*)$. As mentioned at the beginning of this chapter, femtoscopy is traditionally employed to study $S(r^*)$, usually by using π–π or K–K correlations. For these pairs the strong interaction can be neglected [104] and interference occurs mainly because of the fact that the particles are indistinguishable bosons, so called Bose-Einstein correlations. The $\psi(k^*, \vec{r}^*)$ is given by symmetrizing the two free wave functions of the single particles. When the strong or Coulomb interaction has to be taken into account, as it is the case for example for p–p pairs, the $\psi(k^*, \vec{r}^*)$ can either be approximated or directly calculated from the Schrödinger equation, as it will be discussed in Section 2.4. For $S(\vec{r}^*)$ a functional form is usually assumed based on a Gaussian distribution as it will be discussed in the next section.

2.2. Gaussian Source Distribution

A typical parametrization of $S(r^*)$ is obtained by assuming no time and momentum dependence and that the single-particle emitter,

$$s(\mathbf{p}, \mathbf{x}) = \delta(t^*) \exp\left(-\frac{x^{*2} + y^{*2} + z^{*2}}{2(r_{\mathrm{Gauss}})^2}\right), \tag{2.8}$$

follow a spherically symmetric Gaussian distribution with width r_{Gauss}. For two particles with the same $s(\mathbf{p}, \mathbf{x})$, it can then be shown [107, 112] that by describing their spatial coordinates by their relative distance $\vec{r}^* = \vec{x}_1 - \vec{x}_2$,

$$S(\vec{r}^*) = \frac{1}{(4\pi r_{\mathrm{Gauss}}^2)^{3/2}} \exp\left(-\frac{\mid \vec{r}^* \mid^2}{4(r_{\mathrm{Gauss}})^2}\right). \tag{2.9}$$

The emission function $S(r^*) = S(\vec{r}^*)$ then only depends on a scalar $r^* = |\vec{r}^*|$, the relative distance between pairs, and the source size r_{Gauss}. In principle, the width of the single-particle emitters might be different in each individual spatial direction. This can only be investigated, however, by a three dimensional measurement of the correlation function [104]. In high energy collisions, π mesons are produced abundantly enough to detect a sufficient number of same charge π–π pairs for such a measurement [104, 113–115]. In heavy-ion collisions at relativistic energies enough K mesons are produced to extend these studies also to correlations among same charge and neutral K–K pairs [116]. If particles are produced less abundantly, as it is the case for heavier particles or if generally less particles are produced, e.g. in typical pp or p–Pb collisions at similar energies, the correlation function of the corresponding pairs is often measured in one dimension. The source is then parameterized according to Eq. 2.9 and the one-dimensional source size r_{Gauss} is evaluated by using Eq. 2.7 to fit the data [23, 117, 118].

For studies of $S(r^*)$ the correlation function is analyzed for pairs where the $\psi(k^*, \vec{r}^*)$ is well constrained. The aim of this work, however, is to study the interaction of particles and test different models to describe this interaction. Thereby, simultaneously determining the parameters of $S(r^*)$, would introduce too many degrees of freedom in the fit. Event generators like EPOS could deliver a spatial distribution of particle pairs at freeze-out to constraint $S(r^*)$. The resulting prediction for p–p pairs, for which the interaction and hence the $\psi(k^*, \vec{r}^*)$ is well described, nevertheless fails to describe the corresponding measurement in data [119, 120][3]. In this work it is assumed that different particle species share a common source and the correlation function of p–p pairs is used to constrain its size. Since this assumption is one of the building blocks for these studies, it is in the following discussed in more detail.

It is important to note that the femtoscopic correlations develop for pairs where the particle momenta are aligned relatively collinear. This leads to the fact that the measured source size does not necessarily reflect the extend of the whole fireball but the so-called "length of homogeneity" [104, 121]. In the following, this is explained based on the simplified sketches in Fig. 2.2, which depict the emission of particles from two different systems. Particles can originate from any point within the reaction volume, which is represented by the black circle. As an example, particles are produced at four points and the possible orientations of their momenta are shown as arrows. In the sketch in the left panel, the momenta of the emitted particles point in all directions, regardless of their origin. If one particle with any momentum is paired with the others, there are always configurations, as the one indicated in blue, where the momenta align relatively collinear. In turn, this means that in this system the correlations between particles can develop over the entire volume. In contrast, in the scenario depicted right panel, the

---

[3] The direct comparison was never published and is only available internally. Indirectly it can be seen if one considers that in [23] a Gaussian source size of approximately 1.1 fm is reported. In [120] the genuine prediction of $C(k^*)$ for this source size is depicted in Fig. 7 (blue line) and it is not reproduced by the prediction of $C(k^*)$ using the $S(r^*)$ extracted from the EPOS simulations (red line).

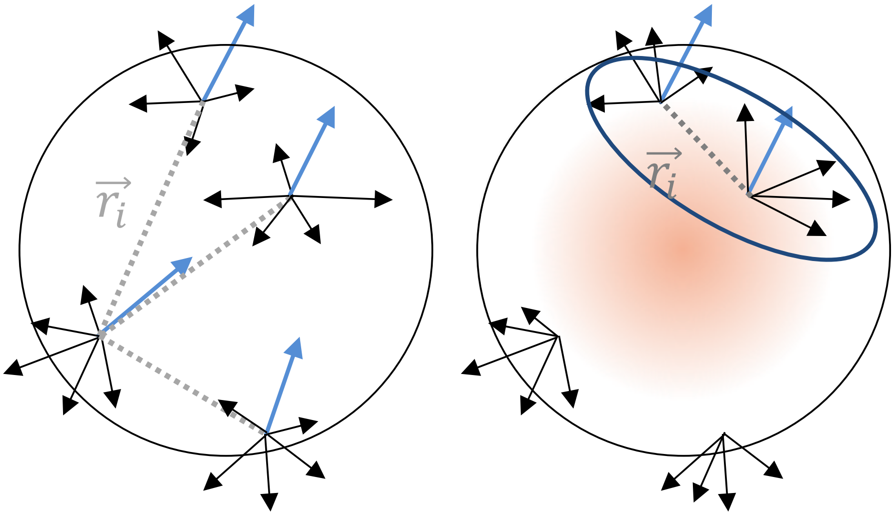

Figure 2.2.: Examples depicting the production points of particles and their momenta (arrows) from a reaction volumes (circle) for two scenarios of their emission. (left) Four particles are produced with momenta which are oriented in entirely random directions. (right) Four particles are produced with momenta which are oriented radially outward. Momenta in blue correspond to possible configurations where the momenta align such that the particles move collinear. As a results the correlations among them develop at a distance $\vec{r}_i$ and probe a different extend of the reaction volume. See text for details.

momenta of the emitted particles are oriented mostly radially outward. In this case, if one particle with a certain momentum is paired with others, the configurations of particles with collinear momenta, as the one indicated in blue, are limited to a sub volume specified by the blue circle. Hence, the correlations develop within a part of the reaction volume and the measured source size only reflects the distance between particles with similar kinematics and therefore is called the length of homogeneity.

The scenario sketched in the left panel is similar to the emission of particles from a system like a thermal bath. The one in the right panel is similar the emission of particles from an system like a fireball, which itself expands outwards. Heavy-ion collisions are understood to create a hot system similar to a thermal bath, but it evolves over time and, like a fireball, expands radially outwards as it cools down.

In these collisions, a collective motion of the emitted particles is observed as (an-)isotropic flow [122, 123]. The observation of collectivity implies that the radial boost, due to the outward expansion of the system, prevails over the thermal motion, due to the temperature of the system. The anisotropies are most pronounced, if the nuclei overlap only partially during the collision. In these cases, the initial reaction volume has an almond like shape and it is understood that this results in additional pressure gradients, which cause a modulation of the radial boost. This way, the initial geometric anisotropy translate into one in momentum space, which supports the picture that particles partake in a collective evolution of the system. The femtoscopic radii are expected to exhibit a common scaling as a function of the transverse mass $m_{\mathrm{T}} = \left(k_{\mathrm{T}}^2 + m^2\right)^{1/2}$ [124]. Here m is the average mass of the particle pair and $k_{\mathrm{T}} = |\vec{p}_{\mathrm{T},\,1} + \vec{p}_{\mathrm{T},\,2}|/2$ the transverse momentum of the pair, where $\vec{p}_{\mathrm{T}}$ is the transverse momentum of each of the particles. This can be understood as an interplay between thermal and collective motion [104, 125]. In the following, as a simplified example, a system is considered, where the mass of all emitted particles is the same. Their respective momenta shall be composed of a collective component, with a constant magnitude that points radially outward, and and a thermal component, with random magnitude and direction. As explained before, femtoscopy measures the entire system size only in case the latter dominates, while in case the former dominates, it measures a smaller size, the length of homogeneity. If both contributions are present, it means that over the whole system the isotropic outward motion is smeared out by the random thermal motion. Thereby, it is possible for the momenta between particle pairs to align collinear over larger distances. Still, particles, and hence also pairs, with the largest momenta are only produced if the thermal component aligns with the collective one. This results in the decreasing behavior of the length of homogeneity as the momentum of the pair k_{T} increases. Since the effect of thermal motion is mass dependent, the radii scale as a function of m_{T}. Of course, in order to describe the exact scaling, it is necessary to take into account the full evolution of heavy-collisions, i.a. a realistic radial boost profile as well as its anisotropies, as for example in [126]. Indeed the measured source sizes of different particle pairs [117] exhibit a m_{T} scaling. It is common for kaon and proton pairs, but seems to be broken for pion pairs. This might be nevertheless be explained by a larger effect of the Lorentz boost for lighter masses, which appears if the three dimensional source size is converted to a one dimensional one [117, 126], or alternatively, by modifications of the source size from the coherent emission of pions from short-lived resonances [127, 128].

In elementary collisions like pp or p–Pb similar studies aim to find evidence for collectivity. In systems with small multiplicities, flow related observables currently as associated with large uncertainties related to non-flow contributions, which scale inversely with the number of produced particles [122]. A smooth transition from small to large collision systems can be observed from the production ratio between hadrons and pions as a function of the number of produced particles. In particular striking is the fact that the amount of particles which contain strangeness is enhanced as the multiplicity increases independent of the collision system. Also the m_{T} and k_{T} dependence of the femtoscopic radii is investigated. In minimum bias data these studies were up to now limited to the low m_{T} region since differential studies were only feasible for π–π and K–K pairs [23, 118]. These studies point to a variation of the radius as a function of the event multiplicity and on the pair m_{T} yet less pronounced than in the heavy-ion system [129–133]. For heavier pairs an analysis of low relative momentum p–p and p–Λ pairs in minimum bias proton-proton (pp) collisions at $\sqrt{s} = 7$ TeV demonstrated that one radius is sufficient to simultaneously describe both correlation functions within the uncertainties [23]. This will be further investigated by an analysis of femtoscopic source sizes of p–p and p–Λ pairs in pp collisions at the highest particles multiplicities as close as possible to that of heavy-ion collisions.

2.3. Modeling of Resonance Contributions

Assuming a common Gaussian source completely neglects the presence of resonances and particles decaying with lifetimes on the scale of the source sizes. Their effect on the correlation function was studied for π–π pairs in heavy-ion collisions and it was shown that they lead to significant exponential tails of the source distribution [134–137]. There are of course also short-lived resonances like the Δ or the N^*, where the decay produces pions but also additional baryons. For pp collisions, the statistical hadronization model (SHM) in the canonical approach can be employed to obtain the composition of the contribution of resonances to the yield of protons and Λ baryons. For these calculations, a freeze-out temperature $T = 157\,\mathrm{MeV}$ and strangeness suppression factor $\gamma_S = 0.76$ [138] was chosen such that measured particles yields of inelastic pp collisions at $\sqrt{s} = 13$ TeV are reproduced. The results are summarized in Table 2.1. Only around 1/3 of all protons and Λ baryons are produced primordially. Looking at the composition in more detail, one can see that protons can be produced in decays of 57 different resonances with lifetimes $0.5\,\mathrm{fm} < c\tau < 13\,\mathrm{fm}$. Besides the primordial contributions, 22% of the total yield of protons is associated with a decay of a Δ^{++} resonance, 15% with the decay of a Δ^{+} resonance, and 7.2% with a Δ^{0} resonance. The

Table 2.1.: SHM estimates for the fraction of primordial protons and Λ baryons produced in pp collisions at $\sqrt{s} = 13$ TeV as well as those resonances with the largest contribution to the total yield of those particles and their lifetimes $c\tau_{\mathrm{res}}$ and masses M_{res}. Additionally, the average values are reported, which are calculated using the complete set of resonances included in the SHM, as well as their lifetimes and branching ratios.

	Contribution	Fraction (%)	$c\tau_{\mathrm{res}}$ (fm)	M_{res} (GeV/c^2)
Proton	Primordial	33		
	Δ^{++}	22	1.67	1.232
	Δ^{+}	15	1.67	1.232
	Δ^{0}	7.2	1.67	1.232
	All Resonances Avg.	67	1.65	1.35
Λ	Primordial	34		
	Σ^{*+}	12	5.51	1.232
	Σ^{*0}	12	5.48	1.232
	Σ^{*-}	12	5.01	1.232
	All Resonances Avg.	64	4.69	1.46

remaining secondary protons originate from heavier N^*, Δ and Λ resonances, which contribute individually with less than 2%. The total yield of Λ baryons is composed of the primordial contribution and 32 resonances with lifetimes $0.5\,\mathrm{fm} < c\tau < 8.5\,\mathrm{fm}$. Most prominently Σ^{*+}, Σ^{*0}, and Σ^{*-} are each the origin of 12% of all Λ baryons, while decays of heavier N^*, Λ, and Σ resonances individually contribute with less than 1%.

The average lifetime $\langle c\tau_{\mathrm{res}}\rangle$ and masses $\langle M_{\mathrm{res}}\rangle$ of the resonances weighted by their abundance and branching ratio, feeding into protons (Λ baryons) is 1.65 fm (4.69 fm), while the weighted average of the masses is $1.36\,\mathrm{GeV}/c^2$ ($1.46\,\mathrm{GeV}/c^2$). Although the amount of secondaries is similar for protons and Λ-baryons, there is a significant difference in the mean lifetime of the corresponding resonances, which is much longer for the Λ baryons.

It is important to notice that decays with $c\tau \gtrsim 20\,\mathrm{fm}$, so for example weak decays of $\Lambda \rightarrow \pi^- + p$ or electromagnetic decays of $\Sigma^0 \rightarrow \Lambda\gamma$, are missing in the above discussion. Also, contributions to the yield of the heavier Ξ^- are limited to decays of the $\Xi(1530) \rightarrow \Xi^- + \pi^{\pm}$, which have a rather long $c\tau{\sim}20\,\mathrm{fm}$ [2]. All these particles live long enough to imprint a correlation signal caused by their own FSI into the measured correlation function and they have to be accounted for by the so-called λ parameters [23], see for example Section 4.1.4.

Driven by this observation and to estimate the magnitude by how much the radii change between the different particle species, it became necessary to develop a way to model $S(r^*)$ accounting for effect of resonances. Ultimately, this effort yielded a new parameterization of $S(r^*)$ [139]. In the following, the concept behind its implementation will only be outlined shortly, since the development of the mathematical formalism and implementation within CATS was for the most part work of [24]. The application of this model to fit correlation functions was part of this work and can be found in Chap. 4.

The following discussion is based on the assumption that the correlation function is measured for a pair of particles a and b, which are either primordial or result from the decay of a resonance[4] $a' \rightarrow a + \pi$ and $b' \rightarrow b + \pi$. This means that the pairs of particles a and b can in total be emitted in four possible configurations, a pair of i) primordial particles a and b, ii) primordial particle a and particle b from the decay of resonance b', iii) particle a from the decay of resonance a' and primordial particle b and iv) particle a and b, both from the decay of resonance a' and b'. With a probability P_a and P_b, particle a and b can be primordial and with a probability $P_{a'} = 1 - P_a$ and $P_{b'} = 1 - P_b$ they can originate from the resonances a' or b'. The probability of each of the above configurations is then given by i) $P_a \cdot P_b$, ii) $P_a \cdot P_{b'}$, iii) $P_{a'} \cdot P_b$ and iv) $P_{a'} \cdot P_{b'}$. Then $S(r^*)$ can be written as

---

[4] Here and in the following the two-body decay of one effective resonance into a π is assumed. This is justified by the fact that these channels are the most prominent for the above resonances according to [2]

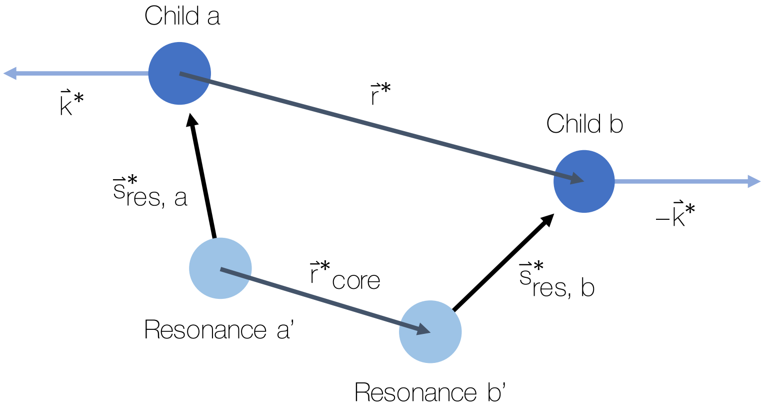

Figure 2.3.: Schematic representation of the modeling of $S(r^*)$ including the effect of resonances. Particles are emitted at a distance $\vec{r}^*_{core}$ sampled from a Gaussian distribution with width r_{core}. In case the particle is a resonance, before the decay occurs, it travels a distance $\vec{s}_{\text{res}}$, where $\mid \vec{s}_{\text{res}} \mid$ is sampled from the exponential decay law according to the lifetime and directions are taken from EPOS (see text for details). The distribution $S(r^*)$ is then sampled from the distance $\mid \vec{r}^* \mid$ between the particles of interest. Figure reproduced from [139].

$$\begin{aligned} S(r^*) = P_a \cdot P_b \times S_{a-b}(r^*) + P_a \cdot P_{b'} \times S_{a-b'}(r^*) \\ + P_{a'} \cdot P_b \times S_{a'-b}(r^*) + P_{a'} \cdot P_{b'} \times S_{a'-b'}(r^*), \end{aligned} \tag{2.10}$$

where $S_{i,j}$ is the source distribution of the individual pairs i)-iv).

The concept of the modeling of the emission profile is schematically depicted in Fig. 2.3. It is assumed that there is an underlying, common emission profile for all primordial pairs, so $a-b$, $a-b'$, $a'-b$ and $a'-b'$. This so-called core source is parameterized by the same Gaussian distribution as in Eq. 2.9 with a width r_{core}. If either particle a or b originates from a resonance, their emission point is shifted according to the lifetime of the resonance t_{res} that follows an exponential distribution with an inverse scale given by $\langle \tau_{res} \rangle$. Effectively, the Gaussian and the exponential distribution have to be folded with each other, accounting for the phase-space distribution of the resonances. This can be done analytically, but results in a extensively long and computationally unstable expression and instead, the problem is approached numerically. The algorithm starts by placing two particles at a distance $\vec{r}^*_{\text{core}}$ sampled from Eq. 2.9 with a width r_{core}. In principle at this point more than one resonance could be considered, however, the following discussion is limited to the case of two resonances $a' \rightarrow a + \pi$ and $b' \rightarrow b + \pi$, as outlined above. All quantities are calculated and evaluated in the PRF of the two measured particles a and b. According to the probabilities P_a and P_b, each particle is assigned to be either a primordial or a resonance, in which case the decay has to be simulated. The distance $\vec{r}^*$ between the two particles a and b is given as

$$\vec{r}^* = \vec{r}^*_{\mathrm{core}} + \vec{s}^*_{res,a} + \vec{s}^*_{res,b}, \tag{2.11}$$

where $\vec{s}^*_{res}$ is the distance a resonance travels before it decays. In case the initial particle is primordial $\vec{s}^*_{res} = 0$. The absolute value $s^*_{res} = \mid \vec{s}^*_{res} \mid$ is calculated from the lifetime t_{res}, momentum p_{res} and mass M_{res} of the resonance

$$s^*_{res} = \gamma_{res}\beta_{res}t_{res} = \frac{p_{res}}{M_{res}}. \tag{2.12}$$

Here, t_{res} is sampled from an exponential distribution

$$T(t) = 1/\langle\tau_{res}\rangle \cdot \exp\left(-t/\langle\tau_{res}\rangle\right), \tag{2.13}$$

where $\langle\tau_{res}\rangle$ is the average lifetime of the resonance. The last ingredient to evaluate Eq. 2.11 are the angles between the three vectors, $\sphericalangle(\vec{r}^*_{\mathrm{core}}, \vec{s}^*_{res,a})$, $\sphericalangle(\vec{r}^*_{\mathrm{core}}, \vec{s}^*_{res,b})$ and $\sphericalangle(\vec{s}^*_{res,a}, \vec{s}^*_{res,b})$. At this point, the distribution $S(r^*)$ can be directly obtained by repeating the above procedure several times and evaluating $\mid \vec{r}^*_{\mathrm{core}} \mid$, where $\vec{r}^*_{\mathrm{core}}$ is calculated according to Eq. 2.11.

Several inputs to the procedure described in the previous paragraph need to be evaluated. The values summarized in Table 2.1, extracted from SHM calculations, are used for the probabilities P_a and P_b, τ_{res} and M_{res}. The remainder, so p_{res} and the angles, depend on the emission process, which cannot be computed trivially and can only be estimated with the help of transport models, for example EPOS [140][5]. Therefore, the freeze-out configuration of particles is simulated for the relevant reaction, e.g. pp collisions at $\sqrt{s} = 13$ TeV, and pairs of primordial protons, Λ baryons or any resonances that feed into either of those particles are identified. Only the pairs with $k^* < 200\,\mathrm{MeV}/c$ are considered, since those are relevant in the following description of the measured correlation function. In EPOS the yields of heavier resonances are significantly over estimated[6]. Therefore, pairs are selected such that the average values of $\langle M_{res}\rangle$ by calculations by the SHM are reproduced. Their kinematic and spatial information as well as the masses of all particles are then available to be used in the above sampling procedure. For each iteration, a pair of the corresponding combination is picked from the pool to fix the values of p_{res} and of the three angles.

---

[5] Also Pythia [141] was used as a cross-check, however, here primordial particles are emitted at the origin and were therefore randomly distributed over a sphere to mimic a radially outward emission. Since those results agreed with the ones from EPOS, the latter was used.

[6] One of the EPOS authors, Klaus Werner, was contacted, and apparently the lighter resonances are partially populated by the decay of heavier ones. Selecting primordial particles then leads to the observed bias.

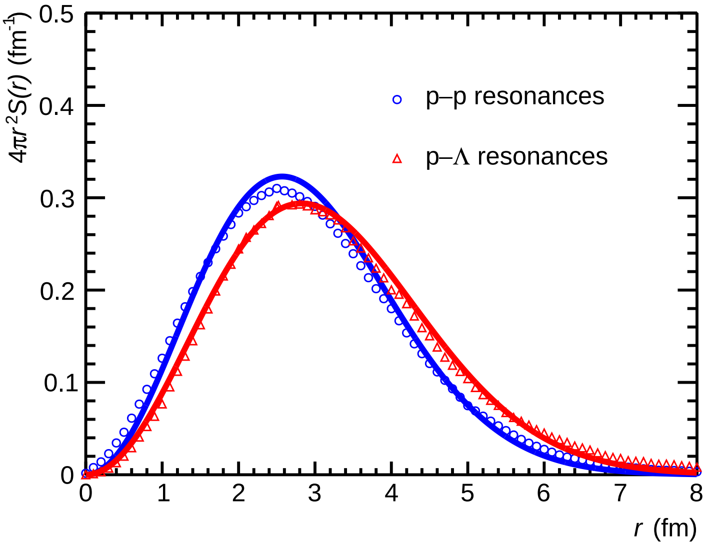

Figure 2.4.: The open blue circles (red triangles) represent the source distributions of p–p (p–Λ) pairs assuming a width $r_{\mathrm{core}} = 1.2\,\mathrm{fm}$ and accounting for resonances (see text for details). An effective source size of r_{eff} of 1.28 fm (1.41 fm) is extracted by a fit with a Gaussian distribution according to Eq. 2.9, depicted by the solid blue (red) line.

Figure 2.4 shows the resulting source distributions for p–p (blue open circles) and p–Λ (red open triangles) pairs, starting from the same core of width of $r_{\mathrm{core}} = 1.2\,\mathrm{fm}$ and normalized such that

$$\int \mathrm{d}r^* S(r^*) = 1. \tag{2.14}$$

Any difference between these source distributions is due to the effect of resonances. The solid lines depict the fit of the distribution by the function in Eq. 2.9 to extract an effective Gaussian source radius r_{eff}. This yields an effective source size of r_{eff} of 1.28 fm (1.41 fm) for p–p (p–Λ) pairs. The resonances decaying into a Λ have a longer lifetime than those decaying into protons. For p–Λ pairs the modification of the Gaussian core distribution lead to an increase of r_{eff} by almost 20%.

2.4. The Two-Particle Wave Function

In most of the past femtoscopy studies, modifications to the $\psi(k^*, \vec{r}^*)$ due to the interaction among particle have been considered using approximations. In case both particles are charged, the presence of the Coulomb interaction can be accounted for by multiplying the (free) two-particle wave function with the Gamow factor [117, 142]. The strong interaction can be described within the effective-range expansion by two scattering parameters: the scattering length a_0 and the effective range d_0. Under the assumption of a Gaussian source distribution, an analytic form of $C(k^*)$ can be derived:

the so-called Lednický-Lyuboshits model [112]. Without any approximations, however, the most natural way to calculate $\psi(k^*,\vec{r}^*)$ is to solve the two-particle Schrödinger equation, taking into account the (anti-)symetrization of the wave function and any Coulomb or strong interaction potential. In most cases, it is necessary to follow a numerical approach as it is is provided by Correlation Analysis Tool Solving the Schrödinger Equation (CATS) [24, 120] for local interaction potentials $V(r^*)$. After the framework calculates $\psi(k^*,\vec{r}^*)$ it computes $C(k^*)$ according to Eq. 2.7 for any source distribution.

For the following discussion, a pair of identical, non-interacting particles is considered. For a pair of bosons, e.g. two pions, the two-particle $\psi(k^*,\vec{r}^*)$ has to be symmetric under exchange of the particle position, which implies that the parity has to fulfill $P = (-1)^{L+S} \overset{!}{=} 1$. For a pair of fermions, e.g. two protons, the two-particle $\psi(k^*,\vec{r}^*)$ has to be anti-symmetric under exchange of the particle position and in this case the parity has to fulfill $P = (-1)^{L+S+1} \overset{!}{=} -1$.

The π meson has $S = 0$ and the π–π pair can only occupy the singlet state $S = 0$. The free wave functions of each of the two particles has to be combined such that $\psi(k^*,\vec{r}^*)$ is symmetric, which yields [143]

$$\mid \psi(k^*,\vec{r}^*) \mid^2 = 1 + \cos\left(2 \cdot k^* r^*\right). \tag{2.15}$$

Protons, however, have $S = 1/2$ and the p–p pairs can occupy both spin states, the singlet $S = 0$ and triplet $S = 1$. In high-energy collisions it can be assumed that the

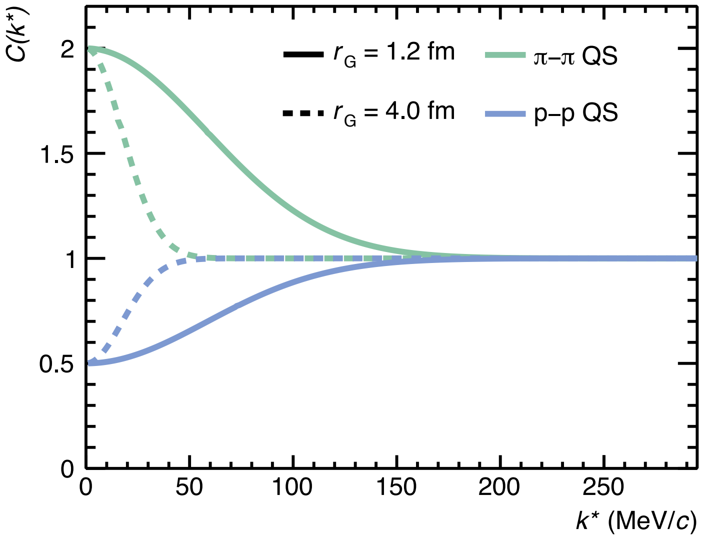

Figure 2.5.: The correlation function of identical, non-interacting pairs of π mesons (green) and protons (blue). The curves were obtained for two Gaussian source sizes: $r_{\text{Gauss}} = 1.2\,\text{fm}$ (solid line) and $r_{\text{Gauss}} = 4.0\,\text{fm}$ (dashed line).

pairs are produced without any preference on their polarization and the probabilities to find a pair in either state are 1/4 and 3/4, respectively. The total wave function for such a pair is then given by as [143]

$$\mid \psi(k^*,\vec{r}^*) \mid^2 = \frac{1}{4} \mid \psi_S(k^*,\vec{r}^*) \mid^2 + \frac{3}{4} \mid \psi_T(k^*,\vec{r}^*) \mid^2 = 1 - \frac{1}{2}\cos\left(2 \cdot k^* r^*\right). \tag{2.16}$$

Figure 2.5 depicts examples of $C(k^*)$ calculated by CATS considering only the effects of QS for π–π (green curve) and p–p (blue curve) pairs under the assumption of Gaussian source distribution for two different source sizes of $r_{\text{Gauss}} = 1.2\,\text{fm}$ (solid line) and $r_{\text{Gauss}} = 4.0\,\text{fm}$ (dashed line). Independently of the source distribution, at $k^* = 0$ the correlation functions converge towards $C(k^*) = 2$ for bosons and $C(k^*) = 0.5$ for fermions, following the expectation from respective $\psi(k^*,\vec{r}^*)$ in Eq. 2.15 and Eq. 2.16. While the intercept of the correlation function due to QS at $k^* = 0$ is independent of $S(r^*)$, it can be seen that the shape of the correlation function at $k^* > 0$ is sensitive to the geometric properties of the source. This can also be understood on the basis of the Heisenberg uncertainty principal, which implies that the more the emission of particles pairs is localized in coordinate space, the wider has to be the distribution of their relative momenta. Under the assumption of a Gaussian source distribution, an analytic relation can be derived for $C(k^*)$ by inserting the corresponding $\psi(k^*,\vec{r}^*)$ into

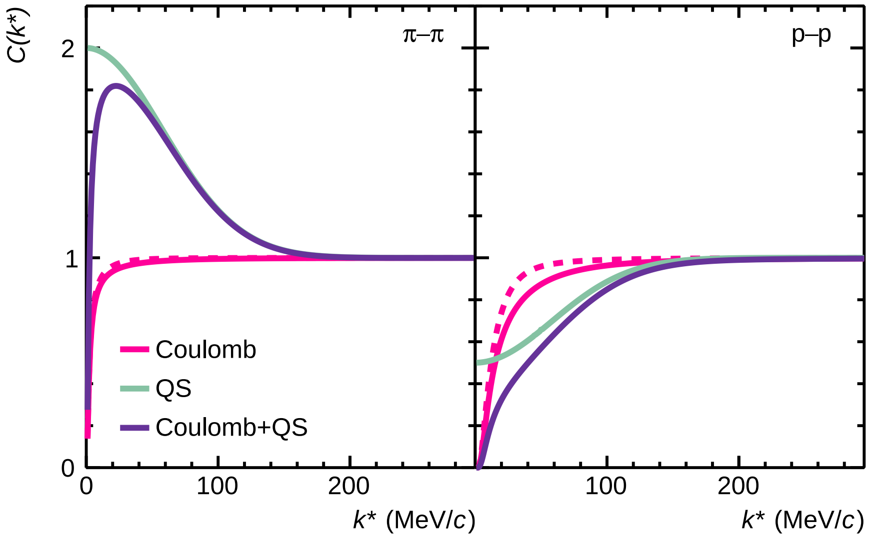

Figure 2.6.: The correlation function of identical pairs of charged π mesons (left) and protons (right) considering only the Coulomb interaction (magenta curves), only the effects of QS (green curve) or the combination of both (violet curve). The results depicted by a solid line were obtained with a Gaussian source sizes of $r_{\text{Gauss}} = 1.2\,\text{fm}$. The correlation function depicted by the dashed line is calculated considering only the Coulomb interaction and a Gaussian source size of $r_{\text{Gauss}} = 4.0\,\text{fm}$.

Eq. 2.7. In turn, it can be shown that the source size is inversely proportional to the width of the correlation signal [108].

Another source of correlations is the Coulomb interaction, and when pairs of particles with identical (opposite) charges are considered, the Coulomb interaction is repulsive (attractive). To explore the effect on the correlation function, the $\psi(k^*, \vec{r}^*)$ was calculated by CATS for π–π and p–p pairs only considering the Coulomb interaction. Under the assumption of a Gaussian source distribution the results for $C(k^*)$ are shown by the magenta curves in the left and right panel of Fig. 2.6 for two different source sizes of $r_{\mathrm{Gauss}} = 1.2\,\mathrm{fm}$ (solid line) and $r_{\mathrm{Gauss}} = 4.0\,\mathrm{fm}$ (dashed line). Regardless of the spatial separation between particles, the long-range repulsion of the Coulomb interaction prohibits pairs with $k^* = 0$ and hence $C(0) = 0$ [111]. It can be seen that the overall sensitivity of these correlations to the source size is much weaker than of those from QS discussed before. The comparison of $C(k^*)$ of π–π and p–p pairs, which have different masses, reveals that for the heavier particle pairs the correlation signal becomes more pronounced and exhibits a more distinctive dependence on the extend of the source.

Because of the sensitivity of QS to the properties of the source, these correlations are usually used to investigate its geometrical properties. In order to fully describe the $C(k^*)$ of charged particle pairs, however, the Coulomb interaction needs to be taken into account. This can be seen by the violet curves in Fig. 2.6, depicting the correlation function due to the combination of QS and Coulomb interaction. For π–π pairs the correlation function for $k^* \gtrsim 60\,\mathrm{MeV}/c$ is described by only considering the effects of QS (green curve), while at low k^* the Coulomb interaction dominates the behavior. For the heavier p–p pairs, the Coulomb interaction extends the region where $C(k^*)$ diverges from the pure QS case to $k^* \lesssim 100\,\mathrm{MeV}/c$.

Of course, also the strong interaction introduces correlations between particles. In the following its effect on $C(k^*)$ is investigated based on the example of p–p pairs. To describe their strong interaction the Argonne v_{18} potential [59] is used, which is well constrained by the precise measurements of the N–N scattering cross sections and phase shifts in several partial waves. The states are in the following denoted as ${}^{2S+1}L_J$, where S is the spin of the pair, L the angular momentum and J the total angular momentum. Both particles are fermions and, as discussed before, only states with $P = (-1)^{L+S+1} \overset{!}{=} -1$ are allowed, while states like ${}^1P_1$ are prohibited. Figure 2.7 presents the correlation functions considering only the strong interaction of p–p pairs individually in the states ${}^1S_0$ (orange curve), ${}^3P_0$ (magenta curve), ${}^3P_1$ (blue Curve) and ${}^3P_2$ (green curve). They were calculated under the assumption of a Gaussian source with size $r_{\mathrm{Gauss}} = 1.2\,\mathrm{fm}$ using CATS. The interaction at low relative momenta ($k^* < 100\,\mathrm{MeV}/c$) is clearly dominated by the S-wave, while the contributions from the interaction in the P-wave only become equally significant in the region at larger k^*.

In the following the S and P wave are considered and the total correlation function is calculated following [120] as

$$C(k^*) = \frac{3}{12}C(k^*, {}^1S_0) + \frac{1}{12}C(k^*, {}^3P_0) + \frac{3}{12}C(k^*, {}^3P_1) + \frac{5}{12}C(k^*, {}^3P_2). \tag{2.17}$$

Besides the strong interaction of the two protons, the Coulomb interaction and QS have to be considered. The total correlation function is shown in left panel Fig. 2.8. The curves were calculated using CATS under the assumption of a Gaussian source with two different sizes $r_{\mathrm{Gauss}} = 1.2\,\mathrm{fm}$ (solid line) and $r_{\mathrm{Gauss}} = 4.0\,\mathrm{fm}$ (dashed line). Also in this case, the Coulomb interaction dominates the behavior of $C(k^*)$ at $k^* \to 0$ and forces the correlation function to 0. As k^* increases, the effects of the strong interaction become more prominent, which for both source sizes lead to an enhancement of $C(k^*)$ above unity. The interplay of strong and Coulomb interaction as well as QS results in a peak around $\sim$20 MeV/c. The individual contributions to the total $C(k^*)$ for $r_{\mathrm{Gauss}} = 1.2\,\mathrm{fm}$ are shown in the bottom right panel of Fig. 2.8. The signals of the strong interaction (orange curve) and of the Coulomb interaction (magenta curve) disappear above $k^* \sim 100\,\mathrm{MeV}/c$ and only the contribution of QS (green curve) differs significantly from unity. As a result, the total correlation function (solid blue line) exhibits a depletion at $k^* \sim 100\,\mathrm{MeV}/c$, which is more clearly visible in the magnified version depicted in the upper right panel of the same figure.

As it was discussed in the first example of this section, with an increasing radius the effects of QS become contained to a smaller region of k^*. Consequently, the depletion at $k^* \sim 100\,\mathrm{MeV}/c$ vanishes in the total correlation function for $r_{\mathrm{Gauss}} = 4.0\,\mathrm{fm}$. More

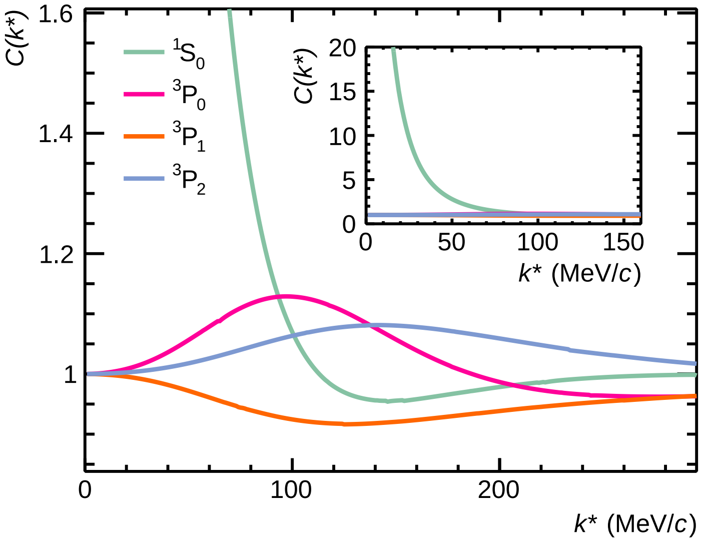

Figure 2.7.: The correlation function of identical pairs of protons considering only the strong interaction parameterized by the Argonne v_{18} potential [59] in different partial waves ${}^{2S+1}L_J$. The results were obtained for a Gaussian source with a size of $r_{\mathrm{Gauss}} = 1.2\,\mathrm{fm}$.

prominently, however, is the change of the amplitude of the strong interaction signal, when the dashed curve and solid curves in the left panel of Fig. 2.8 are compared.

The connection between the source size and the correlation signal due to the strong interaction is best understood with the help of Fig. 2.9, where the shapes of the strong (local) interaction potential and the source distribution are compared. As an example for the strong interaction the Argonne v_{18} $^1S_0$ potential is shown. It has a repulsive core for small r ($r \lesssim 0.7$ fm), an attractive pocket at intermediate r up to ~2 fm and it vanishes for $r \gtrsim 5$ fm, which is typical for the strong interaction because of its short-range nature. The source distribution, so the probability to emit a pair of particles at a certain distance, is calculated assuming a Gaussian source with a size of $r_{\text{Gauss}} = 1.2$ fm (pink curve) and a size $r_{\text{Gauss}} = 4.0$ fm (magenta curve). By comparing the potential and the source distributions it can be seen that in case of a larger source almost all pairs are emitted outside of the region where the strong interaction potentials differs significantly from zero. Correspondingly, the correlation function, as shown by the dashed line in Fig. 2.8, reflects mainly the effects of QS and Coulomb interaction. In contrast, for a small source a large fraction of pairs is emitted with particularly small relative distances in the region left of the black line. Here the particles interact via the strong force and also the

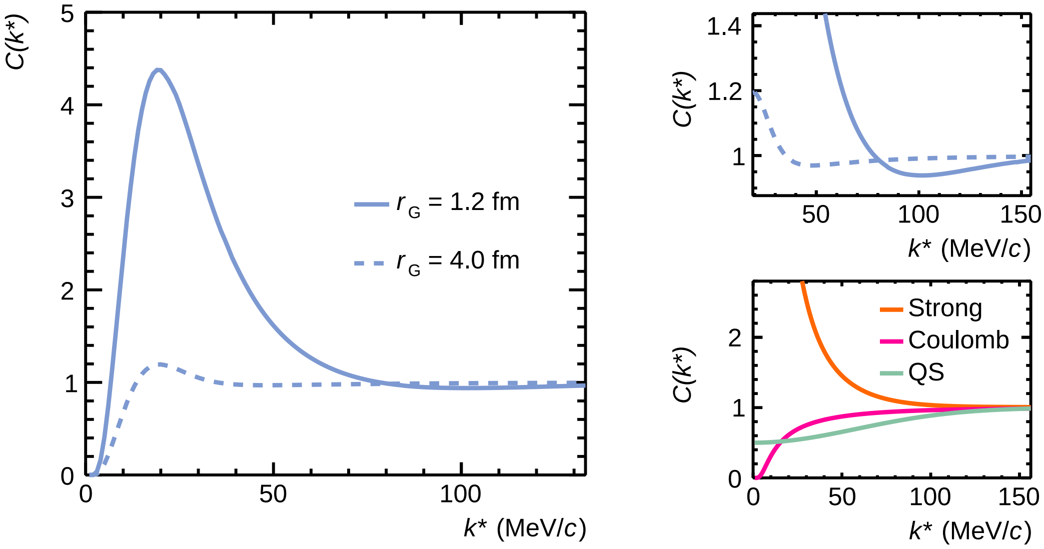

Figure 2.8.: (Left) The correlation function (blue curve) of identical pairs of protons considering the combination of QS, Coulomb and strong interaction, parameterized by the Argonne v_{18} potential [59]. The result depicted by a solid line was obtained with a Gaussian source sizes of $r_{\text{Gauss}} = 1.2$ fm, the one depicted by a dashed line with $r_{\text{Gauss}} = 4.0$ fm. (Top right) Zoomed version of the left plot in the region where the QS deplete the correlation function below unity. (Bottom right) Comparison of the individual correlation functions due to QS (green), Coulomb (magenta) and strong interaction (orange) for a Gaussian source with size $r_{\text{Gauss}} = 1.2$ fm.

modification of correlation function, shown by the solid line in Fig. 2.8, is much more pronounced.

Historically, femtoscopy in heavy-ion collisions was used to investigate $S(r^*)$ via the correlation function of particle pairs like π–π but also p–p, where the interaction and hence $\psi(k^*, \vec{r}^*)$ is well constrained. If this approach is turned around, (non-traditional) femtoscopy can also be used as a unique tool to study the interaction among particles. As it was demonstrated in the last paragraph, it is advantageous if a large amount of pairs is emitted at small relative distances, since it increases the sensitivity of the correlation function to the FSI. Furthermore, the latter can only be probed in detail if the source size matches its range. Hence, in these studies it is preferable to measure the correlation functions in small systems, created e.g. in pp and p–Pb collisions, over those measured in larger systems, created in heavy-ion collisions.

2.5. Coupled Channels

A priori the two-particle interaction can also be inelastic as long as the quantum numbers of the interactions are conserved. For example in the $|S| = 1$ sector, theory predicts unanimously a coupling between the ΛN-ΣN states [14, 65]. Measurements via femtoscopy for the first time are able to resolve this also experimentally. Coupling is also known to exist in the $\overline{\text{K}}$N-$\pi\Sigma$-$\pi\Lambda$ system, where the formalism was successfully

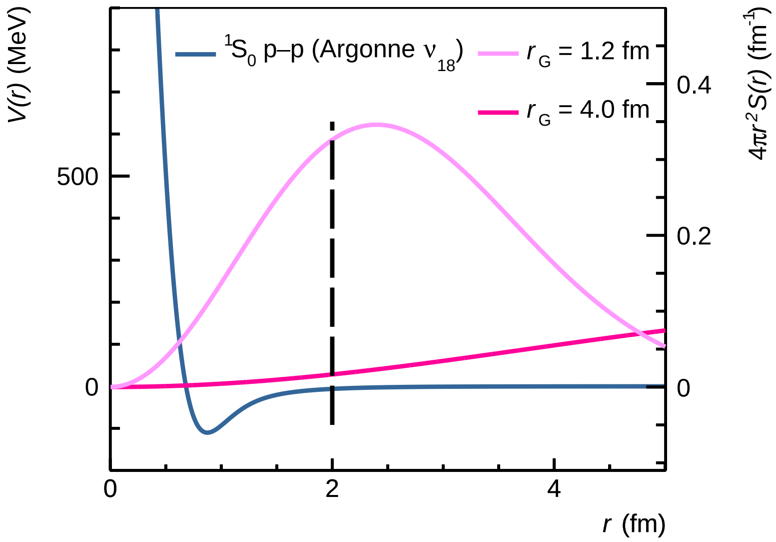

Figure 2.9.: Comparison between the Argonne v_{18} $^1S_0$ interaction potential $V(r)$ (blue curve) and the Gaussian source distribution $4\pi r^2 S(r)$, calculated for a source size $r_{\text{Gauss}} = 1.2\,\text{fm}$ (pink curve) and $r_{\text{Gauss}} = 1.2\,\text{fm}$ (magenta curve). The black line represents the approximate range of $V(r)$.

applied and developed [144–146]. If the inelastic contributions are significant, then this leads to two major conceptual changes from the perspective of femtoscopy.

First, it is not sufficient to obtain $\psi(k^*, \vec{r}^*)$ from the single-channel Schrödinger equation, but a full coupled-channel equation system needs to be solved. For a coupled-channel system with $i = 1, \ldots, M$ pairs that share the same quantum numbers in question, the relevant equation system reads

$$\begin{pmatrix} \mathcal{H}_{1\to1} & \mathcal{H}_{1\to2} & \cdots & \mathcal{H}_{1\to M-1} & \mathcal{H}_{1\to M} \\ \mathcal{H}_{1\to2} & \mathcal{H}_{2\to2} & \cdots & \mathcal{H}_{2\to M-1} & \mathcal{H}_{2\to M} \\ \vdots & \vdots & \ddots & \vdots & \vdots \\ \mathcal{H}_{M\to1} & \mathcal{H}_{M\to2} & \cdots & \mathcal{H}_{M\to M-1} & \mathcal{H}_{M\to M} \end{pmatrix} \cdot \begin{pmatrix} \psi_1(k_1^*, \vec{r}^*) \\ \psi_2(k_2^*, \vec{r}^*) \\ \vdots \\ \psi_M(k_M^*, \vec{r}^*) \end{pmatrix} = E \cdot \begin{pmatrix} \psi_1(k_1^*, \vec{r}^*) \\ \psi_2(k_2^*, \vec{r}^*) \\ \vdots \\ \psi_M(k_M^*, \vec{r}^*) \end{pmatrix} \tag{2.18}$$

The diagonal elements $\mathcal{H}_{i\to i}$ consider the potentials of the elastic channels, while the elements $\mathcal{H}_{i\to j}$, $i \neq j$, consider the (strong) potentials describing the inelastic transitions. Solving this equation system numerically exceeds the current functionality of CATS, and the complete set of $\psi_i(k^*, \vec{r}^*)$ has to be provided by directly by theory.

The second implication for femtoscopy is best understood by considering the effect of coupled channels in the context of a classical scattering experiment. As it is sketched in the left panel of Fig. 2.10, typically a beam of particles of a specific species A hits a target constituting particles of another species B and hence, the pair in the initial state $i = a$ is fixed. Only in the final state after the reaction (pink blob), the pair of particles A and B as well as all pairs coupling to the initial state a are present. As it is depicted in the right panel of the same figure, in femtoscopy this picture is inverted. In a high-energy collision, so in the initial state, the whole set of pairs in the coupled channel system is produced. As they react, they can couple to the particle pair A and B, which is the final state $i = f$ where the correlation function is measured.

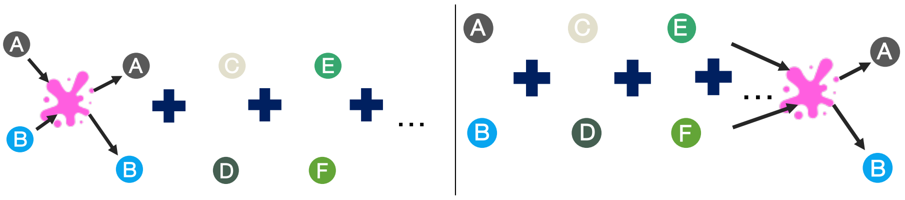

Figure 2.10.: Schematic representation of the reaction of a coupled-channel system in scattering experiments (left) and femtoscopy (right). See text for details.

In order to account for this, Eq. 2.7 has to be written as [145, 146]

$$C(k^*) = \sum_i \int \mathrm{d}^3 r^* w_i \cdot S_i(\vec{r}^*) \mid \widetilde{\psi}_i(k_i^*, \vec{r}^*) \mid^2, \tag{2.19}$$

where the sum runs over all coupled channels $i = 1, \ldots, M$. The final state f gives the asymptotic boundary condition to compute $\psi_i(k_i^*, \vec{r}^*) \to \widetilde{\psi}_i(k_i^*, \vec{r}^*)$. The weights w_i are taken as the ratio of the product of prompt production yields of particles in the coupled channel system to the pair observed in the final state $w_i = N(i_1) \cdot N(i_2)/N(f_1) \cdot N(f_2)$. Since they are impossible to measure directly, they are estimated by the statistical hadronization model [145]. As an example the coupled channels of the $|S| = 2$ and isospin $I = 0, 1$ system are shown, which is of particular interest for this work since it also contains the pΞ^- pair. An overview of pairs, pair masses and the difference of the latter to $m_{p\Xi^-}$ is listed in Table 2.2.

Table 2.2.: Pairs of the coupled channel system $|S| = 2$, $I = 0, 1$, their masses, their difference in mass relative to pΞ^- $\Delta m_{p\Xi}$ and the k^* threshold in the PRF of the p–Ξ^- system to couple to heavier pairs (see explanation below).

Pair		$\Lambda\Lambda$	nΞ^0	pΞ^-	$\Lambda\Sigma^0$	$\Sigma\Sigma$
$m_1 + m_2$	(MeV/c^2)	2232	2255	2260	2309	2386
$\Delta m_{p\Xi}$	(MeV/c^2)	-28	-5	0	49	126
$k^*_{p\Xi}$	(MeV/c)	-	-	-	233	379

From the perspective of the pΞ^- system, lighter pairs ($\Lambda\Lambda$ and nΞ^0) can couple without kinematic constraints. Since they are rather close to the pΞ^- threshold, the magnitude of their contributions to $C(k^*)$ has to be discussed further in the context of interpreting the measurement of the p–Ξ^- correlation function in Section 5. When the heavier pairs couple to the pΞ^- system, the mass difference has to be converted into kinetic energy. Solely assuming energy and momentum conservation yields an estimate of this k^* threshold in the PRF as

$$k^* = \frac{\Delta^2 - (m_1 \cdot m_2)^2}{(m_1^{'} - m_2^{'})^2}, \tag{2.20}$$

where

$$\Delta = \frac{1}{2}\left((m_1^{'} + m_2^{'})^2 - m_1^2 - m_2^2\right). \tag{2.21}$$

Here m_1, m_2, $m_1^{'}$ and $m_2^{'}$ are the masses of the particles in each pair. The masses of particles in the lighter pair are without primes, the ones in the heavier pair are with primes. It should be noted that in reality the coupling is more complex than that and the actual onset also depends on the nature of the interaction. The value nevertheless serves well as an estimate for the region where to look for a cusp in the correlation function. Table 2.2 summarizes this for p–Ξ^- pairs, and it can be seen that a cusp in the corresponding correlation function due to coupling to heavier pair would potentially appear in the region k^* >200 MeV/c. Also this will also be investigated in Section 5.

3. Experiment: ALICE

3.1. CERN LHC

The Large Hadron Collider (LHC) [147] was build between 1998 and 2008 by the European Organization for Nuclear Research (CERN) beneath the French-Swiss border near the city of Geneva. The machine accelerates hadrons and keeps two counter rotating particle beams on a loop with a circumference of 27 km. The LHC as well as the experiments are located around 100 m below earth's surface in a tunnel, which was originally built for the Large Electron-Positron Collider (LEP). The particles can be brought into collision at four interaction points, where all of the major experiments can be found: A Toroidal LHC Apparatus (ATLAS), A Large Ion Collider Expereiment (ALICE), Compact Muon Solenoid (CMS) and Large Hadron Collider beauty (LHCb).

As it can be seen from the schematic representation in Fig. 3.1, the LHC is the last stage of the CERN accelerator complex. For protons the injection process starts from a bottle of hydrogen, and after ionizing the atoms they are accelerated in bunches by the linear accelerator 2 (LINAC 2) to 50 MeV. The protons are transferred into the Proton Synchrotron Booster (PSB), where they stay until they reach energies of 1.4 GeV. From there they are sent to the Proton Synchrotron (PS), where they are accelerated to 25 GeV, and the Super Proton Synchrotron (SPS), where they are accelerated to 450 GeV, before being transferred over to the LHC, where they are accelerated to the nominal collision energy. For Pb ions the injection chain is slightly different. The atoms vaporize off a heated piece of pure Pb and are ionized by an electron beam. The bunches are then accelerated by the linear accelerator 3 (LINAC 3) to 4.5 MeV per nucleon and are further ionized. In the next step, the low Energy Ion Ring (LEIR) increases their energy to 72 MeV per nucleon, which is followed by an acceleration in the PS, where the ions reach energies of 5.9 GeV per nucleon and have the last of their electrons stripped away. The last stage before they are injected into the LHC, is the SPS, which accelerates the beams to 177 GeV per nucleon.

Up to now, the top energy of a proton beam is 6.5 TeV and a Pb beam 2.56 TeV per nucleon. During Run 2 (2015 to 2018) the collider provided collisions of different particles and energies. The data from proton-proton (pp) collisions at a center of mass energy $\sqrt{s} = 13$ TeV in 2016, 2017 and 2018 and the data from proton-Lead (p–Pb) collisions at a center of mass energy per nucleon $\sqrt{s_{\mathrm{NN}}} = 5.02$ TeV in 2016 [149] is particularly relevant for this work.

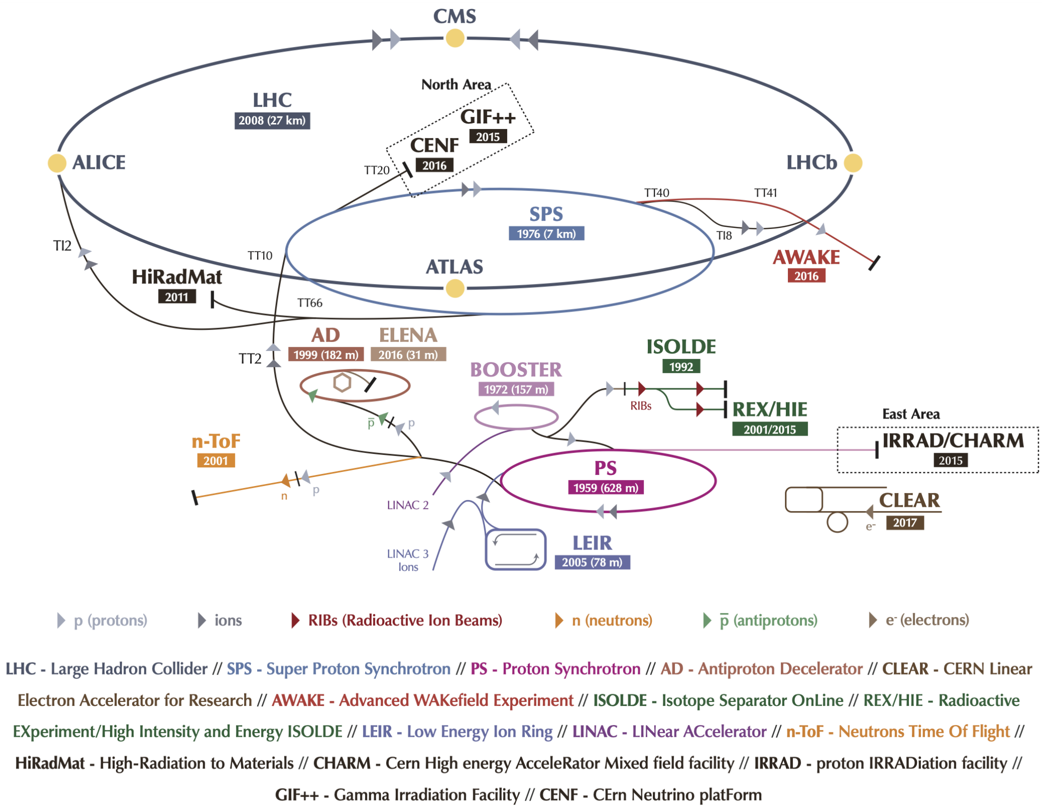

Figure 3.1.: Schematic overview of the accelerators at CERN and their interconnections and links to some of the experiments [148].

3.2. A Large Ion Collider Experiment (ALICE)

The ALICE detector system [150] is located at Interaction Point 2 (P2) of the LHC in France close to the city of Saint-Genis-Pouilly. The spectrometer was designed with the primary aim to explore the properties of the Quark-Gluon Plasma created in ultra-relativistic heavy-ion reactions. The detector was optimized to provide sufficient granularity to track each individual charged particle also in the presence of high track densities and at the same time reconstruct and identify these particles down to momenta p as low as $150\,\mathrm{MeV}/c$. The whole detector system is schematically depicted in Fig. 3.2 and has dimensions of $16 \times 16 \times 26\,\mathrm{m}^3$ and a weight of $\sim 10\,000\,\mathrm{t}$. The solenoid magnet, inherited from the L3 experiment, provides a magnetic field $B = 0.5\,\mathrm{T}$ and houses all of the so-called central barrel detectors. This part of the experiment mainly aims to measure hadrons, electrons and photons. Additionally, in the forward part, a spectrometer is

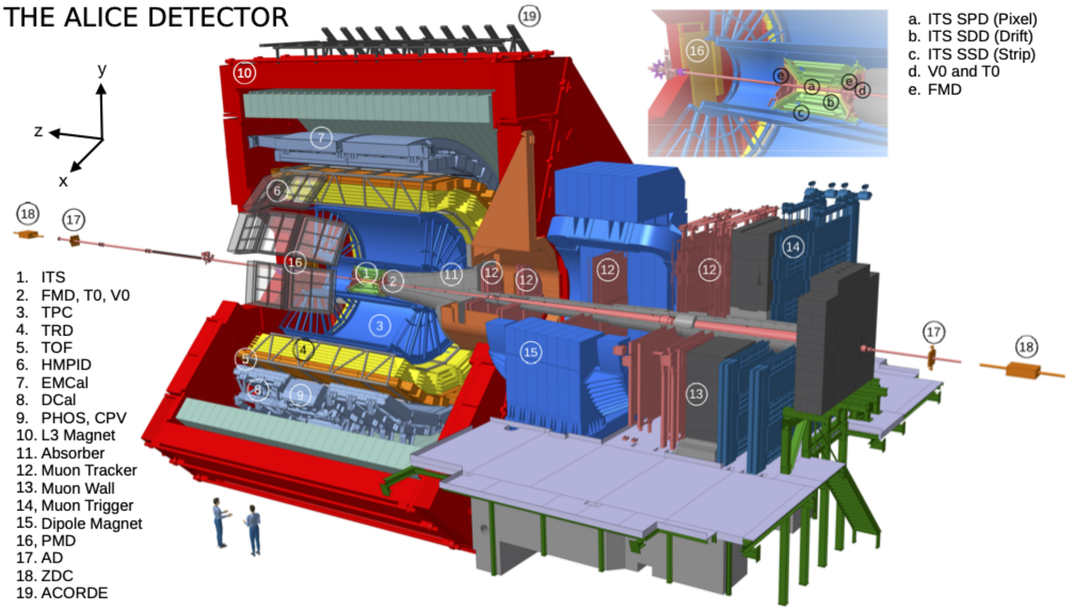

Figure 3.2.: Schematic overview of the ALICE spectrometer and the sub detectors [152]. The inlet magnifies the components directly surrounding the nominal interaction point. The three arrows in the top left corner indicate the reference axes of the ALICE coordinate system.

setup dedicated to measure muons.

The beams collide in the center of the spectrometer around the nominal interaction point corresponding to the origin of the reference system. Within ALICE the coordinates are defined in a right-handed Cartesian coordinate system in laboratory frame [151], depicted by the black arrows in the top left corner of Fig. 3.2. The z axis is oriented parallel to the beam axis with the ATLAS experiment being located in positive z direction (A side) and the muon arm of ALICE and the CMS experiment being located in negative z direction (C side). In the perpendicular transverse plane, the horizontal x axis points towards the center of the LHC and the y axis points upwards towards the surface. Additional variables are the azimuthal angle φ in the xy plane, increasing counter-clockwise from x to y ($\varphi_{x>0,y=0} = 0 \rightarrow \varphi_{x=0,y>0} = \pi/2$), and the polar angle θ defined as the angle relative to the z axis increasing from z to $-z$ ($\theta_{x,y=0,z>0} = 0 \rightarrow \theta_{x,y=0,z<0} = \pi$). The pseudorapitiy η is derived as $\eta = -\ln\left[\tan\left(\frac{\theta}{2}\right)\right]$.

The central barrel contains the Inner Tracking System (ITS), the Time Projection Chamber (TPC), the Transition Radiation Detector (TRD), the Time of Flight (TOF) system, the High-Momentum Particle Identification Detector (HMPID) and electromagnetic calorimeters (EMCal and PHOS). Additionally, several smaller detectors are placed close to the beam pipe, for example the T0 or V0 detectors. The subsystems that are particularly relevant for this work are explained in the following sections.

3.2.1. Inner Tracking System (ITS)

The ITS is the subsystem located closest to the interaction point. It provides precise tracking information, which is crucial for the determination of the collision point, the primary vertex (PV), from which all particles produced in the collision originate. Furthermore, the ITS is able to resolve any offset from this PV, if the particles originate from weak decays of hyperons, D- or B-mesons. Figure 3.3 shows a detailed schematic representation of the ITS. The particle beam is surrounded by the beam pipe, a 800 µm thick Beryllium cylinder with a diameter of 6 cm. It limits the minimum radial distance r of the first detection layer from the nominal interaction point in the transverse plane to 3.9 cm. The outer most layer is located at a radius of 43 cm, to help the matching of tracking information to the TPC. In total, the ITS consists of six layers and uses three different technologies, optimized to provide a high tracking efficiency and resolution. In order to maintain the tracking capabilities of low momentum particles, multiple scattering had to be limited by keeping the material budget of the whole ITS as low as 7.2% of one radiation length X_0 at $\eta = 0$. The outer four layers are equipped with an analogous readout to measure the amplitude of the signal and hence the energy loss of the traversing particle. The ITS covers the full 2π range of φ and up to $|\eta| < 1.98$.

The two innermost layers consist of Silicon Pixel Detectors (SPD) and are located at radial coordinates of $r = 3.9$ cm and 7.6 cm [150]. Specifically the first layer was designed to cope with a charged-particle density of 50 tracks per cm^2. This requires a high granularity on the detection layer, which is achieved by using pixels with a size of 50 µm along $r\varphi$ and of 425 µm along z, and a thickness of roughly 400 µm. Each individual module measures $12.6 \times 69.8\,\text{mm}^2$ and the detector has a spacial resolution of 12 µm along $r\varphi$ and of 100 µm along z. After being triggered, the readout integrates the signals over approximately 300 ns [153], which corresponds to 12 bunch crossings of the LHC, and operates without a dead time because of the multi-event buffer [154].

The third and the fourth layer consist of Silicon Drift Detectors (SDD) and are located at a radial distance $r = 15.0$ cm and 23.9 cm [150]. Here, a maximum charged-particle density of around 7 tracks per cm^2 [150] was expected. The active area of each module measures 70.17 mm along $r\varphi$ and 75.26 mm along z. In the direction of $r\varphi$ the active area is split into two drift regions by a central cathode strip and the readout is located at the anode on either side. Since a potential difference is applied between the two, an electric field is present, which separates the charges created by traversing particles. The difference between the LHC clock and the arrival time of electrons at the anode strips provides the position along $r\varphi$, while the position of the centroid of the charge distribution along the anodes provides the z position. The detector achieves a resolution along $r\varphi$ of less than 35 µm and along z of 25 µm. The integration time of the signal is 6.3 µs (240 LHC bunch crossings [153]) due to the drift velocity of the electrons and after the readout is triggered, the detector has a total dead time of 1024 µs [154].

The two outermost layers use Silicon Strip Detectors (SSD) and are located at $r = 38.0$ cm

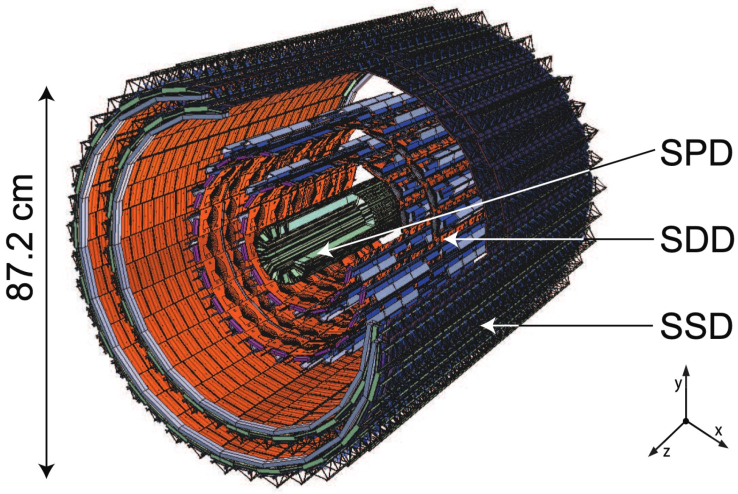

Figure 3.3.: Schematic depiction of the ITS, composed in total of six layers and three sub systems, the SPD, SDD and SSD [155].

and 43.0 cm [150]. Individual strips are spaced by a pitch of 95 µm and are aligned parallel to the z axis. The strip itself gives the position along $r\varphi$, the delay relative to the LHC clock provides the z position. Because of charge sharing among several strips, a spatial resolution along $r\varphi$ of 20 µm and along z of 820 µm is achieved. The integration time is around 1 µs (40 LHC bunch crossings) [153] and after the readout is triggered, the detector has a dead time of around 250 µs [154].

3.2.2. Time Projection Chamber (TPC)

The TPC is the main device used for tracking and identification of charged particles. It consists of a cylindrical barrel with an inner radius of 85 cm and an outer radius of about 250 cm and about 500 cm of length with the nominal interaction point at its center [156]. The volume of 90 m^3 is filled with a counting gas, either a mixture of Ne-CO_2 (90/10), Ne-CO_2-N_2 (90/10/5) or Ar-CO_2 (90/10). As depicted in Fig. 3.4, the central cathode divides the cylinder in two halves. An electric potential difference of $\Delta U \sim 100$ kV, applied between the central membrane and the two end plates, creates an electric drift field parallel to the beam axis. The detector is located within a field cage in order to keep this drift field homogeneous and shield it from distortions [156]. Since there are further subsystems in the outward direction of ALICE, special attention was put on keeping the material budget of the TPC small, which amounts near $\eta = 0$ only to 4.2% of X_0. The working principle is based on ionization of the counting gas by the traversing charged particles. Electrons and ions are separated by the electric field and the positively charged ions drift towards the central membrane, where they get neutralized, while electrons drift towards the end plates. The number of e^-, that

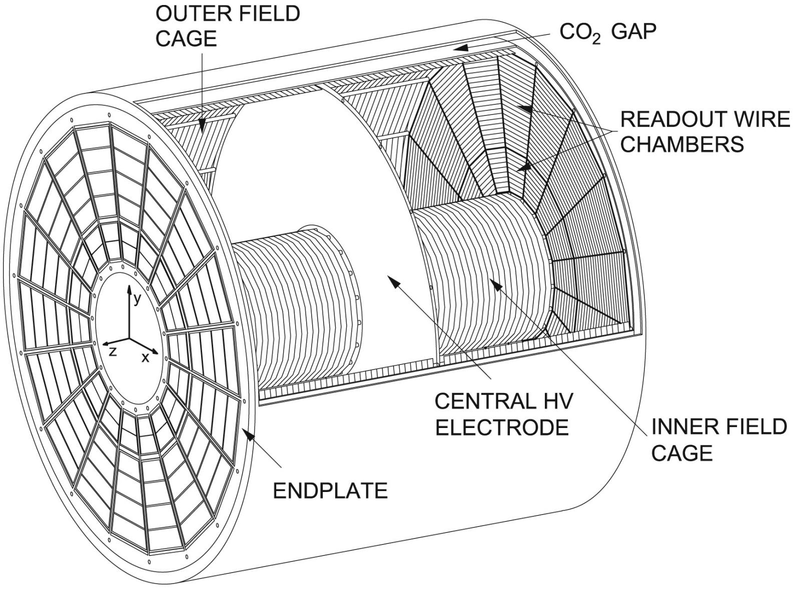

Figure 3.4.: Schematic view of the TPC barrel [156]. The gas volume is divided by the central cathode and the endplates are divided into 18 sectors on each side, which are equipped with a total of 36 readout chambers.

an incoming minimum ionizing particle (MIP) yields per cm, depends mainly on the effective ionization potential of the gas mixture. For example, in Ar-CO$_2$ (90/10) a MIP frees around 75 e$^-$ per cm in the gas, in Ne-CO$_2$ (90/10) only 37 e$^-$ per cm[1]. These charges have to be amplified by Multi Wire Proportional Chambers (MWPCs) such that a detectable signal is induced on the readout. The end plates are segmented into 18 sectors, each covering an azimuthal angular area of 20°. Every sector is mounted with one inner and one outer readout chamber and the signal from the amplification is induced in their pad plane. The latter is subdivided into rows perpendicular to the radial direction and contains a total of 159 rows per sector. There are pads with three different sizes of $4 \times 7.5\,\mathrm{mm}^2$, $6 \times 10\,\mathrm{mm}^2$ and $6 \times 15\,\mathrm{mm}^2$ and the smallest pads can be found in the rows closest to the beam, since in this region the track density is the largest. The complete readout comprises a total of 557 568 pads. Consequently, the electrons created along the track of the particle form a two-dimensional projection of the track on the readout plane. The third dimension can be obtained from the drift velocity and arrival times of the electrons at the pad plane. The amplitude of the signal is proportional to the specific ionization energy loss $\mathrm{d}E/\mathrm{d}x$ of the particle over the length of the individual pad. As it will be discussed in Section 3.5.2, the average of this measurement over many pads provides the information to identify the species of the traversing particle. The best resolution for a track is obtained when all 159 rows are crossed, which is the case for tracks within $|\eta| < 0.9$. Particles in the pseudorapidity

---

[1] These values include the primary ionization of MIP itself, but also secondary ionization produced by the primary ionization.

range of $|\eta| < 1.5$ can also be tracked, however, at a reduced resolution. Except for the gaps and insensitive detector area of 27 mm between the readout chambers, the detector covers the full 2π range in φ. The spatial resolution, investigated with cosmic rays [156], is overall better than 1100 µm in $r\varphi$ and better than 1250 µm along z. The maximum drift time for charge depositions close to the central membrane is around 100 µs (4000 LHC bunch crossings [153]), which defines the integration time of the detector. In the setup described above, a fraction of the ions created by the amplification of electrons by the MWPC close to the readout would drift back to the central cathode and this way distortions of the drift field can emerge. Therefore, a gating grid is installed above the amplification stage that is closed after 100 µs with respect to the trigger to neutralize the charges. The maximum readout rate of the system is hence limited to $\mathcal{O}(1\,\mathrm{kHz})$.

3.2.3. Time of Flight (TOF) System

The TOF measures the arrival time of particles by using Multi-gap Resistive Plate Chambers (MRPCs). The detector modules are strips with a size of $122 \times 13\,\mathrm{cm}^2$ and are placed such that their long side is oriented perpendicular to the radial beam direction. Together with the readout electronics they occupy a volume with a cylindrical shape at a radial distance between 370 to 399 cm from the nominal interaction point. The active area of the modules has a size of $120 \times 7.4\,\mathrm{cm}^2$ and consists of 10 gaps that are filled with a counting gas. In direction of the long side they are segmented into two rows equipped with 48 readout pads with a size of $2.5 \times 3.5\,\mathrm{cm}^2$. The whole detector comprises of 1593 strips and has a total of 157 248 channels. A large and homogeneous electric field over the gaseous volume creates an avalanche from any ionization produced by a traversing charged particle. Since the charge can only move in each gap, there is almost no drift time and the charge is immediately collected at the readout. The integration time of the TOF is around 500 ns, which corresponds to 20 LHC bunch crossings [153]. The arrival time for each particle is measured relative to the event time t_{ev}. Preferably, the latter is provided by the T0 detector comprising of two quartz Cerenkov counters at forward rapidities at each side of the interaction point. The total timing resolution σ_{Tot} is a convolution of the TOF timing resolution σ_{TOF} and event timing resolution σ_{ev} according to $\sigma^2_{\mathrm{Tot}} = \sigma^2_{\mathrm{TOF}} + \sigma^2_{\mathrm{ev}}$. The TOF system has an intrinsic timing resolution of around $\sigma_{\mathrm{TOF}} \approx 80\,\mathrm{ps}$ [150, 157], which was improved in 2017 to $\sigma_{\mathrm{TOF}} = 56\,\mathrm{ps}$ by applying an improved calibration method [158]. In case t_{ev} is measured by the T0 detector, σ_{ev} is negligible compared to σ_{TOF}. Especially in pp collisions, where the multiplicities are small, the limited acceptance of the T0 leads to events without a measurement of t_{ev}. As outlined in [157], the event time can then be estimated from the TOF measurement itself, if at least three tracks are matched to a signal in the TOF and in which case the timing resolution σ_{ev} depends on the number of tracks with a matched signal. For events with 3 matched tracks a timing resolution of $\sigma_{\mathrm{ev}} = 120\,\mathrm{ps}$ is reached, whereas for events with 25 matched tracks the timing resolution becomes as low as $\sigma_{\mathrm{ev}} = 25\,\mathrm{ps}$ and the intrinsic uncertainty of the TOF detector characterizes σ_{Tot}.

For all other cases the time stamp of the LHC bunch crossing is used, which results in a much worse timing resolution between $\sigma_{\mathrm{ev}} \approx 80$–$200\,\mathrm{ps}$ depending on the size of the bunches in the LHC [158].

3.2.4. V0 System

The V0 system uses rings of scintillators located at opposite sites of the interaction point within the central barrel. Side C covers the range of $-3.7 < \eta < -1.7$ and is placed[2] at $z = -0.88\,\mathrm{m}$, side A covers the range of $2.8 < \eta < 5.1$ and is placed at $z = 3.29\,\mathrm{m}$. Both sides are segmented into four concentric rings, each ring subdivided into eight tiles of equal azimuthal width. The scintillator emits light in the visible range when excited by charged particles. The light is then guided by optical fibers to photo-multiplier tubes (PMTs), where light is converted into an electrical signal by the photoelectric effect, which is amplified and read out. The produced light and the resulting signal are directly proportional to the number of charged particles hitting the tile. The time resolution of both counters is better than 1 ns [154]. This is faster than the time between bunch crossings and than the integration time of most detectors. For the previous reasons, most of the trigger decisions are based on a signal in either one or both V0 arrays. Since the charged-particle production at forward and mid rapidity is correlated, and the amplitude of the V0 is proportional to the amount of incoming charged particles, the signal can be further used to select collisions with specific properties, e.g., pp collisions with high multiplicities or head-on Pb–Pb collisions. Additionally, on the analysis level the precise timing information of the signals is used to distinguish collisions of the two nominal bunches from out of bunch collisions for example with residual gas in the beam pipe.

3.3. Software Packages

During the operation of the experiment the raw data is collected until the end of one fill, lasting up to 12 h in case of pp collisions. Afterwards the data is compressed and shipped to the permanent storage and is further processed as computing resources become available. For the data handling and processing, the software package AliROOT [159, 160] was developed. It is based on the ROOT [161] framework. AliROOT is responsible for the reconstruction, calibration, alignment and visualization of the data as well as handling simulations. It also provides a container, the Event Summary Data (ESD), to store the complete information related to each event. A further filtering retains only the part of information necessary for most analyses, which is stored in a second container, the so called Analysis Object Data (AOD). In the context of this work and for the analysis of two-particle correlation functions, the data was further filtered into an even more reduced version, the so called nanoAOD container. These nanoAODs are provided as

---

[2] The position is constrained by the absorber in front of the muon arm of ALICE.

input to the actual analysis in the AliPhysics [162] framework, where the functionality for this work was implemented as part of the FemtoDream classes.

3.4. Event Reconstruction

The details of the reconstruction of the collision vertex and the trajectories can be found in chapter 6 of [154] and here only a short overview is given. Within ALICE, the V0 and SPD detectors have the fastest response after being hit by particles. They are used either separately or in combination to trigger other, associated detectors to read and record their data. All the data related to one trigger signal is then called an event[3]. The signals of each detector are summarized in clusters, to store information like the global position of signals within the detector system, timing information of signals or, if available, the amplitude of the signals. For each event the reconstruction starts from this raw data by estimating the position of the PV as the center point of all SPD tracklets, which are lines defined by the positions of two clusters on individual SPD layers. Track finding and fitting is then performed in three steps that follow an inward-outward-inward scheme. The first iteration begins by finding so-called TPC-only tracks starting from seeds of several clusters at the outermost boundary of the TPC that point towards the PV. The amplitude of clusters along the track is used to estimate the specific energy loss $\langle \mathrm{d}E/\mathrm{d}x \rangle$. To find so-called global tracks, the TPC-only tracks are propagated towards the ITS and if possible, matched with a cluster in each of the six layers[4]. The distance between the last found cluster of a trajectory and the PV is extrapolated until the distance to the PV is minimized. The second iteration uses the clusters associated with tracks found in the previous iteration and refits them in the outward direction. They are matched to clusters in the outward detectors, like TRD and TOF, and the integrated track length and time-of-flight are calculated. The final iteration refits all previously found clusters inwards. At this point the inverse curvature of the track is determined to measure the momentum, which is corrected for energy losses due to elastic scattering in the detector material. The location of the PV is determined again, separately from TPC-only and global tracks.

Inactive sectors in the SPD due to cooling problems introduce dead zones and limit the acceptance of global tracks, while the TPC standalone offers almost full acceptance. Some analyses require a uniform acceptance or suffer from the reduced efficiency, as it is the case for the measurement of the two-particle correlation function. TPC-only tracks have to be extrapolated through the gap between the nominal interaction point and the TPC and, compared to global tracks, have a significantly worse tracking, vertex

---

[3] The readout times of some detectors like the TPC are much longer than that of others like the EMCal. In order to also record data during dead times of slower detectors, while the faster ones are ready to take data, they can trigger themselves or be triggered to take data standalone or in combination with other detectors (e.g. SPD + EMCal).

[4] Standalone ITS tracks are built from clusters in the ITS that are unused at this point and in principle could be used to track particles with transverse momenta as low as $80\,\mathrm{MeV}/c$.

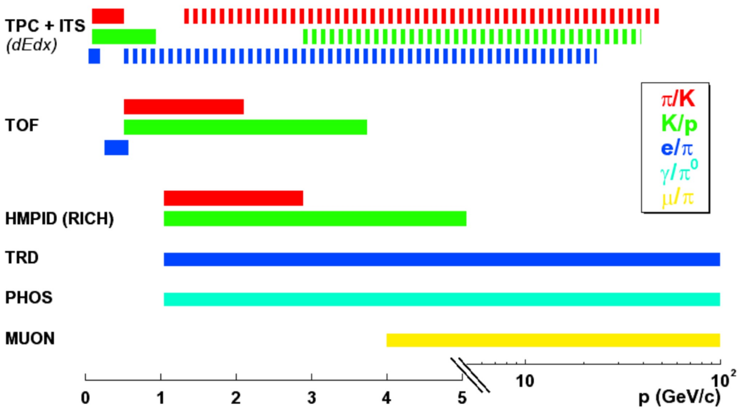

Figure 3.5.: Overview of the PID capabilities of the ALICE detectors at different momenta. The solid lines depict regions where particles can be individually identified [164].

and momentum resolution. This disadvantage can be mitigated by using the PV of the ITS tracklets as an additional constraint in the reconstruction of the TPC-only tracks. It was shown that the momentum resolution up to $10\,\mathrm{GeV}/c$ is similar to that of global tracks [154]. The resolution on the measurement of the transverse momentum p_T for protons, pions and kaons varies and is around 2% for particles with $p_\mathrm{T} = 10\,\mathrm{GeV}/c$ and decreases below 1% for $p_\mathrm{T} < 1\,\mathrm{GeV}/c$.

For each track the so-called distance of closest approach (DCA) to the PV is obtained in the transverse plane DCA_{xy} and along the beam axis DCA_z. The resolution of global tracks is $\sigma_\mathrm{DCA} < 0.5\,\mathrm{mm}$. Correspondingly, a particle is defined as primary if it is either created in the collision or results from the decay of a short-lived particle with a mean proper lifetimes τ less than $1\,\mathrm{cm}/c$ [163]. Some longer-lived, typically neutral particles like Λ or K^0_S, but also charged ones like Ξ^- are still invisible to the detector. Their lifetime is too short to traverse or even reach the detector and they have to be reconstructed from the tracks of their charged decay products. Such particles are reconstructed by applying topological selection criteria as it will be discussed in Section 3.5.4. These are obtained in the last step of the reconstruction. Neutral decay candidates, so-called V^0s, are built by pairing tracks of opposite charge. Moreover, cascade candidates are formed by combining V^0 candidates with an additional charged track, the so-called bachelor.

3.5. Particle Identification (PID)

One of the outstanding features of the ALICE detector is its unique ability to identify particles over a large momentum range. This is achieved by combining the PID capabilities of several sub-detectors. Figure 3.5 gives an overview of the different detectors and particles that can be identified. Several charged hadrons, for example, can be identified on a track-by-track basis within the full acceptance of the central barrel by using ITS, TPC and TOF. At low momenta, individual tracks of (i) $\pi^{\pm}$, (ii) $\mathrm{K}^{\pm}$ and (iii) (anti)protons can be identified by the ITS[5] up to a p_{T} of approximately (i) $0.2\,\mathrm{GeV}/c$, (ii) $0.4\,\mathrm{GeV}/c$ and (iii) $0.7\,\mathrm{GeV}/c$. At intermediate momenta, the TPC provides the necessary PID information to identify tracks up to a p_{T} of approximately (i) $0.8\,\mathrm{GeV}/c$, (ii) $0.5\,\mathrm{GeV}/c$ and (iii) $1.1\,\mathrm{GeV}/c$. It should be noted that with the TPC and within these ranges it is impossible to avoid a contamination by $\mathrm{e}^{\pm}$ in the selection of $\mathrm{K}^{\pm}$ at $p_{\mathrm{T}} \approx 0.5\,\mathrm{GeV}/c$ and in the selection of (anti)protons at $p_{\mathrm{T}} \approx 1.0\,\mathrm{GeV}/c$. At large momenta, the PID on a track-by-track basis is ensured by the TOF, up to a p_{T} of approximately (i) $0.7\,\mathrm{GeV}/c$, (ii) $2.0\,\mathrm{GeV}/c$ and (iii) $3.5\,\mathrm{GeV}/c$. Additionally, there is the HMPID with a limited geometrical and kinematic ($p_{\mathrm{T}} \gtrsim 1.0\,\mathrm{GeV}/c$) acceptance, which is able to distinguish $\mathrm{K}^{\pm}$ and $\pi^{\pm}$ up to $p_{\mathrm{T}} \approx 3\,\mathrm{GeV}/c$ and (anti)protons and $\mathrm{K}^{\pm}$ up to $p_{\mathrm{T}} \sim 5\,\mathrm{GeV}/c$. Some measurements rely on the identification of $\mathrm{e}^{\pm}$, but the PID of ITS or TOF is hampered by the fact that they have a similar signature as $\pi^{\pm}$ at most momenta. Also, their identification in the TPC suffers from a contamination by (anti)protons and $\mathrm{K}^{\pm}$, as discussed before. Therefore, with the TRD exists a dedicated detector, in order to distinguish them from hadrons up to momenta of several GeV/c. Finally, unstable particles or photon conversions are identified, in this case via their decay products. In the following, the concepts relevant for this work and their implementation on analysis level are discussed.

3.5.1. Time of Flight

The relativistic momentum is defined as

$$p = m_0 \beta \gamma = m_0 \beta \frac{1}{\sqrt{1-\beta^2}}, \tag{3.1}$$

where the three variables are the momentum p, the velocity β and the rest mass m_0. In the most straightforward way $\beta = \Delta s / \Delta t$ can be measured by the combination of tracking information and timing measurement in the TOF. Consequently the only unknown in Eq. 3.1 is m_0. An example for the distribution of β as a function of momentum at the inner side of the TPC, p_{TPC}, measured from all particles produced in p–Pb collisions at $\sqrt{s_{\mathrm{NN}}} = 5.02$ TeV with ALICE is shown in Fig. 3.6. The different bands correspond to the masses of $\mathrm{e}^{\pm}$, $\pi^{\pm}$, $\mathrm{K}^{\pm}$, $\mathrm{p}^{\pm}$, d and $\overline{\mathrm{d}}$, as indicated in the plot. The TOF timing resolution, which was discussed in Section 3.2.3, leads to the finite width of the bands. The overall background is a result of mismatches between tracks and timing signals. This effect increases with larger particle multiplicities and is most pronounced for particles with low momentum, because of multiple scattering effects in the material of the TRD. For this reason, it is desirable to use the TOF information only when the PID capabilities of other detectors, especially in the lower momentum region, are not sufficient. As it was discussed at the beginning of this section, it can be seen from the same plot that, as the momentum increases, the track-by-track identification of the different particle species deteriorates, since the different bands begin to merge.

---

[5] This, however, requires global tracks, which are not used by all analyses

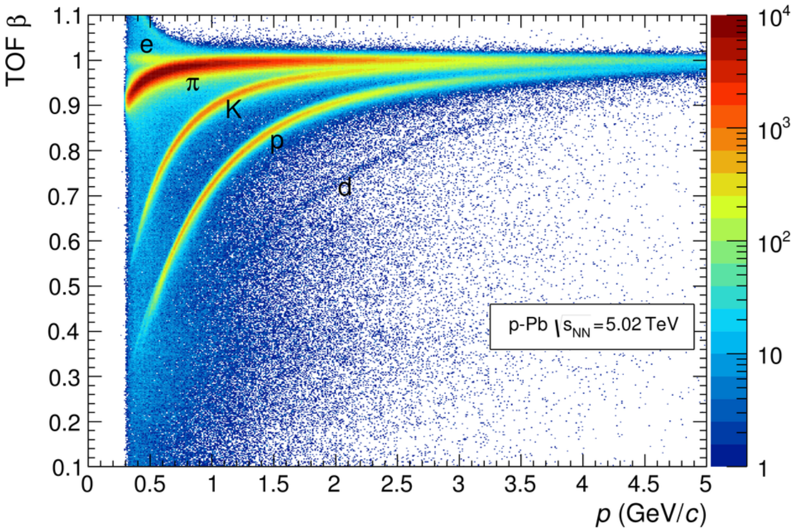

Figure 3.6.: Distribution of the TOF β as a function of the TPC momentum in p–Pb collisions [165].

3.5.2. Specific Energy Loss

As the particles pass through the detector material, they continuously undergo inelastic collisions. Their typical specific energy loss per unit path length, $\mathrm{d}E/\mathrm{d}x$, is of the order of a few keV per traveled centimeter. Thereby, the particles excite and ionize the detector material. The resulting charge depositions in the active material of many detectors are the basis for the signals that are read out and subsequently used to reconstruct their corresponding trajectory. This process can be further exploited to identify the traversing particle, since $\mathrm{d}E/\mathrm{d}x$ is strongly influenced by the velocity $\beta\gamma$ of the projectile. In a thick gaseous medium, like the counting gas of the TPC, the average energy loss is described by the Bethe-Bloch Equation [166–168] and is calculated as function of β, charge of the projectile and several constants, which are all related to the detector material. As previously discussed, a combined measurement of β and of the momentum determines m_0 via the relation given in Eq. 3.1. The charge depositions along the particle trajectories in the TPC gas are amplified by MWPCs, by which a current is induced on the readout plane. The resulting charge Q is proportional to the initial $\mathrm{d}E/\mathrm{d}x$, but it can be distributed over several pads. It is reconstructed over the length of each readout row, by clustering the signals in neighboring pads. Hence, a maximum of 159 measurements are available, if the trajectory crosses all readout rows. At this point, it is important to note that the tails of the distribution of individual $\mathrm{d}E/\mathrm{d}x$ values extend towards infinity [168]. The estimation of the mean of such a variable is significantly biased by few measurements at large values. Instead of the mean $\langle \mathrm{d}E/\mathrm{d}x\rangle$, the most probable value $\langle \mathrm{d}E/\mathrm{d}x\rangle_{\mathrm{m.p.}}$ is obtained via a truncation method. For each single trajectory, the largest charge deposition Q_{max} is evaluated and a fixed fraction of this value is used to define a threshold, according to which clusters with $Q > Q_{\mathrm{max}}$ are discarded. The most probable value is then estimated from the remaining clusters [168]. In Fig. 3.7, the

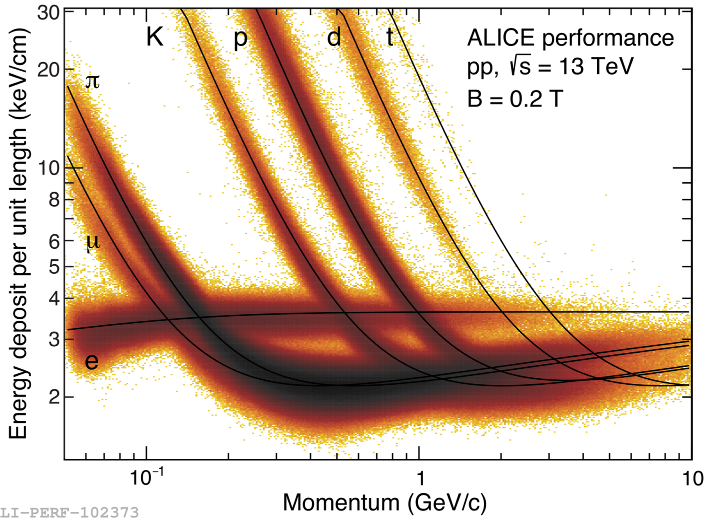

Figure 3.7.: Distribution of the TPC $\langle \mathrm{d}E/\mathrm{d}x \rangle_{\mathrm{m.p.}}$ as a function of the TPC momentum measured from particles produced in pp collisions at $\sqrt{s} = 13$ TeV [2].

ALICE TPC $\langle \mathrm{d}E/\mathrm{d}x \rangle_{\mathrm{m.p.}}$ distribution is shown, as a function of the momentum at the inner side of the TPC. It is measured from particles that were produced in pp collisions at $\sqrt{s} = 13$ TeV. Clear bands emerge around the expectation values for the different particle species depicted by the black curves. The latter are obtained by a fit of the ALEPH parameterization of the Bethe-Bloch formula [154][6]. The spread of the measured values results from the statistical nature of the $\mathrm{d}E/\mathrm{d}x$ measurement in each pad row as well as from the intrinsic detector resolution. In both, the measured distribution and parameterized values of $\mathrm{d}E/\mathrm{d}x$, a minimum appears for the different particles at momenta that are equivalent to $\beta\gamma{\sim}3$–4, which is the velocity, where particles are considered to be MIPs. At larger values of $\beta\gamma$ the energy loss begins to increase and follows the so-called relativistic rise. The same figure clarifies the kinematic ranges that were reported at the beginning of this section, to identify different hadrons and electrons with the TPC[7]. As it can be seen from Fig. 3.7, within these ranges, the measured values of $\mathrm{d}E/\mathrm{d}x$ can be unanimously associated with the individual particle species and are free from any contamination. The TPC information is insufficient, when different bands overlap, as is the case for example for $\mathrm{K}^{\pm}$ and $\mathrm{e}^{\pm}$ at $p \approx 500$–$600\,\mathrm{MeV}/c$. At larger momenta, the $\mathrm{d}E/\mathrm{d}x$ measurement of the TPC is insufficient for a track-by-track identification and the particle species of a trajectory can be evaluated on a probabilistic

---

[6] A description of the fit procedure and a detailed description of the corrections can be found in [169].

[7] The data, which was used to produce Fig. 3.7, was recorded with a lower magnetic field of $B = 0.2\,\mathrm{T}$. This way, tracks with momenta smaller than $150\,\mathrm{MeV}/c$, which usually curl up before they reach the TPC, can then also be reconstructed and it is possible to appreciate the $\mathrm{d}E/\mathrm{d}x$ measurement in the TPC also at these momenta.

basis, e.g., by fitting the spectrum in small momentum ranges by the convolution of Gaussian distributions.

3.5.3. Particle Identification via nσ Values

The PID capabilities of TPC and TOF are designed to supplement each other and will be used in this analysis to identify the candidates. A large fraction of particles are produced in a momentum range where the $\langle \mathrm{d}E/\mathrm{d}x \rangle_{\mathrm{m.p.}}$ is able to distinguish between the different species. At larger momenta, the PID capabilities are preserved by the additional evaluation of the TOF β. In principle, trajectories of a specific species can be identified by graphically defining a selection region around the expectation value of both observables. This "manual" approach, however, fails to take into account the momentum dependence of the PID resolution in a straightforward way. Therefore, the TPC $\langle \mathrm{d}E/\mathrm{d}x \rangle_{\mathrm{m.p.}}$ and the TOF β is first analyzed individually within narrow momentum intervals. The left panel of Fig. 3.8 depicts one exemplary projection of the $\langle \mathrm{d}E/\mathrm{d}x \rangle_{\mathrm{m.p.}}$ distribution measured by the TPC from tracks of particles produced in Pb–Pb collisions at $\sqrt{s_{\mathrm{NN}}} = 2.76$ TeV with $0.73 < p < 0.75\,\mathrm{GeV}/c$. The distribution is a convolution of individual contributions by $\pi^{\pm}$, $\mathrm{K}^{\pm}$, $\mathrm{e}^{\pm}$, protons and anti-protons. For this momentum range, the contributions of d, $\overline{\mathrm{d}}$ and heavier nuclei are well separated and outside of the range shown here. Each contribution can be approximated by a Gaussian [154] or generalized Gaussian [170] function, where the parameterization of $\mathrm{d}E/\mathrm{d}x$ is used to fix the mean values of the respective contributions. Their sum is then used to fit the total experimental distribution and for each particle i the width σ_i is obtained, which corresponds to the PID resolution in this momentum interval. This procedure is applied separately to the spectrum of TPC and TOF in momentum intervals covering the whole

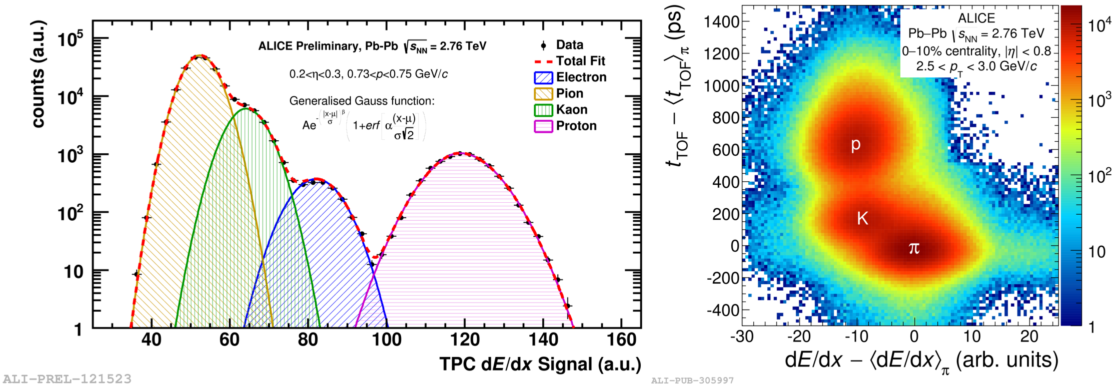

Figure 3.8.: Both plots were obtained from trajectories of particles in Pb–Pb collisions at $\sqrt{s_{\mathrm{NN}}} = 2.76$ TeV [165]. (left) Fit of the TPC $\mathrm{d}E/\mathrm{d}x$ in a narrow momentum interval using generalized Gaussian functions. (right) Two-dimensional distribution of the $\mathrm{d}E/\mathrm{d}x$ measurement in the TPC and the β measurement by the TOF relative to the $\pi^{\pm}$ hypothesis for one p_{T} interval.

kinematic range of ALICE. At this point, the difference, between the $\langle \mathrm{d}E/\mathrm{d}x \rangle$ or β of each individual track and the expectation value of each particle hypothesis i, can be expressed in terms of numbers of standard deviations n_{σ_i}. An advantage of this method is that candidates can conveniently be selected by a constant criterion, while the actual value σ_i varies as a function of p.

A straightforward way to combine the PID of TPC and TOF becomes clear by looking at the right panel of Fig. 3.8. For particles that were produced in Pb–Pb collisions at $\sqrt{s_{\mathrm{NN}}} = 2.76$ TeV and that have a momentum $2.5 < p_{\mathrm{T}} < 3.0\,\mathrm{GeV}/c$, it shows the two dimensional distribution $\mathrm{d}E/\mathrm{d}x$ measured by the TPC (x-axis) and t measured by TOF (y-axis). Both are expressed as the difference to the expectation value of $\pi^{\pm}$ hypothesis. In this momentum range, the $\langle \mathrm{d}E/\mathrm{d}x \rangle$ of the different particle species in the TPC is too similar to distinguish for example protons and K^{+}, but by including the TOF measurement in the analysis a two-dimensional selection can distinguish the particles. On the level of the analysis, for each trajectory the difference to the corresponding particle hypothesis is expressed in terms of $n_{\sigma_{i,\mathrm{TPC}}}$ and $n_{\sigma_{i,\mathrm{TOF}}}$ and candidates can be selected by a combined PID, by evaluating $n_{\sigma_{i,\mathrm{combined}}}$ as

$$n_{\sigma_{i,\mathrm{combined}}} = \left(n^2_{\sigma_{i,\mathrm{TPC}}} + n^2_{\sigma_{i,\mathrm{TOF}}} \right)^{1/2} . \tag{3.2}$$

3.5.4. Invariant Mass and Identification of Decays

The most abundantly produced particles in reactions at the LHC live long enough to be directly reconstructed and identified. Most particles that are known, however, are unstable and have to be reconstructed from their decay products as briefly noted in Section 3.4. The terminology used in the following tags the particle in the initial state as parent, and the particles in the final state as children. Examples representative for the following discussion and work are $\phi \rightarrow \mathrm{K}^{+} + \mathrm{K}^{-}$, $\mathrm{K}^0_{\mathrm{S}} \rightarrow \pi^{+} + \pi^{-}$, $\Lambda \rightarrow \mathrm{p} + \pi^{-}$ or $\Xi^{-} \rightarrow \Lambda + \pi^{-}$. In cases like the Ξ^{-} the Λ itself needs to be reconstructed from its decay products. Usually, a particle can decay via multiple channels that are each associated with different branching ratios. The full kinematic information of the parent can only be reconstructed via channels, where all children are detectable. Properties like the masses and lifetimes of the parent and children are usually known from previous measurements.

In the following paragraph, only the two-body decay is considered, but it is straightforward to extend this to decays into three or more particles. Because of momentum conservation, the momentum of the parent $\vec{p}_{\mathrm{parent}}$ is given by the sum of the child momenta, $\vec{p}_{\mathrm{parent}} = \vec{p}_1 + \vec{p}_2$. Energy conservation requires that the energy before and after the decay are the same, which implies $E^2_{\mathrm{parent}} = (E_1 + E_2)^2$, where the energy for a particle is defined as $E_i^2 = \vec{p}_i^{\,2} c^2 + m^2_{0,i} c^4$. Consequently, this can be solved for the only unknown, which is the invariant mass mass m_{parent}. The signal of correctly identified decays then scatters around the mass of the parent in an interval determined by its lifetime and the detector's momentum resolution. Unfortunately, the candidates that are formed for the experimental search of the parents include combinations of particles from the decay of other particles as well as random combinations with uncorrelated particles. Typically, the signal is overlaid by a background and before applying a selection on the invariant mass, all available criteria related to the topology and the properties of the children should be evaluated.

The decay of a $\mathrm{K^0_S}$ to a π^+ and π^- as well as that of a Ξ^- to a π^- and a Λ, which subsequently decays into a protons and a π^-, is schematically depicted in Fig. 3.9 and should aid the following discussion. The reconstruction and selection of candidates usually starts from the trajectory of children, which are stable long enough to traverse the detector. Naturally, the PID of TPC and TOF can be employed to pick combinations of the correct species. The children are produced at the point where the decay occurs and their trajectories point in principle to this secondary vertex and not the PV. The offset of the point of production, however, depends on the lifetime and momentum of the parent. Owing to the finite tracking resolution this can only be resolved for longer-lived decays like the $\mathrm{K^0_S}$ ($c\tau\sim 2.7$ cm [2]) or the Λ ($c\tau\sim 7.9$ cm [2]) and not short lived ones like

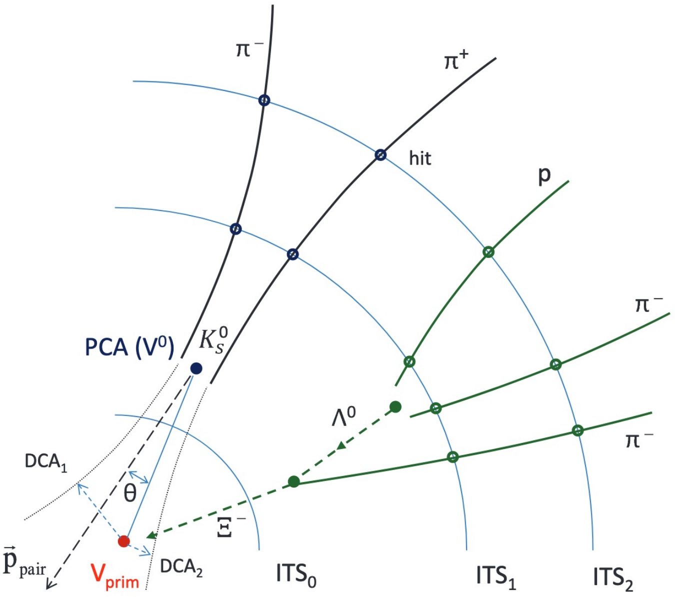

Figure 3.9.: Schematic representation of the reconstruction principle of secondary vertices. The two examples are based on the decays of a $\mathrm{K^0_S}$ and a Ξ^-. The decay points were placed arbitrarily between the first two ITS layers without any attention to scale. The actual trajectory of the charged children are represented by solid lines. The dashed lines represents the extrapolation of the trajectories to the primary vertex as well as several auxiliary vectors [154].

the ϕ ($c\tau{\sim}46\,\mathrm{fm}$ [2]). Consequently, the selection of candidates from long-(short-) lived decays can be enhanced by requiring their trajectories to have a minimum (maximum) DCA to the PV. When identifying longer-lived decays, the spatial coordinates of the secondary vertex are estimated by the point that minimizes the distance to both the trajectories, taking into account the uncertainty related to the track reconstruction. The children are produced at the same point and the DCA between their two trajectories and to the secondary vertex has to be of the order of the tracking resolution. The offset of the secondary vertex from the PV itself is given by the lifetime of the parent. The parent's trajectory can be assumed to be a straight line connecting the PV and the secondary vertex. If the parent is a primary particle, it should align parallel to its momentum. For parents which are secondaries and themselves originate from a decay or for combinatorial background any orientation is possible. In case of a cascade decay like the Ξ^-, the identification via the invariant mass and topology is also applied to the child. A candidate is then formed by the combination with an additional trajectory, the called bachelor track, following the above steps if applicable.

The ranges where candidates are selected need to be tuned carefully in order to keep a high efficiency in the reconstruction of the signal while discarding as much of the background as possible. Therefore, one usually relies on the help of simulations, since the details depend on the detector and the specific particle that should be identified.

3.6. Candidate Selection

To measure two-particle correlation functions, a data set has to be picked, then a sample of events has to be selected and, at last, the particles of interest have to be identified and paired. The criteria that will be discussed in the following can generally be grouped into two classes: the ones that ensure a high reconstruction quality of the event or the candidate and the ones that are used to select individually protons, Λ, Ξ^- and their respective antiparticles from the pool of all candidates.

3.6.1. Data Sample

During the Run 2 campaign, the LHC provided beams of different particle species. In order to choose a data set for this work, several factors had to be considered. The number of particle pairs that can be found within the detector acceptance, determines the statistical significance of the measurement. Collision systems with large particle multiplicities $\mathrm{d}N_{\mathrm{ch}}/\mathrm{d}\eta$ are preferred, not only because of combinatorics, but also due to an enhancement of strangeness production at larger multiplicities [171]. The effect is most pronounced for multi-strange hadrons like, the Ξ^- and Ω^-. Another factor is the size of the system, since sources with small sizes offer the most sensitivity to the interaction at close distances, as discussed in Section 2.4. Table 3.1 gives an overview of typical source sizes and multiplicities in the pp, p–Pb and peripheral and central Pb–Pb

Table 3.1.: Typical source sizes extracted from one dimensional p–p correlations and average charged particle multiplicities for pp INEL collisions at $\sqrt{s} = 13$ TeV [39, 175], for p–Pb INEL collisions at $\sqrt{s} = 5.02$ TeV [176, 177] and for peripheral and head-on Pb–Pb collisions at $\sqrt{s_{\mathrm{NN}}} = 2.76$ TeV [117, 178].

System	r^* (fm)	$\langle \mathrm{d}N_{\mathrm{ch}}/\mathrm{d}\eta \rangle$
pp	~1	7
p–Pb	~1.5	17
Pb–Pb (peripheral)	~2	344
Pb–Pb (head-on)	~4	1448

collisions, where the Pb nuclei overlap partially or fully, respectively. Just considering the number of pairs, the obvious choice would be the Pb–Pb data set. The source size, however, is the smallest in pp and p–Pb collisions and is the largest in Pb–Pb collisions. The significantly larger distance between the emitted particles reduces the sensitivity to the interaction at very small distances. It is further important to consider that the system created in heavy-ion collisions is expected to evolve over timescales of $\mathcal{O}\,(\mathrm{fm}/c)$ [172, 173]. In turn, collective effects significantly modify the spectra of emitted particles and result in mass-dependent modulations of the emission source relative to the orientation of the two nuclei in the lab frame [174]. The latter fluctuates strongly collision by collisions and it consequently becomes more involved to use the source parameters extracted from p–p correlations to constrain the emission source of other baryon pairs. Hence, pp and p–Pb collisions provide a much cleaner environment for a study of particle interactions, since at least one projectile has a point-like shape and the distances between the emission points are much smaller than in Pb–Pb.

Minimum bias triggered p–Pb collision

ALICE recorded p–Pb collisions at two energies. At $\sqrt{s_{\mathrm{NN}}} = 8.16$ TeV the interaction rates were higher than 100 kHz, and only $\sim 150 \times 10^6$ events including the TPC were recorded. They were discarded for this work because of the small number of events and the difficulty to distinguish overlapping collisions (pile-up). Collisions at $\sqrt{s_{\mathrm{NN}}} = 5.02$ TeV were provided by the LHC at more moderate interaction rates between 16 kHz to 20 kHz. The SDD has a busy time of 1024 µs and thereby limits the data taking rate to ~1 kHz. Since all other detectors have a shorter busy time, the rate can be enhanced, by continuing to record data without the SDD. Events are tagged as either `CENT` if they include the SDD information or `FAST` if they do not. The former are reconstructed twice, including and ignoring the SDD information. Accordingly, the `CENT` and `FAST` sample can be combined in a way that they have the same reconstruction efficiency and resolution and a total of 730×10^6 events are available for the analysis. Minimum-bias (MB) refers here to the trigger conditions, which were chosen such that inelastic collisions are recorded as uniformly as possible. A typical example, where inelastic interactions are not correctly reflected in the recorded data, is, when collision occur in a way that the charged particles are produced outside of the acceptance of any detector. This effect is most prominent at low multiplicities and has to be corrected for, e.g., in the measurement of cross sections for particle production.

High-multiplicity triggered pp collisions

Even though $\sim 1.7 \times 10^9$ minimum bias events were recorded from pp collisions at $\sqrt{s} = 13$ TeV, the average multiplicity of $\langle \mathrm{d}N_{\mathrm{ch}}/\mathrm{d}\eta \rangle \sim 7$ is too low to find enough pairs of protons and multi-strange baryons to study their interaction via the two-particle correlation function in a meaningful way. Looking at the events more differential in terms of multiplicity, it was shown that about 1% of the collisions produced multiplicities of around $\langle \mathrm{d}N_{\mathrm{ch}}/\mathrm{d}\eta \rangle \sim 26$, which is similar to the values observed in p–Pb or peripheral Pb–Pb collisions. The ALICE collaboration decided to further investigate these events and at the beginning of Run 2 introduced a high-multiplicity (HM) trigger that includes a minimum threshold of the signal of the V0 system on both sides of the interaction point in the decision. A total of 1.04×10^9 events were collected, with multiplicities that correspond to the highest 0.17% fraction of the multiplicity distribution of all inelastic pp collisions which create at least one hit in the SPD or V0 (INEL > 0).

Monte Carlo data sets

The Pythia [141] (DPMJET [179]) Monte Carlo (MC) generator was used to simulate pp (p–Pb) collisions. As the simulated particles traverse the material of ALICE, a simulation chain estimates the magnitude of the charge depositions with GEANT3 [180] and imitates the resulting detector response. These simulated events are then processed by the same reconstruction algorithm as events from real collisions [154]. On the analysis level, each trajectory is associated with a MC particle that carries the full particle information, for example its species, origin, generated momentum etc. This is used to analyze the performance of the selection criteria and to investigate the effect of the finite momentum resolution. It should be noted that final state interaction is in general not accounted for in MC simulations, the genuine femtoscopic signal is absent and the two-particle correlation functions hence unity.

3.6.2. Event Selection

Table 3.2 summarizes the criteria to select those events that are then used for the analysis. The estimation of the spatial coordinates, where the reaction occurred, is discussed in Section 3.4. The resulting PV is a pivotal anchor point in the reconstruction of the whole event and is crucial to evaluate several particle selection criteria. To ensure a good quality and resolution, the coordinates of the PV obtained from at least two ITS + TPC tracks are preferred over the ones estimated with at least one ITS tracklets. If both are available, the difference between the two along the beam axis Δz has to be less than 5 mm. Events are discarded when the PV is reconstructed with nothing but TPC-only tracks. At the interaction point, the bunches in the LHC are well focused in the transverse xy plane perpendicular to the beam direction, but are spread along the beam in the z direction. Consequently, the position of each reaction fluctuates mostly in z around the nominal interaction point in the center of ALICE. In order to ensure a uniform acceptance within the geometry of ALICE, the z coordinate of the PV has to lay $\pm 10\,\text{cm}$ around the nominal interaction point. Ideally, each event corresponds to single collisions between two beam particles close to the nominal interaction point. However, there can be a contamination caused by two classes of background reactions. The first class consists of out-of-bunch pile-up, which is mainly caused by inelastic reactions of beam particles with other bunches, residual gases down the beam pipe or the structures of the LHC. If they occur outside of the detector system, they can be distinguished by their difference in timing information of the V0 and T0 detectors on A and C side. In case it coincides with a proper beam interaction, the event can be identified by the correlation between the number of SPD clusters and ITS tracklets. Particles originating from an additional interaction, which happens away from the nominal interaction point, will nevertheless create signals in the SPD. But since they typically do not point back to the nominal interaction vertex, the reconstruction will fail in finding corresponding tracks. The second class, in-bunch pile-up, is caused by multiple reactions in the same bunch crossing. These events are identified, if the reconstruction algorithm succeeds in finding a second primary collision vertex [154]. In HM pp collisions at $\sqrt{s} = 13$ TeV it was estimated [25] that this way the contamination by in-bunch pile-up is reduced to be present in a maximum of 1.4% of all selected events. From the point of view of the

Table 3.2.: Event selection criteria.

Quality assurance	
Physics selection	default
Incomplete DAQ	check
z vertex	$\lvert z_{\text{vtx}} \rvert < 10\,\text{cm}$
Contributors to global track vertex	$N_{\text{contrib,track}} > 1$
Contributors to SPD vertex	$N_{\text{contrib,SPD}} > 0$
SPD vertex z resolution	$\sigma_{\text{SPD},z} < 0.25\,\text{cm}$
Distance between global track and SPD vertex	$d_{\text{vtx,track}-\text{SPD}} < 0.5\,\text{cm}$
pile-up rejection	
Multiple vertices	`AliVEvent::IsPileUpFromSPD()`
Cluster vs. Tracklets	`AliEventUtils::IsSPDClusterVsTrackletBG()`
Collision Candidates	
Minimum Bias (MB)	`AliVEvent::kINT7`
High Multiplicity (HM)	`AliVEvent::kHighMultV0`

trigger, collisions that produce large multiplicities and those that overlap share the same characteristics. The resulting high-multiplicity data set is hence much more affected by in-bunch pile-up than the MB p–Pb data set.

After applying all selection criteria, 619×10^6 MB p–Pb events at $\sqrt{s_{\mathrm{NN}}} = 5.02$ TeV and 986×10^6 HM pp events at $\sqrt{s} = 13$ TeV are available to measure the two-particle correlation functions.

3.6.3. Protons

The criteria applied to select protons and anti-protons are summarized in Table 3.3. They are adopted from the femtoscopy analysis in pp collisions at $\sqrt{s} = 7$ TeV [23]. In general, they have the aim to minimize the contamination by other particles and maximize and the fraction of primaries. The p_{T} range was limited to values between $0.5\,\mathrm{GeV}/c$ and $4.05\,\mathrm{GeV}/c$. At smaller p_{T} values a significant fraction of protons originates from spallation reactions of particles with the beam pipe. This contribution, as well as the one of secondaries from weak decays, are further suppressed by restricting the DCA to a maximum of 0.1 cm in the xy-plane and 0.2 cm in the z direction. In order to ensure a good tracking and PID performance, the candidates are selected within $|\eta| < 0.8$ and tracks are required to have more than 80 clusters in the TPC. For the same reason, the ratio between the number of crossed TPC rows to the number of clusters that can potentially be found is required to be larger than 0.83, basically limiting the amount of lost clusters along the trajectory. If clusters are shared with other tracks, the candidates are rejected to suppress auto-correlations in the measurement of the correlation function. Both the TPC and the TOF are used for PID. At low momenta, the $\mathrm{d}E/\mathrm{d}x$ of protons is

Table 3.3.: Proton selection criteria.

Quality assurance	
Pseudorapidity	$\lvert\eta\rvert < 0.8$
Transverse momentum	$0.5 < p_{\mathrm{T}} < 4.05\,\mathrm{GeV}/c$
TPC cluster	$n_{\mathrm{TPC}} > 80$ (out of 159)
Findable TPC clusters	$n_{\mathrm{crossed}}/n_{\mathrm{findable}} > 0.83$
Tracks with shared TPC clusters	rejected
Primary selection	
Distance of closest approach xy	$\lvert\mathrm{DCA}_{xy}\rvert < 0.1\,\mathrm{cm}$
Distance of closest approach z	$\lvert\mathrm{DCA}_{z}\rvert < 0.2\,\mathrm{cm}$
PID	
$p_{\mathrm{TPC}} < 0.75\,\mathrm{GeV}/c$	$\lvert n_{\sigma,\mathrm{TPC}}\rvert < 3$
$p_{\mathrm{TPC}} < 0.75\,\mathrm{GeV}/c$	$n_{\sigma,\mathrm{combined}} = \sqrt{n^2_{\sigma,\mathrm{TPC}} + n^2_{\sigma,\mathrm{TOF}}} < 3$

sufficiently separated from the $\mathrm{d}E/\mathrm{d}x$ of other particles for an unambiguous track-by-track identification and only at larger p it is necessary to consider the timing information of the TOF. The details of the selection based on n_σ values are discussed in Section 3.5.3. The p_T distribution of all selected candidates is shown in the top left panel of Fig. 3.10. A sharp drop off can be seen, when the TOF signal is required and the reconstruction efficiency decreases because of track losses by multiple scattering in the TRD material. In the following, the distribution is used as a p_T weight to evaluate averaged quantities.

Also events and tracks of the MC sample were subjected to the above selection criteria. The species of the particle is stored as the PDG code [2] and allows one to check for each track whether or not the PID succeeded in selecting a proton. The purity is calculated for each p_T interval as $\mathcal{P} = \mathrm{S}/\left(\mathrm{S}+\mathrm{B}\right)$, where S is the number of correctly identified signal candidates, and B the number of those that are background or contamination. In the top right panel of Fig. 3.10 the purity of protons is shown for pp collisions at $\sqrt{s} = 13$ TeV. In pp (p–Pb) collisions at $\sqrt{s} = 13$ TeV ($\sqrt{s_\mathrm{NN}} = 5.02$ TeV) both protons and anti-protons are selected with a p_T-averaged purity of 99.3% (98.4%). MC generators are unable to fully describe the p_T [181] or $\langle \mathrm{d}N_\mathrm{ch}/\mathrm{d}\eta \rangle$ [171] dependent yields of particles in pp and p–Pb collisions. Consequently, the composition of the selected candidates in terms of their origin is not necessarily representative for real data, if those fractions are obtained directly from simulations. In order to evaluate the composition of the selected sample nevertheless, the shapes of the DCA distributions of primary, secondary and material distributions are obtained from MC simulations. They are used as templates to fit the measured DCA_{xy} distribution of the data in 20 p_T intervals. The bottom left panel of Fig. 3.10 shows an example for one such fit in the interval $0.7 < p_\mathrm{T} < 0.9\,\mathrm{GeV}/c$. As it can be seen, the shapes of the distributions of individual contributions differs, which illustrates the sensitivity of this observable to the origin of the particle. The template of primary particles steeply peaks at 0 and its width is only a result of the detector resolution. The template of secondary contributions is much wider, which is caused by the finite lifetime of the parent. At last, the one of material contributions is almost flat. After the fit, the results are evaluated within $|\mathrm{DCA}_{xy}| < 0.1\,\mathrm{cm}$ to estimate the p_T dependent composition of the selected sample. The result is shown for protons in the bottom right panel in the same figure and is found to be consistent with that of anti-protons. Only a weak p_T dependence is observed and the values are averaged taking into account the weight of each p_T bins. For pp (p–Pb) collisions at $\sqrt{s} = 13$ TeV ($\sqrt{s_\mathrm{NN}} = 5.02$ TeV) the sample is found to consist of 82% (86%) primary protons and a negligible amount of protons from material interactions. The remaining protons originate from weak decays of either a Λ or a Σ^+. Their templates are too similar to fit them separately, therefore only the sum of secondaries can be fit. A direct look at the candidates in the MC in both pp and p–Pb event generators reveals that about 70% of the secondary protons originate from the decay of a Λ, while 30% originate from the decay of a Σ^+. These values are found to be rather consistent with the production ratios of the two particles in Z-boson decays [182, 183]. In the following it is assumed that by applying the above selection to the data sets recorded from pp (p–Pb) collisions at

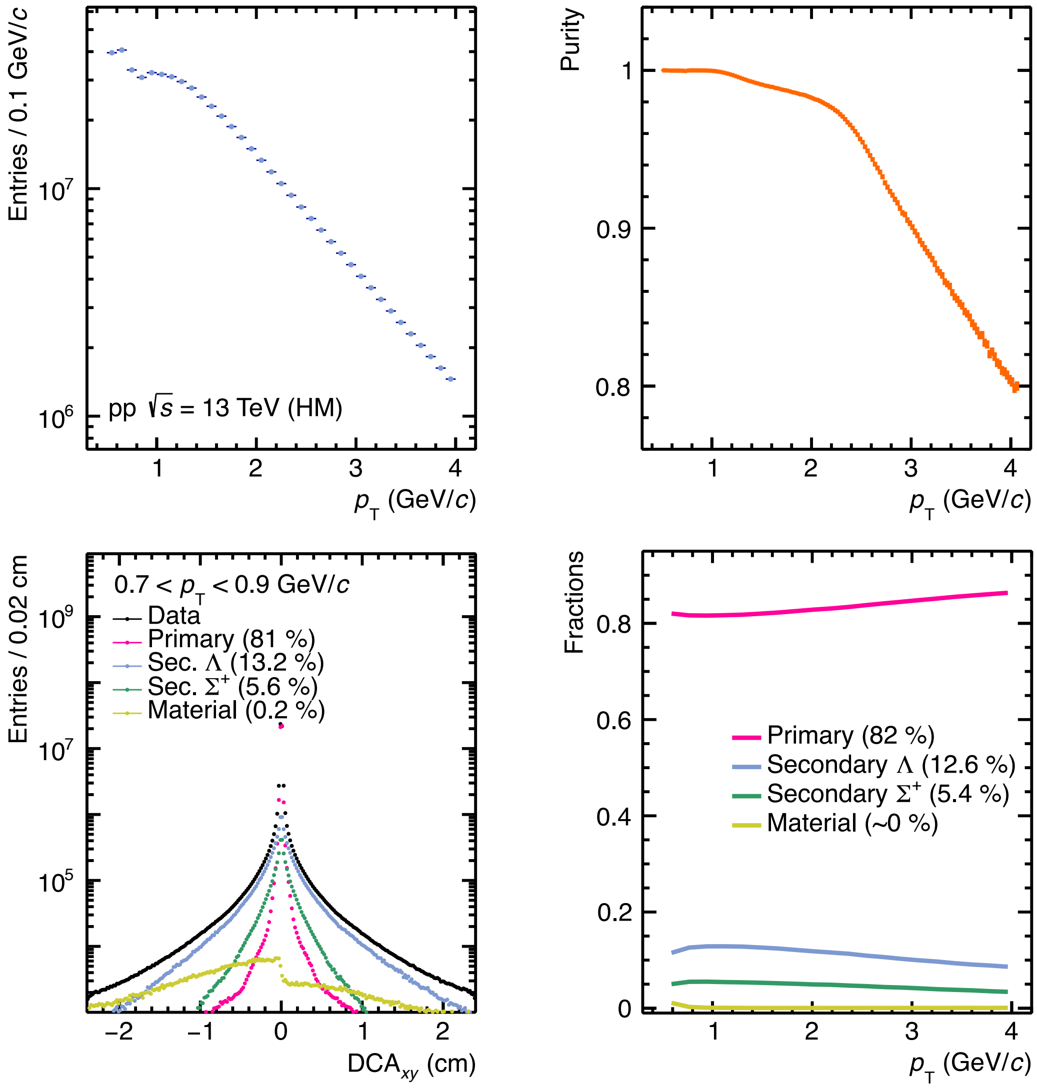

Figure 3.10.: (Top left) p_T distribution and (top right) purity of the proton sample. (Bottom left) Exemplary fit of of the DCA_{xy} distribution in one p_T interval with MC generated templates. (Bottom right) Decomposition of the proton sample over the whole p_T range. Results are shown for the analysis of HM pp collisions at $\sqrt{s} = 13$ TeV and can be found in App. B.1 for p–Pb collisions at $\sqrt{s_{NN}} = 5.02$ TeV.

$\sqrt{s} = 13$ TeV ($\sqrt{s_{NN}} = 5.02$ TeV), about 13% (10%) of the protons from secondary contributions stem from the decay of a Λ, about 5% (4%) from the decay of a Σ^+.

3.6.4. Λ Hyperons

The neutral Λ ($\overline{\Lambda}$) is unstable, with a lifetime $c\tau \sim 7.9\,\mathrm{cm}$ and decays weakly with a branching ratio (BR) of 63.9% to $\Lambda \rightarrow \mathrm{p}\pi^-$ ($\overline{\Lambda} \rightarrow \overline{\mathrm{p}}\pi^+$) [2]. As outlined in Section 3.5.4, the V^0 is reconstructed from the trajectories of its children. Its lifetime is long enough to utilize several geometrical properties of the decay. Table 3.4 provides an overview over the selection criteria that are discussed for the Λ in the following. By switching the particle hypothesis for the children, they are also applicable to identify the $\overline{\Lambda}$. Originally they were tuned via a MC-based study for the analysis of pp collisions at $\sqrt{s} = 7$ TeV [23, 107].

Table 3.4.: Λ selection criteria.

Child track selection criteria	
Pseudorapidity	$\lvert\eta\rvert < 0.8$
TPC cluster	$n_{\mathrm{TPC}} > 70$
Distance of closest approach to PV	$\mathrm{DCA}_{\mathrm{xy}} > 0.05\,\mathrm{cm}$
PID	$\lvert n_{\sigma,\mathrm{TPC}}\rvert < 5$
Out-of-bunch pile-up removal	Hit in ITS SPD or SSD or TOF timing
DCA of the child tracks at the decay vertex	$\mathrm{DCA}(\lvert\mathrm{p},\pi\rvert) < 1.5\,\mathrm{cm}$

V^0 selection criteria	
Transverse momentum	$p_{\mathrm{T}} > 0.3\,\mathrm{GeV}/c$
Λ decay vertex	$\lvert i_{\mathrm{vertex}_\Lambda}\rvert < 100\,\mathrm{cm}$, i=x,y,z
Transverse radius of the decay vertex r_{xy}	$0.2 < r_{xy} < 100\,\mathrm{cm}$
Pointing angle α	$\cos\alpha > 0.99$
$\mathrm{K}^0_{\mathrm{S}}$ rejection	$0.48 < \mathrm{M}_{\pi^+\pi^-} < 0.515\,\mathrm{GeV}/c^2$
Λ selection	$\lvert\mathrm{M}_{\mathrm{p}\pi} - \mathrm{M}_{\Lambda,\mathrm{PDG}}\rvert < 4\,\mathrm{MeV}/c^2$

Similar to the case of (anti)protons discussed above, the proper reconstruction of the child trajectories is ensured by only using candidates within $\lvert\eta\rvert < 0.8$ and with at least 70 clusters within the TPC. Only the $\mathrm{d}E/\mathrm{d}x$ measurement in the TPC is used for PID, since the requirement of a TOF measurement reduces the reconstruction efficiency, especially when the child tracks have a low momentum. In order to select particles originating from weak decays, trajectories are selected, if they have a minimum DCA to the PV in the transverse direction of 0.05 cm and have a maximum DCA to the decay vertex of the Λ of 1.5 cm. The magnetic field causes the trajectories of particles with low momenta to curl up, and they can not be reconstructed as TPC-only or global tracks. This introduces a mass dependent cut-off not only for the tracking, but also for the reconstruction of Λ candidates below $p_{\mathrm{T}} \sim 0.3\,\mathrm{GeV}/c$. Additional selection criteria can be directly applied to the topology of the V^0 candidate. The offset of the secondary vertex to the PV in the transverse plane should at least be 0.2 cm and not exceed 100 cm. Regardless of its relative position to the PV, the coordinates of the secondary vertex have to be within a sphere of 100 cm around the nominal interaction point to ensure that it is located within the fiducial volume of the detectors. To select primary Λ baryons and reject fake candidates the cosine of the pointing angle (CPA) between the momentum vector of the Λ candidate and its trajectory is required to be at least 0.99. The above selection can identify a charged π as a proton, since at momenta $p_{\mathrm{TPC}} > 1.0\,\mathrm{GeV}/c$, the $\mathrm{d}E/\mathrm{d}x$ of these two particles in the TPC is similar. As a consequence, the V^0 candidate might actually originate from the decay of a K^0_S, which produces two oppositely charged π mesons. In order to exclude this contamination, the invariant mass of each V^0 candidate is also calculated assuming the charged π mass for both children. If it lays within a window of $18\,\mathrm{MeV}/c^2$ around the nominal K^0_S mass, the candidate is rejected. Then the invariant mass of the candidate is calculated assuming the nominal proton and charged π mass for the corresponding children. The distribution of all candidates is fitted using the sum of a double Gaussian to describe the signal and a second order polynomial to describe the background. The integrals over the corresponding functions in the selection region are used to estimate the purity $\mathcal{P}$. If the purity is compared among sub-samples of events, which were recorded at different LHC beam conditions, it can be observed to worsen for increasing interaction rates. This behavior points towards an incomplete rejection of out-of-bunch pile-up. Since particles, which are produced in overlapping collisions, are not associated with the reconstructed PV, their trajectories carry a similar signature as those of the children of V^0 candidates. In order to check whether or not an individual trajectory is associated to the collision that triggered the event, the timing information of detectors, with good timing resolution and and short integration times, is evaluated relative to the timestamp of the bunch crossing. Therefore, child trajectories were required to have a hit in either one of the SPD and SSD layers or the in the TOF, which results in a purity independent of data taking period and interaction rate.

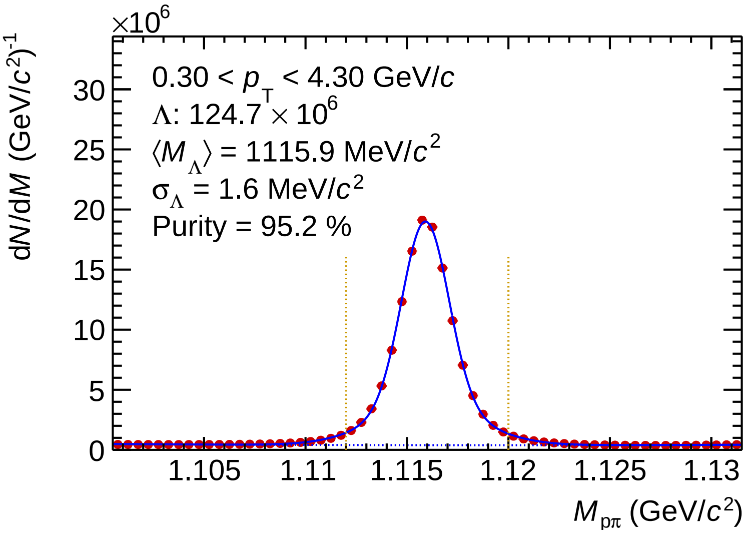

Figure 3.11.: Invariant proton and π^- mass distribution, integrated in p_T, obtained from pp collisions at $\sqrt{s} = 13$ TeV

As it can be seen in Fig. 3.11, a clear peak arises in the invariant mass spectrum around the nominal Λ mass. The fit in several individual p_{T} intervals is shown in Fig. B.2. It was found that the Λ and $\overline{\Lambda}$ is reconstructed with a resolution σ between $1.5\,\mathrm{MeV}/c^2$ and $1.8\,\mathrm{MeV}/c^2$. The purity and number of selected Λ candidates is estimated and

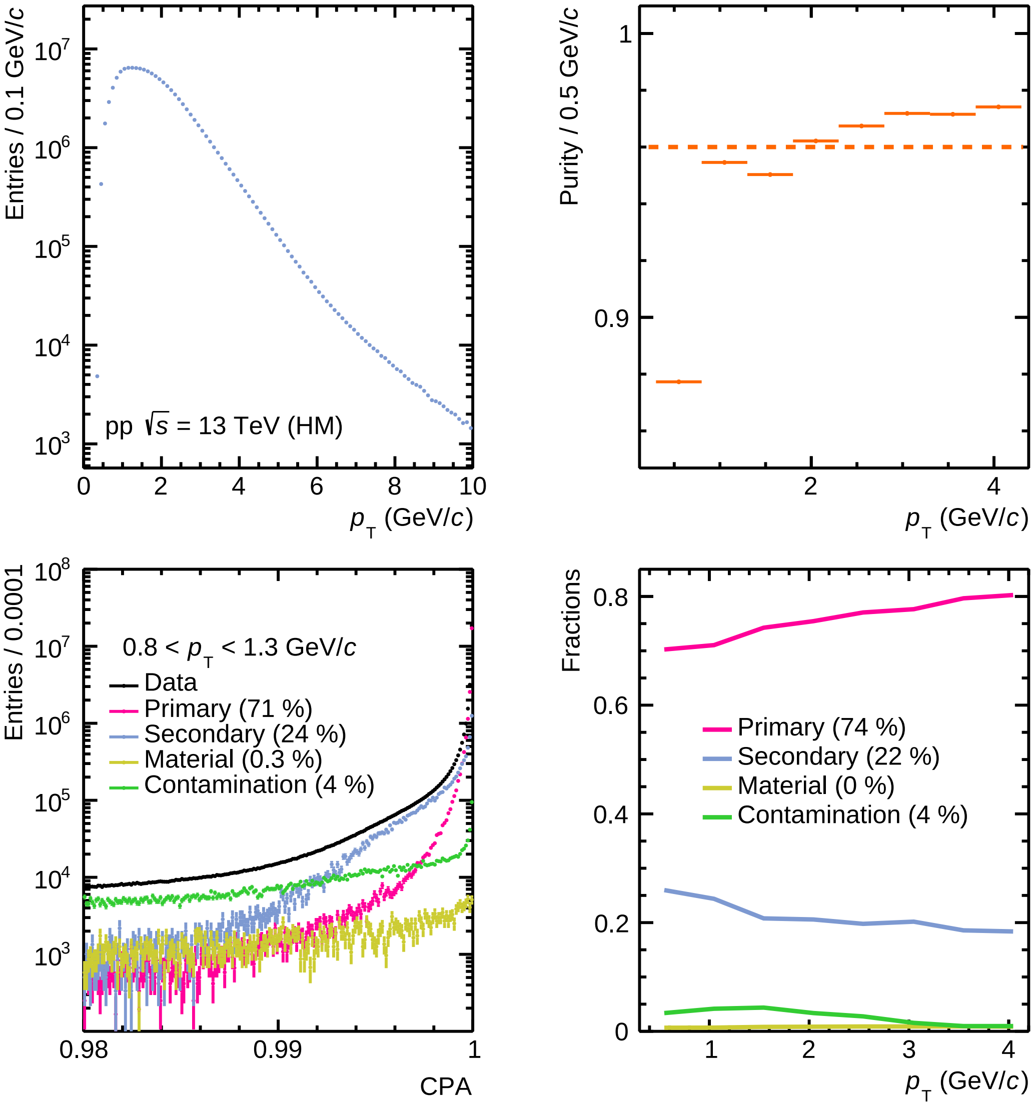

Figure 3.12.: (Top left) p_{T} distribution and (top right) purity of the Λ sample. (Bottom left) Exemplary fit of of the CPA distribution in one p_{T} interval with MC generated templates. (Bottom right) Decomposition of the Λ sample over the whole p_{T} range. Results are shown for the analysis of HM pp collisions at $\sqrt{s} = 13$ TeV

presented in the upper panels of Fig. 3.12. The p_{T} averaged purity in pp collisions at $\sqrt{s} = 13$ TeV is 96%. In order to investigate the composition of the selected sample, the CPA distribution of primary, secondary and material Λ baryons and misidentified candidates are obtained from MC simulations. As for (anti)protons, they are used as templates to fit the integrated CPA distribution of the data in a total of 8 p_{T} intervals. As an example, the bottom left panel of Fig. 3.12 shows the result in the interval for $0.8 < p_{\mathrm{T}} < 1.3\,\mathrm{GeV}/c$. While the template of both primaries and secondaries has a maximum at CPA $= 1$, a much more pronounced peak appears for primaries than for secondaries. The template of material contributions and of fake candidates is rather flat, since for them any orientation between momentum and trajectory is possible. It should be noted that the Σ^0 is not included in the secondary contributions. It decays electromagnetically and produces a Λ, but its lifetime of $c\tau{\sim}22\,\mathrm{pm}$ is too short to distinguish it from a primary Λ by any observable. Their contribution can then be calculated from the production ratio between the Λ and the Σ^0, which is expected to be 1/3 [184] due to isospin considerations. Also experimental measurements support this [182, 183, 185–187], albeit the rather large uncertainties of around 20% for hadronic collisions at higher energies. With this, 55% of the selected candidates are Λ baryons produced directly in the collision, while 19% of the selected candidates originate from electromagnetic decays of a Σ^0. A fraction of 22% is found to originate from weak decays, which can exclusively be attributed to Ξ baryons, since the production of heavier particles that decay into a Λ like the Ω^- is suppressed by at least a factor of 10 [188]. The neutral and charged Ξ is produced equally and consequently each contribute with 11%. At last, material interactions and combinatorial background amounts to 4%.

3.6.5. Ξ Hyperons

The Ξ^- baryon is also unstable and has a lifetime $c\tau{\sim}5\,\mathrm{cm}$ and decays weakly with a BR of almost 100% to $\Xi^- \rightarrow \Lambda\pi^-$ ($\overline{\Xi}^+ \rightarrow \overline{\Lambda}\pi^+$) [2]. The selection criteria shown in Table 3.5 are based on a previous analysis [189]. They were slightly modified in order to obtain a higher purity and adapted to deal with the increased pile-up due to the higher interaction rates during the data taking in Run 2. The same selection criteria can also be used to identify $\overline{\Xi}^+$, if the particle hypothesis of the child trajectories is switched accordingly.

Most of the selection criteria discussed in last section are also applicable here, to the Ξ^- and to one of its children, the Λ. For the latter the selection has be adjusted such that secondary, not primary particles are identified. It is crucial to keep a high efficiency in selecting the signal, since two consecutive weak decays have to be reconstructed that each produce a charged π with low momentum. The TPC PID selection criteria of all three child trajectories were tightened compared to the ones in the last section to $\mid n_{\sigma,\mathrm{TPC}} \mid < 4$. A hit in one of the ITS layers or a matched TOF signal is required in order to use the timing information to remove the contribution of particles stemming from out-of-bunch pile-up. Only those candidates are selected, where all three children have a minimum DCA to the PV of 0.05 cm and the two children of the Λ have a maximum DCA to its decay vertex of 1.5 cm. The Λ candidate itself, this time a secondary, is requested to have an offset between its decay vertex and the nominal interaction point

Table 3.5.: Ξ^- selection criteria.

Child track selection criteria	
Pseudorapidity	$\lvert\eta\rvert < 0.8$
TPC cluster	$n_{\mathrm{TPC}} > 70$
Transverse Momentum	$p_{\mathrm{T}} > 0.3\,\mathrm{GeV}/c$
Distance of closest approach to PV	$\mathrm{DCA}_{\mathrm{xy}} > 0.05\,\mathrm{cm}$
Particle identification	$\lvert n_{\sigma,\mathrm{TPC}}\rvert < 4$
Out-of-bunch pile-up removal	Hit in ITS SPD or SSD or TOF timing
V^0 selection criteria	
Λ Pointing angle α	$\cos\alpha > 0.97$
Transverse radius of the Λ decay vertex r_{xy}	$1.4 < r_{xy} < 200\,\mathrm{cm}$
DCA of the child tracks at the Λ decay vertex	$\mathrm{DCA}(\lvert p, \pi\rvert) < 1.5\,\mathrm{cm}$
DCA of the Λ to the PV	$\mathrm{DCA} > 0.07\,\mathrm{cm}$
Λ selection	$\lvert \mathrm{M}_{\mathrm{p}\pi} - \mathrm{M}_{\Lambda,\mathrm{PDG}}\rvert < 6\,\mathrm{MeV}/c^2$
Cascade selection criteria	
Ξ^- Pointing angle α	$\cos\alpha > 0.98$
Transverse radius of the Ξ^- decay vertex r_{xy}	$0.8 < r_{xy} < 200\,\mathrm{cm}$
DCA of the child tracks at the Ξ^- decay vertex	$\mathrm{DCA}(\lvert p, \pi, \pi\rvert) < 1.6\,\mathrm{cm}$
Ω rejection	$1.667 < \mathrm{M}_{\Lambda\mathrm{K}^-} < 1.677\,\mathrm{GeV}/c^2$
Ξ^- selection	$\lvert \mathrm{M}_{\Lambda\pi^-} - \mathrm{M}_{\Xi^-,\mathrm{PDG}}\rvert < 5\,\mathrm{MeV}/c^2$

of 1.4 to 200 cm and to have a CPA > 0.97. The invariant mass, calculated assuming the nominal proton and charged π mass for the children, has to lay within $6\,\mathrm{MeV}/c^2$ around the nominal Λ mass.

The track of a charged π candidate is combined with a Λ candidate to form a Ξ^- candidate and to evaluate its decay vertex. This way, additional topological selection criteria become available. The charged π and Λ are required to have a maximum DCA to the Ξ^- decay vertex of 1.5 cm. The latter should have a distance between 0.8 cm and 200 cm from the nominal interaction point. Fake candidates are rejected by selecting only those with a CPA> 0.98. Nevertheless, the selection can include candidates from decays of an Ω^- ($\Omega^- \to \Lambda\mathrm{K}^-$), if the bachelor is a misidentified charged K. Hence, the invariant mass of the cascade candidate is calculated assuming the nominal mass of the charged K and the Λ for its children and those candidates within $5\,\mathrm{MeV}/c^2$ around the nominal Ω^- mass are rejected.

For the remaining candidates, the invariant mass is calculated using the nominal charged π and Λ mass. Figure 3.13 shows the resulting distribution, fit by the sum of a double

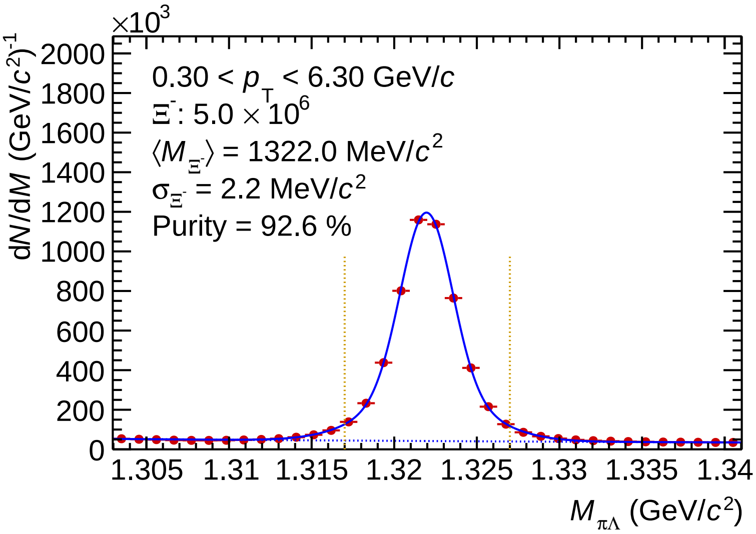

Figure 3.13.: Invariant Λ and π^- mass distribution, integrated in p_T, obtained from pp collisions at $\sqrt{s} = 13$ TeV.

Gaussian to describe the signal and a second order polynomial for the combinatorial background. The analysis in separate p_T intervals is shown in Fig. B.4 and B.3. The Ξ^- mass resolution in both collision systems is found to increase from 2.1 MeV/c^2 at low p_T to 2.7 MeV/c^2 at larger p_T, with a p_T averaged value of 2.3 MeV/c^2. Particles and antiparticles are selected within a 5 MeV/c^2 window around the nominal Ξ^- mass and are reconstructed with a p_T average purity of 92% (86%).

In the following the composition of the sample is analyzed in terms of primary and secondary contributions. The only particles which decay such that a Ξ^- is produced in the final state are the Ω^- and the negatively charged and neutral $\Xi(1530)$ resonances. A CPA fit, as it was applied to the distribution of selected Λ candidates, would only be

Table 3.6.: Production cross sections measured in pp collisions at $\sqrt{s} = 7$ TeV and branching ratios to the Ξ^- for the Ξ^-, Ω^-, $\Xi^0(1530)$ and $\Xi^-(1530)$, and calculation of the composition of the sample of candidates by the Ξ^- selection. For the references see text.

Particle	Ξ^-	$\Omega^- \to \Xi^-\pi^0$	$\Xi^0(1530) \to \Xi^-\pi^+$	$\Xi^-(1530) \to \Xi^-\pi^0$
$\mathrm{d}N_\mathrm{ch}/\mathrm{d}\eta$ ($\times 10^3$)	7.9	0.67	2.48	2.48
BR	1	0.085	1/3	2/3
BR$\cdot\mathrm{d}N_\mathrm{ch}/\mathrm{d}\eta$ ($\times 10^3$)	7.9	0.0057	0.83	1.65
Relative contrib.	76%	0.05%	8%	16%

sensitive to the contribution of the weakly decaying Ω^-, not the contribution of the two strongly decaying resonances. As it was argued in the last section, none of the selection criteria will alter the relative contributions of short-lived particles ($c\tau \lesssim 1\,\mathrm{cm}$) in the sample and the composition can be estimated from the production yields. The values of the $\mathrm{d}N_{\mathrm{ch}}/\mathrm{d}\eta$ for the Ξ^-, the Ω^- [188, 189] and the $\Xi^0(1530)$ [190, 191] were measured by ALICE. The charged $\Xi^-(1530)$ is assumed to be produced in the same amount as its neutral partner. All values for pp collisions at $\sqrt{s} = 7$ TeV are summarized in Table 3.6, where also the corresponding BR [2] of the channels to a Ξ^- in the final state are shown. The absolute contribution is calculated as the product of $\mathrm{d}N_{\mathrm{ch}}/\mathrm{d}\eta$ and the BR. The relative contribution is calculated by dividing the absolute contribution of each particle by the sum over all particles. The result shows, that 76% of all correctly identified Ξ^- are produced directly in the collision, 16% stem from the decay of a $\Xi^-(1530)$, 8% originate from the decay of a $\Xi^0(1530)$ and only a negligible fraction comes from the contribution of the Ω^-. These values are found to be consistent with those in p–Pb collisions at $\sqrt{s_{\mathrm{NN}}} = 5.02$ TeV.

3.7. Measurement of Pair distributions

The two-particle correlation function is measured according to Eq. 2.2. Event-by-event the identified particles are combined to built the pairs of interest and to measure the distribution $N_{\mathrm{same}}(k^*)$ of correlated pairs. The momenta of individual particles have to be boosted into the PRF, and here the nominal mass of the particle is always used. The number of pairs that can be found in the femtoscopic region within $k^* < 200\,\mathrm{MeV}/c$ for the different particle combinations that are used in this work are shown in Table 3.7, individually for each of the two data sets. All identified particles, including those that could not be paired, are buffered to also built pairs of particles from different events and to measure the distribution $N_{\mathrm{mixed}}(k^*)$ of uncorrelated pairs. In this step, it is important to avoid any bias due to a difference in acceptance and tracking performance and hence,

Table 3.7.: Pair yield of the different particle combinations in the relative momentum region $k^* < 200\,\mathrm{MeV}/c$ for the data sets from MB p–Pb collisions at $\sqrt{s_{\mathrm{NN}}} = 5.02$ TeV and HM pp collisions at $\sqrt{s} = 13$ TeV.

System **Pair**	p–Pb MB	pp HM
p–p	574.2×10^3	1728.2×10^3
$\overline{\mathrm{p}}$–$\overline{\mathrm{p}}$	412.9×10^3	1258.7×10^3
p–Λ	–	630.8×10^3
$\overline{\mathrm{p}}$–$\overline{\Lambda}$	–	495.5×10^3
p–Ξ^-	3.3×10^3	20.6×10^3
$\overline{\mathrm{p}}$–$\overline{\Xi}^+$	2.6×10^3	16.6×10^3

only events with similar event properties are considered for the mixing. For this purpose the events are grouped according to the z-position of their vertex in 10 bins with a width of 2 cm and according to their multiplicity, estimated by the number of global tracks in $|\eta| < 0.8$, in 41 bins covering a range from [0,3], [4,7], $\dots$, [156,159], [160,∞[. The individual buffer for each bin and particle species can store up to 10 events.

4. A common Source of Baryons

In order to study the details of the p–Ξ^- interaction via the measurement of their two-particle correlation function, the source distribution $S(r^*)$ of the pair has to be constrained. As it is discussed in Section 2.2 and 2.4, by assuming that baryon pairs share a common emission profile, the source can then be obtained from the measurement of the p–p correlation function, where the interaction is well understood. In the following, the validity of this assumption is tested by a comparison of the results to those extracted from the correlation function of p–Λ pairs. It will be demonstrated that only by explicitly modeling modifications of the source distribution due to the decay of short-lived resonances a common m_T scaling of the size of the Gaussian core source can be observed. These findings are summarized in a publication, see [139].

4.1. The p–p and p–Λ Correlation Functions

Besides the two-particle final-state interaction, responsible for the genuine femtoscopic signal of the individual pair, experimental effects can influence the measurement of the correlation function. The latter is obtained from the distributions $N_\mathrm{same}(k^*)$ and $N_\mathrm{mixed}(k^*)$, which have to be normalized. Their respective measurement depends on effects related to the detection of single particles, namely track splitting and merging, and the finite momentum resolution of the ALICE detector. It is further experimentally difficult or even impossible to avoid residual correlations due to non-femtoscopic sources and due to final state interactions of misidentified particles. As a result, several corrections have to be applied before the theoretical prediction can be compared to the measurement.

4.1.1. Normalization and Multiplicity Re-weighting

In principle, an arbitrary number of pairs can be created by mixing particles from different events. Mixing particles with those of up to 10 other events reduces the statistical uncertainty of the distribution $N_\mathrm{mixed}(k^*)$ compared to that of $N_\mathrm{same}(k^*)$ at least by a factor of 5. As a result, the measurement of the latter defines almost solely the overall statistical uncertainty on $C(k^*)$. The difference in the number of entries between the two distributions is equalized by the normalization factor $\mathcal{N}$ [104], which was already introduced in Eq. 2.2. In the femtoscopic region ($k^* \lesssim 200\,\mathrm{MeV}/c$) the shape of the two distributions can differ due to final state effects, therefore $\mathcal{N}$ has to be calculated

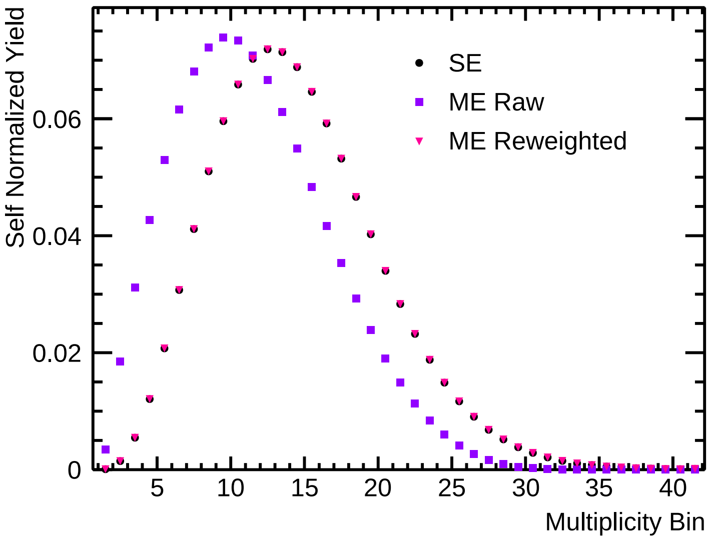

Figure 4.1.: Self-normalized yield of p–p pairs in p–Pb collisions at $\sqrt{s_{\mathrm{NN}}} = 5.02$ TeV as a function of the multiplicity bin in the range $200 < k^* < 900\,\mathrm{MeV}/c$. The distribution obtained from same event pairs is represented by black dots, the ones obtained from the mixed event pairs before and after the re-weighting are represented by violet squares and magenta triangles, respectively.

where they are expected to be equal and $C(k^*) = 1$. The upper range of this region can be limited by the presence of (non-)femtoscopic signals, which will be discussed in more detail later in this chapter. Accordingly, the normalization for both, p–p and p–Λ pairs, was calculated in the region $240 < k^* < 340\,\mathrm{MeV}/c$. Another important fact to consider when calculating correlation functions can be understood from Fig. 4.1, where the yield of p–p pairs in p–Pb collisions at $\sqrt{s_{\mathrm{NN}}} = 5.02$ TeV is shown as a function of the multiplicity. These distributions were measured by integrating the raw same event (black dots) and mixed event (violet squares) distributions outside of the femtoscopic region in the range $200 < k^* < 900\,\mathrm{MeV}/c$. In order to easily compare the resulting distributions, they were normalized such that the total sum is 1. It can be observed, that the mixed event distribution gives a much larger weight to lower multiplicity bins than the same event distribution. Events with only one identified particle are most frequent at low multiplicities and can not contribute to the correlated sample. They are nevertheless included in the mixing in order to properly reflect the single particle properties in the shape of the uncorrelated sample. This, however, means that at low multiplicities an increased amount of pairs is available for the mixing of different events. This effect is caused by combinatorics and is equalized by scaling the relative momentum distribution $N_{\mathrm{mixed}}(k^*)$ in each individual multiplicity bin by a re-weighting factor, such that it reproduces the yield of $N_{\mathrm{same}}(k^*)$ within the range $200 < k^* < 900\,\mathrm{MeV}/c$.

The correlation functions of p–p and $\overline{\mathrm{p}}$–$\overline{\mathrm{p}}$ pairs measured in MB p–Pb collisions at

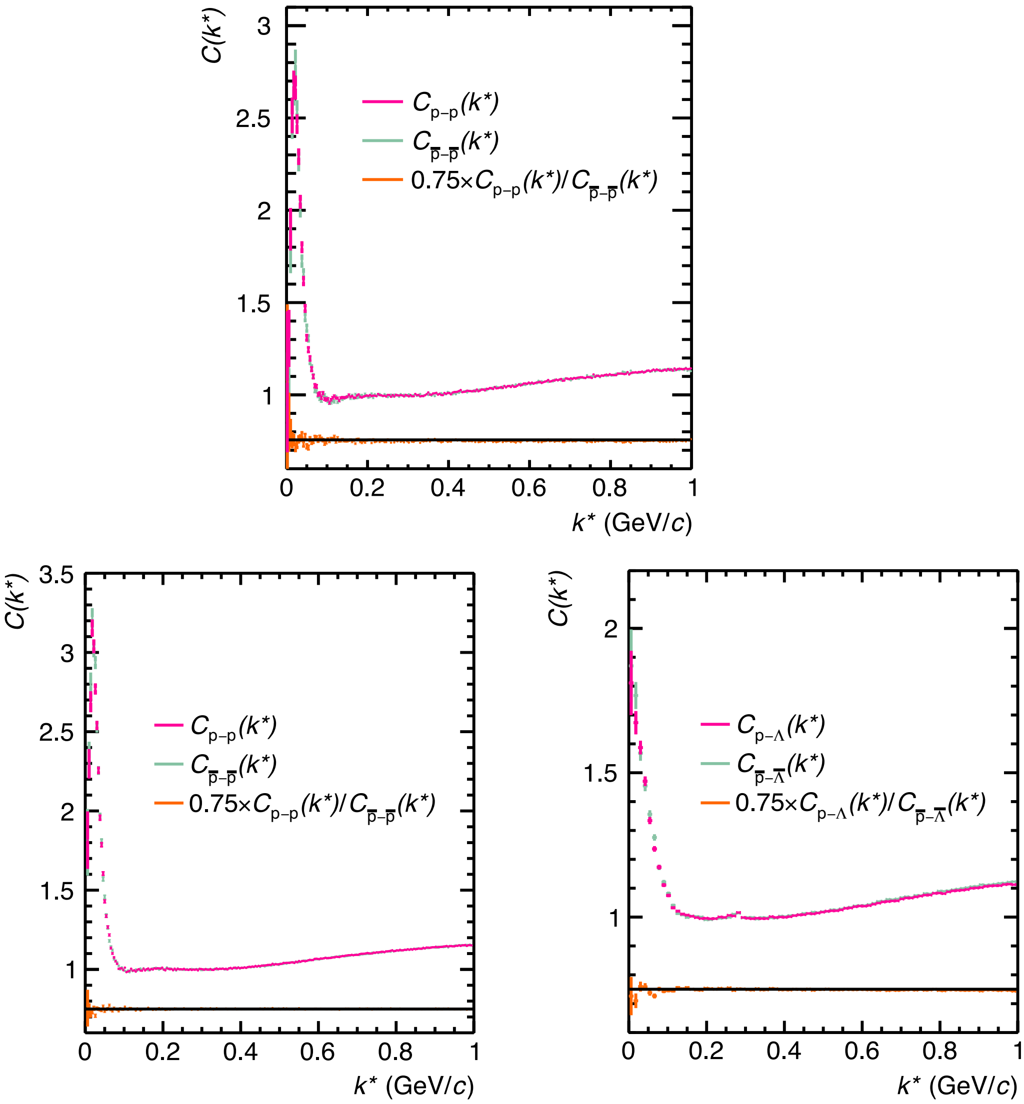

Figure 4.2.: Top Panel: The correlation functions measured in p–Pb collisions at $\sqrt{s_{\text{NN}}} = 5.02$ TeV of p–p (magenta points) and $\overline{\text{p}}$–$\overline{\text{p}}$ (green points) pairs. **Bottom Panel**: The correlation functions measured in HM pp collisions at $\sqrt{s} = 13$ TeV, for baryon pairs (magenta points), p–p in the left and p–Λ in the right panel, as well as antibaryon pairs (green points), $\overline{\text{p}}$–$\overline{\text{p}}$ in the left and $\overline{\text{p}}$–$\overline{\Lambda}$ in the right panel. The ratio between the $C(k^*)$ of baryon and antibaryon pairs (orange points) was scaled for all cases by a factor of 0.75 for visibility.

$\sqrt{s_{\text{NN}}} = 5.02$ TeV are shown in the top panel of Fig. 4.2, those of p–p, $\overline{\text{p}}$–$\overline{\text{p}}$, p–Λ and $\overline{\text{p}}$–$\overline{\Lambda}$ pairs measured in HM pp collisions at $\sqrt{s} = 13$ TeV in the bottom panel of the same figure. As it is seen best from the ratios (orange points), which was scaled by a factor of 0.75 in order to improve the visibility, the correlation functions between the pairs of baryons (b–b) and corresponding pairs of antibaryons ($\overline{b}$–$\overline{b}$) agree. Without taking into account the statistical uncertainties, the difference between the two is at maximum 4% for p–p and $\overline{\text{p}}$–$\overline{\text{p}}$ pairs, and at maximum 5% for p–Λ and $\overline{\text{p}}$–$\overline{\Lambda}$ pairs. Therefore, the $C(k^*)$ of each k^*_i bin is combined to improve the statistical significance and in the following p–p denotes the combination of p–p $\oplus$ $\overline{\text{p}}$–$\overline{\text{p}}$ and accordingly for p–Λ. Already at this point, the typical correlation signal of p–p pairs, as it was discussed in Section 2.4, can be indeed observed to reflect the features of the Coulomb and strong interaction as well as effects of QS. The p–Λ correlation function exhibits an enhancement above unity, which expected due to their attractive interaction, as discussed later in this chapter.

4.1.2. Detector Effects

The two particles of pair with small relative momenta, are emitted with almost collinear trajectories at the PV. If the particles carry different charges, their trajectories will be well separated as they move through the ALICE detector, because of a different bending in the magnetic field. Trajectories of particles with the same charge, however, continue to move almost in parallel. As a result, their reconstruction is hampered by effects of track splitting and merging [154], which denotes the case when one trajectory is reconstructed as two or two trajectories are reconstructed as one, respectively. In this analysis, this contribution is particularly relevant for p–p and $\overline{\text{p}}$–$\overline{\text{p}}$ pairs, and for this reason the proton selection criteria include a shared cluster cut in order to reject those candidates. As a result, the reconstruction efficiency of close pairs is reduced at small relative momenta. Since the trajectories in different events are not simultaneously reconstructed and hence, are not affected by these selection criteria, the same event distribution at small k^* might be depleted with respect to the mixed event distribution. As a result, the $C(k^*)$ would be suppressed, even in absence of any femtoscopic signal. The effect of close pairs is studied by looking at the distribution of the opening angles $\langle \Delta\varphi^* \rangle$ and $\Delta\eta$ between two trajectories. Instead of φ, the azimuthal angle at the PV, it is recalculated at a radial distance r within the TPC volume as

$$\varphi^* = \varphi + \arcsin \frac{0.3e \cdot r \cdot B}{2p_{\mathrm{T}}} \cdot \frac{1}{\mathrm{T\,m}}, \tag{4.1}$$

by taking into account the bending of the trajectory in the magnetic field. MC generated events are used, since here final state interactions are not accounted for and no femtoscopic signal is present. For p–p pairs from same and mixed events the average $\langle \Delta\varphi^* \rangle$ is calculated from the φ_i at nine different distances r_i between 85 and 245 cm from the nominal interaction point. The resulting distributions are shown in the left and right panel of Fig. 4.3. It can be seen that for pairs from different events, the distribution is completely uniform, while for pairs in the same event a depletion appears at $\langle \Delta\varphi^* \rangle = \Delta\eta = 0$, which is caused by the rejection of tracks with shared clusters. In order to mitigate this deficiency and at the same time measure $C(k^*)$ as close to $k^* = 0$ as possible, a close pair rejection (CPR) is implemented, by rejecting p–p and $\overline{\text{p}}$–$\overline{\text{p}}$ pairs

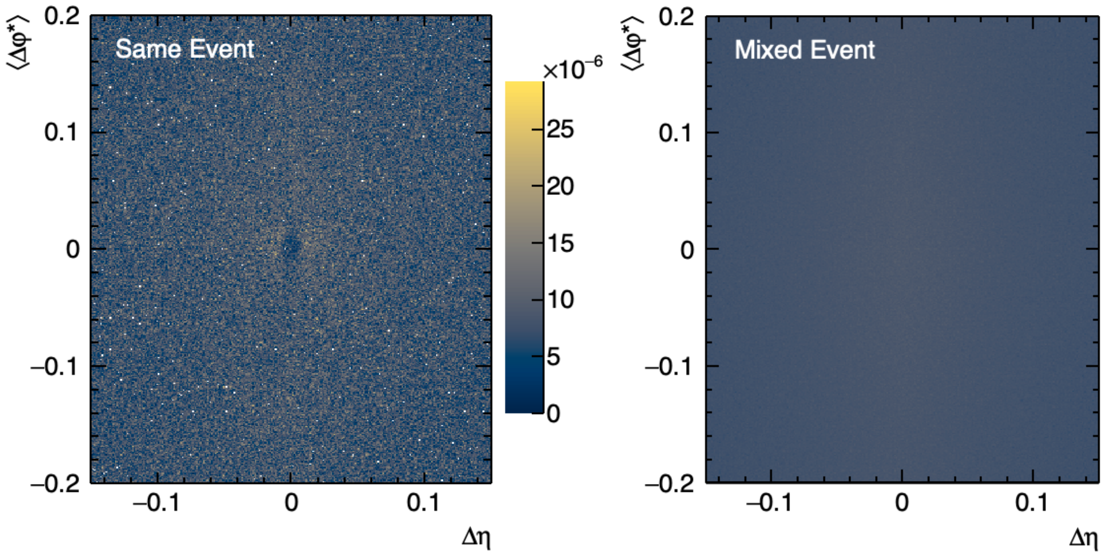

Figure 4.3.: The same (left) and mixed (right) event self-normalized distributions of $\langle\Delta\varphi^*\rangle$ and $\Delta\eta$ of p–p pairs in MC simulated events anchored to HM pp collisions at $\sqrt{s} = 13$ TeV.

with $\sqrt{\langle\Delta\varphi^*\rangle^2 + \Delta\eta^2} < 0.014$. Using the angle φ^* instead of φ, has the advantage that the rejection is less stringent but still sufficient.

The number of p–Λ pairs in MC generated events is insufficient for a similar study. Instead, the correlation functions in data are compared, obtained with and without the CPR criterion applied between the proton and each of the Λ children. As expected they agree, since the Λ is reconstructed from its decay products, and consequently, no such rejection is required for p–Λ pairs. Nevertheless, auto-correlations are introduced to the measurement of $C(k^*)$, if the proton trajectory is used as both, a primary proton and a possible decay product of the Λ candidate. Therefore, the unique track labels of all trajectories, which are associated with the particle pair, are compared among each other and if a match is found, the Λ candidate is rejected.

The finite momentum resolution affects the measurement of each single particle and therefore, also the measurement of k^*. Its effect is studied with the help of MC generated events, by relating the reconstructed momentum of the particles to their true momentum at the collision vertex. Figure 4.4 shows the results for p–p pairs in HM pp collisions at $\sqrt{s} = 13$ TeV. Only a limited number of MC generated events and hence same event pairs are available for such an analysis and as a result the femtoscopic region is only populated scarcely. Alternatively, pairs from mixed events can be used to obtain these distributions. The distributions of same and mixed event pairs agree within their respective uncertainties and evidently, the resolution of the relative momentum is a consequence of the finite resolution of the single particle measurement. From the left

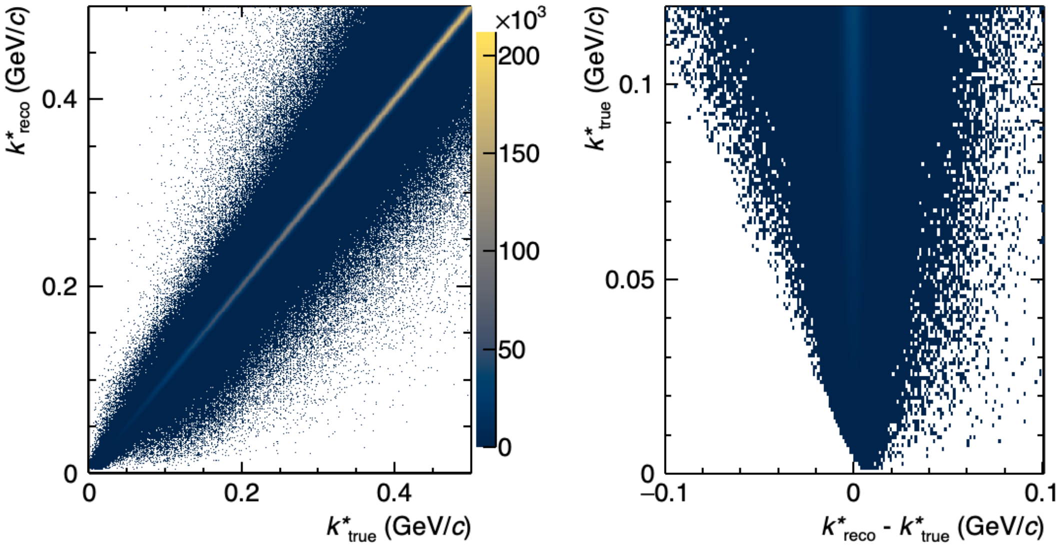

Figure 4.4.: Correlation between the true relative momentum (k^*_{true}) and reconstructed relative momentum (k^*_{reco}) of p–p pairs. Evaluated with MC events anchored to HM pp collisions at $\sqrt{s} = 13$ TeV.

panel of Fig 4.4 it can be seen that for most k^* the reconstructed momentum scatters symmetrically around the true momentum. The right panel of the same figure show a different representation, which focuses of the femtoscopic region. It can be seen that as k^*_{true} approaches zero, an offset between the true and reconstructed momentum remains. The entries of the histogram within $0 < k^*_{\mathrm{true}} < 0.04\,\mathrm{GeV}/c$ are projected onto the abscissa and the resulting distribution is fitted by a Gaussian. It has a mean of $0.006\,\mathrm{GeV}/c$ and a width of $0.002\,\mathrm{GeV}/c$. This is caused by resolution effects, which for particles with almost parallel trajectories can only result in an increase of their pair momenta. The matrices were obtained for all combinations of particles and collisions systems, and they are shown in Appendix B.

A distribution, as it is depicted in the left panel of Fig. 4.4, corresponds to a discrete transformation matrix $M(k^*_{\mathrm{reco}}, k^*_{\mathrm{true}})$ between the true and the reconstructed momentum and can be applied to unfold the k^* distributions. This, however, requires to numerically invert M, which will be explored later in this work. An equivalent and much simpler approach, which is commonly used c.f. [14], is to instead smear the modelled correlation function $C(k^*_{\mathrm{true}})$ by M. In case of a binned matrix $M(k^*_{i,\mathrm{reco}}, k^*_{j,\mathrm{true}})$ and a correlation function at the corresponding values of k^*, the smeared correlation function $C(k^*_{i,\mathrm{reco}})$ is then calculated as

$$C(k^*_{i,\mathrm{reco}}) = \frac{\sum_j M(k^*_{i,\mathrm{reco}}, k^*_{j,\mathrm{true}}) \cdot C(k^*_{j,\mathrm{true}})}{\sum_j M(k^*_{i,\mathrm{reco}}, k^*_{j,\mathrm{true}})}. \tag{4.2}$$

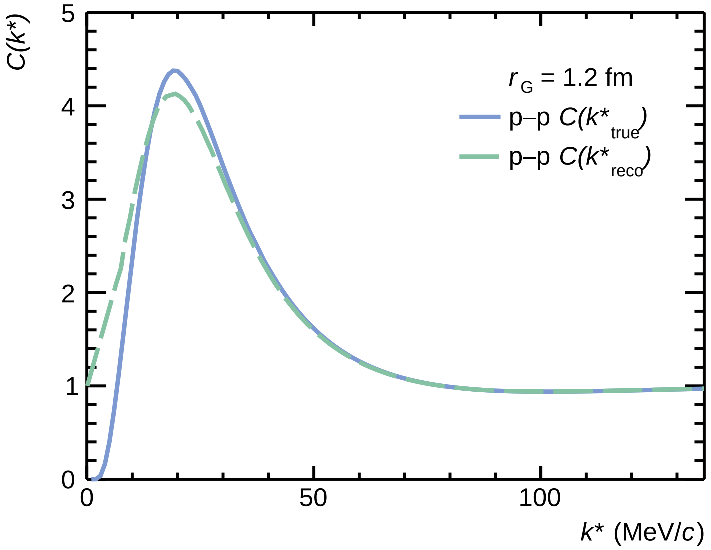

Figure 4.5.: The p–p correlation function for $k^*_{\rm true}$ (blue solid line) and $k^*_{\rm reco}$ after transforming it via $M(k^*_{i,\rm reco}, k^*_{j,\rm true})$ as shown in the left panel of Fig. 4.4. The genuine p–p correlation was calculated with CATS and a Gaussian source size of $r_{\rm Gauss} = 1.2\,\rm fm$.

The dashed green and the blue curves in Fig 4.5 depict the genuine and smeared p–p correlation functions. The former is calculated with CATS as discussed in Section 2.4, it is calculated with CATS employing a Gaussian source with a size of $r_{\rm Gauss} = 1.2\,\rm fm$. The obtained correlation function is then smeared according to Eq. 4.2 utilizing the matrix $M(k^*_{i,\rm reco}, k^*_{j,\rm true})$ depicted in the left panel of Fig. 4.4. The resulting smeared correlation function in Fig. 4.5 as shown as a function of $k^*_{\rm reco}$. As it can be seen, the modifications are most pronounced in the region $k^* \lesssim 50\,\rm MeV/\it c$, which is caused not only by the difference of $k^*_{\rm true}$ and $k^*_{\rm reco}$, but also by the fact that $C(k^*)$ itself changes quite strongly as a function of k^*.

4.1.3. Description of the Non-Femtoscopic Baseline

The comparison of correlation functions in data and MC simulations is further useful to study, if non-femtoscopic signals are present after applying the normalization, the re-weighting and the CPR. Figure 4.6 shows the p–p correlation functions in HM pp collisions at $\sqrt{s} = 13$ TeV for both data and MC. In the femtoscopic region ($k^* \lesssim 200\,\rm MeV/\it c$), the measurement in data (magenta points) exhibits the typical femtoscopic signal of p–p pairs. The correlation function measured in MC generated data (green points) remains close to unity, except for the first bin where $C(k^*) \approx 1.4$. The comparison of the individual p–p and $\overline{\rm p}$–$\overline{\rm p}$ correlation functions, it can be seen that only for p–p pairs, the correlation function in MC generated events shows such an enhancement. Such an asymmetry is not observed in the correlation function of p–p and $\overline{\text{p}}$–$\overline{\text{p}}$ pairs in data. This indicates that this is an effect solely present for p–p pairs in

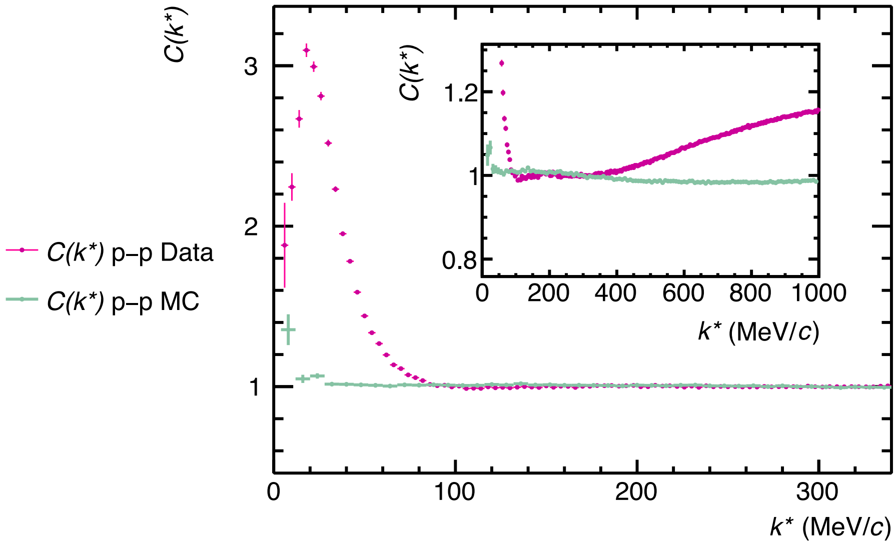

Figure 4.6.: p–p Correlation function measured in HM pp collisions at $\sqrt{s}$ = 13 TeV (magenta points) and measured in MC generated events anchored to the same data (green points).

MC generated events and might be related to the simulation of protons originating from spallation processes and material interactions. In order to ensure that this introduces no bias to the analysis, the fit of the p–p correlation function, which will be explained in detail later in this chapter, is repeated excluding this first bin. The measured radius is not modify in this way. Up to $k^* \lesssim 400\,\mathrm{MeV}/c$, both correlation functions agree and are almost flat. For this reason, as previously discussed, the normalization is computed within this region. Nevertheless, it can be seen that for both, data and simulation, a linear behavior with a slight negative slope remains. At even larger values of k^*, the correlation function measured from data increases above unity and deviates significantly from the one measured from simulated data. In systems with low multiplicities, effects of global energy and momentum conservation have to be considered on the pair level [108]. They become more pronounced the more the particles are emitted back-to-back or equivalently, with a large k^* [192]. In the femtoscopic and intermediate k^* region the resulting baseline is described by a linear function [23]. Contributions of mini-jets, which typically appear for meson pairs [114] or baryon-antibaryon pairs [107], is found to be suppressed in the analysis of p–p and p–Λ pairs, as generally observed for for baryon-baryon pairs [23].

4.1.4. Genuine and Residual Correlations

By considering the effects discussed up to this point, the only missing ingredient to extract the source parameter by a fit of the measured $C(k^*)$ is the theoretical prediction. It was demonstrated in Section 3.6.3 and 3.6.4 that the selection of protons and Λ baryons includes misidentified particles and secondaries from weak and electromagnetic decays. Since they are also included in the pairing, the measured correlation function consists not only of the genuine signal, but also of so called residual correlations. This means for example that by including protons from decays of a Λ or a Σ^+ in the measurement of the p–p correlation function, one has to consider correlations not only due to the genuine p–p interaction, but in principle also due to the p–Λ and p–Σ^+ interaction. It was shown in [23] that these residual contributions can be included in the description of the femtoscopic signal $C_{\mathrm{model}}(k^*)$ as

$$C_{\mathrm{model}}(k^*) = 1 + \sum_i \lambda_i (C_i(k^*) - 1), \tag{4.3}$$

where the sum runs over all possible combinations of genuine, impurity and feed-down contributions. The $\mathrm{C_i}(k^*)$ then represent the corresponding correlation functions and the parameters λ_{i} the relative weights of these contributions. The weights are calculated from purity and feed-down fractions of the single particles [23] and are summarized for p–p and p–Λ pairs in HM pp collisions at $\sqrt{s} = 13$ TeV and p–p pairs in MB p–Pb collisions at $\sqrt{s_{\mathrm{NN}}} = 5.02$ TeV in Table 4.1. Here, $\tilde{\mathrm{X}}$ denotes misidentified particles and X_Y particles originating from the decay of Y.

Table 4.1.: Weight parameters of the individual components of the p–p and p–Λ correlation function in HM pp collisions at $\sqrt{s} = 13$ TeV (p–p correlation function in MB p–Pb collisions at $\sqrt{s_{\mathrm{NN}}} = 5.02$ TeV). Misidentifications of particle species X are denoted as $\tilde{\mathrm{X}}$ and feed-down contributions have the mother particle listed as a sub-index. For the contributions in bold text, the correlation functions are modelled according to the interaction potential, while the others are assumed to be flat.

p–p		p–Λ			
Pair	λ_i (%)	Pair	λ_i (%)	Pair	λ_i (%)
$\mathbf{pp}$	**67 (72)**	$\mathbf{p}\boldsymbol{\Lambda}$	**46**	$\mathrm{p}_{\Sigma^+}\Lambda_{\Xi^0}$	1
$\mathbf{p}_{\boldsymbol{\Lambda}}\mathbf{p}$	**20 (16)**	$\mathbf{p}\boldsymbol{\Lambda}_{\boldsymbol{\Xi}^-}$	**9**	$\mathrm{p}_{\Sigma^+}\Lambda_{\Sigma^0}$	1
$\mathrm{p}_{\Lambda}\mathrm{p}_{\Lambda}$	2 (1)	$\mathrm{p}\Lambda_{\Xi^0}$	9	$\tilde{\mathrm{p}}\Lambda$	0
$\mathrm{p}_{\Sigma^+}\mathrm{p}$	9 (7)	$\mathbf{p}\boldsymbol{\Lambda}_{\boldsymbol{\Sigma}^0}$	**15**	$\tilde{\mathrm{p}}\Lambda_{\Xi^-}$	0
$\mathrm{p}_{\Sigma^+}\mathrm{p}_{\Sigma^+}$	0 (0)	$\mathrm{p}_{\Lambda}\Lambda$	7	$\tilde{\mathrm{p}}\Lambda_{\Xi^0}$	0
$\mathrm{p}_{\Lambda}\mathrm{p}_{\Sigma^+}$	1 (1)	$\mathrm{p}_{\Lambda}\Lambda_{\Xi^-}$	1	$\tilde{\mathrm{p}}\Lambda_{\Sigma^0}$	0
$\tilde{\mathrm{p}}\mathrm{p}$	1 (3)	$\mathrm{p}_{\Lambda}\Lambda_{\Xi^0}$	1	$\mathrm{p}\tilde{\Lambda}$	3
$\tilde{\mathrm{p}}\mathrm{p}_{\Lambda}$	0 (0)	$\mathrm{p}_{\Lambda}\Lambda_{\Sigma^0}$	2	$\mathrm{p}_{\Lambda}\tilde{\Lambda}$	1
$\tilde{\mathrm{p}}\mathrm{p}_{\Sigma^+}$	0 (0)	$\mathrm{p}_{\Sigma^+}\Lambda$	3	$\mathrm{p}_{\Sigma^+}\tilde{\Lambda}$	0
$\tilde{\mathrm{p}}\tilde{\mathrm{p}}$	0 (0)	$\mathrm{p}_{\Sigma^+}\Lambda_{\Xi^-}$	1	$\tilde{\mathrm{p}}\tilde{\Lambda}$	0

Genuine Correlations

It can be seen from Table 4.1 that the measured correlation function of both the p–p and p–Λ pairs is dominated by the genuine contribution. Their correlation functions can be modelled directly from Eq. 2.7 in CATS [120] if the source distribution $S(r^*)$ is assumed to be either Gaussian or a Gaussian core with resonances.

For p–p pairs are affected by QS, the Coulomb and the strong interaction and the resulting behavior of their $C(k^*)$ was already discussed in Section 2.4. Accordingly the local form of the Argonne v_{18} potential [59] is used in the following to describe the strong interaction among two protons.

In case of p–Λ pairs, solely effects of the strong interaction define the behavior of the genuine $C(k^*)$. For the strangeness sector, experimental constraints of the latter are at least two orders of magnitude less precise than those available for the N–N sector [20, 65, 77]. Experimentally, more data is available for this pair than for other N–Y pair, which includes measurements of the scattering cross sections and several observations of Λ-hypernuclei [26]. Nevertheless, there is a certain ambiguity between the different theoretical descriptions of the strong interaction of p–Λ pairs. The correlation functions for p–Λ pairs shown in Fig. 4.7 are computed assuming a Gaussian source distribution with a width of $r_{\text{Gauss}} = 1.2\,\text{fm}$ and considering different S-wave functions in both spin states $S = 0$ and $S = 1$. The latter was either calculated by CATS with the Usmani potential [193] or obtained from from chiral effective field theory calculations (χEFT)

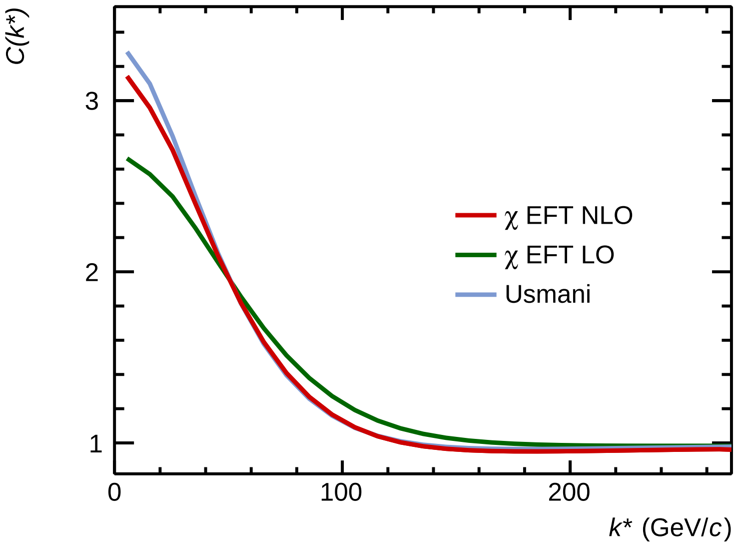

Figure 4.7.: The p–Λ correlation function for a Gaussian source distribution with a size of 1.2 fm. The $\psi(k^*, \vec{r}^*)$ is obtained from χEFT calculations in leading-order (LO [66], green curve), next-to-leading order (NLO [65], red curve) and calculated with CATS using the Usmani potential [193] (blue curve).

in leading order [66] (LO) and next-to-leading order [65] (NLO). The measurements by scattering experiments and the observation of Λ-hypernuclei support the hypothesis of an overall attractive p–Λ interaction. This is also reflected by the $C(k^*)$, which in the femtoscopic region is enhanced above unity for all cases. The resulting $C(k^*)$ for the Usmani potential and the χEFT calculations in NLO are very similar, while the LO result differs within the whole femtoscopic region. From a theoretical perspective, the result of the NLO calculation is expected to be more accurate than the one of the LO calculation, however, the limited amount of experimental data leaves room for both descriptions [65].

Residual Correlations

In order to describe the measured correlation function according to Eq. 4.3, the shape $C_i(k^*)$ of the residual contributions needs to be modelled. If a source distribution, e.g. with a Gaussian shape is assumed and the wave-function that describes the interaction is available, the genuine $C(k^*)$ of the residual pair can also be obtained using Eq. 2.7. The resulting correlation function, however, has be further modified in order to account for the kinematic change caused by the decay, since children carry only a fraction of the momentum of the parent particle. Consequently, if they are used in the pairing, the correlation signal due to the interaction of the parent will be smeared. The kinematic distributions can for example be simulated with `GENBOD` [194], which can be subsequently used to obtain a transformation matrix $D(k^*_{i,\mathrm{parent}}, k^*_{j,\mathrm{child}})$. As an example,

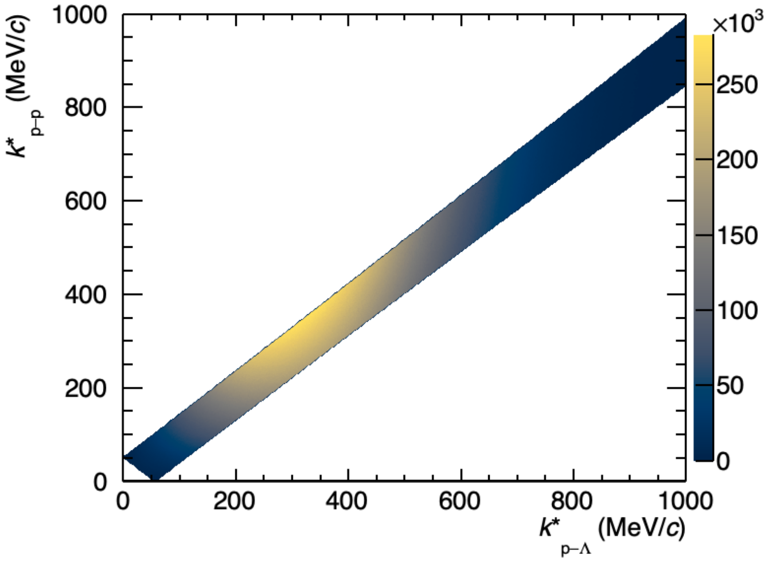

Figure 4.8.: Transformation matrix simulated with `GENBOD` [194], which accounts for the decay kinematics to convert the p–Λ correlation signal to the p–p reference frame.

Fig. 4.8 shows the transformation matrix, which is used to model the contribution of the p–Λ correlation function in the p–p momentum basis. In the rest frame of the Λ, the its

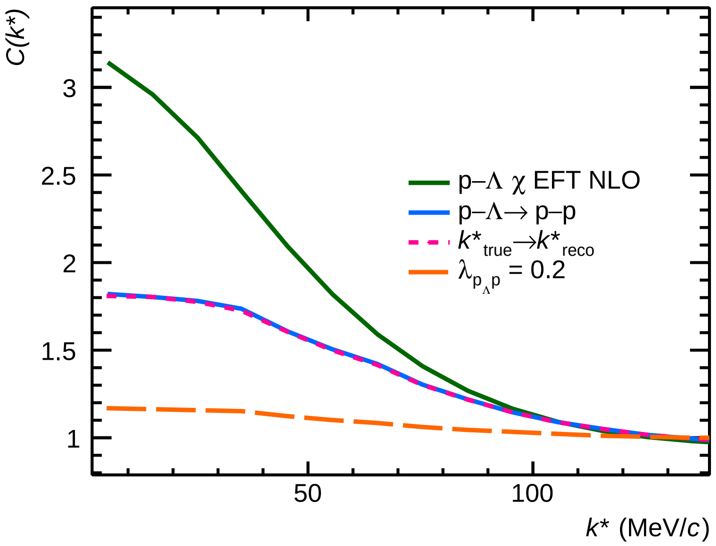

Figure 4.9.: Modeling of the residual contribution of p–Λ pairs to the p–p correlation function. The genuine $C(k^*)$ of p–Λ is modelled with χEFT in NLO (green curve) and then transformed into the p–p momentum basis (blue curve). Subsequently it is smeared to account for the momentum resolution (pink dashed curve), which in the last step is scaled by the λ parameter of 0.2 (orange curve).

difference to the proton and π^- mass defines the amount of kinetic energy that can be distributed between the decay products. This in combination with the transformation to the p–p and p–Λ PRF leads to the depicted distribution. Similar to the treatment of the finite momentum resolution, the transformation $C(k^*_{\mathrm{parent}}) \rightarrow C(k^*_{\mathrm{child}})$ can then be calculated according to Eq. 4.2 if M is replaced by D.

The modeling of the residual contribution of p–Λ pairs to the p–p correlation function is shown in Fig. 4.9. The genuine p–Λ correlation (green curve) function is obtained from χEFT NLO calculations, as shown in Fig. 4.7. In the first step the correlation function is transformed by the decay matrix (blue curve). In a second step, this correlation function is smeared to account for the finite momentum resolution of the p–p pair (pink dashed curve) and then, in the last step, the previous curve is scaled by the λ parameter $\lambda_{\mathrm{p}_\Lambda \mathrm{p}} = 0.2$ (orange dashed curve), which was taken from Table 4.1. It can be seen that accounting for the decay kinematics and the relative weight of the contribution alters and suppresses the genuine p–Λ correlation signal in the measurement of the p–p correlation function. In fact, for most residual contributions the above procedure leads to a $C_i(k^*) \sim 1$ and hence, the actual shape of their genuine $C(k^*)$ can be neglected.

Consequently, in order to describe the p–p (p–Λ) correlation function, residual correlations from p–Λ (p–Σ^0 and p–Ξ^-) pairs are explicitly modelled, all other contributions are assumed to be flat. The theoretical descriptions of their interactions follows [65, 66]

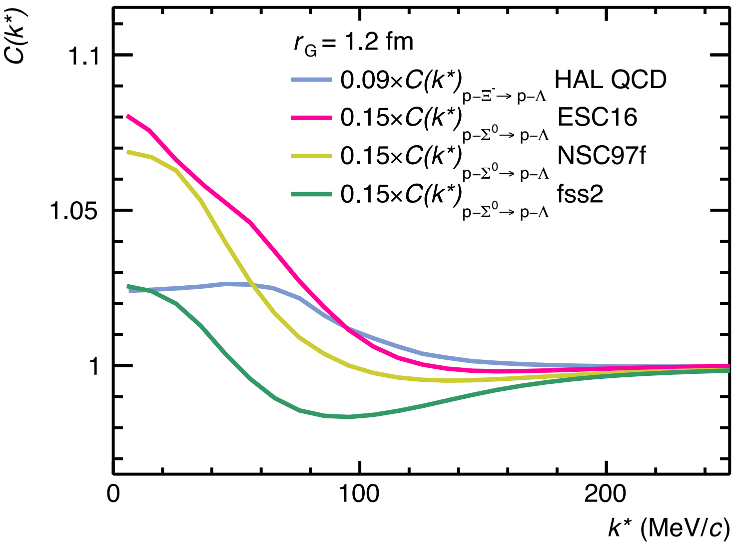

Figure 4.10.: Residual contributions due to p–Ξ^- and p–Σ^0 pairs to the measured p–Λ correlation functions. The genuine signal is modelled assuming a Gaussian source size of $r_{\text{Gauss}} = 1.2\,\text{fm}$ and the different interaction potentials discussed in the text. It is then transformed by the respective decay matrix and scaled by the corresponding λ_i reported in the legend in order to obtain the depicted curves.

for p–Λ, [71] for p–Ξ^- and [14, 195, 196] for p–Σ^0. As it will be later shown in this work, the HAL QCD calculations are validated by the p–Ξ^- correlation function [176]. Also the p–Σ^0 interaction was studied via femtoscopy [10, 25] and due to the limited precision of the data all three mentioned models are in agreement with the measured data. Figure 4.10 shows the different residual contributions to the measured p–Λ correlation function, where the genuine signal is modelled assuming a Gaussian source size of $r_{\text{Gauss}} = 1.2\,\text{fm}$ and then subsequently transformed to $k^*_{\text{p–}\Lambda}$ and scaled for the respective λ_i. Within the femtoscopic region the different descriptions of the p–Σ^0 interaction result in an uncertainty related to the modeling of the residual contribution of up to 6%.

4.1.5. Fit Functions

At this point, in order to extract the source size, the function $C_{\text{fit}}(k^*)$ is fitted to the measured $C(k^*)$ by minimizing the χ^2 via Minuit [197]. Besides the normalization and re-weighting, all corrections are directly applied to $C_{\text{fit}}(k^*)$. In general, it can be written as

$$C_{\text{fit}}(k^*) = C_{\text{non-femto}}(k^*) \cdot C_{\text{model}}(k^*), \tag{4.4}$$

where $C_{\text{non-femto}}(k^*)$ is either a constant $C_{\text{non-femto}}(k^*) = a$ or a linear $C_{\text{non-femto}}(k^*) =$

$a + b \cdot k^*$ function. The constant factor can, if necessary, introduce a slight correction to the normalization $\mathcal{N}$ and allows for a result which is independent of the choice of normalization region. In order to consider the previously discussed effects of energy and momentum conservation [23, 192], the linear baseline function extrapolates any remaining slope of $C(k^*)$ in the normalization region to the femtoscopic region. Based on Eq. 4.3, the description of the femtoscopic signal, $C_{\mathrm{model}}(k^*)$, of p–p and p–Λ pairs is constructed as

$$C_{\mathrm{model,p\text{–}p}}(k^*) = 1 + \lambda_{\mathrm{p\text{–}p}}(C_{\mathrm{p\text{–}p}}(k^*) - 1) + \lambda_{\mathrm{p\text{–}p_\Lambda}}(C_{\mathrm{p\text{–}p_\Lambda}}(k^*) - 1), \tag{4.5}$$

and

$$\begin{aligned} C_{\mathrm{model,p\text{–}\Lambda}}(k^*) = 1 + \lambda_{\mathrm{p\text{–}\Lambda}}(C_{\mathrm{p\text{–}\Lambda}}(k^*) - 1) + \lambda_{\mathrm{p\text{–}\Lambda_{\Sigma^0}}}(C_{\mathrm{p\text{–}\Lambda_{\Sigma^0}}}(k^*) - 1) \\ + \lambda_{\mathrm{p\text{–}\Lambda_{\Xi^-}}}(C_{\mathrm{p\text{–}\Lambda_{\Xi^-}}}(k^*) - 1). \end{aligned} \tag{4.6}$$

The genuine and residual correlations are modelled assuming the same radii and, as previously discussed, transforming the latter into either the p–p or p–Λ momentum basis by using the decay matrices. The momentum resolution is taken into account by applying the corresponding momentum resolution matrix via Eq. 4.2 to each $C_{\mathrm{model}}(k^*)$. At this point the only free parameters are related to $C_{\mathrm{non\text{-}femto}}(k^*)$ and the source distribution $S(r^*)$ and can be estimated by a fit of the corresponding measured correlation function. In case of the p–p correlation function, the default range to conduct the fit is $0 < k^* < 375\,\mathrm{MeV}/c$. As it can be seen in Fig. 4.6 or the top or bottom left panel of Fig. 4.2, at $k^* \gtrsim 400\,\mathrm{MeV}/c$ the behavior of $C(k^*)$ deteriorates significantly from a flat or linear behavior. This is due to effects of energy and momentum conservation and in particular at large k^* their description becomes more involved than a linear function [192]. The femtoscopic signal, however, vanishes already at smaller k^* and the fit range is limited accordingly. In case of the p–Λ correlation function, the fit parameters are extracted within $0 < k^* < 244\,\mathrm{MeV}/c$. The limitation of the upper range is due to the appearance of a cusp at $k^* \approx 280\,\mathrm{MeV}/c$, due to the coupling between the N–Λ and N–Σ system [24, 65, 66]. Its theoretical description has to still be tested, which is currently explored as part of [24].

4.2. Determination of the Gaussian Source Size

In the following, the source $S(r^*)$ is assumed to be described by the one-dimensional Gaussian distribution of Eq. 2.9. The only free parameter is its width, also called the Gaussian source size r_{Gauss}. The function $C_{\mathrm{fit}}(k^*)$, where Eq. 4.5 is inserted into Eq. 4.4 and is fitted to the measured p–p correlation function. Before these results can be discussed, it is necessary to estimate the associated systematic uncertainties.

4.2.1. Evaluation of Systematic Uncertainties

Table 4.2.: Systematic variations of the Proton selection criteria.

Selection Criteria	Default	Variation	
Max. $\|\eta\|$	0.8	down	0.7
		up	0.9
Min. p_T (GeV/c)	0.5	down	0.4
		up	0.6
Min. $n_{\text{cluster TPC}}$	80		90
Max. n_σ for PID	3	down	2
		up	5
Proton Tracking	TPC-only tracks		Global Tracks

The systematic uncertainties are estimated from two sources. Either they are related to the selection criteria of particles and the subsequent measurement of the correlation function or they are related to the parameters and ingredients that are handed to the fit of $C_{\text{fit}}(k^*)$.

For the data set collected from p–Pb collisions at $\sqrt{s_{\text{NN}}} = 5.02$ TeV, each single particle selection criterion of protons is varied individually within the ranges listed in Table 4.2. It is important to note that as k^* approaches zero the number of identified particle pairs decreases and accordingly, the statistical uncertainties of $C(k^*)$ increase. In order to avoid any bias by statistical fluctuations, the variations of the criteria were chosen such as to modify the single particle yield of protons by less than ±15%. Additionally, the systematic uncertainties are evaluated in intervals of 40 MeV/c in k^*. For each variation of the selection criteria, the relative difference between the measured correlation function and the default one is calculated. Whenever this results in two systematic uncertainties, i.e. by a up and down variation, the average is taken into account. The relative uncertainties of all variations are summed in quadrature and extrapolated to the binning of 4 MeV/c by fitting a polynomial of second order. The so obtained systematic uncertainties are largest in the lowest k^* bin, where they amount to about 5.1%. The uncertainties considered by the femtoscopic fit are calculated as the squared sum of statistical and systematic uncertainties. A variation of the proton DCA selection is not taken into account for the computation of the systematic uncertainties since it dilutes (enhances) the correlation signal by introducing more (less) secondaries in the sample, which would correspond to a change in the λ parameter.

Additional systematic uncertainties of the fit and of the radius r_0 are evaluated by: i) varying the range of the fit region up to 350 or 400 MeV/c, ii) altering the λ parameters by modifying the secondary contributions by ±20% while keeping the total secondary fraction constant, iii) replacing the χEFT prediction in NLO to describe the p–p$_\Lambda$ feed down contribution by the prediction in LO and iv) replacing the normalization $C_{\text{non-femto}}(k^*) = a$ by a linear function. By varying the fitting range, any ambiguity related to the choice of normalization range is automatically taken into account. Variations of the k^* range, where the re-weighting factor for the mixed event distribution is calculated, are found to have a negligible influence.

4.2.2. Results

Figure 4.11 shows the p–p correlation function measured in MB p–Pb collisions at $\sqrt{s_{\mathrm{NN}}} = 5.02$ TeV. The data reflect the interplay of the different final state effects between two protons can be appreciated, which were from a purely theoretical side already discussed in Section 2.4. At large k^* the two protons do not interact hence the correlation function is unity. As k^* decreases the effects of QS create a slight depletion, better seen by the magnification of the region in the inlet, but are soon overshadowed by the effects of the strong interaction, which are overall attractive. Accordingly, the correlation function is enhanced above unity. As k^* approaches 0 the repulsive nature of the Coulomb interaction should result in $C(k^*) = 0$ but, as it was demonstrated in Section 4.1.2, the finite momentum resolution and the scaling by the λ parameter result in a significant enhancement of the measured $C(k^*)$.

The femtoscopic fit yields the blue curve, where its width correspond to one standard deviation of the total systematic error of the fit. The fit with default parameters results in a $\chi^2/\mathrm{NDF} = 1.46$, which is directly used to extract the quoted central value of the radius and its associated statistical uncertainties. The distribution of radii obtained from all the variations the fitting procedure is used to extract the systematic uncertainty of the radius measurement as the limits of the interval containing 34% of the measurement below and above the default value. This results in a Gaussian source size measured from p–p correlations of $r_{\mathrm{Gauss}} = 1.427 \pm 0.007\ (\mathrm{stat.})^{+0.001}_{-0.014}\ (\mathrm{syst.})$ fm.

In Fig. 4.12, this radius is compared to the radii measured from correlations of same-charged Kaons [118]. The radii of these pairs decrease with increasing k_{T}, at least for the highest multiplicities. Consequently, these radii scale with m_{T}, which is typically understood as a signature of a collectively expanding system, as it is discussed in Section 2.2. The source size of p–p pairs was only measured at one larger value of k_{T}, but nevertheless, it is slightly increased compared to that of same charge Kaon pairs at a similar $\mathrm{d}N_{\mathrm{ch}}/\mathrm{d}\eta$. This means, that in p–Pb collisions the common m_{T} scaling of Gaussian source sizes, which was observed for Kaons and protons in Pb–Pb collisions [117], seems to be broken. A comparison of p–p $\oplus$ p–Λ radii in pp collisions at $\sqrt{s} = 7$ TeV [23] results in the same behavior. In general, the study of source sizes of various meson and baryon pairs in pp collisions point towards its variation as a function of event multiplicity and pair m_{T} [129, 130, 132, 133, 198]. However, aside of a β_{T} scaling, which was derived from qualitative considerations [199], no quantitative description could be determined so far.

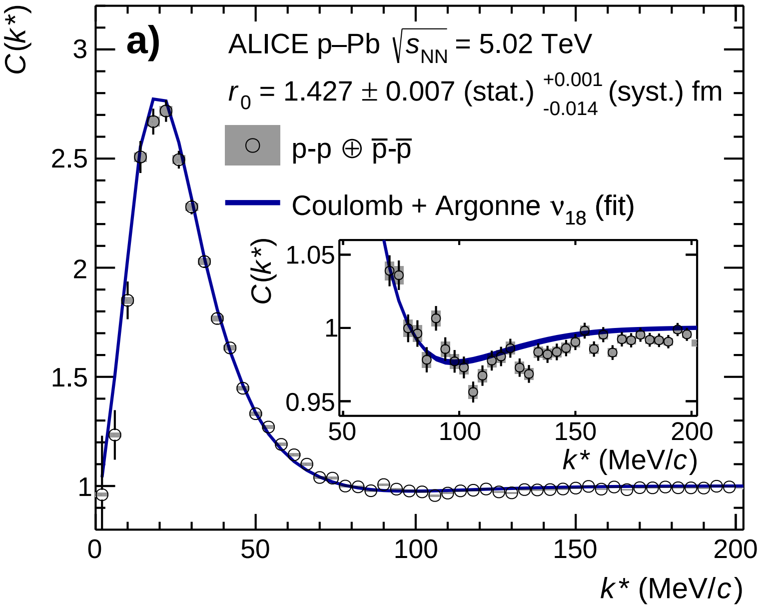

Figure 4.11.: The p–p correlation functions shown as a function of k^*. Statistical (bars) and systematic uncertainties (boxes) are shown separately. The filled bands denote the results from the fit with Eq.. Their widths correspond to one standard deviation of the systematic error of the fit.

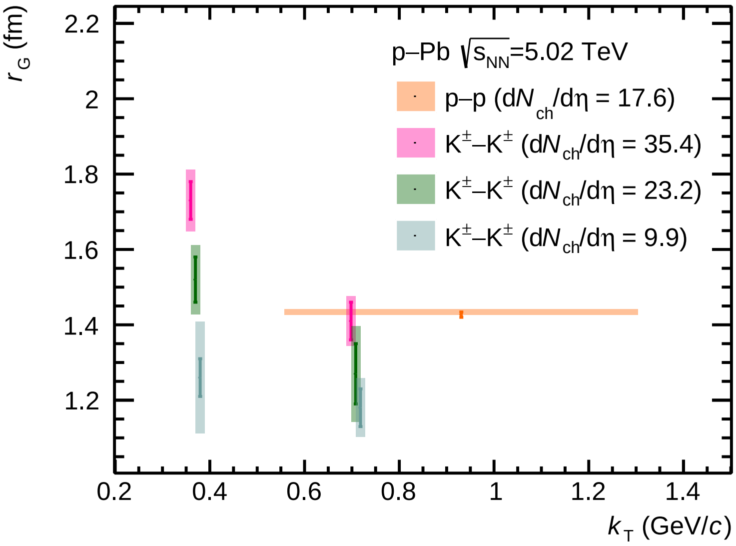

Figure 4.12.: Comparison of radii obtained from same-charged Kaon femtoscopy for different charged particle multiplicity intervals in the p–Pb collision system at $\sqrt{s_{NN}}$ = 5.02 TeV [118]. The error bars correspond to statistical and the shaded regions to the systematic uncertainty. The charged particle multiplicity $dN_{ch}/d\eta$ in p–Pb collisions at $\sqrt{s_{NN}}$ = 5.02 TeV is taken from [200].

4.3. Observation of a Common m_T Scaling

In [118] it was demonstrated that the radii of Kaon pairs in p–Pb collisions can only be reproduced by EPOS if the hadronic cascade phase, simulated with UrQMD, is included. Here, the presence of collective effects and of resonances leads to significant modifications of the spectra and of the emission profile of particle pairs [201]. If these effects are also present for protons and hyperons, the modifications of the source depends on the species and mass of the particle. For this purpose and to investigate if there is a common source of baryon pairs, the p–p and p–Λ correlation functions are analyzed individually in the following. The large amount of pairs in HM pp collisions at $\sqrt{s} = 13$ TeV permits a measurement of the correlation function in 7, respectively 6 individual m_T ranges, which in turn allows the investigation of the presence of collective effects. In order to continue and compare to the previous study, at first the respective source distributions are assumed to be described by a Gaussian function. Then, modifications due to the decay of short-lived resonances are explicitly taken into account by applying the source model described in Section 2.3.

4.3.1. Evaluation of Systematic Uncertainties

Due to the development of nanoAODs[1], the usage of computing resources to perform the correlation analysis on the grid was significantly reduced. Hence, the systematic uncertainties could be estimated more accurately taking into account correlations among the different selection criteria. The individual variations of the latter are reported for protons in Table 4.3 and Λ baryons in Table 4.4. The analysis is performed over the same data set in parallel 44 times, where in every single iteration the default, up or down

Table 4.3.: Systematic variations of the Proton selection criteria. The CPR is only applied to p–p pairs.

Selection Criteria	**Default**	**Variation**	
Max. $\|\eta\|$	0.8	down	0.77
		up	0.85
Min. p_T (GeV/c)	0.5	down	0.4
		up	0.6
Min. $n_{\text{cluster TPC}}$	80	down	70
		up	80
Max. n_σ for PID	3	down	2.5
		up	3.5
Max. $\sqrt{\langle\Delta\varphi^*\rangle^2 + \Delta\eta^2}$	0.014		0.019

---

[1] These is a filtered datatype, where only variables required for femtoscopic analysis was extracted from the standard data format (AODs)

Table 4.4.: Systematic variations of the Λ selection criteria.

Selection Criteria	Default	Variation	
Child track selection criteria			
Max. $\|\eta\|$	0.8	down	0.77
		up	0.83
Min. $\mathrm{DCA}_{\mathrm{xy}}$ to PV (cm)	0.05		0.06
Max. $\mathrm{DCA}_{\mathrm{xy}}$ to V^0 vertex (cm)	1.2		1.5
Min. $n_{\text{cluster TPC}}$	70		80
Max. n_σ for PID	5		4
V^0 selection criteria			
Min. $\cos\alpha$	0.99		0.995

value of each selection criterion is picked at random. The bias of statistical fluctuations is limited by considering only those results which change the m_T integrated pair yield with respect to the default one by a maximum of 20%. This way, additional to the correlation functions measured for the default selection criteria of p–p (p–Λ) pairs, 26 (42) variations of the latter were available for the further analysis. The uncertainties are visualized in the later plots as gray boxes. They are estimated individually in each k^* bin from the minimum and maximum value of $C(k^*)$ from all those variations and assuming a uniform distribution.

The systematic uncertainties associated to the fit procedure of the p–p correlation functions are evaluated by: i) varying the range of the fit region up to 350 or 400 MeV/c, ii) altering the λ parameters by modifying the secondary contributions by ±20% while keeping the secondary fraction constant, iii) replacing the χEFT prediction in NLO to describe the p–p_Λ feed down contribution by the prediction in LO and iv) replacing the normalization $C_{\text{non-femto}}(k^*) = a$ by a linear function.

The systematic uncertainties associated with the fit procedure of the p–Λ correlation functions are evaluated by: i) changing the upper limit of the fit region to 204 MeV/c and 244 MeV/c, ii) modifying the λ parameters by varying $R_{\Sigma^0/\Lambda}$ by ±20% and iii) replacing the normalization constant $C_{\text{non-femto}}(k^*) = a$ by a linear function. The fit of the p–Λ correlation function is performed twice, where the S wave function once from χEFT calculations at LO [66] and once from χEFT calculations NLO [65].

When the modifications of the source distribution due to resonances is modelled and the Gaussian core is folded with the exponential tail, the uncertainties associated to the lifetime and fractions of short-lived resonances decaying into protons (Λ baryons) are accounted for by additionally including variations of the effective resonance mass of 0.2% (0.6%) and variations of the lifetimes of 2% (13%) [2].

The final systematic uncertainty on the source size is obtained by repeating the fit procedure for all variations of the experimental correlation function and for all possible combinations of the fit parameters. The p–Λ result is reported separately for the fit with the wave function from LO and NLO calculations. The central value and the standard deviation of the resulting distribution for r_0 are considered as the quoted radius and its associated systematic uncertainty. The statistical uncertainty is extracted as the standard deviation of the distribution of uncertainties obtained from the χ^2 minimization of each fit.

4.3.2. Results

For the assumption of a Gaussian source distribution, the p–p and p–Λ correlation functions and their fits are shown for one representative m_{T} interval in Fig. 4.13[2]. The magnitude of the systematic uncertainties of the data are visualized by the gray boxes, which represent the 1σ range extracted from all the before mentioned variations assuming a flat distribution in each k^* interval. In the same way, the width of the fit curves corresponds to the 1σ range extracted from all combinations of data and fit parameters. As discussed previously, the behavior of the p–p correlation function results from the effects of quantum statistics, Coulomb and strong interaction. The p–Λ pairs, however, are only affected by the strong interaction, which is attractive and results in a $C(k^*)$ that is enhanced above unity. In the depicted m_{T} interval, the fit results in a description of the p–p (p–Λ) correlation function with a $\chi^2/\mathrm{NDF} = 1.9$ (0.67 (NLO) and 0.91 (LO)).

The fits are applied to the correlation functions of all m_{T} intervals and the resulting radii are shown in the left panel of Fig. 4.14. The solid lines represent the statistical uncertainties, while the hashed boxes represent the systematic uncertainties. Remarkably, even in pp collisions a decrease of the Gaussian source size with increasing m_{T} can be observed, which is consistent with the expectation from the hydrodynamic picture. The common scaling, expected from the latter, is absent as it can be seen from the clear offset between the measured source sizes of the two particle pairs. The offset appears to be rather constant and generally shift the radii of p–Λ towards larger values, which suggests that there is a difference in the emission of protons and Λ baryons.

As it is noted in Section 2.2, the SHM predicts a similar amount of feed-down from short-lived resonances to protons and Λ baryons. The average lifetime of those decaying to a Λ ($\langle c\tau \rangle \sim 4.7\,\mathrm{fm}$), however, is significantly larger than those decaying to a proton ($\langle c\tau \rangle \sim 1.7\,\mathrm{fm}$). As it is demonstrated in Fig. 2.4, for the same core source this produces a significantly wider source distribution for p–Λ pairs than for p–p pairs and hence, offers a possible explanation for the observed difference. Therefore, the fit of all correlation functions in each m_{T} interval is repeated, but instead of the Gaussian source distribution, the Gaussian core source folded with an exponential tail is employed. The latter is modelled according to the specific contributions of the corresponding resonances. The

---

[2] The complete set of correlation functions and fits for p–p and p–Λ pairs are shown in the appendix in Fig. B.8,B.9,B.10 and B.10

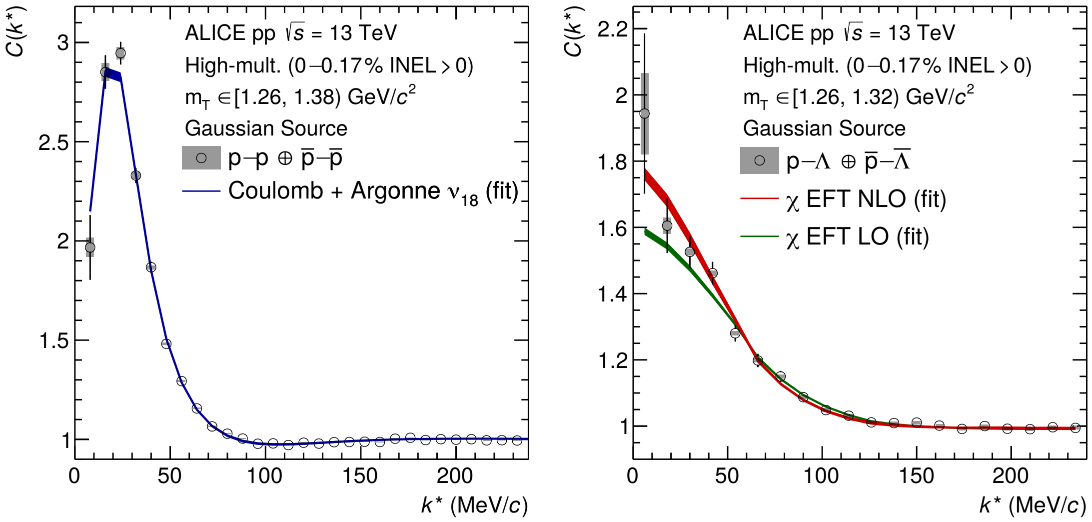

Figure 4.13.: The correlation function of p–p (left) and p–Λ (right) as a function of k^* in one exemplary m_T interval. Statistical (bars) and systematic (boxes) uncertainties are shown separately. The filled bands depict 1σ uncertainties of the fits with $C_{\text{fit}}(k^*)$ and are obtained by using the Argonne v_{18} [59] (blue), χEFT LO [66] (green) and χEFT NLO [65] (red) potentials. See text for details.

individual fitting curves resulting from the two source assumptions are almost identical and yield a similar χ^2. This is due to fact that the source distribution including the modeling of the effect of resonances, can still be described by a Gaussian distribution.

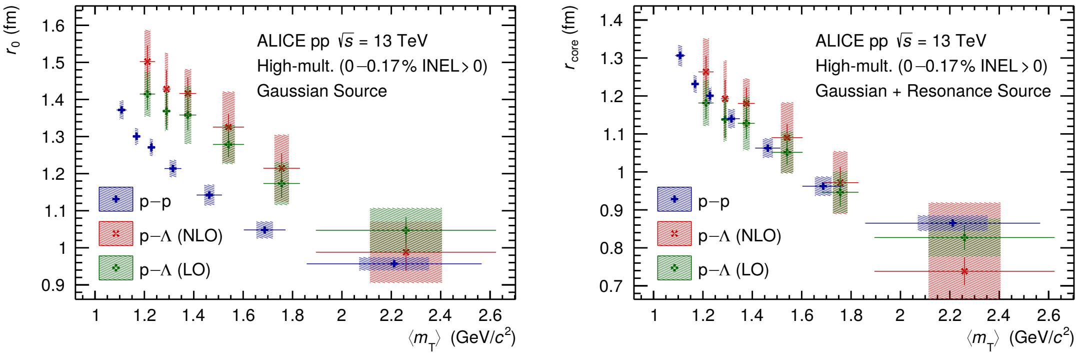

Figure 4.14.: Source radius r_0 (=r_{Gauss}) for the assumption of a purely Gaussian source (left) and source radius r_{core} for the assumption of a Gaussian source with added resonances (right) as a function of $\langle m_T \rangle$. The blue crosses result from fitting the p–p correlation function with the strong Argonne v_{18} [59] potential. The green squared crosses (red diagonal crosses) result from fitting the p–Λ correlation functions with the strong χEFT LO [66] (NLO [65]) potential. Statistical (lines) and systematic (boxes) uncertainties are shown separately.

The resulting radii of p–p and p–Λ pairs for the different m_{T} intervals are presented in the right panel of Fig. 4.14. The solid lines represent the statistical uncertainties, while the hashed boxes represent the systematic uncertainties. The source size becomes smaller if the modifications due to resonances are accounted for and as already suspected, the effect is more pronounced for p–Λ pairs than for p–p pairs. The radii still decrease with increasing m_{T}, but it is noticeable that the radii exhibit a common scaling among the two pairs. The mass and therefore also the Lorentz factor γ_{T} due to the transverse boost is similar for protons and Λ baryons, and hence this analysis of the source size in one dimension [202] already indicates that there is a common source of these baryons and parent resonances. Also first measurements of flow coefficients, angular correlations or the strangeness production [171, 203–205] indicate the presence of collective effects in high-multiplicity pp collisions, which seem to be have unexpected similarities to heavy-ion reactions. In the future, detailed studies of the m_{T} dependence of the core radius of other pairs, in particular including mesons e.g.,π–π pairs, will enable complementary investigations of collective phenomena in small collision systems. In particular for this work, this result can be used to constrain the particle emitting source of p–Ξ^{-} pairs, which will be discussed in the next chapter.

5. Observation of the strong interaction of p–Ξ^- pairs

The study in the previous chapter provides the necessary constraints to determine the source distribution $S(r^*)$ of p–Ξ^- pairs. This way, the sensitivity of the correlation function to the interaction of these two particles can be fully exploited. The measurement is performed in two independent collision systems, MB p–Pb collisions at $\sqrt{s_{\mathrm{NN}}} = 5.02$ TeV and HM pp collisions at $\sqrt{s} = 13$ TeV. Modifications of the measurement due to experimental effects are investigated and are taken into account in a comparison to theoretical predictions. It will be demonstrated that an attractive strong interaction between the proton and the Ξ^- is necessary to reproduce the measured correlation function. Further, the predictions of this interaction by lattice calculations performed by the HAL QCD collaboration [71] are corroborated by a comparison to the data. These studies are also summarized in the corresponding publication, see [176] and [77].

5.1. p–Ξ^- correlation function

As for the p–p and p–Λ correlation function, the analysis of the p–Ξ^- correlation function needs to take into account modifications of the measurement due to experimental effects. These can either be incorporated in the modelled correlation function or taken into account by correcting the measured correlation function. The former is the standard approach that is also used in the study of the source properties presented in Chapter 4 and is employed in the analysis of the data set collected from MB p–Pb collisions. The latter approach is followed during the analysis of HM pp collision, to provide experimental correlation functions that can be directly compared to different model predictions in a more straightforward way.

5.1.1. Normalization and Multiplicity re-weighting

As discussed in Section 4.1.1, the normalization factor $\mathcal{N}$ between the same and mixed distributions is calculated within $240 < k^* < 340\,\mathrm{MeV}/c$. Then, the factors for the re-weighting of the mixed event multiplicity distribution are computed in the region $200 < k^* < 900\,\mathrm{MeV}/c$. The resulting p–$\Xi^-$ and $\overline{\mathrm{p}}$–$\overline{\Xi}^+$ correlation functions for both collisions systems are depicted in the left and right panel of Fig. 5.1. As it can be seen from the

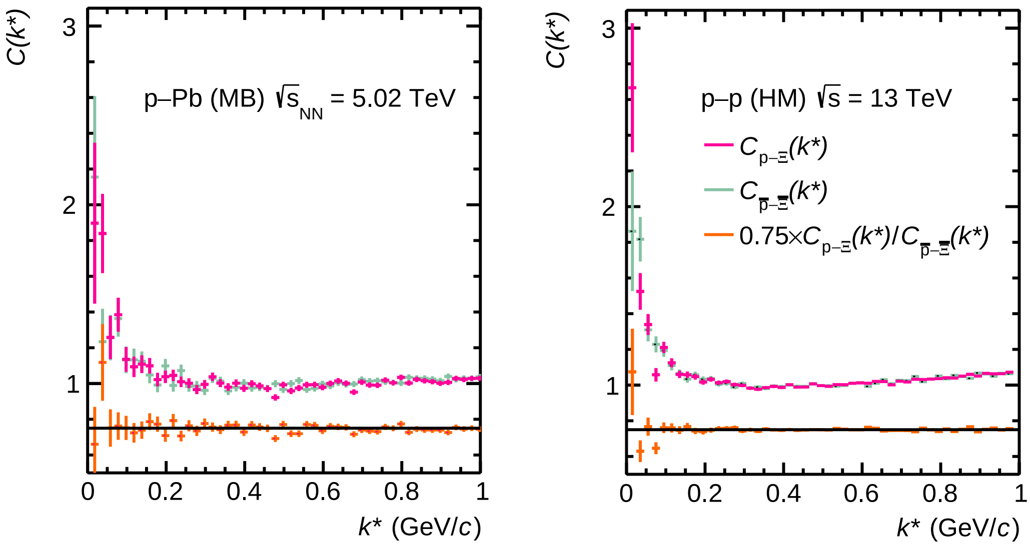

Figure 5.1.: The p–Ξ^- (magenta points) and $\overline{\text{p}}$–$\overline{\Xi}^+$ (green points) correlation function and their ratio (orange points) which for better visibility is scaled by a factor of 0.75 for p–Pb MB collisions at $\sqrt{s_{\text{NN}}} = 5.02$ TeV (left panel) and pp HM collisions at $\sqrt{s} = 13$ TeV (right panel).

ratio between the two, the correlation functions agree within uncertainties. They are combined and hence further on p–Ξ^- denotes the combination p–$\Xi^- \oplus \overline{\text{p}}$–$\overline{\Xi}^+$. Already at this point, it can be observed that at $k^* \to 0$ the $C(k^*)$ features an enhancement above unity. The amplitude of the signal is slightly more pronounced for the measurement in HM pp collisions, which is expected due to the decreased source size, see Sec. 4.3.2 and 4.2.2. The observed enhancement above unity is indicative for presence of final state effects among the proton and the Ξ^-, which are attractive. In the following, it will be investigated if the Coulomb interaction, which among the oppositely charged particles is attractive, is sufficient to describe this signal or if there has to be an additional contribution by the strong interaction.

5.1.2. Detector Effects

The resolution of the k^* measurement is obtained in a MC-based study by comparing the simulated to the generated relative momentum of the particle pair. As for the study of p–p and p–Λ correlations, discussed in Section 4.1.2, the population of entries in the momentum resolution matrix is enhanced by using pairs of particles from several different events. The resulting distribution of true and reconstructed k^* values measured in MC events anchored to HM pp collisions at $\sqrt{s} = 13$ TeV is depicted in Fig. 5.2. The distribution has similar features as that of MC events anchored to p–Pb collisions at $\sqrt{s_{\text{NN}}} = 5.02$ TeV, which can be found in Fig. B.7 in the appendix. In the analysis of

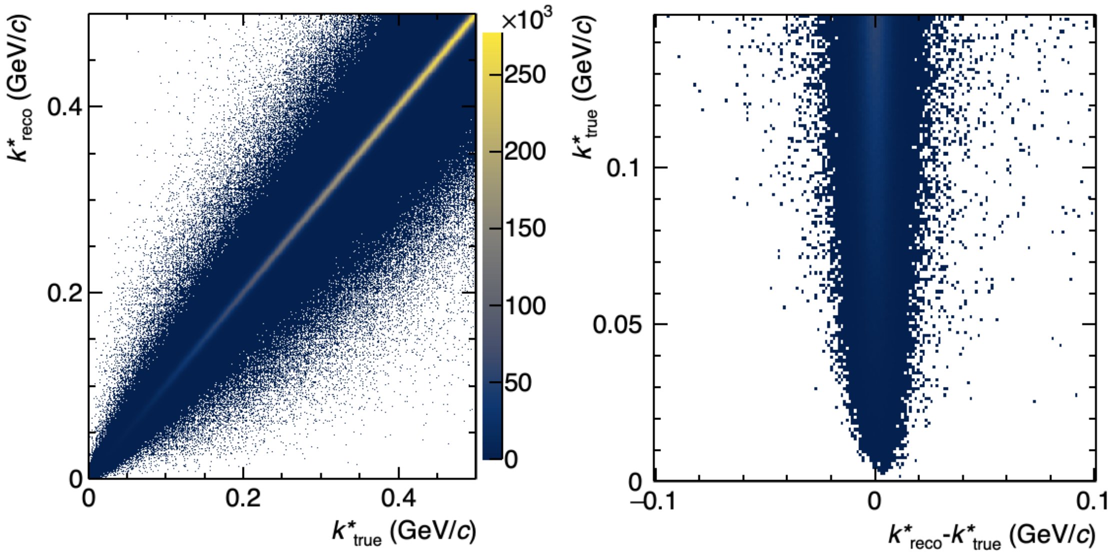

Figure 5.2.: Correlation between the true relative momentum ($k^*_{\rm true}$) and reconstructed relative momentum ($k^*_{\rm reco}$) of p–Ξ^- pairs. Evaluated with MC events anchored to HM pp collisions at $\sqrt{s} = 13$ TeV. For MB p–Pb collisions at $\sqrt{s_{\rm NN}} = 5.02$ TeV see Fig. B.7.

MB p–Pb collisions at $\sqrt{s_{\rm NN}} = 5.02$ TeV, the modelled correlation function is smeared according to the finite resolution utilizing Eq. 4.2. In the analysis of HM pp collisions at $\sqrt{s} = 13$ TeV the measured relative momentum distributions of same and mixed events are unfolded by inverting Eq. 4.2. Since this procedure includes a matrix inversion, which typically lacks any analytic solution, numerical methods have to be employed. The most intuitive example of such a method is the bin-by-bin unfolding of a histogram that covers a certain range and which is filled by measuring an observable several times. The histogram then consists of several bins i with entries $N(i)$, where $0 \leq i < M$ and M is the last bin of the histogram. A multiplicative correction factor $a_i \geq 0$ is assigned to each bin and assigned a random value. This a_i is then multiplied with the contents of each bin $N(i)$ to obtain a corrected histogram. In order to evaluate the quality of the guess for a_i, the corrected histogram is smeared for the finite resolution and compared to the measured distribution. In case of a k^* distribution, this means that the momentum resolution matrix is applied by using Eq. 4.2. In practice, the measurement is unfolded by a fit, which is used to determine the optimal values of the parameters a_i by minimizing the difference between the measured and the corrected and smeared histogram. There are more sophisticated approaches that also account for the migration of counts between the individual bins or so-called misses, when an event is not observed due to detection inefficiencies. These methods are typically applied to investigate signals that are not only smeared due to a limited resolution but also suppressed by background contributions. Several different algorithms are implemented in a C++ framework called RooUnfold [206, 207]. The so-called RooUnfoldResponse stores the distributions to relate the measured value of an observable to its true value as well as the distribution of the detection efficiency. This container can be either filled directly in MC generated events by passing pairs of the reconstructed and true values of an observable or by using the momentum resolution matrix. This analysis follows the latter approach, but in order to be able to investigate systematic effects of the unfolding related to the measurement of the resolution matrix, it is not used directly. Instead, the momentum resolution matrix is projected on the k^*_{reco} axis in intervals of k^*_{true} with a width of $0.005\,\mathrm{GeV}/c$. In each interval of k^*_{true} the projection is fit by a so-called folded normal distribution, which is defined as the sum of two Gaussian functions G with equal width σ but opposite mean μ. For two intervals, $k^*_{\mathrm{true}} < 0.005\,\mathrm{GeV}/c$ and $0.025 < k^*_{\mathrm{true}} < 0.030\,\mathrm{GeV}/c$, the projection and the fit is shown in Fig. 5.3. In particular in the lowest k^*_{true} interval, it is necessary to use a folded normal distribution instead of simple Gaussian in order to properly describe the distribution. This is due to the definition of k^* as the absolute value of the difference between two momenta, which means that counts at negative values are reflected to their positive values. The center value of each k^*_{true} interval and a value sampled according to the obtained parameterization are used to setup the RooUnfoldResponse with pairs of (k^*_{true}, k^*_{reco}). The number of pairs is chosen such that the distribution of k^*_{reco} values reproduces the behavior of the mixed event distribution measured in data. In this analysis, the iterative Bayesian unfolding [208] is used as a default, since it is straightforward to handle and provides the most stable results, even when the binning of the momentum resolution matrix and/or correlation function is varied. This method estimates the initial counts from the posterior probability that is computed from the measured distribution and probabilities stored in the RooUnfoldResponse by using the Bayes theorem [50]. The procedure has to be repeated for several iterations

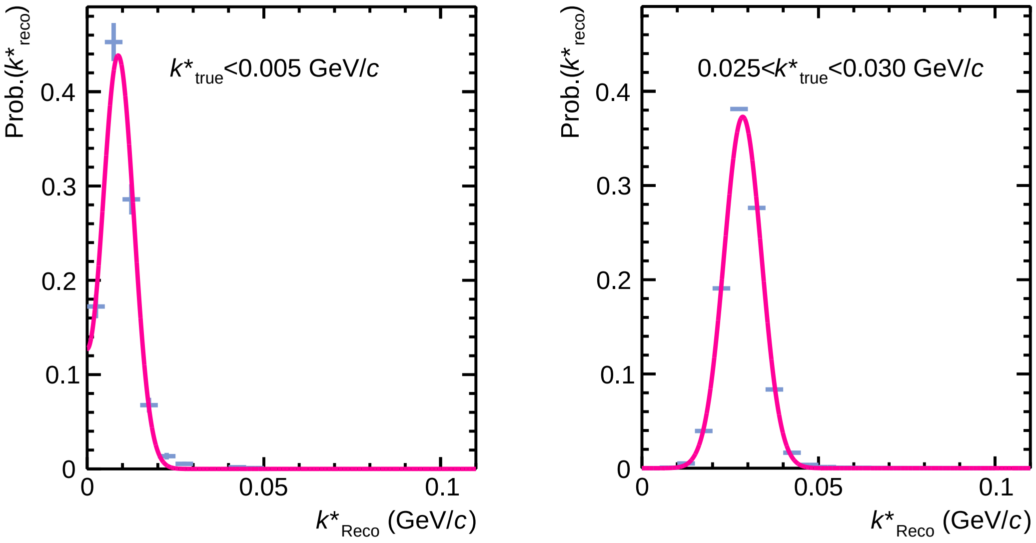

Figure 5.3.: Projection of the momentum resolution matrix as a function of k^*_{reco} in two intervals of k^*_{true} and parameterization by a folded normal distribution (magenta curve).

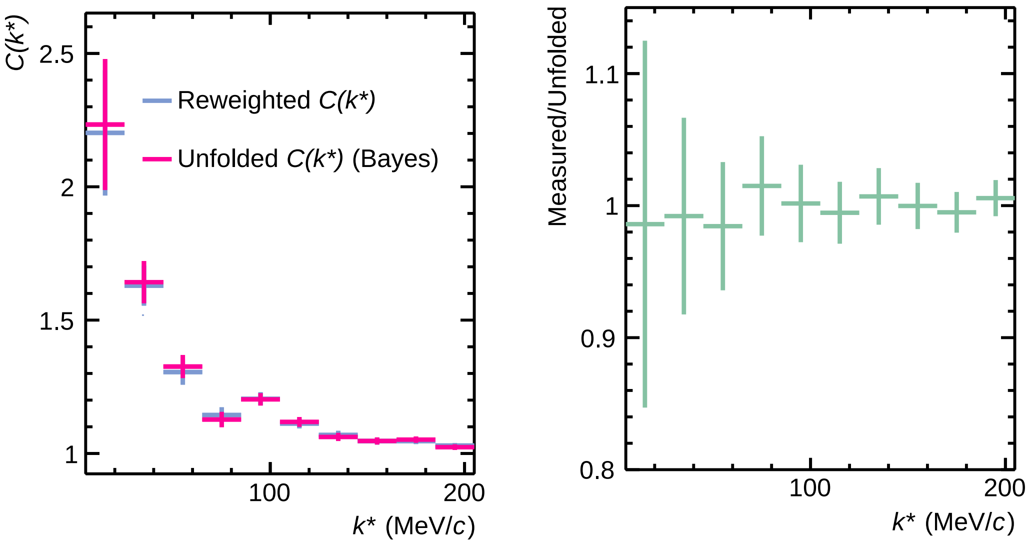

Figure 5.4.: The p–Ξ^- correlation function (left panel) before (blue points) and after (magenta points) unfolding with the k^* distributions of same and mixed events with the Bayes method as well as the ratio between the two (right panel).

until a stable posterior is obtained. The authors of RooUnfold state that a reasonable performance is achieved without fine-tuning the number of iterations [207]. Indeed, after applying more than two iterations the resulting unfolded k^* distributions of same and mixed events are found to change by few percent, after more than six iterations, however, the uncertainties are observed to increase. In the following a value of four iterations is used as a default, since it is found to minimize the difference between the reconstructed and the true k^* distribution in a Monte Carlo based study. Figure 5.4 shows the correlation function before and after unfolding the k^* distributions of same and mixed events p–Ξ^- pairs in HM pp collisions at $\sqrt{s} = 13$ TeV. It should be noted, that the unfolding is applied to the k^* distributions binned in intervals of $5\,\mathrm{MeV}/c$. The counts of four consecutive bins are then summed up and the final result is reported in intervals with a width of $20\,\mathrm{MeV}/c$. The modifications of $C(k^*)$ are only minor and the results before and after the unfolding agree within their respective uncertainties. In order to investigate systematic uncertainties related to the unfolding algorithm, also the bin-by-bin unfolding and the iterative dynamically stabilized unfolding (IDS) [209] are employed. The IDS method [209] inverts the momentum resolution matrix and takes into account the migration of counts among different bins. In order to increase the sensitivity to signals covered by a background, the measured distribution is compared to the expectation, e.g. as it is stored in the RooUnfoldResponse[1]. A probability is assigned to the counts of each interval based on their deviation from the background with the help of a regularization function, where a regularization parameter steers the sensitivity

---

[1] In case of the momentum resolution matrix, this is the projection on the k^*_{Reco}-axis

of this function. During the unfolding, this probability is used to control how far entries can migrate in order to keep signal counts accumulated. The distribution is unfolded in multiple iterations, where the regularization parameter decreases steadily the sensitivity of the regularization function in order to remove statistical fluctuations. In this analysis, the unfolded k^* distributions of same and mixed events in MC and experimental data are both found to be rather insensitive to the number of iterations, but the uncertainties start to increase after more than five iterations.

5.1.3. Description of the non-femtoscopic baseline

After applying the corrections for the finite momentum resolution, the presence of a non-femtoscopic baseline is investigated. The broad structure related to mini-jet background in the k^* region below $1\,\mathrm{GeV}/c$, as it is typically observed pairs including mesons or pairs of baryons and anti-baryons [107, 114], is in general found to be suppressed for baryon–baryon pairs [23]. Figure 5.5 shows the correlation functions in pp collisions at $\sqrt{s} = 13$ TeV for both data and MC. The correlation function in MC generated events has larger uncertainties than the one measured in data. In the region $k^* \gtrsim 200\,\mathrm{MeV}/c$, both correlation functions show only slight deviations and are almost flat. In the femtoscopic region, $k^* \lesssim 200\,\mathrm{MeV}/c$, the correlation function measured in MC generated data (green points) is consistent with unity within the statistical uncertainties, while the measurement in data (magenta points) exhibits the femtoscopic p–Ξ^- signal. In principle, in this region energy and momentum conservation can introduce a baseline

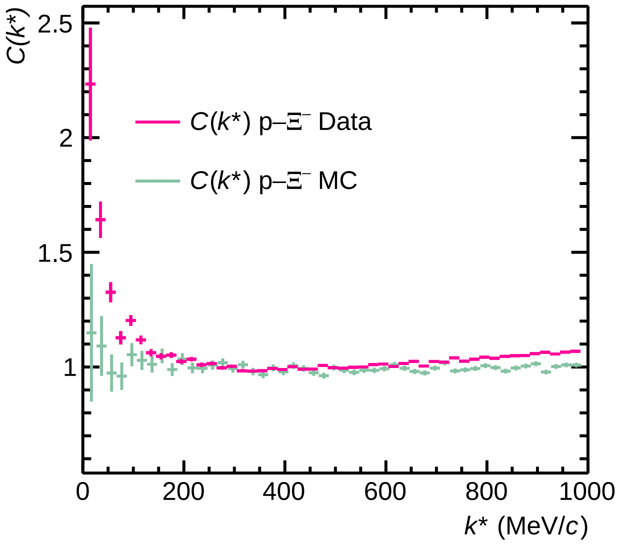

Figure 5.5.: p–Ξ^- Correlation function measured in HM pp collisions at $\sqrt{s} = 13$ TeV (magenta points) and measured in MC generated events anchored to the same data (green points).

described by a linear function, as it is discussed for the study of p–p and p–Λ pairs in Sec. 4.1.3. The uncertainties of the MC based study, however, are too large to clearly exclude or identify the presence of any structure in this region.

5.1.4. Source Distribution

The study of the interaction via the two-particle correlation function is only feasible if the source distribution in Eq. 2.7 is sufficiently constrained. In the following, the model of a common Gaussian core source modified by resonances, as it is described in Sec. 2.3, is used to obtain the $S(r^*)$ of p–Ξ^- pairs. In Chapter 4 the core radius as a function of m_{T} is measured from p–p correlations in HM pp collisions at $\sqrt{s} = 13$ TeV. A parameterization by $r_{\mathrm{core}} = a \cdot m_{\mathrm{T}}^{b} + c$, which is shown by the green curve in Fig. 5.6 and was taken from [10], is then used to obtain an interpolation between the measured points. The width of the band represents the 3σ limits of this parameterization taking into account statistical and systematic uncertainties of the measurement. The average $\langle m_{\mathrm{T}} \rangle$ of p–Ξ^- pairs is $1.9\,\mathrm{GeV}/c$, which consequently yields a core radius of r_{core} $=(0.93 \pm 0.04)$ fm. The Gaussian core source has to be convoluted by an exponential function that describes the modifications by short-lived resonances decaying into a proton or a Ξ^-. Therefore, it is necessary to estimate their contribution to the yield of the respective particles. For protons this is already discussed in the context of Tab. 2.1. The same SHM calculations as used for protons predict that only a few hadrons decay into a Ξ^-, all of which have lifetimes of $c\tau \gtrsim 20\,\mathrm{fm}$. Due to their live long lifetime, these particles introduce no modifications of the source distribution and instead introduce a residual signal to the measurement. As it will be discussed later, these contributions are

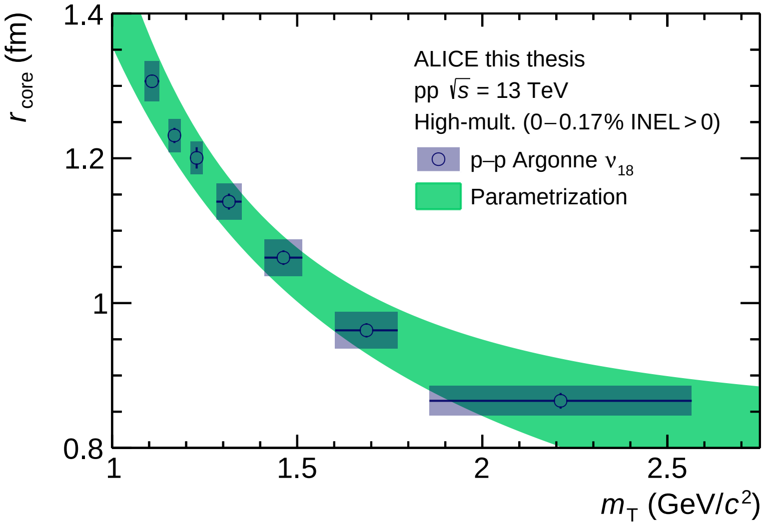

Figure 5.6.: Parameterization of the source size r_{core} as a function of m_{T} by a power function [10].

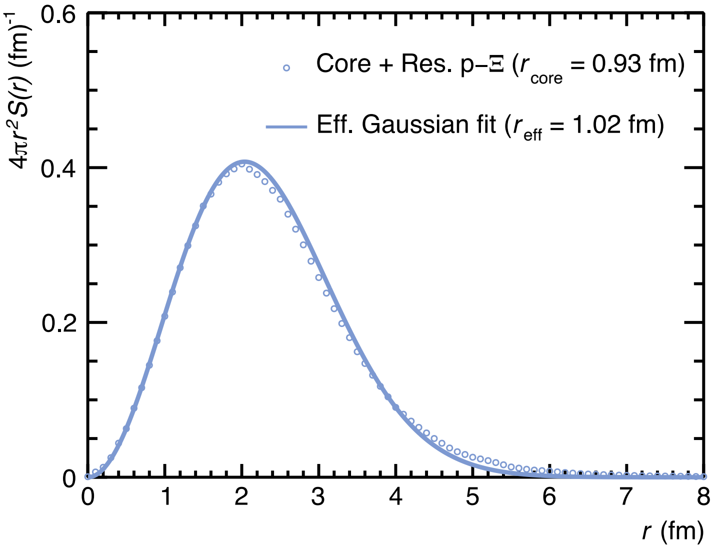

Figure 5.7.: Source distribution $S(r^*)$ of p–Ξ^- pairs for a Gaussian core source with a size of 0.93 fm and added resonances due to their contributions to the selected protons (open circles). Gaussian fit (solid line) to extract an effective source size of 1.02 fm.

instead taken into account as secondaries by the λ parameters. Hence, only short-lived resonances decaying into protons cause a modification of the p–Ξ^- source. In Fig. 5.7 the resulting source distribution is shown for a core source size of $r_{\mathrm{core}} = 0.93$ fm by the open circles. A fit is used describe this distribution by a Gaussian function as defined in Eq. 2.9 and an effective Gaussian source size of 1.02 fm is extracted. As expected, the modifications of resonances lead to an overall widening of the Gaussian core source, which leads to a larger effective source size than core source size.

In MB p–Pb collisions, an m_{T} integrated source size of $r_{\mathrm{Gauss}} = 1.427$ fm is measured from p–p correlations. At the time of the study of the corresponding p–Ξ^- correlation function, only a preliminary version of the source model including the description of resonances was available. It was estimated that the source distribution of p–Ξ^- pairs is narrower and its size might be decreased by up to 20%. This can now retrospectively be evaluated from the study in HM pp collisions. A Gaussian source size of approximately 1.2 fm is extracted from the measurement of the m_{T} integrated p–p correlation function [25]. As it was just demonstrated, the effective size of the source distribution of p–Ξ^- pairs is 1.02 fm, which is decreased by almost 20% compared to the Gaussian source size of p–p pairs.

5.1.5. Genuine and Residual correlations

The sample of selected protons and Ξ^- baryons is contaminated by impurities due to misidentifications of the candidates and by feed-down from longer-lived decays.

Hence, the measured p–Ξ^- correlation function contains not only the genuine signal of p–Ξ^- pairs, but also additional signals due to residual correlations. Following the discussion of Section 4.1.4, the latter are taken into account by summing the correlation functions weighted by their relative contribution to the total pair yield, the so-called λ parameters [14]. They are calculated by using the purity and feed-down fractions of protons and Ξ^- baryons, which are discussed in Section 3.6.3 and 3.6.5, respectively. It should be noted, that the feed-down fractions account for longer-lived decays ($c\tau \gtrsim$ 20 fm), which are expected to live long enough to introduce themselves a residual correlation signal. Short-lived decays are taken into account as modifications to the source distribution. Table 5.1 shows them for both collision systems, HM pp collisions at $\sqrt{s} = 13$ TeV and MB p–Pb collisions at $\sqrt{s_{\mathrm{NN}}} = 5.02$ TeV.

Genuine Correlation

Table 5.1 shows that the λ parameter of the genuine p–Ξ^- pair is the largest and its associated signal is expected to dominate the measurement. The corresponding correlation function is computed considering different instances for the p–Ξ^- interaction. Since the strong interaction among a proton and a Ξ^- baryon was never directly observed and the two particles carry an opposite electromagnetic charge, the null hypothesis is given by considering solely the attractive Coulomb interaction. Predictions of the p–Ξ^- interaction via the strong force are currently available from χ EFT [146], from the ESC16 meson exchange model [14] and by lattice calculations from the HAL QCD collaboration [71]. The authors of the χ EFT calculations provide the wave-function only

Table 5.1.: Weight parameters of the individual components of the p–Ξ^- correlation function in pp HM collisions at $\sqrt{s} = 13$ TeV (p–Pb MB collisions at $\sqrt{s_{\mathrm{NN}}} = 5.02$ TeV). Misidentifications of particle species X are denoted as $\tilde{\mathrm{X}}$ and feed-down contributions have the parent particle listed as a sub-index. For the contributions in bold text, the correlation functions are modelled according to the interaction potential, while the others are assumed to be flat.

Pair	λ_i (%)	Pair	λ_i (%)
p–Ξ^-	**58 (51)**	p_{Σ^+}–$\Xi^-_{\Xi^0(1530)}$	0 (1)
p–$\Xi^-_{\Xi^-(1530)}$	**7 (8)**	p_{Σ^+}–Ξ^-_{Ω}	0 (0)
p–$\Xi^-_{\Xi^0(1530)}$	13 (16)	**$\tilde{\mathrm{p}}$–Ξ^-**	**0 (0)**
p–Ξ^-_{Ω}	1 (1)	$\tilde{\mathrm{p}}$–$\Xi^-_{\Xi^-(1530)}$	0 (0)
p_{Λ}–Ξ^-	8 (6)	$\tilde{\mathrm{p}}$–$\Xi^-_{\Xi^0(1530)}$	0 (0)
p_{Λ}–$\Xi^-_{\Xi^-(1530)}$	1 (1)	$\tilde{\mathrm{p}}$–$\Xi^-_{\Omega^-}$	0 (0)
p_{Λ}–$\Xi^-_{\Xi^0(1530)}$	2 (2)	**p–$\tilde{\Xi}^-$**	**7 (8)**
p_{Λ}–$\Xi^-_{\Omega^-}$	0 (0)	p_{Λ}–$\tilde{\Xi}^-$	1 (1)
p_{Σ^+}–Ξ^-	1 (2)	p_{Σ^+}–$\tilde{\Xi}^-$	0 (0)
p_{Σ^+}–$\Xi^-_{\Xi^-(1530)}$	0 (0)	**$\tilde{\mathrm{p}}$–$\tilde{\Xi}^-$**	**0 (0)**

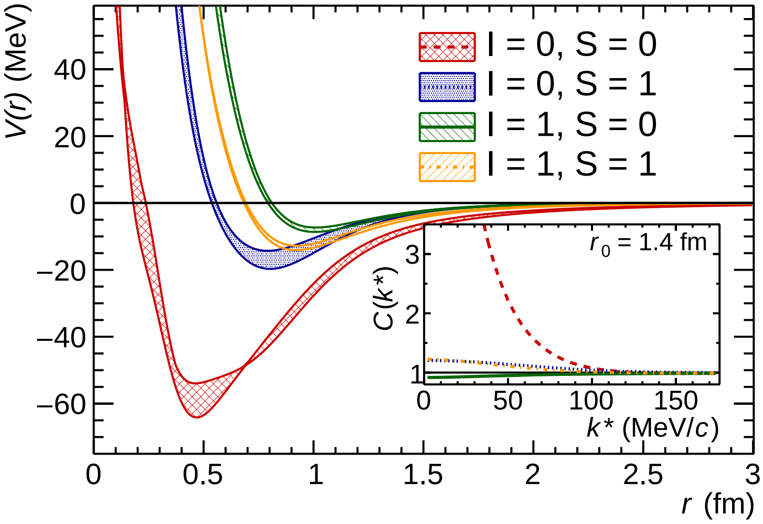

Figure 5.8.: Predictions for the Ξ-nucleon potential by the HAL-QCD Collaboration for the different spin (S) and isospin (I) states based on the parameterization proposed in [71]. The error bands refer to different Euclidean times considered in the calculation. The inset shows the correlation function computed with the central value of the potential for each of the different states and a source radius of 1.4 fm.

without considering the Coulomb interaction and hence can not be tested. The ESC16 model has its p–Ξ^- potential tuned to be repulsive, since the formation of bound states is supposed to be suppressed for $|S| \neq 0$. As discussed in Chapter 2, this repulsion results is expected to result in a suppression of the correlation function below the Coulomb hypothesis. The lattice calculations by the HAL QCD collaboration yield local potentials $V(r)$ for the individual isospin and spin channels of the NΞ interaction [71], which are depicted in Fig. 5.8. The width of the curves reflects the uncertainties due to different ratios between the spacing of the lattice grid a and the euclidean time t, where besides the default $t/a = 12$, the potentials are available for $t/a = 11$ and $t/a = 13$ [16, 71][2]. All isospin and spin channels feature a repulsive core at $r \to 0$ and an attractive pocket at intermediate particle distances. All potentials quickly converge to zero for distances $r > 2$ fm as typically observed for the short-ranged strong interaction. The inlet of Fig. 5.8 depicts the resulting correlation functions for a Gaussian source distribution with a size of 1.4 fm. The inlet illustrates the unique feature of collision systems with small source sizes. Even though the potentials of the different channels are similar at distances $r > 1.5$ fm the resulting correlation functions differ significantly and hence, femtoscopy in pp or p–Pb collisions provides the means to test potentials even at small relative distances.

In order to compute a prediction for the measured p–Ξ^- correlation function from these

---

[2] The lattice spacing stays fixed, however, the cut off in time or the so-called sink-time, were the observables are estimated is changed.

potentials, it has to be considered that both the proton and the Ξ^- baryons are spin and isospin 1/2 particles. Therefore, the pairs can be observed in four different states with isospin $I = 0$ or $I = 1$ and spin $S = 0$ (singlet) or $S = 1$ (triplet). The genuine p–Ξ^- correlation function for $L = 0$ (s-wave), can be written taking into account statistical weights of different isospin and spin states

$$\begin{aligned} C_{\mathrm{p}-\Xi^-} &= \frac{1}{8}C_{N-\Xi}(I=0,\ S=0) + \frac{3}{8}C_{N-\Xi}(I=0,\ S=1) \\ &+ \frac{1}{8}C_{N-\Xi}(I=1,\ S=0) + \frac{3}{8}C_{N-\Xi}(I=1,\ S=1), \end{aligned} \tag{5.1}$$

since particles in high energy collisions are produced without a preferred isospin or spin direction.

In principle, the pairs in the $|S| = 2$ sector, as they are listed in Table 2.2, can couple among each other. A strong coupling between pΞ^- pairs and the heavier $\Lambda\Sigma^0$ or $\Sigma\Sigma$ pairs would imply a cusp in the p–Ξ^- correlation function at $k^* \sim 230\,\mathrm{MeV}/c$ and $k^* \sim 380\,\mathrm{MeV}/c$, respectively. The measured correlation function, e.g. depicted in Fig. 5.5, shows no indication for such a behavior at the corresponding k^*. Hence, modifications of $C(k^*)$ due to the coupling in these channels, especially in the region $k^* < 200\,\mathrm{MeV}/c$, can be neglected [65]. Below the threshold it is possible for the pΞ^- pairs to couple to the lighter $\Lambda\Lambda$ pair, if they are in the $^1S_0$ state [65], and the nΞ^0 pair. The analysis of the Λ–Λ correlation function by the ALICE collaboration [39] could not find any indication for a cusp and the measurement further confirmed the scattering parameters of the Λ–Λ interaction predicted by the HAL QCD lattice calculations, which imply only a weak coupling between these two pairs [71]. The measurement of the n–Ξ^0 correlation function is impossible since ALICE is unable to detect neutral neutrons. In the context of theoretical calculations, a discussion of the effects of coupling between the different channels in a quantitative way is so far only available on the basis of χ EFT [146], however, without considering the effect of the Coulomb interaction. Lattice calculations [71] take into account the coupling among the different pairs and the off-diagonal elements of the $|S| = 2$ sector are available in order to define the full equation system of Eq. 2.18. At the moment, however, no numerical solver is available to compute the corresponding $\psi(k^*, \vec{r}^*)$ and hence $C(k^*)$, but there is an ongoing effort to extend previous work from the KN sector to the $|S| = 2$ sector [145, 210]. Preliminary results, where also the Coulomb interaction is taken into account, predict only minor modifications of the correlation functions due to the coupling between pΞ^- and nΞ^0 of less than 5%.

In the following, the single-channel Schrödinger Equation is solved by CATS in order to compute the prediction for the correlation functions and the off diagonal contributions are neglected. Nevertheless, coupled channel effects are at least partially taken into account, since their presence also influences the computation of the diagonal potential elements. In Fig. 5.9 the correlation functions relevant in the following discussion are computed for a Gaussian source distribution with a size of $r_{\mathrm{Gauss}} = 1.02\,\mathrm{fm}$. The

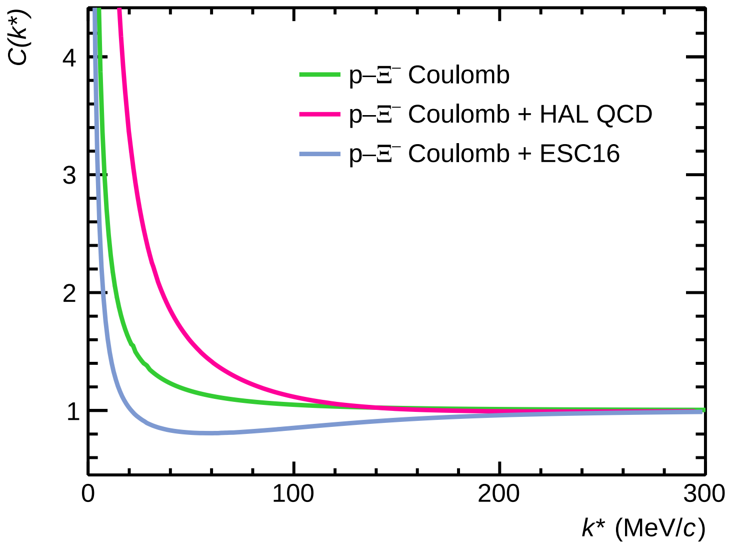

Figure 5.9.: The genuine p–Ξ^- correlation function, when only the Coulomb interaction (green curve) and the Coulomb and strong interaction is considered. For the latter the local potentials from the HAL QCD lattice calculations [71] (magenta curve) and the ESC16 model [14] (blue curve) are used. The source function is assumed to have a Gaussian shape with a size of $r_{\mathrm{Gauss}} = 1.02\,\mathrm{fm}$.

attractive nature of the Coulomb interaction between two particles with opposite charge alone results in the enhancement of $C(k^*)$ (green curve) above unity. The strong interaction, included by considering the attractive lattice potential in the Schrödinger Equation, leads to an enhancement of $C(k^*)$ (magenta curve) above the Coulomb only case. In contrast, the ESC16 potential predicts a repulsive strong interaction and consequently leads to a depletion in the intermediate k^* range. Without a detailed comparison, it can already be seen that this is clearly not reproduced by the measured correlation function.

Residual Correlations

The selected sample of Ξ^- baryons is contaminated by misidentified cascade candidates. The corresponding residual contribution is evaluated in a data driven way by conducting the analysis in the side-band region, next to the signal. Instead of selecting cascade candidates around the invariant mass of the Ξ^- ($M_{\Lambda\pi^-} = (1321.7 \pm 5.0)\,\mathrm{MeV}/c^2$), they are selected above ($M_{\Lambda\pi^-} = (1368 \pm 28)\,\mathrm{MeV}/c^2$) and below ($M_{\Lambda\pi^-} = (1282 \pm 28)\,\mathrm{MeV}/c^2$) this region[3]. The results are normalized within $400\,\mathrm{MeV}/c < k^* < 600\,\mathrm{MeV}/c$ and are averaged to properly represent the background in the signal region. The correlation function measured in this way is depicted in Fig. 5.10 and the shape is expected to be

---

[3] The high purity of the Ξ^- selection requires a rather wide window in order to select a sufficient amount of pairs

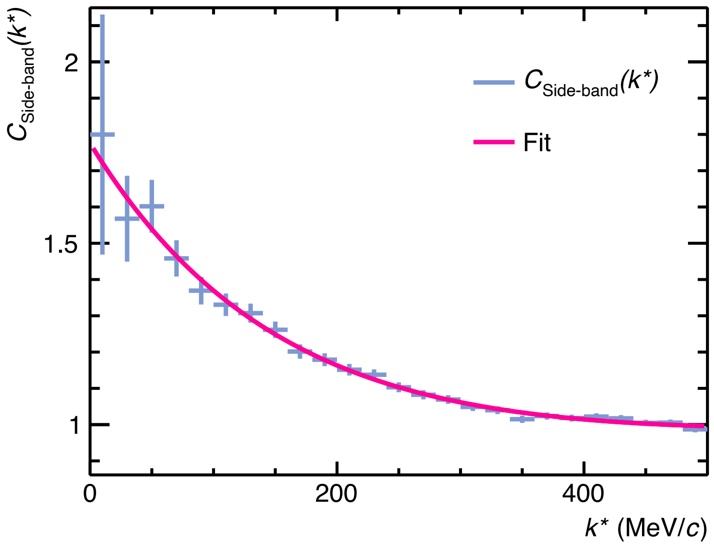

Figure 5.10.: Correlation function $C_{\tilde{\mathrm{p}}-\tilde{\Xi}^-}(k^*)$ measured by using protons and cascade candidates from the invariant mass region outside of the Ξ^- selection interval in HM pp collisions at $\sqrt{s} = 13$ TeV. The fit function is defined as the sum of an exponential function and a polynomial of second order.

at least partially introduced by correlated p–Λ pairs that are subsequently smeared by the random momentum of an unrelated π meson [10]. Any kinematic bias, due to the selection of candidates in a different invariant mass region, is found to be negligible. For a stable extrapolation to the final binning of the measurement, it is fit by a function composed of the sum of an exponential function and a polynomial function of second order, which is depicted by the pink line. The nature of the strong interaction of the proton and the $\Xi(1530)$ resonances is unknown. The feed-down contributions of pairs, which interact purely via a moderate strong force, are rather flat, as it was seen from the discussion residual correlations of p–Λ pairs to the p–p correlation function in Section 4.1.4 and Fig. 4.9. Therefore, only the Coulomb interaction between the p–$\Xi^-_{\Xi^-(1530)}$ is taken into account. This correlation function is modelled with the same radius as the p–Ξ^- pairs and is transformed according to the kinematic of the decay simulated with `GENBOD` [194]. All residual contributions are depicted in Fig. 5.11, the green and blue curves correspond to the side band contribution and the p–$\Xi^-(1530)$ contribution, respectively. The dashed curve depicts the respective correlation signal transformed into the p–Ξ^- momentum basis, the solid curve the residual correlation function scaled by the specific λ parameter. In both cases, it can be seen that at low k^* the residual contributions are only minor compared to the total measured signal .

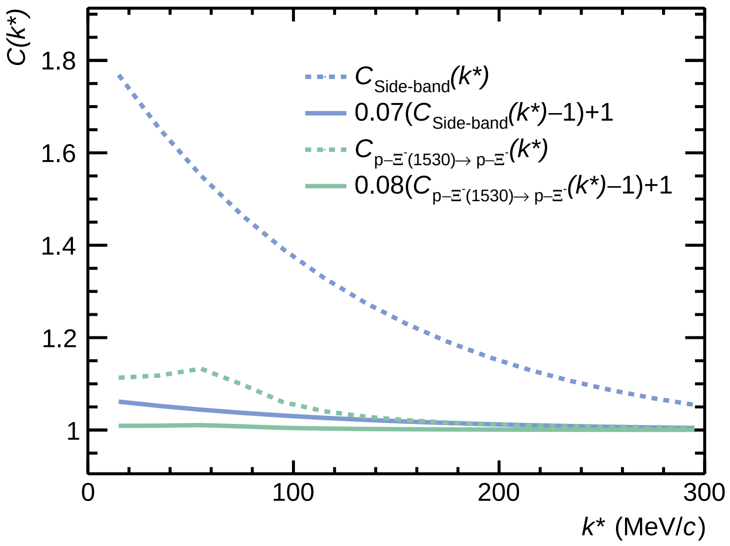

Figure 5.11.: The correlation functions of residual contributions due to the contamination of the selected Ξ^- (blue curves) and the p–Ξ^- (1530) pairs (green curve) in HM pp collisions at $\sqrt{s}$ = 13 TeV before (dashed lines) and after (solid lines) scaling by their respective λ parameters.

5.2. p–Ξ^- correlations in MB p–Pb collisions at $\sqrt{s_{\text{NN}}} = 5.02$ TeV

At this point the measured correlation function is compared to the theoretical expectation. In the analysis of the data set recorded from MB p–Pb collisions at $\sqrt{s_{\text{NN}}} = 5.02$ TeV, which are published in [176], the corrections are applied to the prediction and the modelled correlation function is written as

$$C_{\text{model,p–}\Xi^-}(k^*) = 1+\lambda_{\text{p–}\Xi^-}(C_{\text{p–}\Xi^-}(k^*)-1)+\lambda_{\tilde{\text{p}}\text{–}\tilde{\Xi}^-}(C_{\tilde{\text{p}}\text{–}\tilde{\Xi}^-}(k^*)-1)+ \\ \lambda_{\text{p–}\Xi^-_{\Xi^-(1530)}}(C_{\text{p–}\Xi^-_{\Xi^-(1530)}}(k^*)-1). \tag{5.2}$$

The result is smeared for the momentum resolution via Eq. 4.2 and the non-femtoscopic baseline is taken into account by the total correlation function, written as

$$C_{\text{tot,p–}\Xi^-}(k^*) = C_{\text{non-femto}}(k^*)\cdot C_{\text{model,p–}\Xi^-}(k^*). \tag{5.3}$$

By default $C_{\text{non-femto}}(k^*) = a$ is a constant, which is fixed by a fit of the measured correlation function outside of the femtoscopic signal in the region $250\,\text{MeV}/c < k^* < 450\,\text{MeV}/c$. As discussed in Sec. 5.1.3, a linear shape of $C_{\text{non-femto}}(k^*)$ can not be excluded and is therefore taken into account as part of the systematic variations.

5.2.1. Evaluation of Systematic Uncertainties

The systematic uncertainties associated with the selection of single particles are evaluated by repeating the analysis for individual variations of the single particle selection criteria. The ranges that are used for the different variables related to the selection of protons are reported in Table 4.2 and those of Ξ^- baryons in Table 5.2. In order to avoid any bias by statistical fluctuations, the variations of the criteria were chosen such as to change the single particle yield of protons and Ξ^- baryons by less than ±15% and the systematic uncertainties are evaluated in intervals of 200 MeV/c width in k^*. For each variation of the selection criteria the relative difference between the measured correlation function and the default one is calculated. Whenever this results in two systematic uncertainties, i.e. by a up and down variation, the average value is used. The relative uncertainties of

Table 5.2.: Systematic variations of the Ξ^- selection criteria in MB p–Pb collisions at $\sqrt{s_{\mathrm{NN}}}$ = 5.02 TeV.

Selection Criteria	**Default**	**Variation**	
Child track selection criteria			
Max. $\lvert\eta\rvert$	0.8	down	0.7
		up	0.9
Min. $\mathrm{DCA}_{\mathrm{xy}}$ to PV (cm)	0.05	down	0.04
		up	0.06
Max. $\mathrm{DCA}_{\mathrm{xy}}$ to cascade vertex (cm)	1.6	down	1.3
		up	1.9
Max. $\mathrm{DCA}_{\mathrm{xy}}$ to V^0 vertex (cm)	1.5	down	1.3
		down	1.4
Max. n_σ for PID	4	down	3
		up	4.5
V^0 selection criteria			
Min. $\cos\alpha$	0.97	up	0.99
Min. transverse radius (cm)	1.4	down	1.1
		up	1.7
Min. $\mathrm{DCA}_{\mathrm{xy}}$ to PV (cm)	0.07	down	0.06
		up	0.08
Cascade selection criteria			
Min. $\cos\alpha$	0.98	up	0.985
		up	0.99
Min. transverse radius (cm)	0.8	down	0.6
		up	1.0
Min. p_{T} (GeV/c)	0.3	up	0.8
		up	1.2

all variations are summed in quadrature and extrapolated to the finer binning by fitting a polynomial of second order. The so obtained systematic uncertainties are the largest in the lowest k^* bin, where they amount to about 3.2%.

The modeling of the correlation functions for both the Coulomb only case and the Coulomb + lattice case has an uncertainty related to the source distribution and the estimation of the baseline. Per default, the Gaussian source of p–Ξ^- pairs is assumed to have a size equal to that of p–p pairs, where the analysis of the correlation function yields a central value of $r_{\text{Gauss}} = 1.427\,\text{fm}$ [176]. The uncertainties of this assumption are associated with the statistical and systematic uncertainties of the measurement, but also with differences between the source distributions of p–p and p–Ξ^- pairs due to modifications by strongly decaying resonances. As discussed in Sec. 2.2, the source size of p–Ξ^- pairs is estimated to decrease by as much as 20% when compared to that of p–p pairs. Therefore, this difference with respect to the default value is added in quadrature with the statistical (0.007 fm) and systematic (0.014 fm) uncertainties in order to estimate the lower boundary of the radius ($r_{\text{Gauss}} = 1.141\,\text{fm}$). The upper boundary of the radius is estimated from the squared sum of statistical (0.007 fm) and systematic (0.007 fm) uncertainties ($r_{\text{Gauss}} = 1.434\,\text{fm}$). A possible contribution to the correlation function due to energy and momentum conservation, is estimated by replacing the constant baseline ($C_{\text{non-femto}}(k^*) = a$) by a linear one ($C_{\text{non-femto}}(k^*) = a + b \cdot k^*$). Also the baseline parameters are varied within their uncertainties evaluated from the χ^2 minimization. In case of the linear baseline the correlation between the parameters a and b is taken into account by using their combined minimum and maximum values along the $\chi^2/n.d.f. = 1$ contour. The baseline parameters and their variations are summarized in Table 5.3. The λ parameters are varied by altering the measured production cross section of the $\Xi^-(1530)$ baryon by 20%. Additionally, the normalization range for the measurement of the p–Ξ^- side-band background was varied to $450 < k^* < 650\,\text{MeV}/c$ and $500 < k^* < 700\,\text{MeV}/c$. Variations of the invariant mass region where the side-band candidates are selected, are found to have a negligible influence. The uncertainties related to the lattice calculations are evaluated by recalculating $\psi(k^*, \vec{r}^*)$ for the potentials with $t/a = 11$ and 13. The predictions of $C_{\text{tot,p–}\Xi^-}(k^*)$ for all these variations are computed and bin-by-bin the minimum and maximum value of $C(k^*)$ is used to evaluate the 1σ uncertainty, where a uniform distribution was assumed.

Table 5.3.: Default parameters and their systematic variations for the constant and linear baseline.

		a	$b \times 10^5$ (MeV$/c$)$^{-1}$
Constant		0.989 ± 0.005	0
Linear	default	1.010	-5.647
	up	0.977	3.379
	down	1.044	-0.0001

5.2.2. Results in p–Pb collisions

In Fig. 5.12 the measurement of the p–Ξ^- correlation function and the comparison to the prediction for the Coulomb only (green curve) and for the combination of Coulomb and strong interaction (orange curve), described by the lattice calculations, is presented. The 1σ uncertainty obtained from the systematic variations of the data selection is represented by the gray boxes, the uncertainty due to the modeling is shown by the width of the respective curves. The measured data by itself exhibits a clear enhancement above unity, which corresponds to an attractive interaction. It can be clearly seen that this trend is not reproduced by the prediction for the Coulomb only case (green curve). Moreover, the incompatibility can be quantified by the number of standard deviations $n\sigma$. In several thousand iterations a new correlation function is sampled at each bin center within $k_i^* < 140\,\mathrm{MeV}/c$ from a Gaussian distribution, where both the mean and the width are fixed to the measured value $C(k_i^*)$ and the magnitude of the systematic uncertainties. Each time, the χ^2 value is computed for the upper and the lower limit of the model prediction taking into account the statistical uncertainties and then converted into a p-value and a $n\sigma$ value. As a result the Coulomb only hypothesis is excluded by 3.6 to 5.3 standard deviations. The difference can only be explained by

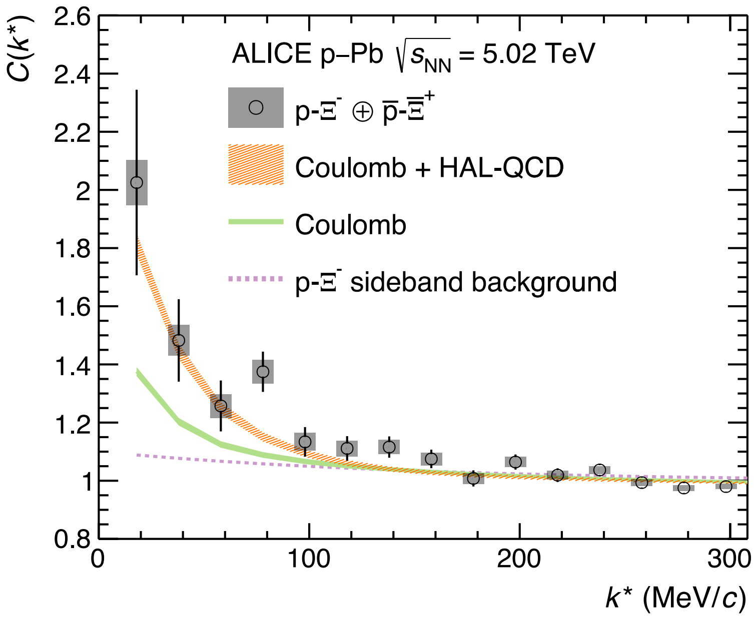

Figure 5.12.: The p–Ξ^- correlation functions shown as a function of k^* in MB p–Pb collisions at $\sqrt{s_{\mathrm{NN}}} = 5.02$ TeV [176]. Statistical (bars) and systematic uncertainties (boxes) are shown separately. The widths of the filled bands correspond to one standard deviation of the systematic error of the fit. The HAL QCD curve uses potentials obtained from [71]. The dashed line shows the contribution from misidentified p–$\tilde{\Xi}^-$ pairs from the side-bands scaled by its λ parameter.

a missing attractive interaction, which for the p–Ξ^- pair can only originate from the strong interaction. Hence, from this measurement, the presence of the attractive nature of the strong interaction among a proton and a Ξ^- baryon becomes evident for the first time [176]. Furthermore, the lattice calculations, which describe this strong interaction, are tested by comparing their prediction to the data. The same procedure was used to calculate the corresponding $n\sigma$ values and were found to range from 1.8 to 3.7, and are hence in agreement with the measurement. Before discussing the implication of this measurement in the context of neutron stars, a second measurement of the correlation function is presented.

5.3. p–Ξ^- correlations in HM pp collision at $\sqrt{s} = 13$ TeV

The study of the p–Ξ^- interaction via the measurement of the correlation function is extended to HM pp collisions at $\sqrt{s} = 13$ TeV, published in [77]. The increased number of pairs and the stricter constraints of the source distribution are used for a complementary measurement and for a further test of the lattice calculations. The correlation function is unfolded for experimental effects and the genuine p–Ξ^- correlation signal is extracted in order to provide correlation functions that can be directly compared to any theoretical prediction.

Before the measured correlation function is computed, the k^* distributions of same and mixed events are unfolded for the effects of the finite momentum resolution with the Bayes method, as reported in Section 5.1.2. The non-femtoscopic background $C_{\text{non-femto}}(k^*) = a$ is then constrained by a fit of $C(k^*)$ within $500\,\text{MeV}/c < k^* < 800\,\text{MeV}/c$. The residual correlations are modelled following the procedure outlined in Section 5.1.5. At this point, the description of the measured correlation function $C_{\text{tot,p}-\Xi^-}(k^*)$, given by Eq. 5.2 and Eq. 5.3, is solved for $C_{\text{p}-\Xi^-}(k^*)$ and the genuine correlation function is extracted.

5.3.1. Evaluation of Systematic Uncertainties

Due to the development of nanoAODs[4], the systematic uncertainties of the single particle selection criteria could be estimated more accurately by taking into account correlations between them. The individual variations of the latter are reported for protons in Table 4.3 and Ξ^- baryons in Table 5.4. The analysis is performed over the same data set in parallel 45 times, where in every single iteration the default, up or down value of each selection criterion is picked at random. With respect to the default, the variations alter the pair yield by a maximum of 20% and the purity of the selected cascade candidates by less than 3%. Additional to the correlation function measured for the default selection criteria of p–Ξ^- pairs, 44 variations of the correlation function are

---

[4] These is a filtered datatype, where only variables required for femtoscopic analysis was extracted from the standard data format (AODs)

Table 5.4.: Systematic variations of the Ξ^- selection criteria in HM pp collisions at $\sqrt{s}\,=\,13$ TeV.

Selection Criteria	**Default**	**Variation**	
Child track selection criteria			
Max. $\lvert\eta\rvert$	0.8	down	0.77
		up	0.83
Min. $\mathrm{DCA_{xy}}$ to PV (cm)	0.05		0.06
Max. $\mathrm{DCA_{xy}}$ to cascade vertex (cm)	1.6	down	1.3
		up	1.9
Max. $\mathrm{DCA_{xy}}$ to V^0 vertex (cm)	1.5	down	1.3
		down	1.4
Max. n_σ for PID	4	down	3
		up	4.5
V^0 selection criteria			
Min. $\cos\alpha$	0.97	down	0.96
		up	0.99
Min. transverse radius (cm)	1.4		1.7
Min. $\mathrm{DCA_{xy}}$ to PV (cm)	0.07	down	0.06
		up	0.08
Cascade selection criteria			
Min. $\cos\alpha$	0.98		0.99
Min. transverse radius (cm)	0.8	down	0.6
		up	1.0
Min. p_T (GeV/c)	0.3	up	0.8
		up	1.2

available for the further analysis. The uncertainties related to the selection criteria are estimated individually in each k^* bin from the minimum and maximum value of $C(k^*)$ from all those variations by assuming a uniform distribution of $C(k^*)$ in each k^* interval. This yields the relative uncertainty as it is depicted in the top left panel of Fig. 5.13, which reaches a maximum value of about 5% in the first measured k^* interval.

Furthermore, uncertainties due the shape and the estimation of the parameters related to the baseline $C_\text{non-femto}(k^*)$ are considered. The constant factor $C_\text{non-femto}(k^*) = a$ is replaced by a linear function $C_\text{non-femto}(k^*) = a + b \cdot k^*$ and the fit range, where the parameters a and if needed b are estimated, is varied. Therefore, the lower (upper) boundary is increased up to 800 MeV/c (decreased down to 700 MeV/c) in steps of 100 MeV/c, while ensuring that the fit range of the baseline covers a minimum width of 200 MeV/c. In each k^* bin the uncertainty is computed from the minimum and maximum value of $C(k^*)$ from all possible combinations assuming a uniform distribution. The resulting relative systematic uncertainty is depicted in the top right panel of Fig. 5.13,

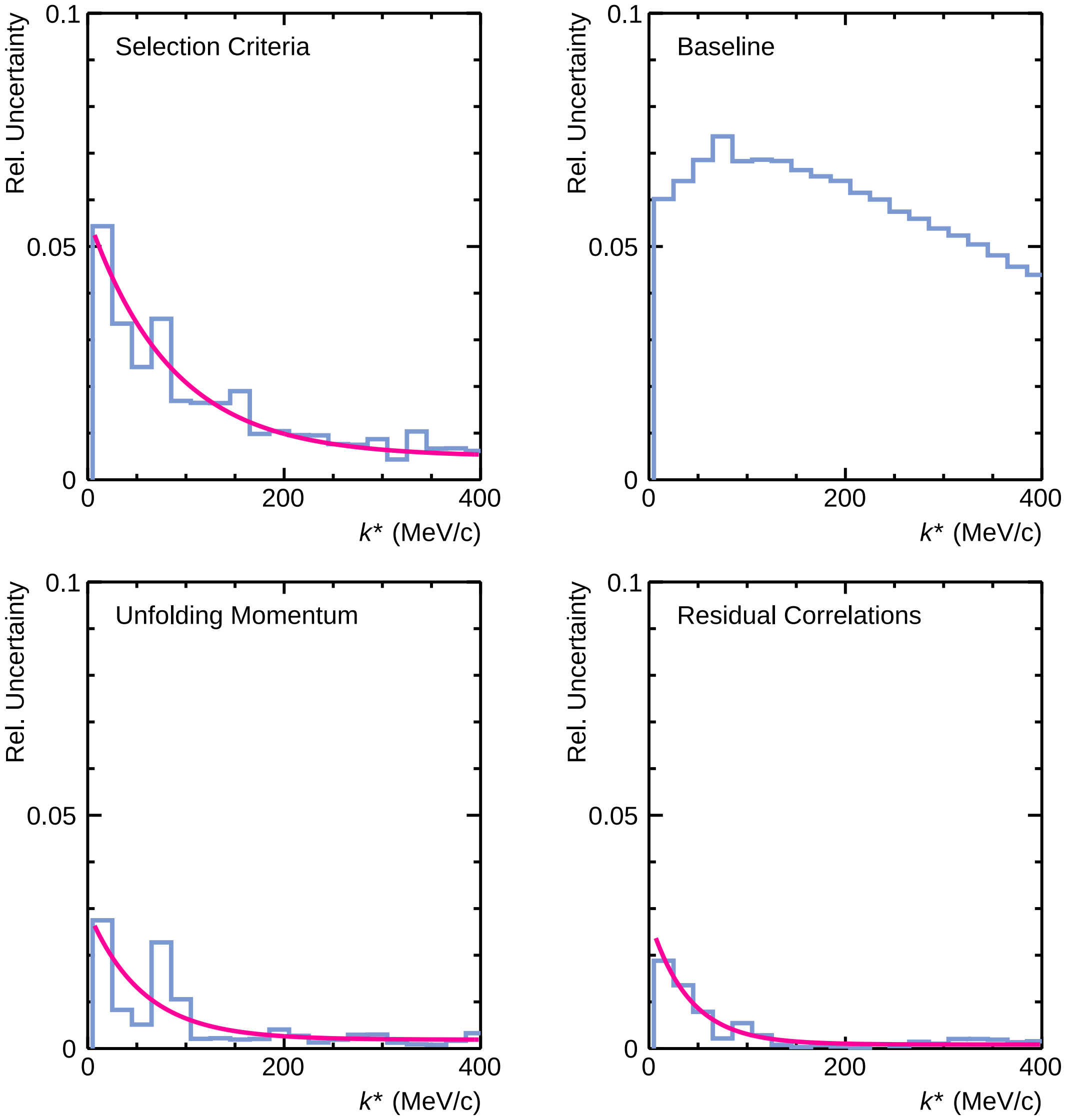

Figure 5.13.: Overview of the different source of systematic uncertainties related to the measurement of the genuine p–Ξ^- correlation function in HM pp collisions at $\sqrt{s}$ = 13 TeV. The different contributions are classified in those related to the selection of single particles (top left), to the estimation of the baseline (top right), to the unfolding for the finite momentum resolution (bottom left) and to the unfolding for the residual correlations (bottom right). The results are smoothed by fitting a function composed of an exponential function multiplied by a linear function, if the corresponding pink curve is shown.

which reaches a maximum value of 7.3% at $k^* = 75\,\mathrm{MeV}/c$.

Moreover, uncertainties related to the unfolding for effects of the finite momentum resolution are analyzed. For the Bayes method, the number of iterations are increased and decreased by up to two. The algorithm of the unfolding is varied by employing the bin-by-bin as well as the IDS method instead of the Bayes method. Also for the latter the parameter defining the number of iterations is varied between 0 to 4. In this context also the uncertainty related to the momentum resolution matrix is taken into account. Therefore, a response function is filled with pairs sampled from a folded normal distribution, where the mean and width are varied within their respective uncertainties. For each k^* bin, the minimum and maximum value of $C(k^*)$ from all possible combinations is computed and the systematic uncertainty is extracted by assuming a uniform distribution. The relative systematic uncertainty is depicted in the bottom left panel of Fig. 5.13, which reaches maximum value of 3% in the first k^* interval.

Last but not least, the systematic uncertainties due to the description of the residual correlations are estimated. The production fractions of the $\Xi^-(1530)$ resonance and the Ω^- are varied individually within the uncertainties of their measurement, which amount to approximately ±20% [182, 183, 188–191]. Further, also the uncertainty due to the contribution of misidentified cascade candidates is estimated by normalizing the k^* distributions of p–$\tilde{\Xi}^-$ pairs in the region between $450 < k^* < 650\,\text{MeV}/c$ and $500 < k^* < 700\,\text{MeV}/c$. Variations of the invariant mass region region, where the $\tilde{\Xi}^-$ candidates are selected, can be neglected[5]. The uncertainty is computed individually in each k^* bin from the minimum and maximum variation of $C(k^*)$ assuming a uniform distribution. The relative systematic uncertainty associated with these variations is presented as a function of k^* in the bottom right panel of Fig. 5.13, which reaches a maximum value of 2% in the lowest k^* bin.

All relative systematic uncertainties except the ones related to the baseline are smoothed by a fit function composed of an exponential function multiplied by a linear function, as represented by the magenta curve in Fig. 5.13. The total systematic uncertainty is then calculated as the quadratic sum of the individual contributions. It is the largest in the first k^* interval and amounts to about 8.4%.

The uncertainties associated to the predictions are solely related to those of source and of the model itself. In order to evaluate the former, the core radius is varied by ±0.04 fm, which yields a variation of the effective source of $r_{\text{eff}} = (1.02 \pm 0.05)$ fm. The HAL QCD potential is available for three different sink-times [71], corresponding to different values of t/a. At the time of this study, the HAL QCD collaboration additionally provided 23 Jackknife variations [211] for the potential at each individual t/a. The Jackknife method estimates the uncertainty of an observable from the same sample by computing it several times, where each time one or more different elements of a sample are ignored. The variations of the predictions due to (i) the uncertainty of the radii, (ii) the different

---

[5] Pairs, where the cascade candidates were selected in four different regions that varied in both width and position, create an absolute spread of $\lambda_{\text{p}-\tilde{\Xi}^-}(C(k^*) - 1)$ of 0.04, which corresponds to a relative difference of less than 1% to the total measured correlation function.

t/a and (iii) Jackknife variations were computed independently. For (i) and (ii) the resulting uncertainties with respect to the default are evaluated by computing the maximum deviated from the default. Following the formalism of the Jackknife method, the uncertainty of (iii) has to be evaluated by calculating at each k^* as

$$\sigma(k_i^*) = \sqrt{\frac{N_{N_{\mathrm{Jk}}}-1}{N_{N_{\mathrm{Jk}}}} \cdot \sum_{j=0}^{N^{\mathrm{Jk}}} \left(C_j(k_i^*)\right)^2 - \frac{1}{N_{N_{\mathrm{Jk}}}} \cdot \left(\sum_{j=0}^{N^{\mathrm{Jk}}} C_j(k_i^*)\right)}, \tag{5.4}$$

where N_{Jk} is the total number of Jackknife variations. All uncertainties are then combined by adding them in quadrature.

5.3.2. Results in pp collisions

The resulting comparison of the experimental p–Ξ^- correlation function to the predictions is presented in Fig. 5.14. This figure shows the comparison between the unfolded measurement and the predictions for the cases when only the Coulomb or the Coulomb and strong interaction are considered. The experimental k^* distributions are measured

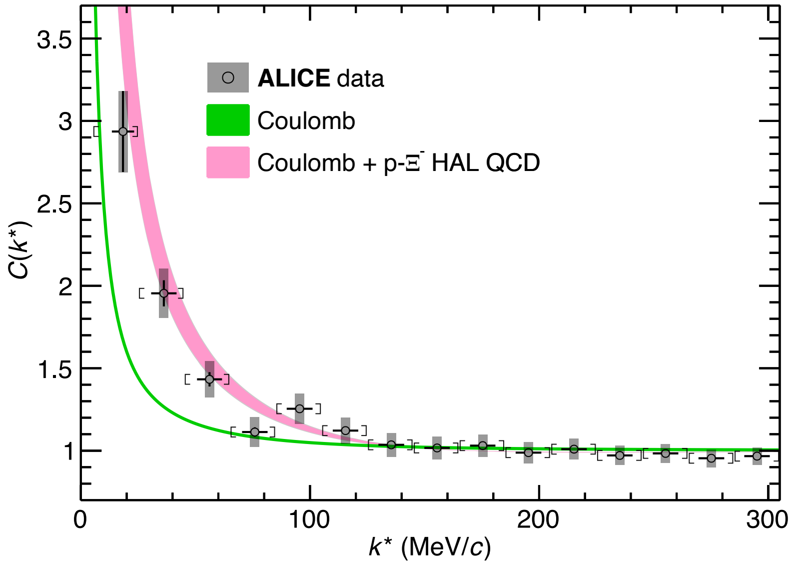

Figure 5.14.: Measured p–Ξ^- correlation functions in high multiplicity pp collisions at $\sqrt{s}$ = 13 TeV [176]. The experimental data are shown as black symbols. The black vertical bars and the gray boxes represent the statistical and systematic uncertainties, respectively. The square brackets show the bin width. The theoretical predictions, shown as colored bands, use either the assumption of a pure Coulomb (green curve) or of a Coulomb+strong interactions (magenta curve). The width of the curves represents the 1σ uncertainty associated with the calculation.

in intervals of 5 MeV/c and the mean k^* is computed from four consecutive bins. It is then used as the corresponding central value to report the final $C(k^*)$, where the width of each k^* interval is visualized in Fig. 5.14 by the black vertical bars. The 1σ intervals of the statistical and systematic uncertainties of the measurement are represented by the black bars and gray boxes, respectively. The width of the curves for the different predictions represents the 1σ interval of their total uncertainty. The measured $C(k^*)$ exhibits a clear enhancement above unity, which is again indicative of the attractive nature of the p–Ξ^- interaction. The Coulomb interaction alone (green curve) is unable to reproduce the measurement and demonstrates again the presence of an additional attractive strong interaction among the proton and the Ξ^-. Since the data are unfolded, its uncertainties are uncorrelated with these related to the modeling and can be added in quadrature in order to compute the number of deviations $n\sigma$ simply from the χ^2 value. In this way, the prediction Coulomb-only hypothesis s found to deviate significantly by $n\sigma = 5.0$. The potential by the HAL QCD collaboration, describing this strong interaction, in combination with the Coulomb interaction yields a correlation function (magenta curve) which is in good agreement with the measurement and is found to be in agreement with the measurement with $n\sigma = 0.81$.

5.4. Discussion

The presence of the attractive strong interaction is demonstrated by the measurements in two independent collision systems, which exhibit a clear enhancement above the expectation of a Coulomb-only interaction. Furthermore, the NΞ^- potentials predicted by lattice simulations of the HAL QCD collaboration are tested by including them in the modeling of the correlation function. Overall, a good qualitative agreement is found between the measured and predicted correlation function within 1.8 to 3.7 standard deviations in p–Pb collisions and within 0.81 standard deviations in HM pp collisions. It should be noted that in HM pp collisions the prediction shows a tendency to lay on the upper edge of the uncertainty band in data. This might be improved in a calculation including all coupled-channel effects, which for p–Ξ^- pairs are expected to dampen the correlation function [210]. It should be highlighted, however, that this measurement demonstrates for the fist time a direct qualitative and quantitative agreement of first principle lattice calculations of the interaction among baryons. In general, the results of these lattice simulations for the $|S| = 2$ sector are in good agreement with several measurements [75, 77, 176]. At this point, it is therefore interesting to explore the role of the Ξ^- in the EoS of neutron stars based on the lattice results. As it is discussed in Sec. 1.2.2, the single particle potential of the Ξ^- at ρ_0 can be computed from state-of-the-art these NΞ^- lattice potentials with the Brueckner-Hartree-Fock approximation [75]. With a value of $U_{\Xi^-} \approx -4$ MeV, a shallow attractive interaction is predicted in SNM at saturation density. This value is noticeably lower than the canonical value of $U_{\Xi^-} \approx -15$ MeV that is assumed in theoretical calculations of the EoS of a neutron stars [94, 98]. Hence, a different behavior of the Ξ^- in a neutron rich

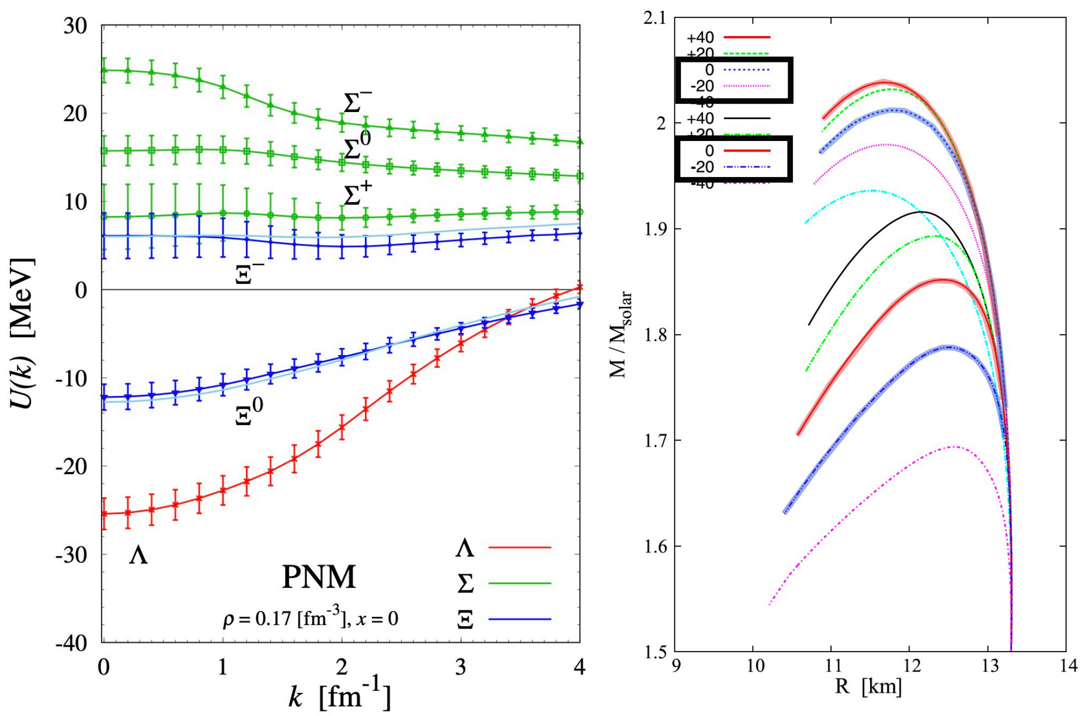

Figure 5.15.: (left) Single particle potentials of hyperons in PNM utilizing the predictions of the potentials from lattice calculations by the HAL QCD collaboration in Brueckner-Hartree-Fock calculations. Figure taken from [75]. (right) Mass radius relations for different values of U_{Ξ^-}. The curves in the upper (lower) branch represent the calculations with (without) a repulsive Y–Y interaction [96].

environment is expected from these lattice simulations. This is best understood from the single particle potential in PNM, as it is disused in the introduction in Sec. 1.2.2 and for convenience is reproduced in the left panel of Fig. 5.15. It can be seen that based on the lattice potentials a shallow repulsion of $U_{\Xi^-} = 6\,\mathrm{MeV}$ is predicted. Consequently, the threshold for the appearance of the Ξ^- in a neutron star shifts towards larger densities than typically assumed. Therefore, a different value of U_{Ξ^-} in SNM implies a change of the behavior of the EoS, which can be explored with the help of theoretical RMF calculations [96], as they are presented at the end of Sec. 1.3. The result is reproduced in the right panel of Fig. 5.15. The individual curves show the mass radius relation, where the EoS is computed for different values of U_{Ξ^-} in SNM in steps of 20 MeV. The upper (lower) four curves correspond to a calculation, where an (no) additional repulsion between hyperons is taken into account. It is evident from the highlighted curves that a difference of the single-particle potential by 10 MeV is expected to already yield a sizable modification of the mass radius relation of a neutron star and the maximum mass that can be supported by the corresponding EoS.

In this way, the strong interaction can be constrained by measurements of the p–Ξ^-

correlation function, which is crucial to improve the understanding of neutron stars. In particular, the good agreement of the predictions based on the NΞ^- lattice potentials is a compelling argument for future theoretical calculations of the EoS of neutron stars to take into account a Ξ^- single particle potential of $U_{\Xi^-} = -4\,\mathrm{MeV}$ and demonstrates the importance for future measurements to investigate this difference.

6. Summary

A precise understanding of the Equation of State of dense baryonic matter, realized for instance in the inner core of neutron stars, is limited by the knowledge of details of the interactions among possible constituents, including hyperons, and the precision of the models describing the latter. Currently, the only feasible approach to experimentally investigate the hyperon-nucleon and hyperon-hyperon interaction are femtoscopic measurements, which are sensitive to the source of particle emission and to the interaction of the particle pair.

In this work, the femtoscopy method is used to directly observe for the first time the attractive strong interaction among a proton and a Ξ^- baryon by studying the two-particle correlation function in high-multiplicity pp collisions at $\sqrt{s} = 13$ TeV and minimum-bias p–Pb collisions at $\sqrt{s_{\mathrm{NN}}} = 5.02$ TeV at the LHC measured by ALICE.

The unambiguous interpretation of final-state effects among p–Ξ^- pairs from the measured correlation function is only possible due to the precise constraints of the emission source that are obtained by the analysis presented in the first part of this work. The source is studied with p–p and p–Λ pairs, where the Argonne v_{18} potential and the results from chiral effective field theory provide a sufficient theoretical description of the respective interaction. The correlation functions are analyzed in several intervals of the transverse mass $m_{\mathrm{T}} = \left(k_{\mathrm{T}}^2 + m^2\right)^{1/2}$, where m and k_{T} are the average mass and the average transverse momentum of the particle pair.

For a source distribution, modeled as a Gaussian function with width r_{Gauss}, the measured radii of p–p and p–Λ pairs decrease with increasing m_{T}, but exhibit a clear offset indicating a possible difference in the emission process. The offset can be explained by an effective enlargement of the source due to resonances feeding to the particle pair of interest which are incorporated by modeling the source distribution as a convolution of a core and a non-Gaussian halo. The former represents the universal emission profile of all particles and has a Gaussian shape with width r_{core}, while the latter appears due to the decay of the short-lived resonances and introduces an exponential tail. In this new procedure, the modification of the source distribution due to the effect of short-lived resonances is, for the first time, quantified and taken into account explicitly in a measurement of the source size. The modeling is based on the output of the statistical hadronization model and the EPOS transport model. The average lifetime of resonances that produce a proton ($c\tau = 1.65\,\mathrm{fm}$) is much shorter than of those that produce a Λ ($c\tau = 4.69\,\mathrm{fm}$) and thereby a smaller halo is expected for p–p pairs than for p–Λ pairs. Indeed, this effect is sufficient to account for the offset observed for a purely Gaussian source and the measured core source sizes of both pairs agree. A common, decreasing scaling of $r_{\mathrm{core}} \in [0.85, 1.3]$ fm within $m_{\mathrm{T}} \in [1.1, 2.2]$ GeV/c^2 is observed, which indicates the presence of a common source for protons and Λs. Compared to the source sizes measured for a purely Gaussian source distribution the core radius is decreased by as much as 20%, which highlights the importance to consider the effect of short-lived resonances also in future femtoscopic analyses.

The observed scaling of the source sizes as a function of m_{T} for both pairs in itself is interesting, since in heavy-ion collisions this is understood as one of the signatures of radial and (an-)isotropic flow. This observation is in line with several other experimental measurements that indicate the presence of collective effects in elementary collisions. In order to further investigate this, the treatment of resonances will be crucial to compare in a straightforward way the m_{T} dependent radii of additional pair combinations such as π–π or p–K$^-$.

Furthermore, the assumption of a common core source, modified by the resonances feeding to the particle pair of interest, allows for a quantitative description of the emission profile for any kind of particle pair. This is relevant for coalescence approaches addressing the production of (anti) (hyper) nuclear clusters from single particles. In addition, the constraint of the source distribution is the basis for a high-precision study of the interaction potentials of p–Ξ^- pairs.

The second part of this work presents the study of the p–Ξ^- correlation function, which is measured with ALICE in both pp and p–Pb collisions. The baseline of the measurement is established by an investigation of background and experimental effects. The identification of the Ξ^- by its decay into a Λ and a π^- includes random combinations of $\Lambda\pi^-$ pairs. The correlation signal of p–($\Lambda\pi^-$) is analyzed by selecting $\Lambda\pi^-$ pairs in the invariant-mass region next to the Ξ^- and is thereby considered as a residual contribution in the description of the measured p–Ξ^- correlation function. Moreover, the finite resolution of the measured particle momentum is taken into account in the analysis of p–Pb collisions by smearing the modeled prediction and in the analysis of pp collisions by unfolding the measured data.

Based on the results in the first part of this work, the emission source for p–Ξ^- pairs is modeled as a Gaussian distribution with size r_{core} that is modified by a halo due to the decay of short-lived resonances. The size of the core source is determined from the measurement of r_{core} from p–p correlations. All modifications of the source distribution are due to short-lived resonances that produce a proton, since no such resonances feed to the Ξ^-. The resulting source distribution is used to model different theoretical predictions of the p–Ξ^- correlation function in order to investigate the nature of the final-state effects that produce the observed signal.

It is demonstrated that the Coulomb interaction among the oppositely charged proton and Ξ^- alone is not sufficient to describe the signal in the measured correlation functions. The Coulomb-only hypothesis is excluded within 3.6 to 5.3 standard deviations in the measurement in p–Pb collisions and by 5.0 standard deviations in the measurement in pp collisions. The enhancement above the Coulomb-only prediction demonstrates an

additional contribution by an attractive strong interaction among the two particles has to be present, which is directly observed for the first time.
The measurements are used to test theoretical calculations that describe the strong interaction among a proton and Ξ^-. Employing the Correlation Analysis Tool solving the Schrödinger Equation, the two-particle wave-function is computed by solving the single-channel Schrödinger equation for a given p–Ξ^- interaction potential. The wave-function is subsequently used to obtain a prediction for the correlation function. Due to the small mass differences and the same relevant quantum numbers of pairs in the $|S| = 2$ sector, the strong interaction leads to coupling in the $\Lambda\Lambda$-nΞ^0-pΞ^--$\Lambda\Sigma$-$\Sigma\Sigma$ system. It has to be noted, that in the present approach, coupled-channel effects are only partially taken into account by their influence on the genuine interaction potentials. So far, calculations which compute the wave-functions of the entire coupled-channel system, as well as the correlation function taking into account contributions of all connected states, either neglect the Coulomb interaction or are in a very preliminary state. These results nevertheless indicate, that the additional effects of coupled channels introduce only minor modifications to the p–Ξ^- correlation function.
The phenomenological ESC16 meson exchange model predicts a repulsive p–Ξ^- interaction and hence yields a difference of more than 5 standard deviations to both measurements. In contrast, the first principle lattice calculations by the HAL QCD collaboration suggest an attractive interaction, which is able to reproduce the measurement in p–Pb collisions within 1.8 to 3.7 standard deviations and the measurement in pp collisions within 0.81 standard deviations. Consequently, for the N–Ξ interaction the validity of lattice QCD calculations is demonstrated for the first time.

The validation of the lattice QCD calculation has important implications for the modeling of the Equation of State of dense baryonic matter. The single-particle potential of the Ξ^-, which is computed based on the lattice simulations, differs from the contemporary theoretical calculations of the equation of state typically assume a canonical value by approximately 10 MeV more attractive. In pure neutron matter, a shallow repulsive interaction of $U_{\Xi^-} = 6\,\text{MeV}$ is predicted, which suggests that the density threshold for the appearance of the Ξ^- in dense baryonic matter is expected to be located at even larger densities than usually assumed. Consequently, a stiffer EoS than typically predicted is expected and has to be explored by future theoretical calculations based on the updated single-particle potential.

The future collection of elementary collision data by ALICE at the LHC during the upcoming Run 3 is therefore particularly interesting. Upgrades of several detector components are currently ongoing or have been completed, which will provide the capabilities to record collisions at significantly higher rates. Additionally, there are plans for dedicated data-taking schemes in order to record specifically only those collisions, in which the production of a hyperon is detected. Consequently, it will be possible to measure the p–Ξ^- correlation function with significantly improved uncertainties. This will be important in order to investigate in detail coupled-channel effects. At the same time, the study of pairs with more complicated decay channels or smaller particle production cross sections will become feasible yielding the solution to the Equation of State of dense baryonic matter.

Acknowledgments

The successful completion of this work became a reality only due to the incredible support of many people.

I would like to thank Prof. Laura Fabbietti for opening the doors to her group of wonderful people for me and for her support ever since I started my master's thesis. Thanks to her, I was able to work on this interesting, challenging and rewarding analysis, which without her would have never reached such heights. I appreciate the opportunity to have worked on an analysis with impactful results. Furthermore, it was a great pleasure to present on several conferences and to learn more about physics on my many visits to workshops and summer schools. Also, thanks to Prof. Fabietti, I was able to realize a long standing dream of mine, to visit CERN and finally see the ALICE detector.

The underground office, which took me in as one of their own when I started my PhD, has been an important pillar of moral support. I want to thank Piotr Gasik, who has been my mentor and friend. His guidance, but also his happiness, passion and a sample of his determination gave me inspiration when I needed it. I want to further thank Andreas Mathis, good friend and comrade in dire times, for his help, discussions, explanations and motivating words, but more so for the great times we had and have together in the office and on our joint travels. Hummus on, man! Thanks to Thomas Klemenz and Lukas Lautner, for making the underground complete and for adding to the common Pfanding collection.

Femto is not what it is without the Femtogang. Thanks a lot to Andi, Dimitar Mihaylov, Valentina Mantovani Sarti and Oton Vazquez Doce. Thank you, Dimitar, for sharing your jokes, pictures of Bulgaria, knowledge about Quantum Mechanics and CATS-pertise. Vale, a huge thank you for answering all my questions about theory, Isospin is not a mystery to me anymore! Oton, I am happy we worked together on our two papers and thank you for teaching me the in and outs of analysis during that. I would also like to mention the honorary founding member of the Femtogang: Oliver Arnold, whose pioneering work we base our mass production of results upon. Good luck to the next generation of Femtoscopists - Stefan Heckel, Emma Chizzali, Max Korwieser, and Bhawani Singh, Laura Šerkšnytė and Raffaele Del Grande.

In the context of analysis, I would like to express my acknowledgment to the ALICE Collaboration for all the input provided over the years, in particular from several members within the Femto PAG. Thank you to Johann Haidenbauer, Tom Rijken and the HAL QCD collaboration for their input and feedback from the theoretical side of these studies.

The E62 group includes many other people, who I want to thank all for creating such a nice and happy work environment. I would like to thank the former group members Joana Wirth, Steffen Maurus, Martin Berger, Jia-Chii Berger-Chen and Robert Münzer for our coffee breaks, feedback, support, explanations and advice. Thanks for the happy times. Thank you to honorary member Alessandro Grelli, for promoting me in Munich as well as in Utrecht and at Nikhef. Many thanks to Petra Zweckinger and Sigrid Weichs for all their help dealing with the jungle of bureaucracy and to Ralf Lang for his technical support.

Thank you for all the corrections I received from Andi, Laura, Oton, Piotr, Stefan and Vale, which have given this work the final touch.

My appreciation goes out to my mother, brother and family, but also to my friends for their support and believe, as well as the good times that we had together.

Above all, I would like to acknowledge my better half, my wonderful wife Margot, for her love, her unconditional moral support, unbiased input and patience. Thank you moving to Germany, so that we could live together and start our joint little project, I am looking forward to our time as three, taking our bakfiets to our new family home in Den Bosch.

"Men have forgotten this truth," said the fox. "But you must not forget it. You become responsible, forever, for what you have tamed. You are responsible for your rose"

Antoine de Saint Exupéry, The Little Prince

A. List of relevant publications

A.1. Relevant Publications

The author has contributed to the following publications, with the highlighted ones being subject of this work

- Mihaylov, D. L. and Mantovani Sarti, V. and Arnold, O. W. and Fabbietti, L. and Hohlweger, B. and Mathis, A. M., femtoscopic Correlation Analysis Tool using the Schrödinger equation (CATS) Eur. Phys. J.(2018) 78, 394
- **ALICE TPC Collaboration** collaboration, M. M. Aggarwalet al., Particle identification studies with a full-size 4-GEM prototype for the ALICE TPC upgrade, Nucl. Instrum. Meth. A903 (2018) 215
- **ALICE** collaboration, S.Acharya et al., First Observation of an Attractive Interaction between a Proton and a Cascade Baryon, Phys. Rev. Lett. 123 (2019) 112002
- **ALICE** collaboration, S.Acharya et al., Search for a common baryon source in high-multiplicity pp collisions at the LHC, Phys. Lett. B 811 (2020), 135849
- **ALICE** collaboration, S.Acharya et al., Unveiling the strong interaction among hadrons at the LHC, Nature 588 (2020), 232–238

A.2. Additional Contributions

- Extraction of the experimental p–Λ and Λ–Λ correlation functions from minimum bias p–Pb collisions at $\sqrt{s_{\mathrm{NN}}} = 5.02$ TeV
- ALICE Service task: GEM foil glueing for the TPC upgrade
- Co-development and maintenance of the `FemtoDream` analysis and `GentleFemto` post-processing framework for Femtoscopy analysis in ALICE
- Implementation and validation of `NanoAOD` data for femtoscopic analysis

A.3. Supervised Thesis

- L. Nyffeneger, Production of antiparticles in p-Pb collisions at $\sqrt{s_{\mathrm{NN}}}$=5.02 TeV measured with ALICE at the LHC, Bachelor Thesis, Technical University of Munich, 2017
- P. Voigt, Analyzing Ω-hyperons measured with ALICE at the LHC, Technical University of Munich, 2018

B. Supplementary material: Plots

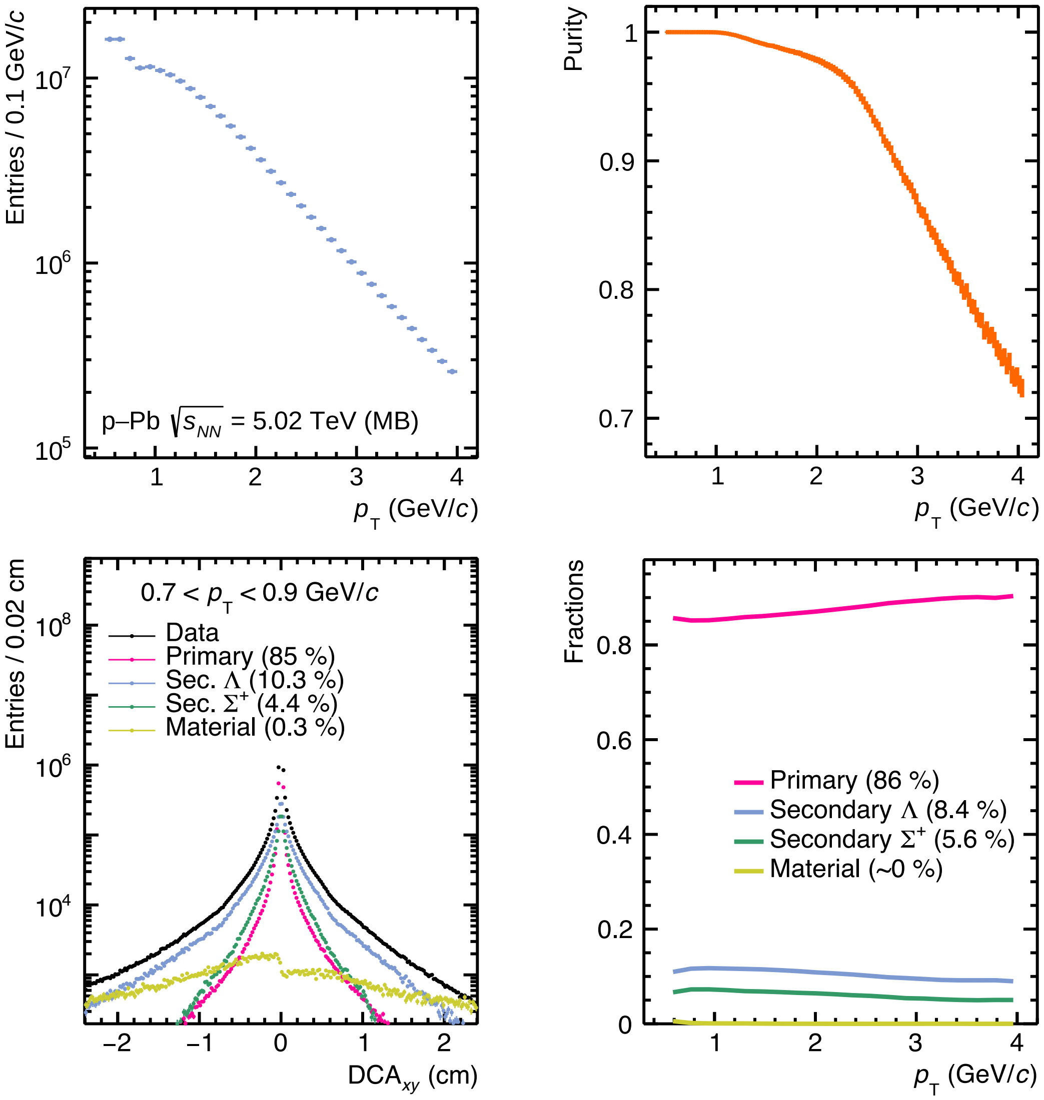

Figure B.1.: (Top left) p_T distribution and (top right) purity of the proton sample. (Bottom left) Exemplary fit of of the DCA_{xy} distribution in one p_T interval with MC generated templates. (Bottom right) Decomposition of the proton sample over the whole p_T range. Results are shown for the analysis of p–Pb collisions at $\sqrt{s_{\mathrm{NN}}} = 5.02$ TeV.

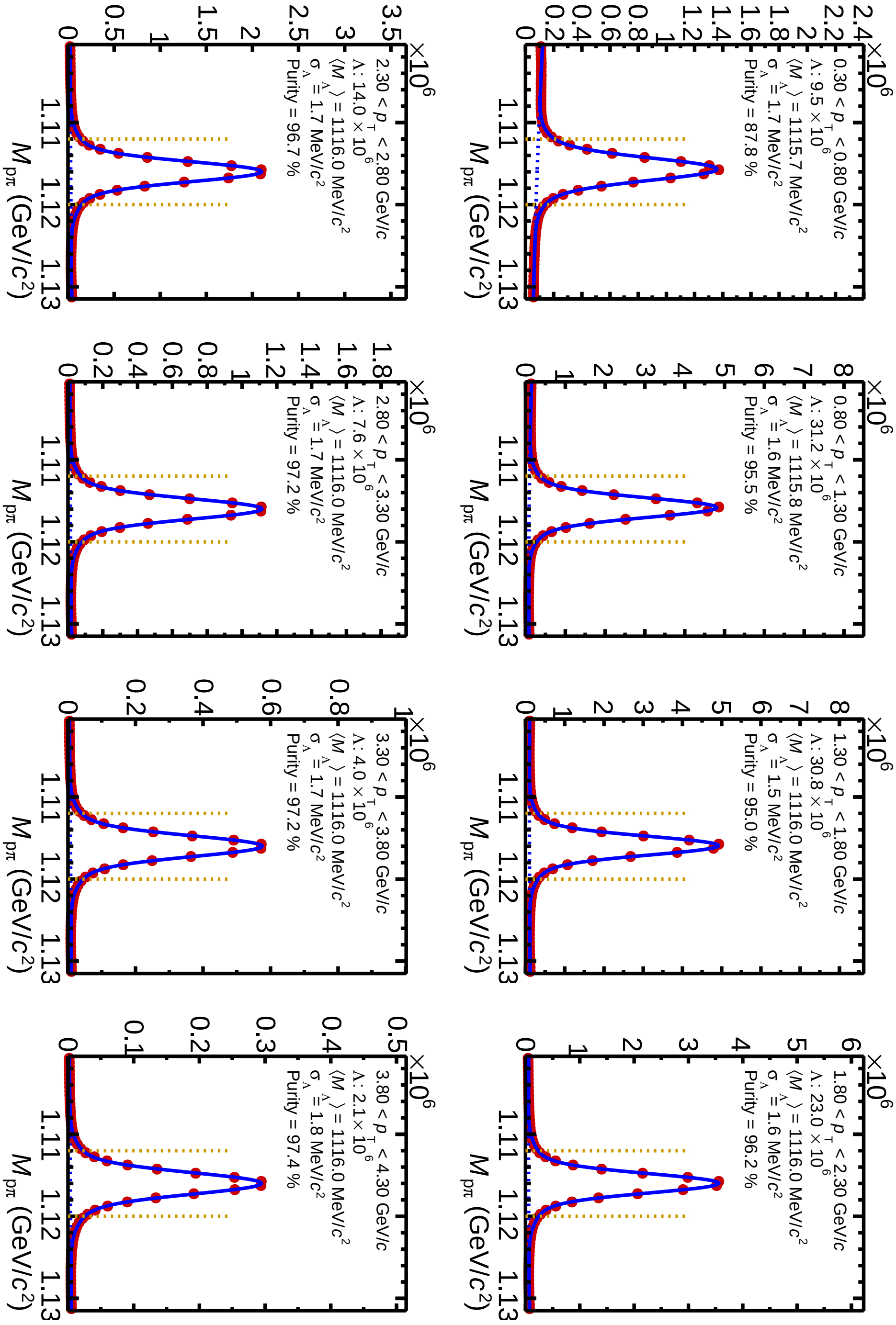

Figure B.2.: Invariant mass distribution close to the mass of the Λ reconstructed from proton and π^- pairs in high-multiplicity triggered pp collisions at $\sqrt{s} = 13$ TeV. Details of the selection are found in Sec. 3.6.4.

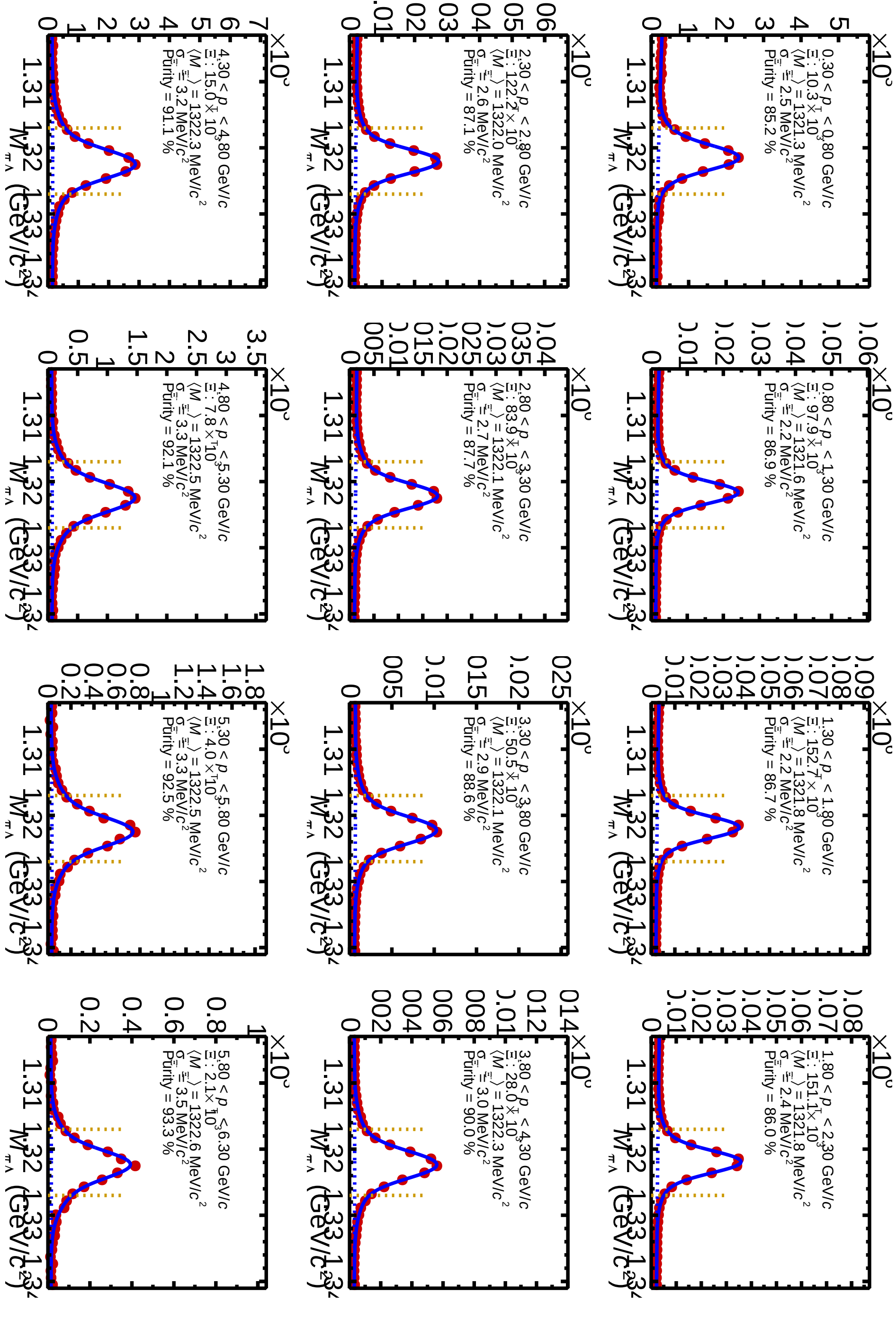

Figure B.3.: Invariant mass distribution close to the mass of the Ξ^- reconstructed from Λ and π^- pairs in minimum-bias triggered p–Pb collisions at $\sqrt{s_{\mathrm{NN}}} = 5.02$ TeV. Details of the selection are found in Sec. 3.6.5.

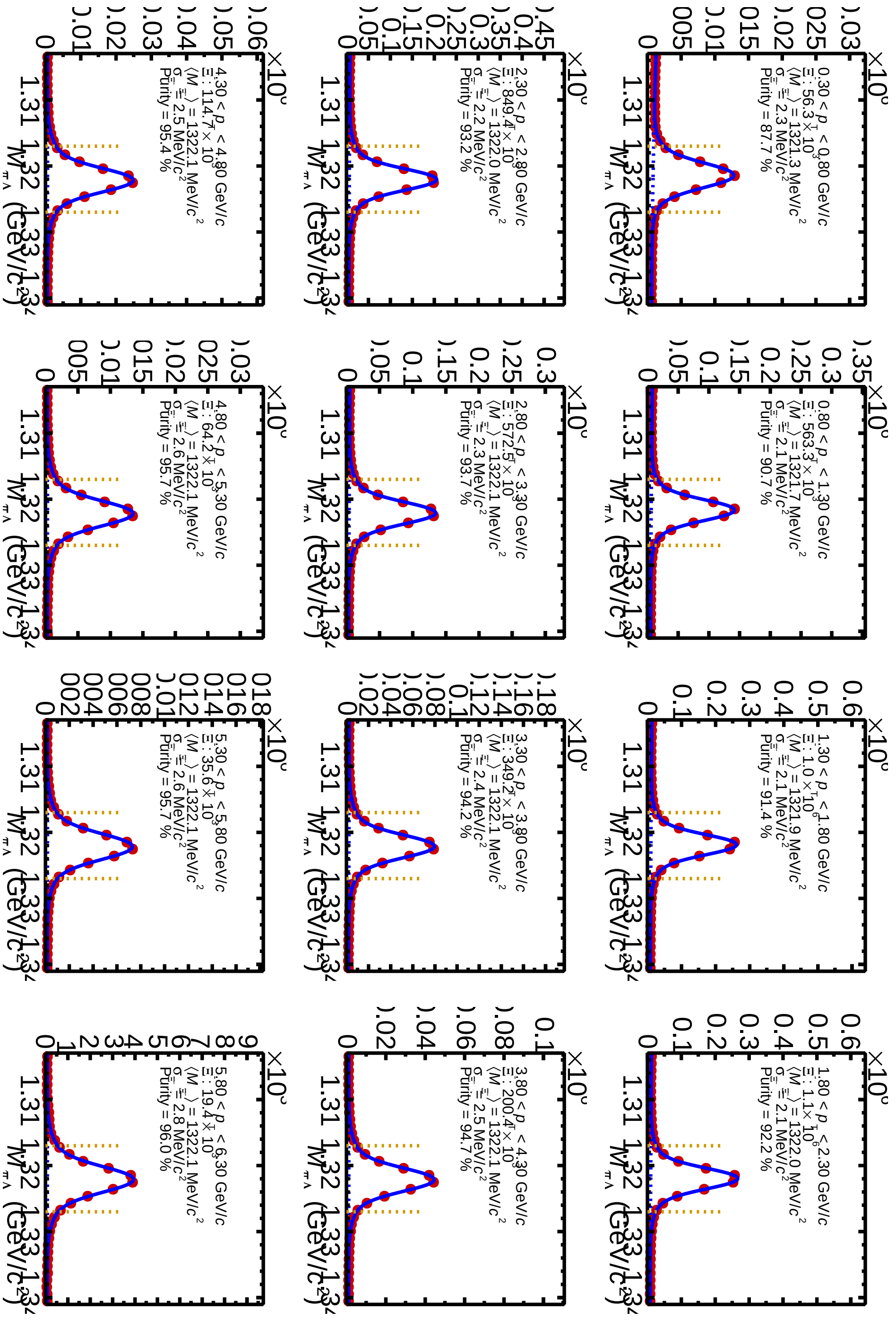

Figure B.4.: Invariant mass distribution close to the mass of the Ξ^- reconstructed from Λ and π^- pairs in high-multiplicity triggered pp collisions at $\sqrt{s} = 13$ TeV. Details of the selection are found in Sec. 3.6.5.

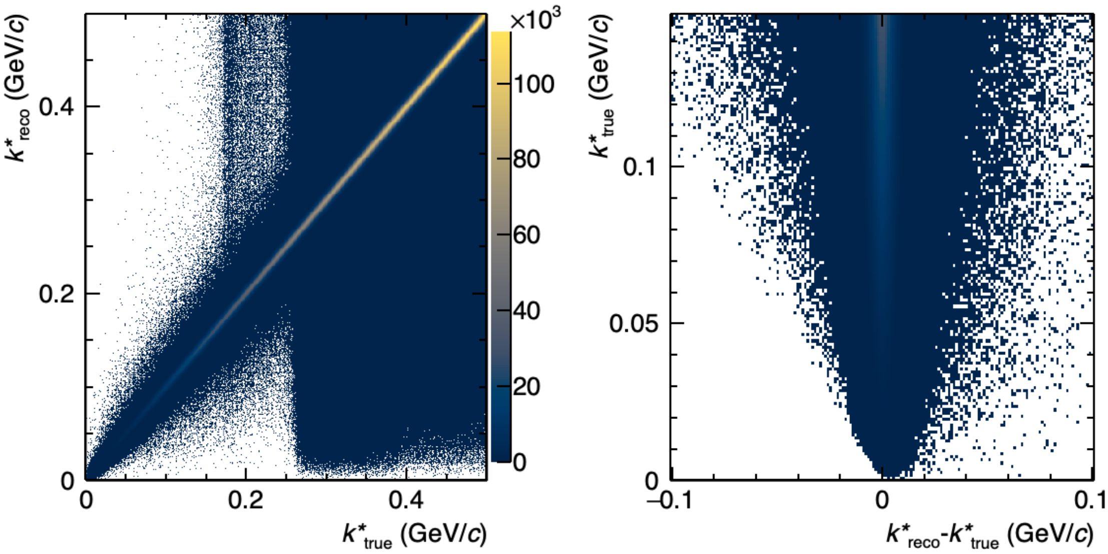

Figure B.5.: Correlation between the true relative momentum (k^*_{true}) and reconstructed relative momentum (k^*_{reco}) of p–Λ pairs. Evaluated with MC events anchored to HM triggered pp collisions at $\sqrt{s} = 13$ TeV.

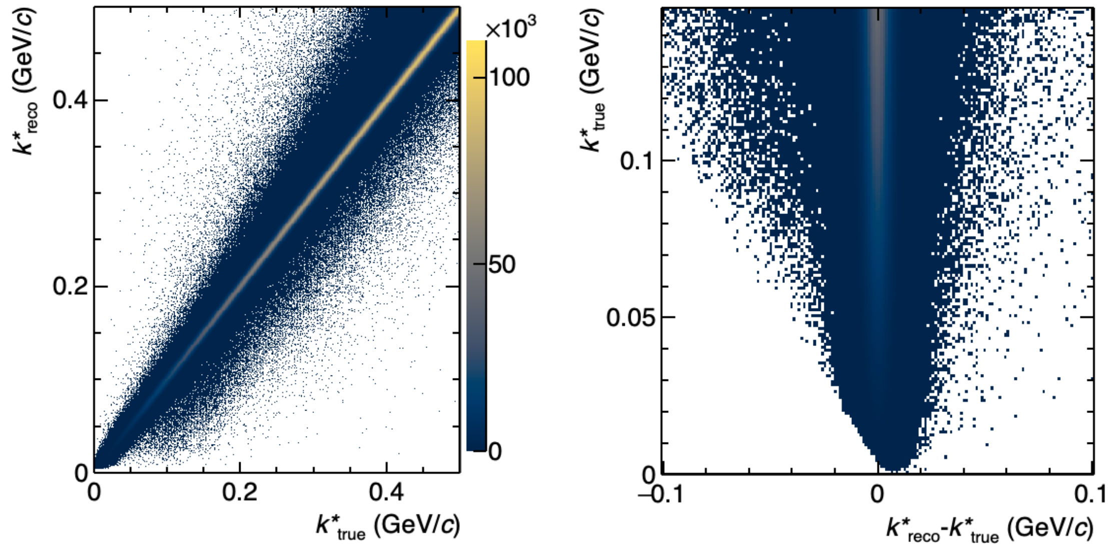

Figure B.6.: Correlation between the true relative momentum (k^*_{true}) and reconstructed relative momentum (k^*_{reco}) of p–p pairs. Evaluated with MC events anchored to MB triggered p–Pb collisions at $\sqrt{s_{\mathrm{NN}}} = 5.02$ TeV.

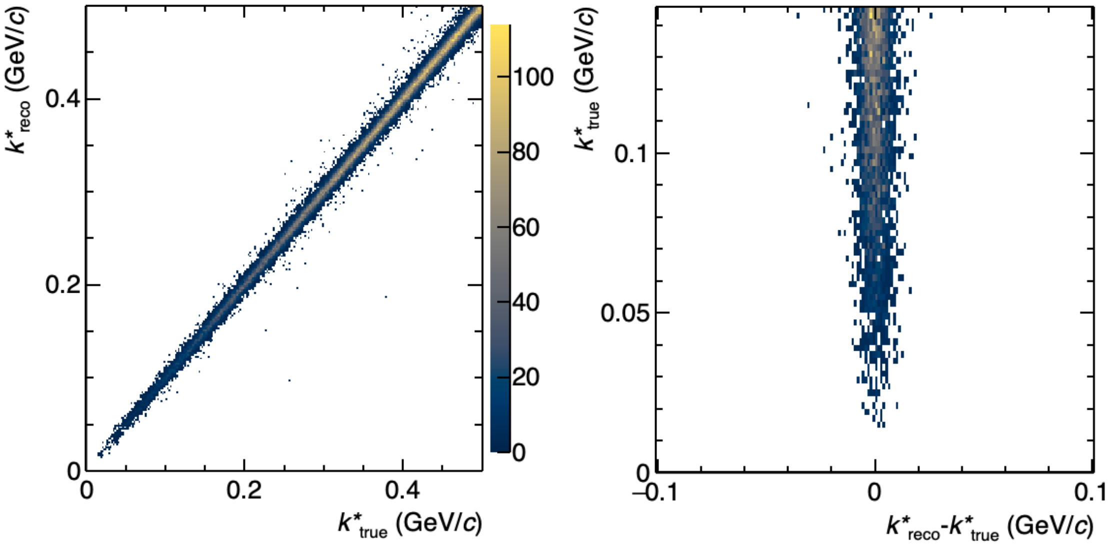

Figure B.7.: Correlation between the true relative momentum (k^*_{true}) and reconstructed relative momentum (k^*_{reco}) of p–Ξ^- pairs. Evaluated with MC events anchored to MB triggered p–Pb collisions at $\sqrt{s_{\mathrm{NN}}} = 5.02$ TeV.

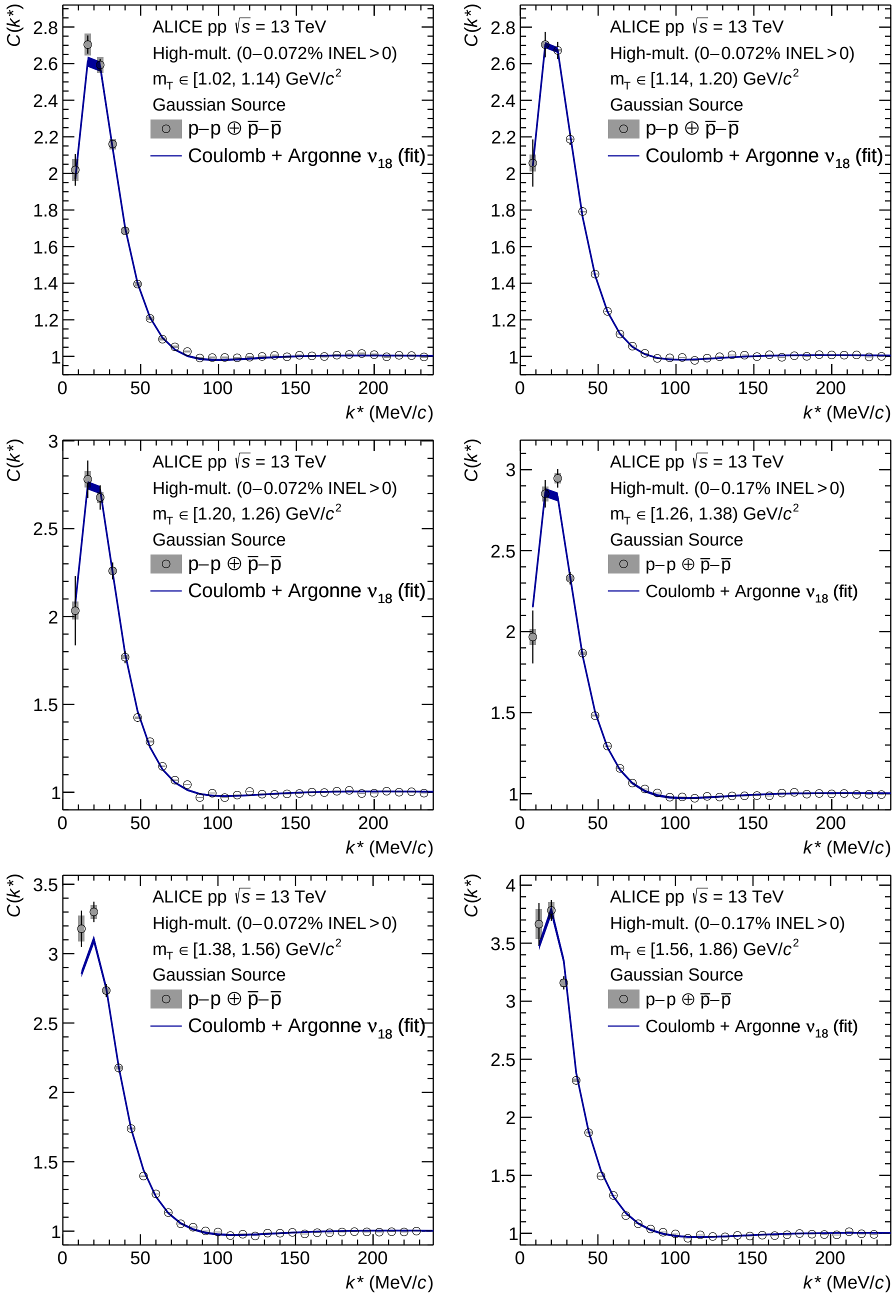

Figure B.8.: The correlation function of p–p as a function of k^* in the different m_T intervals. Statistical (bars) and systematic (boxes) uncertainties are shown separately. The filled bands depict 1σ uncertainties of the fits with $C_{\text{fit}}(k^*)$ and are obtained by using the Argonne v_{18} [59] (blue) potential.

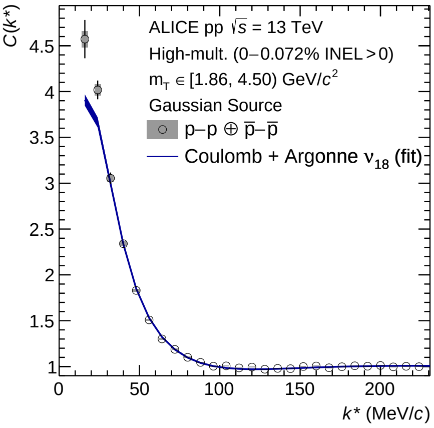

Figure B.9.: See Fig. B.8

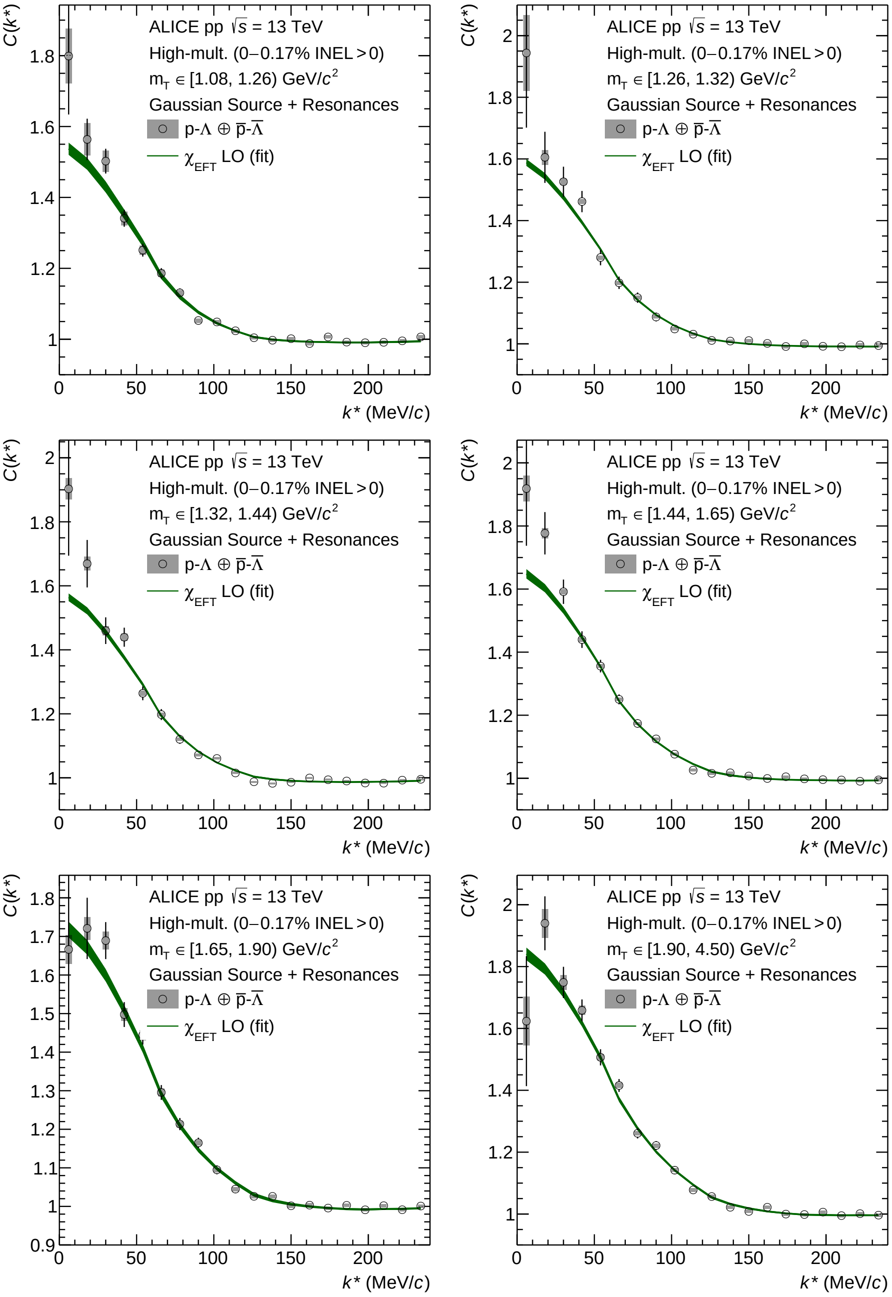

Figure B.10.: The correlation function of p–Λ as a function of k^* in the different m_T intervals. Statistical (bars) and systematic (boxes) uncertainties are shown separately. The filled bands depict 1σ uncertainties of the fits with the wave function of χEFT LO [66] (green) calculations.

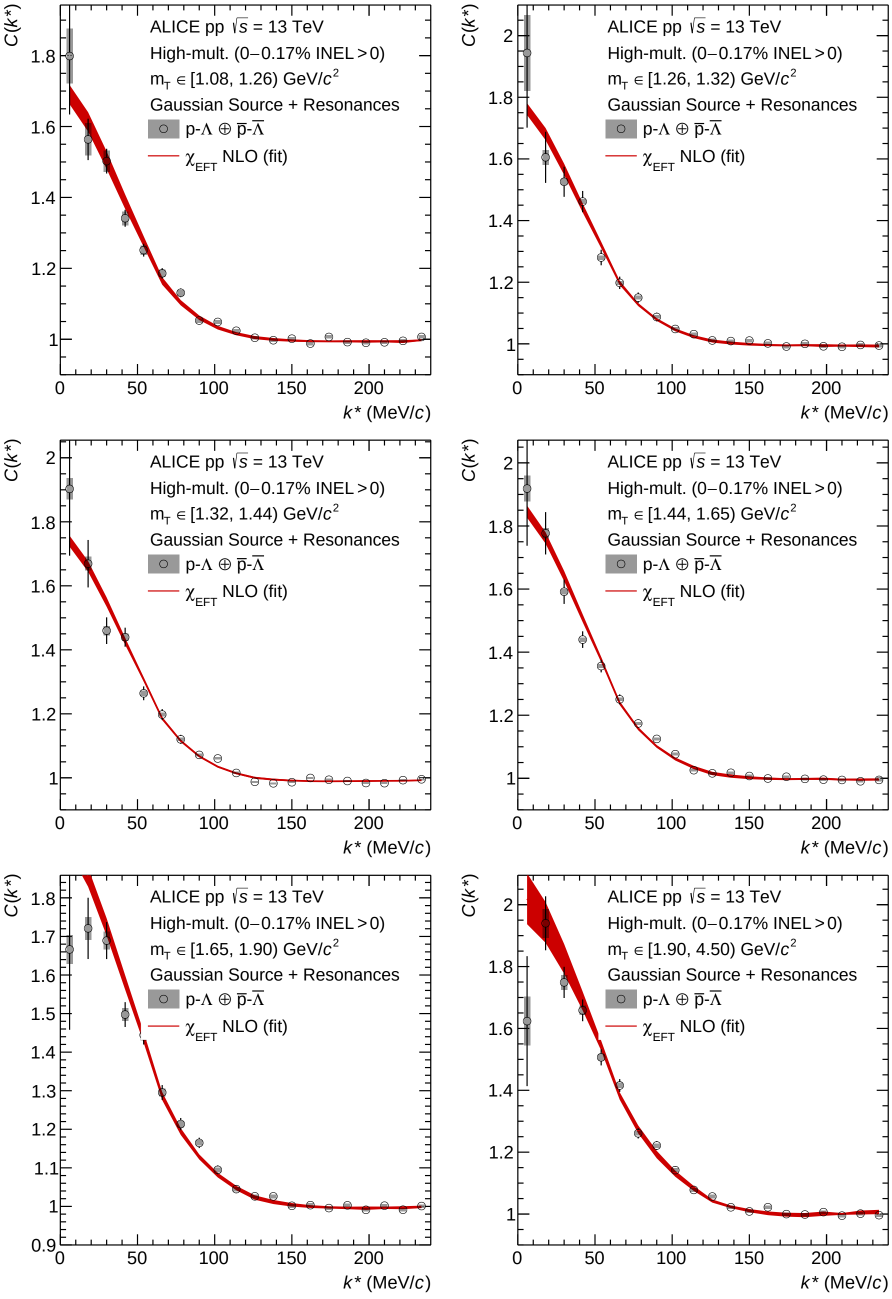

Figure B.11.: The correlation function of p–Λ as a function of k^* in the different m_T intervals. Statistical (bars) and systematic (boxes) uncertainties are shown separately. The filled bands depict 1σ uncertainties of the fits with the wave function of χEFT NLO [65] (red) calculations.

List of Figures

List of Tables

Bibliography

1. Griffiths, D. *Introduction to elementary particles* (2008) (cit. on pp. 1–3).
2. Tanabashi, M. *et al.* Review of Particle Physics. *Phys. Rev.* **D98,** 030001 (Aug. 2018) (cit. on pp. 1–3, 27, 51, 54, 55, 60, 62, 65, 68, 89).
3. Roberts, C. D. Three Lectures on Hadron Physics. *Journal of Physics: Conference Series* **706,** 022003 (2016) (cit. on pp. 2, 3).
4. Higgs, P. Broken symmetries, massless particles and gauge fields. *Physics Letters* **12,** 132–133 (1964) (cit. on p. 3).
5. Higgs, P. W. Broken Symmetries and the Masses of Gauge Bosons. *Phys. Rev. Lett.* **13,** 508–509 (1964) (cit. on p. 3).
6. Englert, F. & Brout, R. Broken Symmetry and the Mass of Gauge Vector Mesons. *Phys. Rev. Lett.* **13,** 321–323 (1964) (cit. on p. 3).
7. Machleidt, R. & Entem, D. Chiral effective field theory and nuclear forces. *Physics Reports* **503,** 1–75 (2011) (cit. on pp. 3–5, 10).
8. Rapp, R., Wambach, J. & van Hees, H. *The Chiral Restoration Transition of QCD and Low Mass Dileptons: Datasheet from Landolt-Börnstein - Group I Elementary Particles, Nuclei and Atoms Volume 23* Copyright 2010 Springer-Verlag Berlin Heidelberg (cit. on p. 3).
9. Epelbaum, E., Hammer, H.-W. & Meißner, U.-G. Modern theory of nuclear forces. *Rev. Mod. Phys.* **81,** 1773–1825 (2009) (cit. on pp. 3, 4).
10. Mathis, A. M. First Measurement of the Proton-Σ^0 Interaction via the Femtoscopy Method Dissertation (Technische Universität München, München, 2020) (cit. on pp. 3, 83, 99, 105).
11. Oakes, R. J. Baryon-Baryon Interactions and the Eightfold Way. *Phys. Rev.* **131,** 2239–2241 (1963) (cit. on p. 4).
12. DeSouza, P. D., Snow, G. A. & Meshkov, S. *S*-Wave Hyperon-Nucleon Interactions and SU_3 Symmetry. *Phys. Rev.* **135,** B565–B567 (1964) (cit. on p. 4).
13. Wagman, M. L. *et al.* Baryon-baryon interactions and spin-flavor symmetry from lattice quantum chromodynamics. *Phys. Rev.* **D 96,** 114510 (2017) (cit. on pp. 4, 5).
14. Nagels, M. M., Rijken, T. A. & Yamamoto, Y. Extended-soft-core baryon-baryon model ESC16. II. Hyperon-nucleon interactions. *Phys. Rev.* **C99,** 044003 (2019) (cit. on pp. 4, 36, 76, 83, 101, 104).

15. Ishii, N., Aoki, S. & Hatsuda, T. Nuclear Force from Lattice QCD. *Phys. Rev. Lett.* **99,** 022001 (2007) (cit. on pp. 4, 5).
16. Hatsuda, T. private communication. May 21, 2020 (cit. on pp. 5, 102).
17. Orginos, K. *et al.* Two nucleon systems at $m_\pi \sim 450$ MeV from lattice QCD. *Phys. Rev.* **D92,** 114512 (2015) (cit. on p. 5).
18. Hatsuda, T. Lattice quantum chromodynamics and baryon-baryon interactions. *Front. Phys. (Beijing)* **13,** 132105 (2018) (cit. on p. 5).
19. Aoki, S. & Doi, T. Lattice QCD and Baryon-Baryon Interactions: HAL QCD Method. *Frontiers in Physics* **8,** 307 (2020) (cit. on pp. 6, 11).
20. Stoks, V. G. J., Klomp, R. A. M., Rentmeester, M. C. M. & de Swart, J. J. Partial-wave analysis of all nucleon-nucleon scattering data below 350 MeV. *Phys. Rev.* **C48,** 792–815 (1993) (cit. on pp. 6, 80).
21. Alexander, G. *et al.* Study of the lambda-n system in low-energy lambda-p elastic scattering. *Phys. Rev.* **173,** 1452–1460 (1968) (cit. on p. 6).
22. Sechi-Zorn, B., Kehoe, B., Twitty, J. & Burnstein, R. Low-energy lambda-proton elastic scattering. *Phys. Rev.* **175,** 1735–1740 (1968) (cit. on p. 6).
23. Acharya, S. *et al.* p-p, p-Λ and Λ-Λ correlations studied via femtoscopy in pp reactions at $\sqrt{s}$ = 7 TeV. *Phys. Rev.* **C99,** 024001 (2019) (cit. on pp. 6, 10, 23, 25–27, 59, 62, 78, 79, 84, 86, 98).
24. Mihaylov, D. L. Analysis techniques for femtoscopy and correlation studies in small collision systems and their applications to the investigation of p–Λ and Λ–Λ interactions with ALICE in preparation. Dissertation (Technische Universität München, München, 2020) (cit. on pp. 6, 27, 31, 84).
25. Acharya, S. *et al.* Investigation of the p-Σ^0 interaction via femtoscopy in pp collisions. *Phys. Lett.* **B805,** 135419 (2020) (cit. on pp. 6, 10, 58, 83, 100).
26. Hashimoto, O. & Tamura, H. Spectroscopy of Λ hypernuclei. *Prog. Part. Nucl. Phys.* **57,** 564–653 (2006) (cit. on pp. 6, 80).
27. Gal, A., Hungerford, E. V. & Millener, D. J. Strangeness in nuclear physics. *Rev. Mod. Phys.* **88,** 035004 (3 2016) (cit. on p. 6).
28. Nagae, T. *et al.* Observation of a ${}^4_\Sigma$He Bound State in the ${}^4He(K^-, \pi^-)$ Reaction at $600 MeV/c$. *Phys. Rev. Lett.* **80,** 1605–1609 (8 1998) (cit. on p. 6).
29. Hayano, R. *et al.* Evidence for a bound state of the ${}^4_\Sigma$He hypernucleus. *Physics Letters* **B231,** 355–358 (1989) (cit. on p. 6).
30. Noumi, H. *et al.* Sigma-Nucleus Potential in $A = 28$. *Phys. Rev. Lett.* **89,** 072301 (7 2002) (cit. on p. 6).
31. Saha, P. K. *et al.* Σ-nucleus potential studied with the (π^-, K^+) reaction on medium-to-heavy nuclear targets. *Phys. Rev.* **C 70,** 044613 (4 2004) (cit. on p. 6).

32. Jaffe, R. L. Perhaps a Stable Dihyperon. *Phys. Rev. Lett.* **38,** 195–198 (1977) (cit. on p. 7).

33. Adam, J. *et al.* Search for weakly decaying $\overline{\Lambda n}$ and $\Lambda\Lambda$ exotic bound states in central Pb-Pb collisions at $\sqrt{s_{\mathrm{NN}}}$ = 2.76 TeV. *Phys. Lett.* **B752,** 267–277. arXiv: `1506.07499 [nucl-ex]` (2016) (cit. on p. 7).

34. Kim, B. H. *et al.* Search for an H-Dibaryon with a Mass near $2m_\Lambda$ in $\Upsilon(1S)$ and $\Upsilon(2S)$ Decays. *Phys. Rev. Lett.* **110,** 222002 (2013) (cit. on p. 7).

35. Yoon, C. J. *et al.* Search for the H-dibaryon resonance in ^{12}C $(K^-, K^+\Lambda\Lambda X)$. *Phys. Rev.* **C75,** 022201 (2007) (cit. on p. 7).

36. Iijima, T. *et al.* (K-, K+) reaction on nuclear targets at PK = 1.65 G. *Nuclear Physics* **A 546,** 588–606 (1992) (cit. on p. 7).

37. Adamczyk, L. *et al.* $\Lambda\Lambda$ Correlation Function in Au + Au Collisions at $\sqrt{s_{NN}} =$ 200 GeV. *Phys. Rev. Lett.* **114,** 022301 (2015) (cit. on p. 7).

38. Morita, K., Furumoto, T. & Ohnishi, A. $\Lambda\Lambda$ interaction from relativistic heavy-ion collisions. *Phys. Rev.* **C91,** 024916 (2015) (cit. on p. 7).

39. Acharya, S. *et al.* Study of the Λ-Λ interaction with femtoscopy correlations in pp and p-Pb collisions at the LHC. *Phys. Lett.* **B797,** 134822 (2019) (cit. on pp. 7, 11, 56, 103).

40. Takahashi, H. *et al.* Observation of a $^{6}_{\Lambda\Lambda}He$ Double Hypernucleus. *Phys. Rev. Lett.* **87,** 212502 (2001) (cit. on p. 7).

41. Nakazawa, K. Double-Lambda hypernuclei via the Ξ^- hyperon capture at rest reaction in a hybrid emulsion. *Nucl. Phys.* **A 835,** 207–214 (2010) (cit. on p. 7).

42. Dalmeijer, R., De Groot, A., Kluyver, J., De Lijser, E. & Tiecke, H. M. The observation of two xi- p elastic-scattering events. *Lett. Nuovo Cim.* **4S1,** 373–376 (1970) (cit. on pp. 7, 8).

43. Charlton, G. *et al.* Hyperon-proton interactions between 0.5 and 4.0 GeV/c. *Physics Letters* **B 32,** 720–722 (1970) (cit. on pp. 7, 8).

44. Muller, R. Observation of cascade hyperon interactions. *Physics Letters* **B 38,** 123–124 (1972) (cit. on pp. 7, 8).

45. Experimental study of Λp and Ξ0p interactions in the range 1 – 10 GeV/c. *Nuclear Physics* **B125,** 29–51 (1977) (cit. on pp. 7, 8).

46. Aoki, S. *et al.* Quasifree p(K-, K+)Ξ^- reaction in nuclear emulsion. *Nuclear Physics* **A644,** 365–385 (1998) (cit. on pp. 7, 8).

47. Ahn, J. *et al.* Scalar and vector meson production and two-step processes in the (K-, K+) reaction on 12C. *Nuclear Physics* **A 625,** 231–250 (1997) (cit. on pp. 7, 8).

48. Ahn, J. *et al.* Measurement of the Ξ-p scattering cross sections at low energy. *Physics Letters* **B 633,** 214–218 (2006) (cit. on pp. 7, 8).

49. Tamagawa, T. *et al.* The ΞN interaction in quasi-free Ξ^- production. *Nuclear Physics* **A691,** 234–237 (2001) (cit. on pp. 7, 8).
50. d'Agostini, G. *et al.* Search for strange (S = -2) dibaryons in the reaction K^- + d $\rightarrow$ K^+ + MM at 1.4 GeV/c. *Nuclear Physics* **B 209,** 1–15 (1982) (cit. on pp. 7, 96).
51. Goyal, D. P., Misra, J. N. & Sodhi, A. V. Observation of enhancement in $\Xi^- p$ invariant-mass spectrum. *Phys. Rev.* **D 21,** 607–610 (1980) (cit. on p. 7).
52. Godbersen, M. Recent results from WA89 in the double Λ and Σ^- proton channels. *AIP Conf. Proc.* **338** (ed Seestrom, S.) 533–537 (2008) (cit. on p. 7).
53. Haidenbauer, J., Meißner, U.-G. & Petschauer, S. Strangeness S=-2 baryon–baryon interaction at next-to-leading order in chiral effective field theory. *Nuclear Physics* **A 954,** 273–293 (2016) (cit. on pp. 7, 10, 11).
54. Khaustov, P. *et al.* Evidence of Ξ hypernuclear production in the $^{12}\mathrm{C}(K^-, K^+)^{12}_{\Xi}\mathrm{Be}$ reaction. *Phys. Rev.* **C 61,** 054603 (2000) (cit. on pp. 7, 9).
55. Kohno, M. & Hashimoto, S. Ξ^--Nucleus Potential and (K-, K+) Inclusive Spectrum at Ξ^- Production Threshold Region. *Progress of Theoretical Physics* **123,** 157–167 (2010) (cit. on p. 9).
56. Nakazawa, K. *et al.* The first evidence of a deeply bound state of Ξ^-–^{14}N system. *Progress of Theoretical and Experimental Physics* **2015** (Mar. 2015) (cit. on p. 9).
57. NAGAE, P. T. *Status and future perspectives of hypernuclear physics* Hadron2019. 2019. `https://indico.ihep.ac.cn/event/9119/session/2/contribution/198/material/slides/0.pdf` (cit. on p. 10).
58. Hayakawa, S. H. Study of Ξ-nucleus interaction by measurement of twin hypernuclei with hybrid emulsion method PhD thesis (Osaka University, 2019). `https://doi.org/10.18910/72648` (cit. on p. 10).
59. Wiringa, R. B., Stoks, V. G. J. & Schiavilla, R. Accurate nucleon-nucleon potential with charge-independence breaking. *Phys. Rev.* **C51,** 38–51 (1995) (cit. on pp. 10, 33–35, 80, 91, 134).
60. Coraggio, L. *et al.* Nuclear-matter equation of state with consistent two- and three-body perturbative chiral interactions. *Phys. Rev.* **C89,** 044321 (2014) (cit. on p. 10).
61. Tews, I., Krüger, T., Hebeler, K. & Schwenk, A. Neutron Matter at Next-to-Next-to-Next-to-Leading Order in Chiral Effective Field Theory. *Phys. Rev. Lett.* **110,** 032504 (2013) (cit. on p. 10).
62. Drischler, C., Carbone, A., Hebeler, K. & Schwenk, A. Neutron matter from chiral two- and three-nucleon calculations up to N^{3}LO. *Phys. Rev.* **C 94,** 054307 (5 2016) (cit. on p. 10).
63. Hebeler, K., Lattimer, J. M., Pethick, C. J. & Schwenk, A. Equation of State and Neutron Star Properties Constrained by Nuclear Physics Observation. *The Astrophysical Journal* **773,** 11 (2013) (cit. on pp. 10, 15, 16).

64. Haidenbauer, J. *et al.* Hyperon–nucleon interaction at next-to-leading order in chiral effective field theory. *Nuclear Physics* **A915,** 24–58 (2013) (cit. on pp. 10, 11).
65. Haidenbauer, J., Meißner, U.-G. & Nogga, A. Hyperon-nucleon interaction within chiral effective field theory revisited. *Eur. Phys. J.* **A56,** 91 (2020) (cit. on pp. 10, 36, 80–82, 84, 89, 91, 103, 137).
66. Polinder, H., Haidenbauer, J. & Meißner, U.-G. Hyperon–nucleon interactions—a chiral effective field theory approach. *Nucl. Phys.* **A779,** 244–266 (2006) (cit. on pp. 10, 80–82, 84, 89, 91, 136).
67. Petschauer, S., Haidenbauer, J., Kaiser, N., Meißner, U.-G. & Weise, W. Hyperon-Nuclear Interactions From SU(3) Chiral Effective Field Theory. *Frontiers in Physics* **8,** 12 (2020) (cit. on p. 10).
68. Gerstung, D., Kaiser, N. & Weise, W. Hyperon–nucleon three-body forces and strangeness in neutron stars. *Eur. Phys. J.* **A 56,** 175 (2020) (cit. on pp. 10, 13, 17).
69. Haidenbauer, J. & Meißner, U.-G. In-medium properties of a ΞN interaction derived from chiral effective field theory. *Eur. Phys. J.* **A55,** 23 (2019) (cit. on pp. 10, 12, 13).
70. Doi, Takumi *et al.* Baryon interactions from lattice QCD with physical quark masses - Nuclear forces and $\Xi\Xi$ forces -. *EPJ Web Conf.* **175,** 05009 (2018) (cit. on p. 11).
71. Sasaki, K. *et al.* $\Lambda\Lambda$ and NΞ interactions from Lattice QCD near the physical point. *Nuclear Physics* **A 998,** 121737 (2020) (cit. on pp. 11, 12, 83, 93, 101–104, 109, 113).
72. Hiyama, E., Kamimura, M., Motoba, T., Yamada, T. & Yamamoto, Y. Four-body cluster structure of $A = 7$–10 double-Λ hypernuclei. *Phys. Rev.* **C 66,** 024007 (2002) (cit. on p. 11).
73. Faddeev–Yakubovsky calculations for light $\Lambda\Lambda$ hypernuclei. *Nuclear Physics* **A707,** 491–509 (2002) (cit. on p. 11).
74. Kohno, M. Ξ hyperons in the nuclear medium described by chiral NLO interactions. *Phys. Rev.* **C 100,** 024313 (2019) (cit. on p. 12).
75. Inoue, T. Strange nuclear physics from QCD on lattice. *AIP Conference Proceedings* **2130,** 020002 (2019) (cit. on pp. 12, 13, 115, 116).
76. Nemura, H. Hyperon-nucleon interaction from lattice QCD at (mπ, mK) $\approx$ (146, 525) MeV. *AIP Conference Proceedings* **2130,** 040005 (2019) (cit. on p. 12).
77. Acharya, S. *et al.* Unveiling the strong interaction among hadrons at the LHC. arXiv: `2005.11495 [nucl-ex]` (2020) (cit. on pp. 13, 80, 93, 110, 115).
78. Iritani, T. *et al.* NΩ dibaryon from lattice QCD near the physical point. *Physics Letters* **B 792,** 284–289 (2019) (cit. on p. 13).
79. Gongyo, S. *et al.* Most Strange Dibaryon from Lattice QCD. *Phys. Rev. Lett.* **120,** 212001 (2018) (cit. on p. 13).

80. Andronic, A., Braun-Munzinger, P., Redlich, K. & Stachel, J. Decoding the phase structure of QCD via particle production at high energy. *Nature* **561,** 321–330 (2018) (cit. on p. 14).
81. Danielewicz, P., Lacey, R. & Lynch, W. G. Determination of the Equation of State of Dense Matter. *Science* **298,** 1592–1596 (2002) (cit. on p. 14).
82. Schaffner-Bielich, J. *Compact Star Physics* (Cambridge University Press, 2020) (cit. on p. 14).
83. Lattimer, J. M. The Nuclear Equation of State and Neutron Star Masses. *Annual Review of Nuclear and Particle Science* **62,** 485–515 (2012) (cit. on p. 14).
84. Oppenheimer, J. R. & Volkoff, G. M. On Massive Neutron Cores. *Phys. Rev.* **55,** 374–381 (4 1939) (cit. on p. 14).
85. Tolman, R. C. Static Solutions of Einstein's Field Equations for Spheres of Fluid. *Phys. Rev.* **55,** 364–373 (4 1939) (cit. on p. 14).
86. Demorest, P., Pennucci, T., Ransom, S., Roberts, M. & Hessels, J. A two-solar-mass neutron star measured using Shapiro delay. *Nature* **467,** 1081–1083 (2010) (cit. on p. 14).
87. Antoniadis, J. *et al.* A Massive Pulsar in a Compact Relativistic Binary. *Science* **340** (2013) (cit. on p. 14).
88. Cromartie, H. T. *et al.* Relativistic Shapiro delay measurements of an extremely massive millisecond pulsar. *Nature Astron.* **4,** 72–76. eprint: `1904.06759` (2020) (cit. on p. 14).
89. Abbott, B. P. *et al.* GW170817: Observation of Gravitational Waves from a Binary Neutron Star Inspiral. *Phys. Rev. Lett.* **119,** 161101 (16 2017) (cit. on p. 14).
90. Abbott, B. P. *et al.* GW170817: Measurements of Neutron Star Radii and Equation of State. *Phys. Rev. Lett.* **121,** 161101 (2018) (cit. on p. 14).
91. Annala, E., Gorda, T., Kurkela, A. & Vuorinen, A. Gravitational-Wave Constraints on the Neutron-Star-Matter Equation of State. *Phys. Rev. Lett.* **120,** 172703 (2018) (cit. on p. 15).
92. Kurkela, A., Fraga, E. S., Schaffner-Bielich, J. & Vuorinen, A. Constraining Neutron Star Matter with Quantum Chormodynamics. *The Astrophysical Journal* **789,** 127 (2014) (cit. on p. 15).
93. Annala, E., Gorda, T., Kurkela, A., Nättilä, J. & Vuorinen, A. Evidence for quark-matter cores in massive neutron stars. *Nature Phys.* (2020) (cit. on p. 16).
94. Tolos, L. & Fabbietti, L. Strangeness in nuclei and neutron stars. *Progress in Particle and Nuclear Physics* **112,** 103770 (2020) (cit. on pp. 16, 115).
95. Ambartsumyan, V. A. & Saakyan, G. S. The Degenerate Superdense Gas of Elementary Particles. *Soviet Astronomy* **4,** 187 (Oct. 1960) (cit. on p. 16).

96. Weissenborn, S., Chatterjee, D. & Schaffner-Bielich, J. Hyperons and massive neutron stars: the role of hyperon potentials. *Nucl. Phys.* **A881,** 62–77 (2012) (cit. on pp. 16–18, 116).
97. Tolos, L., Centelles, M. & Ramos, A. Equation of State for Nucleonic and Hyperonic Neutron Stars with Mass and Radius Constraints. *Astrophys. J.* **834,** 3 (2017) (cit. on pp. 16, 17).
98. Katayama, T. & Saito, K. Hyperons in neutron stars. *Physics Letters* **B 747,** 43–47 (2015) (cit. on pp. 16, 115).
99. Lonardoni, D., Lovato, A., Gandolfi, S. & Pederiva, F. Hyperon Puzzle: Hints from Quantum Monte Carlo Calculations. *Phys. Rev. Lett.* **114,** 092301 (2015) (cit. on pp. 16, 17).
100. Haidenbauer, J., Meißner, U.-G., Kaiser, N. & Weise, W. Lambda-nuclear interactions and hyperon puzzle in neutron stars. *Eur. Phys. J.* **A53,** 121 (2017) (cit. on p. 17).
101. Hanbury Brown, R. & Twiss, R. A Test of a new type of stellar interferometer on Sirius. *Nature* **178,** 1046–1048 (1956) (cit. on p. 19).
102. Goldhaber, G., Fowler, W. B., Goldhaber, S. & Hoang, T. Pion-pion correlations in antiproton annihilation events. *Phys. Rev. Lett.* **3,** 181–183 (1959) (cit. on p. 19).
103. Goldhaber, G., Goldhaber, S., Lee, W.-Y. & Pais, A. Influence of Bose-Einstein statistics on the anti-proton proton annihilation process. *Phys. Rev.* **120,** 300–312 (1960) (cit. on p. 19).
104. Lisa, M. A., Pratt, S., Soltz, R. & Wiedemann, U. Femtoscopy in relativistic heavy ion collisions. *Ann. Rev. Nucl. Part. Sci.* **55,** 357–402 (2005) (cit. on pp. 19, 21–23, 25, 71).
105. Heinz, U. & Jacak, B. V. Two-particle correlations in relativistic heavy-ion collisions. *Ann. Rev. Nucl. Part. Sci.* **49,** 529–579 (1999) (cit. on p. 19).
106. Morita, K. *et al.* Probing $\Omega\Omega$ and $p\Omega$ dibaryons with femtoscopic correlations in relativistic heavy-ion collisions. *Phys. Rev.* **C101,** 015201 (2020) (cit. on p. 21).
107. Arnold, O. W. Study of the hyperon-nucleon interaction via femtoscopy in elementary systems with HADES and ALICE Dissertation (Technische Universität München, München, 2017) (cit. on pp. 21, 22, 62, 78, 98).
108. Pratt, S. Pion Interferometry for Exploding Sources. *Phys. Rev. Lett.* **53,** 1219–1221 (1984) (cit. on pp. 21, 33, 78).
109. Lednicky, R. Finite-size effects on two-particle production in continuous and discrete spectrum. *Phys. Part. Nucl.* **40,** 307–352 (2009) (cit. on p. 21).
110. Lednicky, R. Correlation femtoscopy of multiparticle processes. *Phys. Atom. Nucl.* **67,** 72–82 (2004) (cit. on p. 21).

111. Koonin, S. E. Proton pictures of high-energy nuclear collisions. *Physics Letters* **B70,** 43–47 (1977) (cit. on pp. 22, 33).

112. Lednicky, R. & Lyuboshits, V. Final State Interaction Effect on Pairing Correlations Between Particles with Small Relative Momenta. *Sov. J. Nucl. Phys.* **35,** 770 (1982) (cit. on pp. 22, 31).

113. Aamodt, K. *et al.* Two-pion Bose-Einstein correlations in central Pb-Pb collisions at $\sqrt{s_{NN}} = 2.76$ TeV. *Phys. Lett.* **B696,** 328–337 (2011) (cit. on p. 23).

114. Aamodt, K. *et al.* Femtoscopy of pp collisions at $\sqrt{s} = 0.9$ and 7 TeV at the LHC with two-pion Bose-Einstein correlations. *Phys. Rev.* **D84,** 112004 (2011) (cit. on pp. 23, 78, 98).

115. Adam, J. *et al.* Two-pion femtoscopy in p-Pb collisions at $\sqrt{s_{\mathrm{NN}}} = 5.02$ TeV. *Phys. Rev.* **C91,** 034906 (2015) (cit. on p. 23).

116. Acharya, S. *et al.* Kaon femtoscopy in Pb-Pb collisions at $\sqrt{s_{\mathrm{NN}}}$ = 2.76 TeV. *Phys. Rev.* **C96,** 064613 (2017) (cit. on p. 23).

117. Adam, J. *et al.* One-dimensional pion, kaon, and proton femtoscopy in Pb-Pb collisions at $\sqrt{s_{\mathrm{NN}}}$ =2.76 TeV. *Phys. Rev.* **C92,** 054908 (2015) (cit. on pp. 23, 25, 30, 56, 86).

118. Acharya, S. *et al.* One-dimensional charged kaon femtoscopy in p-Pb collisions at $\sqrt{s_{\mathrm{NN}}}$ = 5.02 TeV. *Phys. Rev.* **C100,** 024002 (2019) (cit. on pp. 23, 25, 86–88).

119. Mihaylov, D. Results using CATS `http://www.das.ktas.ph.tum.de/Discussions/FilesFemto/PresCATS0.3_04Apr2017.pdf`. Accessed: 2020-08-20 (cit. on p. 23).

120. Mihaylov, D. L. *et al.* A femtoscopic Correlation Analysis Tool using the Schrödinger equation (CATS). *Eur. Phys. J.* **C78,** 394 (2018) (cit. on pp. 23, 31, 33, 80).

121. Akkelin, S. & Sinyukov, Y. The HBT interferometry of expanding sources. *Phys. Lett. B* **356,** 525–530 (1995) (cit. on p. 23).

122. Snellings, R. Elliptic flow: a brief review. *New Journal of Physics* **13,** 055008 (2011) (cit. on pp. 24, 25).

123. Snellings, R. Collective expansion at the LHC: selected ALICE anisotropic flow measurements. *Journal of Physics G: Nuclear and Particle Physics* **41,** 124007 (2014) (cit. on p. 24).

124. Akkelin, S. & Sinyukov, Y. The HBT-interferometry of expanding sources. *Physics Letters* **B356,** 525–530 (1995) (cit. on p. 25).

125. Stachel, J. & Reygers, K. Quark-GLuon Plasma Physics `https://www.physi.uni-heidelberg.de/~reygers/lectures/2019/qgp/qgp_lecture_ss2019.html`. Accessed: 2020-08-23 (cit. on p. 25).

126. Kisiel, A., Gałażyn, M. & Bożek, P. Pion, kaon, and proton femtoscopy in Pb–Pb collisions at $\sqrt{s_{\mathrm{NN}}}$=2.76 TeV modeled in (3+1)D hydrodynamics. *Phys. Rev.* **C90,** 064914 (2014) (cit. on p. 25).

127. Csorgo, T., Lorstad, B. & Zimanyi, J. Bose-Einstein correlations for systems with large halo. *Z. Phys.* **C71,** 491–497 (1996) (cit. on p. 25).

128. Bolz, J., Ornik, U., Plümer, M., Schlei, B. R. & Weiner, R. M. Resonance decays and partial coherence in Bose-Einstein correlations. *Phys. Rev.* **D47,** 3860–3870 (1993) (cit. on p. 25).

129. Sirunyan, A. M. *et al.* Bose-Einstein correlations in pp, pPb, and PbPb collisions at $\sqrt{s_{\mathrm{NN}}} = 0.9$–$7$ TeV. *Phys. Rev.* **C97,** 064912 (2018) (cit. on pp. 25, 86).

130. Aad, G. *et al.* Two-particle Bose–Einstein correlations in pp collisions at $\sqrt{s}$=0.9 and 7 TeV measured with the ATLAS detector. *Eur. Phys. J.* **C75,** 466 (2015) (cit. on pp. 25, 86).

131. Abelev, B. *et al.* Charged kaon femtoscopic correlations in pp collisions at $\sqrt{s} = 7$ TeV. *Phys. Rev.* **D87,** 052016 (2013) (cit. on p. 25).

132. Abelev, B. *et al.* $K^0_s - K^0_s$ correlations in pp collisions at $\sqrt{s} = 7$ TeV from the LHC ALICE experiment. *Phys. Lett.* **B717,** 151–161 (2012) (cit. on pp. 25, 86).

133. Sirunyan, A. M. *et al.* Bose-Einstein correlations of charged hadrons in proton-proton collisions at $\sqrt{s} = 13$ TeV. *JHEP* **03,** 014 (2020) (cit. on pp. 25, 86).

134. Wiedemann, U. A. & Heinz, U. W. Resonance contributions to HBT correlation radii. *Phys. Rev. C* **56,** 3265–3286 (1997) (cit. on p. 26).

135. Kisiel, A., Florkowski, W. & Broniowski, W. Femtoscopy in hydro-inspired models with resonances. *Phys. Rev. C* **73,** 064902 (2006) (cit. on p. 26).

136. Sinyukov, Y. M., Shapoval, V. M. & Naboka, V. Y. On m_T dependence of femtoscopy scales for meson and baryon pairs. *Nucl. Phys. A* **946,** 227–239 (2016) (cit. on p. 26).

137. Kisiel, A. Nonidentical-particle femtoscopy at $\sqrt{s_{\mathrm{NN}}} = 200$ GeV in hydrodynamics with statistical hadronization. *Phys. Rev.* **C81,** 064906 (2010) (cit. on p. 26).

138. Becattini, F., Castorina, P., Milov, A. & Satz, H. Predictions of hadron abundances in pp collisions at the LHC; The results on the amount of primordial protons and Λ's are private communications based on this work. *J. Phys. G* **38,** 025002 (2011) (cit. on p. 26).

139. Acharya, S. *et al.* Search for a common baryon source in high-multiplicity pp collisions at the LHC. *Phys. Lett.* **B811,** 135849 (2020) (cit. on pp. 27, 28, 71).

140. Pierog, T., Karpenko, I., Katzy, J. M., Yatsenko, E. & Werner, K. EPOS LHC: Test of collective hadronization with data measured at the CERN Large Hadron Collider. *Phys. Rev. C* **92,** 034906 (2015) (cit. on p. 29).

141. Sjöstrand, T. *et al.* An Introduction to PYTHIA 8.2. *Comput. Phys. Commun.* **191,** 159–177 (2015) (cit. on pp. 29, 57).

142. Sinyukov, Y., Lednicky, R., Akkelin, S., Pluta, J. & Erazmus, B. Coulomb corrections for interferometry analysis of expanding hadron systems. *Physics Letters* **B432,** 248–257 (1998) (cit. on p. 30).

143. Morita, K., Furumoto, T. & Ohnishi, A. $\Lambda\Lambda$ interaction from relativistic heavy-ion collisions. *Phys. Rev. C* **91,** 024916. arXiv: `1408.6682 [nucl-th]` (2015) (cit. on pp. 31, 32).
144. Acharya, S. *et al.* Scattering studies with low-energy kaon-proton femtoscopy in proton-proton collisions at the LHC. *Phys. Rev. Lett.* **124,** 092301 (2020) (cit. on p. 37).
145. Kamiya, Y., Hyodo, T., Morita, K., Ohnishi, A. & Weise, W. K^-p Correlation Function from High-Energy Nuclear Collisions and Chiral SU(3) Dynamics. *Phys. Rev. Lett.* **124,** 132501 (2020) (cit. on pp. 37, 38, 103).
146. Haidenbauer, J. Coupled-channel effects in hadron–hadron correlation functions. *Nucl. Phys.* **A981,** 1–16 (2019) (cit. on pp. 37, 101, 103).
147. Evans, L. & Bryant, P. LHC Machine. *Journal of Instrumentation* **3,** S08001–S08001 (2008) (cit. on p. 39).
148. Mobs, E. The CERN accelerator complex. General Photo. `https://cds.cern.ch/record/2636343` (Aug. 2018) (cit. on p. 40).
149. Wenninger, J. Operation and Configuration of the LHC in Run 2. `https://cds.cern.ch/record/2668326` (Mar. 2019) (cit. on p. 39).
150. Aamodt, K. *et al.* The ALICE experiment at the CERN LHC. *J. Instr.* **3,** S08002 (2008) (cit. on pp. 40, 42, 43, 45).
151. Definition of the ALICE Coordinate System and Basic Rules for Sub-detector Components Numbering `https://edms.cern.ch/document/406391/2`. ALICE-INT-2003-038, Accessed: 2020-03-21 (cit. on p. 41).
152. Tauro, A. *ALICE Schematics* General Photo. May 2017. `https://cds.cern.ch/record/2263642` (cit. on p. 41).
153. Physics selection news - Pile up supression on track level `https://indico.cern.ch/event/489470/contributions/2191959/attachments/1286968/1914817/2016-06-08-kryshen-ps-forum.pdf`. Accessed: 2020-03-22 (cit. on pp. 42, 43, 45).
154. Abelev, B. B. *et al.* Performance of the ALICE Experiment at the CERN LHC. *Int. J. Mod. Phys.* **A29,** 1430044 (2014) (cit. on pp. 42, 43, 46–48, 51, 52, 54, 57, 58, 74).
155. Aamodt, K. *et al.* Alignment of the ALICE Inner Tracking System with cosmic-ray tracks. *JINST* **5,** P03003 (2010) (cit. on p. 43).
156. Alme, J. *et al.* The ALICE TPC, a large 3-dimensional tracking device with fast readout for ultra-high multiplicity events. *Nucl. Instrum. Meth* **A622,** 316–367 (2010) (cit. on pp. 43–45).
157. Akindinov, A. *et al.* Performance of the ALICE Time-Of-Flight detector at the LHC. *Eur. Phys. J. Plus* **128,** 44 (2013) (cit. on p. 45).
158. Carnesecchi, F. Performance of the ALICE Time-Of-Flight detector at the LHC. *JINST* **14,** C06023–C06023 (2019) (cit. on pp. 45, 46).

159. *AliROOT: Alice software framework* https://github.com/alisw/AliRoot. Acessed: 02.06.2020 (cit. on p. 46).

160. Brun, R. *et al.* Computing in ALICE. *Nuclear Instruments and Methods in Physics Research Section A: Accelerators, Spectrometers, Detectors and Associated Equipment* **502.** Proceedings of the VIII International Workshop on Advanced Computing and Analysis Techniques in Physics Research, 339–346 (2003) (cit. on p. 46).

161. Brun, R. & Rademakers, F. ROOT: An object oriented data analysis framework. *Nucl. Instrum. Meth.* **A389,** 81–86 (1997) (cit. on p. 46).

162. *AliPhysics: ALICE Analysis Repository* https://github.com/alisw/AliPhysics. Acessed: 02.06.2020 (cit. on p. 47).

163. The ALICE definition of primary particles. `https://cds.cern.ch/record/2270008` (June 2017) (cit. on p. 48).

164. Wiechula, J. Commissioning and calibration of the ALICE-TPC Dissertation (Goethe-Universität Frankfurt am Main, Frankfurt am Main, 2010) (cit. on p. 48).

165. *ALICE Figure repository* https://alice-figure.web.cern.ch/. Acessed: 02.06.2020 (cit. on pp. 50, 52).

166. Bethe, H. Zur Theorie des Durchgangs schneller Korpuskularstrahlen durch Materie. *Annalen der Physik* **397,** 325–400 (1930) (cit. on p. 50).

167. Bloch, F. Zur Bremsung rasch bewegter Teilchen beim Durchgang durch Materie. *Annalen der Physik* **408,** 285–320 (1933) (cit. on p. 50).

168. Blum, W., Rolandi, L. & Riegler, W. *Particle detection with drift chambers* (2008) (cit. on pp. 50, 51).

169. Hess, B. A. Particle Identification in Jets and High-Multiplicity pp Events with the ALICE TPC PhD thesis (Eberhard Karls Universität Tübingen, June 2015). `https://cds.cern.ch/record/2058633` (cit. on p. 51).

170. Acharya, S. *et al.* Relative particle yield fluctuations in Pb-Pb collisions at $\sqrt{s_{\rm NN}} =$ 2.76 TeV. *Eur. Phys. J.* **C79,** 236 (2019) (cit. on p. 52).

171. Adam, J. *et al.* Enhanced production of multi-strange hadrons in high-multiplicity proton-proton collisions. *Nature Phys.* **13,** 535–539 (2017) (cit. on pp. 55, 60, 92).

172. Heinz, U. & Snellings, R. Collective flow and viscosity in relativistic heavy-ion collisions. *Ann. Rev. Nucl. Part. Sci.* **63,** 123–151 (2013) (cit. on p. 56).

173. Busza, W., Rajagopal, K. & van der Schee, W. Heavy Ion Collisions: The Big Picture, and the Big Questions. *Ann. Rev. Nucl. Part. Sci.* **68,** 339–376 (2018) (cit. on p. 56).

174. Adamova, D. *et al.* Azimuthally differential pion femtoscopy in Pb-Pb collisions at $\sqrt{s_{\rm NN}} = 2.76$ TeV. *Phys. Rev. Lett.* **118,** 222301 (2017) (cit. on p. 56).

175. Adam, J. *et al.* Pseudorapidity and transverse-momentum distributions of charged particles in proton-proton collisions at $\sqrt{s} = 13$ TeV. *Phys. Lett.* **B753,** 319–329 (2016) (cit. on p. 56).

176. Acharya, S. *et al.* First Observation of an Attractive Interaction between a Proton and a Cascade Baryon. *Phys. Rev. Lett.* **123,** 112002 (2019) (cit. on pp. 56, 83, 93, 106, 108–110, 114, 115).

177. Abelev, B. *et al.* Pseudorapidity density of charged particles in p + Pb collisions at $\sqrt{s_{NN}} = 5.02$ TeV. *Phys. Rev. Lett.* **110,** 032301 (2013) (cit. on p. 56).

178. Aamodt, K. *et al.* Centrality dependence of the charged-particle multiplicity density at mid-rapidity in Pb-Pb collisions at $\sqrt{s_{NN}} = 2.76$ TeV. *Phys. Rev. Lett.* **106,** 032301 (2011) (cit. on p. 56).

179. Roesler, S., Engel, R. & Ranft, J. The Monte Carlo Event Generator DPMJET-III in *Advanced Monte Carlo for Radiation Physics, Particle Transport Simulation and Applications* (Springer Berlin Heidelberg, Berlin, Heidelberg, 2001), 1033–1038 (cit. on p. 57).

180. Brun, R., Bruyant, F., Maire, M., McPherson, A. C. & Zanarini, P. GEANT3 (1987) (cit. on p. 57).

181. Adam, J. *et al.* Measurement of pion, kaon and proton production in proton-proton collisions at $\sqrt{s} = 7$ TeV. *Eur. Phys. J.* **C75,** 226 (2015) (cit. on p. 60).

182. Acciarri, M. *et al.* Inclusive Σ^+ and Σ^0 production in hadronic Z decays. *Phys. Lett.* **B479,** 79–88 (2000) (cit. on pp. 60, 65, 113).

183. Acciarri, M. *et al.* Measurement of inclusive production of neutral hadrons from Z decays. *Phys. Lett.* **B328,** 223–233 (1994) (cit. on pp. 60, 65, 113).

184. Sibirtsev, A., Haidenbauer, J., Hammer, H. W. & Meissner, U. G. Phenomenology of the Lambda/Sigma0 production ratio in pp collisions. *Eur. Phys. J.* **A29,** 363–367 (2006) (cit. on p. 65).

185. Adamczewski-Musch, J. *et al.* Σ^0 production in proton nucleus collisions near threshold. *Phys. Lett.* **B781,** 735–740 (2018) (cit. on p. 65).

186. Van Buren, G. The Sigma0 / Lambda ratio in high energy nuclear collisions. *J. Phys.* **G31,** S1127–S1130 (2005) (cit. on p. 65).

187. Borissov, Alexander. Production of Σ^0 Hyperons at LHC with ALICE. *EPJ Web Conf.* **222,** 02002 (2019) (cit. on p. 65).

188. Abelev, B. *et al.* Multi-strange baryon production in pp collisions at $\sqrt{s} = 7$ TeV with ALICE. *Phys. Lett.* **B712,** 309–318 (2012) (cit. on pp. 65, 68, 113).

189. Adam, J. *et al.* Multi-strange baryon production in p-Pb collisions at $\sqrt{s_{\mathbf{NN}}} = 5.02$ TeV. *Phys. Lett.* **B758,** 389–401 (2016) (cit. on pp. 65, 68, 113).

190. Abelev, B. B. *et al.* Production of $\Sigma(1385)^{\pm}$ and $\Xi(1530)^0$ in proton-proton collisions at $\sqrt{s} = 7$ TeV. *Eur. Phys. J.* **C75,** 1 (2015) (cit. on pp. 68, 113).

191. Adamova, D. *et al.* Production of $\Sigma(1385)^{\pm}$ and $\Xi(1530)^{0}$ in p-Pb collisions at $\sqrt{s_{\mathrm{NN}}} = 5.02$ TeV. *Eur. Phys. J.* **C77,** 389 (2017) (cit. on pp. 68, 113).
192. Bock, N. Femtoscopy of proton-proton collisions in the ALICE experiment PhD thesis (Ohio State University, 2011). `https://cds.cern.ch/record/2283140` (cit. on pp. 78, 84).
193. Bodmer, A. R., Usmani, Q. N. & Carlson, J. Binding energies of hypernuclei and three-body ΛNN forces. *Phys. Rev.* **C29,** 684–687 (1984) (cit. on p. 80).
194. Kleiss, R., Stirling, W. & Ellis, S. A new Monte Carlo treatment of multiparticle phase space at high energies. *Computer Physics Communications* **40,** 359–373 (1986) (cit. on pp. 81, 105).
195. Stavinskiy, A., Mikhailov, K., Erazmus, B. & Lednický, R. Residual correlations between decay products of $\pi^0\pi^0$ and $p\Sigma^0$ systems. arXiv: `0704.3290 [nucl-th]` (2007) (cit. on p. 83).
196. Fujiwara, Y., Suzuki, Y. & Nakamoto, C. Baryon–Baryon interactions in the SU(6) quark model and their applications to light nuclear systems. *Prog. Part. Nucl. Phys.* **58,** 439–520 (2007) (cit. on p. 83).
197. James, F. & Roos, M. Minuit: A System for Function Minimization and Analysis of the Parameter Errors and Correlations. *Comput. Phys. Commun.* **10,** 343–367 (1975) (cit. on p. 83).
198. Abelev, B. *et al.* Charged kaon femtoscopic correlations in pp collisions at $\sqrt{s}$=7 TeV. *Phys. Rev. D* **87,** 052016 (2013) (cit. on p. 86).
199. Humanic, T. J. Transverse-velocity scaling of femtoscopy in $\sqrt{s} = 7$ TeV proton-proton collisions. *J. Phys. G* **45,** 055101 (2018) (cit. on p. 86).
200. Adam, J. *et al.* Multiplicity dependence of charged pion, kaon, and (anti)proton production at large transverse momentum in p-Pb collisions at $\sqrt{s_{\mathrm{NN}}}$ = 5.02 TeV. *Phys. Lett.* **B760,** 720–735 (2016) (cit. on p. 87).
201. Knospe, A. G., Markert, C., Werner, K., Steinheimer, J. & Bleicher, M. Hadronic resonance production and interaction in partonic and hadronic matter in the EPOS3 model with and without the hadronic afterburner UrQMD. *Phys. Rev.* **C 93,** 014911 (2016) (cit. on p. 88).
202. Kisiel, A., Gałażyn, M. & Bożek, P. Pion, kaon, and proton femtoscopy in Pb–Pb collisions at $\sqrt{s_{NN}}$=2.76 TeV modeled in (3+1)D hydrodynamics. *Phys. Rev.* **C90,** 064914 (2014) (cit. on p. 92).
203. Khachatryan, V. *et al.* Evidence for collectivity in pp collisions at the LHC. *Phys. Lett.* **B 765,** 193–220 (2017) (cit. on p. 92).
204. Khachatryan, V. *et al.* Observation of Long-Range Near-Side Angular Correlations in Proton-Proton Collisions at the LHC. *JHEP* **09,** 091 (2010) (cit. on p. 92).
205. Acharya, S. *et al.* Multiplicity dependence of light-flavor hadron production in pp collisions at $\sqrt{s}$ = 7 TeV. *Phys. Rev.* **C99,** 024906 (2019) (cit. on p. 92).

206. Adye, T. Unfolding algorithms and tests using RooUnfold, 313–318. 6 p. `http://cds.cern.ch/record/1349242` (May 2011) (cit. on p. 95).

207. *RooUnfold* https://gitlab.cern.ch/RooUnfold/RooUnfold. Acessed: 21.07.2020 (cit. on pp. 95, 97).

208. D'Agostini, G. Improved iterative Bayesian unfolding. arXiv: `1010.0632 [physics.data-an]` (Oct. 2010) (cit. on p. 96).

209. Malaescu, B. An Iterative, dynamically stabilized method of data unfolding. arXiv: `0907.3791 [physics.data-an]` (July 2009) (cit. on p. 97).

210. Yuki, K. private communication. July 28, 2020 (cit. on pp. 103, 115).

211. Efron, B. & Stein, C. The Jackknife Estimate of Variance. *Ann. Statist.* **9,** 586–596 (May 1981) (cit. on p. 113).